UNIVERSITY OF CALIFORNIA,
IRVINE

The Interstellar Medium of Dusty Galaxies, Photometric Redshifts with Self-Organizing Maps, and Cosmic Infrared Background Fluctuations

DISSERTATION

submitted in partial satisfaction of the requirements
for the degree of

DOCTOR OF PHILOSOPHY

in Physics

by

Derek Nathaniel Diaz Wilson

Dissertation Committee:
Professor Asantha Cooray, Chair
Professor Michael Cooper
Professor David Kirkby

2021

DEDICATION

To

my family and friends

TABLE OF CONTENTS

LIST OF FIGURES

LIST OF TABLES

ACKNOWLEDGEMENTS

I would like to express my gratitude to my advisor, Professor Asantha Cooray, for his support and guidance over the duration of my graduate studies.

I would also like to express my gratitude to my fellow graduate students and post-docs in the research group for their support and friendship. Thank you to Milad Pourrahmani, Hooshang Nayyeri, Hasitha Eranda, and Kevin Andrade for the insightful conversations.

In addition, I would like to thank my committee members, Professor Michael Cooper, Professor David Kirkby, and Professor David Buote (advancement committee).

A significant portion of the text in this dissertation is a reprint of the material as it appears in "Stacked Average Far-infrared Spectrum of Dusty Star-forming Galaxies from the *Herschel*/SPIRE Fourier Transform Spectrometer" (ApJ, 848, 30) and "Photometric Redshift Estimation with Galaxy Morphology Using Self-Organizing Maps" (ApJ, 888, 83). Some of the co-authors listed in these publications directed and supervised research which forms the basis for the following dissertation. I would like to acknowledge the Astrophysical Journal for granting permission to reproduce my previously published works in this dissertation. A thank you as well to the co-authors who contributed to my published works: Asantha Cooray, Hooshang Nayyeri, Matteo Bonato, Charles Bradford, David Clements, Gianfranco De Zotti, Tanio Díaz-Santos, Duncan Farrah, Georgios Magdis, Michał Michałowski, Chris Pearson, Dimitra Rigopoulou, Ivan Valtchanov, Lingyu Wang, Julie Wardlow, and Boris Häußler.

I would like to make a few acknowledgements regarding funding, data, and scientific instruments used over my graduate career. Support for Chapters 1 and 2 was provided in part by NSF grant AST-1313319, NASA grant NNX16AF38G, GAANN P200A150121, HST-GO-13718, HST-GO-14083, and National Science Foundation Award #1633631. Support for Chapter 3 came partially from SPHEREx, CIBER, and a UCI Irvine Department of Physics Fellowship.

I would thank Rodrigo Herrera-Camus, Eckhard Sturm, Javier Gracia-Carpio, and SHINING for sharing a compilation of [C II], [O III], and [O I] line measurements as well as FIR data to which I compare my results in Chapter 1. I also wish to thank Paul Van der Werf for the very useful suggestions and recommendations regarding Chapter 1.

Concerning the scientific instruments used in my work, the *Herschel* spacecraft was designed, built, tested, and launched under a contract to ESA managed by the

Herschel/Planck Project team by an industrial consortium under the overall responsibility of the prime contractor Thales Alenia Space (Cannes), and including Astrium (Friedrichshafen) responsible for the payload module and for system testing at spacecraft level, Thales Alenia Space (Turin) responsible for the service module, and Astrium (Toulouse) responsible for the telescope, with in excess of a hundred subcontractors. SPIRE has been developed by a consortium of institutes led by Cardiff University (UK) and including Univ. Lethbridge (Canada); NAOC (China); CEA, LAM (France); IFSI, Univ. Padua (Italy); IAC (Spain); Stockholm Observatory (Sweden); Imperial College London, RAL, UCL-MSSL, UKATC, Univ. Sussex (UK); and Caltech, JPL, NHSC, Univ. Colorado (USA). This development has been supported by national funding agencies: CSA (Canada); NAOC (China); CEA, CNES, CNRS (France); ASI (Italy); MCINN (Spain); SNSB (Sweden); STFC, UKSA (UK); and NASA (USA). HIPE is a joint development by the *Herschel* Science Ground Segment Consortium, consisting of ESA, the NASA *Herschel* Science Center, and the HIFI, PACS and SPIRE consortia. My research has made use of the NASA/IPAC Extragalactic Database (NED) which is operated by the Jet Propulsion Laboratory, California Institute of Technology, under contract with the National Aeronautics and Space Administration. Chapter 2 contains work based on observations taken by the CANDELS Multi-Cycle Treasury Program with the NASA/ESA HST, which is operated by the Association of Universities for Research in Astronomy, Inc., under NASA contract NAS5-26555. Chapter 3 work is based [in part] on observations made with the *Spitzer* Space Telescope, which was operated by the Jet Propulsion Laboratory, California Institute of Technology under a contract with NASA. And finally, I would like to express my gratitude to the developers of Python, and in particular Numpy, Matplotlib, and Pandas, whose software I used extensively.

CURRICULUM VITAE

Derek Nathaniel Diaz Wilson

EDUCATION

Doctor of Philosophy in Physics **2021**

University of California, Irvine *Irvine, CA*

Master of Science in Physics **2019**

University of California, Irvine *Irvine, CA*

Bachelor of Arts in Physics & Astrophysics **2015**

University of California, Berkeley *Berkeley, CA*

RESEARCH EXPERIENCE

Graduate Researcher **2015 – 2021**

University of California, Irvine *Irvine, CA*

Research Assistant **2015**

Berkeley Space Sciences Laboratory *Berkeley, CA*

TEACHING EXPERIENCE

Graduate Teaching Assistant **2019**

University of California, Irvine *Irvine, CA*

Graduate Teaching Assistant **2015**

University of California, Irvine *Irvine, CA*

PUBLICATIONS

"Stacked Average Far-infrared Spectrum of Dusty Star-forming Galaxies from the *Herschel*/SPIRE Fourier Transform Spectrometer",
Wilson, D., Cooray, A., Nayyeri, H., et al., *The Astrophysical Journal*, 848:30(31pp), 2017

"Photometric Redshift Estimation with Galaxy Morphology Using Self-Organizing Maps",
Wilson, D., Nayyeri, H., Cooray, A., et al., *The Astrophysical Journal*, 888:83(9pp), 2020

"iPTF16geu: A Multiply Imaged, Gravitationally Lensed Type 1A Supernova",
Goobar, A., **et al.**, *Science,* 356:291(5pp), 2017

"SOFIA/HAWC+ Detection of a Gravitationally Lensed Starburst Galaxy at z = 1.03",
Ma, J., **et al.**, *The Astrophysical Journal*, 864:60(8pp), 2018

ABSTRACT OF THE DISSERTATION

The Interstellar Medium of Dusty Galaxies, Photometric Redshifts with Self-Organizing Maps, and Cosmic Infrared Background Fluctuations

by

Derek Nathaniel Diaz Wilson

Doctor of Philosophy in Physics

University of California, Irvine, 2021

Professor Asantha Cooray, Chair

In this dissertation, we present three studies of various extragalactic sources at infrared wavelengths. In Chapter 1, we used stacking to find the average far-infrared spectra of a sample of 197 dusty, star-forming galaxies (DSFGs) at $0.005 < z < 4$ using about 90% of the *Herschel* Space Observatory SPIRE Fourier Transform Spectrometer (FTS) extragalactic data archive based on 3.5 years of science operations. These spectra explore an observed-frame 447 GHz - 1568 GHz frequency range allowing us to observe the main atomic and molecular lines emitted by gas in the interstellar medium. These stacked spectra are used to determine the average gas density and radiation field strength in the photodissociation regions (PDRs) of dusty, star-forming galaxies. For the high-z ($0.8 < z < 4$) sample, PDR models suggest a molecular gas distribution in the presence of a radiation field that is at least a factor of 10^3 larger than the Milky-Way and with a neutral gas density of roughly $10^{4.5}$ to $10^{5.5}$ cm^{-3}. The corresponding PDR models for the low-z sample suggest a UV radiation field and gas density comparable to those at high-z. In Chapter 2, we use

multi-band optical and near-infrared photometric observations of galaxies in the Cosmic Assembly Near-Infrared Deep Extragalactic Legacy Survey (CANDELS) to predict photometric redshifts using an artificial neural network called a Self-Organizing Map (SOM). The multi-band observations span over 0.39 μm to 8.0 μm for a sample of ~1000 galaxies in the GOODS-S field for which robust size measurements are available from *Hubble* Space Telescope Wide Field Camera 3 observations. We use the SOM to map the multi-dimensional photometric and galaxy size observations while taking advantage of existing spectroscopic redshifts at $0 < z < 2$ for independent training and testing sets. We show that use of photometric and morphological data led to redshift estimates comparable to redshift measurements from SED modeling and from self-organizing maps without morphological measurements. In Chapter 3, power spectrum methods are used to study fluctuations in the cosmic infrared background with hopes of finding a signature of intra-halo light. We use images of the North Ecliptic Pole (NEP) region observed by *Spitzer* and the *Herschel* Space Observatory to compute the cross-power spectra between *Spitzer* 3.6 μm and 4.5 μm sky maps and *Herschel* 250 μm, 350 μm, and 500 μm sky maps. Weak correlations are found between each of the *Spitzer* × *Herschel* wavelengths (e.g., 3.6 μm × 250 μm), suggesting that there might be some weak correlated emission between near- and far-infrared wavelengths.

Chapter 1: Stacked Average Far-infrared Spectrum of Dusty Star-forming Galaxies from the *Herschel*/SPIRE Fourier Transform Spectrometer

Introduction

Our understanding of galaxy formation and evolution is directly linked to understanding the physical properties of the interstellar medium (ISM) of galaxies [126, 136, 106, 145, 194]. Dusty star-forming galaxies (DSFGs), with star-formation rates in excess of 100 $M_{\odot}$ yr^{-1}, are an important contributor to the star-formation rate density of the Universe [42, 68]. However, our knowledge of the interstellar medium within these galaxies is severely limited due to high dust extinction with typical optical attenuations of $A_V \sim 6$ - 10 mag [40].

Instead of observations of rest-frame UV and optical lines, crucial diagnostics of the ISM in DSFGs can be obtained with spectroscopy at mid- and far-infrared wavelengths [207]. In particular, at far-infrared wavelengths, the general ISM is best studied through atomic fine-structure line transitions, such as the [C II] 158 μm line transition. Such studies complement rotational transitions of molecular gas tracers, such as CO, at mm-wavelengths that are effective at tracing the proto-stellar and dense star-forming cores of DSFGs (e.g. [36]).

Relative to the total infrared luminosities, certain atomic fine-structure emission lines can have line luminosities that are the level of a few tenths of a percent [208, 36, 185, 8, 204, 98]. Far-infrared fine-structure lines are capable of probing the ISM over the whole

range of physical conditions, from those that are found in the neutral to ionized gas in photodissociation regions (PDRs; [223, 104, 105, 243, 199, 124]) to X-ray dominated regions (XDRs; [135, 14, 149, 153]), such as those associated with an AGN, or shocks [79]. Different star-formation modes and the effects of feedback are mainly visible in terms of differences in the ratios of fine-structure lines and the ratio of fine-structure line to the total IR luminosity [211, 128, 74]. Through PDR modeling and under assumptions such as local thermodynamic equilibrium (LTE), line ratios can then be used as a probe of the gas density, temperature, and the strength of the radiation field that is ionizing the ISM gas. An example is [C II]/[O I] vs. [O III]/[O I] ratios that are used to separate starbursts from AGNs (e.g. [205, 77]).

In comparison to the study presented here using *Herschel* SPIRE/FTS [175, 88]) data, we highlight a similar recent study by Wardlow et al. 2017 [237] on the average rest-frame mid-IR spectral line properties using all of their archival high-redshift data from the *Herschel*/PACS instrument [176]. While the sample observed by SPIRE/FTS is somewhat similar, the study with SPIRE extends the wavelength range to rest-frame far-IR lines from the mostly rest-frame mid-IR lines detected with PACS. In a future publication, we aim to present a joint analysis of the overlap sample between SPIRE/FTS and PACS, but here we mainly concentrate on the analysis of FTS data and the average stacked spectra as measured from the SPIRE/FTS data. We also present a general analysis with interpretation based on PDR models and comparisons to results in the literature on ISM properties of both low- and high-z DSFGs. This chapter is organized as follows. In Sections 2 and 3, we describe the archival data set and the method by which the data were stacked, respectively. Section 4 presents the stacked spectra. In Section 5, the average emission from detected

spectral lines is used to model the average conditions in PDRs of dusty, star-forming galaxies. In addition, the fluxes derived from the stacked spectra are compared to various measurements from the literature. We discuss my results and conclude with a summary. A flat-ΛCDM cosmology of $\Omega_{m,0} = 0.27$, $\Omega_{\Lambda,0} = 0.73$, and $H_0 = 70$ km s^{-1} Mpc^{-1} is assumed. With *Herschel* operations now completed, mid- and far-IR spectroscopy of DSFGs will not be feasible until the launch of next far-IR mission, expected in the 2030s, such as SPICA [202] or the Origins Space Telescope [154]. The average spectra present here will remain the standard in the field and will provide crucial input for the planning of the next mission.

Data

Despite the potential applications of mid- and far-IR spectral lines, the limited wavelength coverage and sensitivity of far-IR facilities have restricted the vast majority of observations to galaxies in the nearby universe. A significant leap came from the *Herschel* Space Observatory [175], thanks to the spectroscopic capabilities of the Fourier Transform Spectrometer (FTS; [162, 216]) of the SPIRE instrument [88]. SPIRE covered the wavelength range of 194 μm - 671 μm, making it useful in the detection of ISM fine structure cooling lines, such as [C II] 158 μm, [O III] 88 μm, [N II] 205 μm, and [O I] 63 μm, in high-redshift galaxies and carbon monoxide (CO) and water lines (H_2O) from the ISM of nearby galaxies. The *Herschel* data archive contains SPIRE/FTS data for a total of 231 galaxies, with 197 known to be in the redshift interval $0.005 < z < 4.0$, completed through multiple programs either in guaranteed-time or open-time programs. While most of the galaxies at $0.5 < z < 4$ are intrinsically ultra-luminous IR galaxies (ULIRGS; [190]), with

luminosities greater than 10^{12} $L_{\odot}$, archival observations at $z > 2$ are mainly limited to the brightest dusty starbursts with apparent $L > 10^{13}$ $L_{\odot}$ or hyper-luminous IR galaxies (HyLIRGs). Many of these cases, however, are gravitationally lensed DSFGs and their intrinsic luminosities are generally consistent with ULIRGS. At the lowest redshifts, especially in the range $0.005 < z < 0.05$, many of the targets have $L < 10^{12}$ $L_{\odot}$ or are luminous IR galaxies (LIRGs). While fine-structure lines are easily detected for such sources, most individual archival observations of brighter ULIRGs and HyLIRGs at $z > 1$ do not reveal clear detections of far-infrared fine-structure lines despite their high intrinsic luminosities [81], except in a few very extreme cases such as the Cloverleaf quasar host galaxy [225]. Thus, instead of individual spectra, we study the averaged stacked spectra of DSFGs, making use of the full SPIRE/FTS archive of *Herschel*.

Given the wavelength range of SPIRE and the redshifts of observed galaxies, to ease stacking, we subdivide the full sample of 197 galaxies into five redshift bins (Figure 1), namely, low-redshift galaxies at $0.005 < z < 0.05$ and $0.05 < z < 0.2$, intermediate redshifts $0.2 < z < 0.5$, and high-redshift galaxies at $0.8 < z < 2$ and $2 < z < 4$. Unfortunately, due to lack of published redshifts, we exclude observations of 24 targets or roughly 10% of the total archival sample (231 sources) from the stacking analysis expected to be mainly at $z > 1$ based on the sample selection and flux densities. This is due to the fact that redshifts are crucial to shift spectra to a common redshift, usually taken to be the mean of the redshift distribution in each of the bins. For these 24 cases we also did not detect strong individual lines, which would allow us to establish a redshift conclusively with the SPIRE/FTS data. Most of these sources are likely to be at $z > 1$ and we highlight this subsample in the Appendix to encourage follow-up observations. We also note that the

SPIRE/FTS archive does not contain any observations of galaxies in the redshift interval of 0.5 to 0.8 and even in the range of $0.8 < z < 2$, observations are simply limited to 8 galaxies, compared to attempted observations of at least 28 galaxies, and possibly as high as 48 galaxies when including the subsample without redshifts, at $z > 2$.

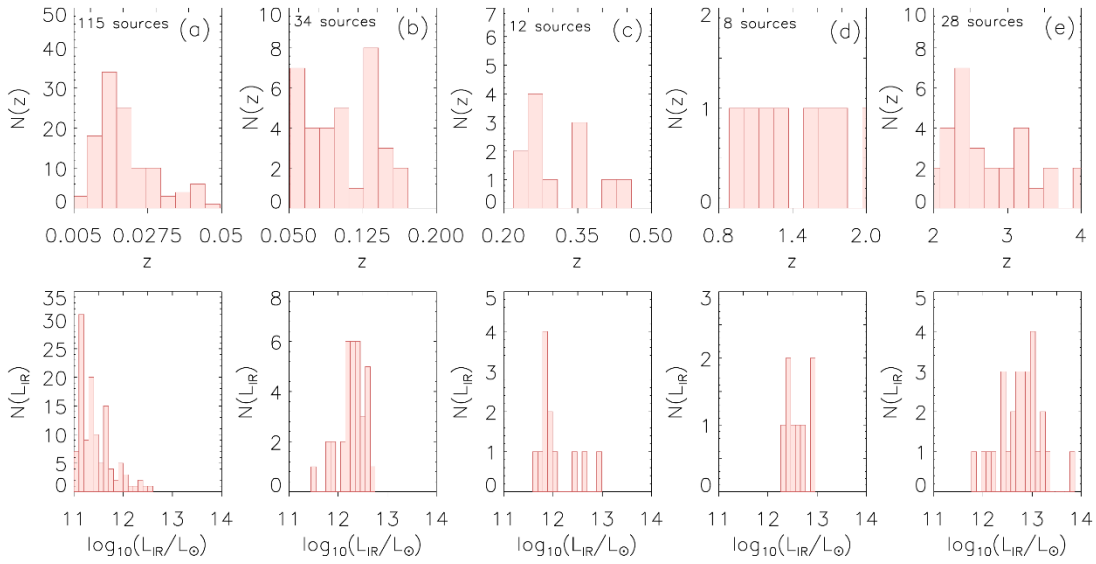

Figure 1: FTS redshift and luminosity histograms.

Top: Distribution of redshifts for sources included in each of the five redshift bins: (a) 115 sources with $0.005 < z < 0.05$, (b) 34 sources with $0.05 < z < 0.2$, (c) 12 sources with $0.2 < z < 0.5$, (d) 8 sources with $0.8 < z < 2$, and (e) 28 sources with $2 < z < 4$. The low number of sources in the two intermediate redshift bins of $0.2 < z < 0.5$ and $0.8 < z < 2$ is due to lack of observations. *Bottom*: Total infrared luminosities (rest-frame 8-1000 μm) for sources included in each of the five redshift bins above with a median luminosity of $\log_{10}(L_{IR}/L_{\odot}) = 11.35, 12.33, 11.89, 12.53$, and 12.84, respectively. For lensed sources in the $2 < z < 4$ range, we have made a magnification correction using best-determined lensing models published in the literature.

The data used in the analysis consist of 197 publicly-available *Herschel* SPIRE/FTS spectra, as part of various Guaranteed Time (GT) and Open-Time (OT) *Herschel* programs summarized in the Appendix (Table 9: Observation IDs and Integration Times). Detailed properties of the sample are also presented in the Appendix (Table 10) for both low and high redshifts where the dividing line is at z = 0.8, with 161 and 36 objects respectively. Table 10 also lists 34 sources at the end with existing FTS observations but which were not used in the analysis. The majority of unused sources have unknown or uncertain spectroscopic redshifts. This includes MACS J2043-2144 for which a single reliable redshift is currently uncertain as there is evidence for three galaxies with z = 2.040, z = 3.25, and z = 4.68 within the SPIRE beam [255]. The sources SPT 0551-50 and SPT 0512-59 have known redshifts but do not have magnification factors. The low-redshift sample is restricted to DSFGs with z > 0.005 only. This limits the bias in the stacked low-z spectrum from bright near-by galaxies such as M81 and NGC 1068. The selection does include bright sources such as Arp 220 and Mrk 231 in the stack, but we study their impact by breaking the lowest redshift sample into luminosity bins, including a ULIRG bin with $L_{IR} > 10^{12}\ L_{\odot}$. The *Herschel* sample of dusty, star-forming galaxies is composed of LIRGS with $10^{11}\ L_{\odot} < L < 10^{12}\ L_{\odot}$ and ULIRGS with $L > 10^{12}\ L_{\odot}$. The sample is heterogeneous, consisting of AGN, starbursts, QSOs, LINERs, and Seyfert types 1 and 2. The low-redshift SPIRE/FTS spectra were taken as part of the HerCULES program ([188]; PI van der Werf), HERUS program ([171]; PI Farrah), and the Great Observatory All-Sky LIRG Survey (GOALS; [11, 142], PI: N. Lu) along with supplementary targets from the KPGT_wilso01_1 (PI: C. Wilson) and OT2_drigopou_3 (PI: D. Rigopoulou) programs. At 0.2 < z < 0.5, the SPIRE/FTS sample of 11 galaxies is limited to Magdis et al. 2014 [146], apart from one source, IRAS 00397-1312, from Helou & Walker

1988 [96] and Farrah et al. 2007 [70]. Note that the Magdis et al. 2014 sample contained two galaxies initially identified to be at $z < 0.5$, but later found to be background $z > 2$ galaxies that were lensed by the $z < 0.5$ foreground galaxy. Those data are included in the high-redshift sample.

The high-redshift sample at $z > 0.8$ primarily comes from open-time programs that followed-up lensed galaxies from HerMES [166] and *H*-ATLAS [66], and discussed in [81]. Despite the boosting from lensing, only a few known cases of individual detections exist in the literature: NB.v1.43 at $z = 1.68$ [82, 224], showing a clear signature of [C II] that led to a redshift determination for the first-time with a far-IR line, SMMJ2135-0102 (Cosmic eyelash; [114]), ID.81 and ID.9 [164].

With lens models for *Herschel* -selected lensed sources now in the literature (e.g., [33, 34]), the lensing magnification factors are now known with reasonable enough accuracy that the intrinsic luminosities of many of these high-redshift objects can be established. The $z > 0.8$ sample is composed of 30 high-redshift, gravitationally-lensed galaxies (e.g., OT1_rivison_1, OT2_rivison_2) and 6 un-lensed galaxies (OT1_apope_2 and one each from OT1_rivison_1 and OT2_drigopou_3).

The distribution of redshifts can be found in Figure 1, where we have subdivided the total distribution into five redshift bins: $0.005 < z < 0.05$, $0.05 < z < 0.2$, $0.2 < z < 0.5$, $0.8 < z < 2$, and $2 < z < 4$. The mean redshifts in the five redshift bins are $z = 0.02$, $z = 0.1$, and $z = 0.3$, $z = 1.4$, and $z = 2.8$, respectively. For reference, in Figure 1, we also show the 8-1000 μm luminosity distribution in the five redshift bins. The distribution spans mostly from LIRGS at low redshifts to ULIRGS at $0.05 < z < 0.2$ and above. In the highest redshift bins, we find ULIRGS again, despite increase in redshift, due to the fact that most of these are

lensed sources; with magnification included, the observed sources will have apparent luminosities consistent with HyLIRGS. Unfortunately, there is a lack of data between redshifts of $z \sim 0.2$ and $z \sim 1$, with the Magdis et al. 2014 [146] sample and the spectrum of IRAS 00397-1312 from HERUS [171] being the only SPIRE/FTS observed spectra in this range.

In general, SPIRE/FTS observations we analyze here were taken in high resolution mode, with a spectral resolving power of 300-1000 through a resolution of 1.2 GHz and frequency span of 447 GHz-1568 GHz. The data come from two bolometer arrays: the spectrometer short wavelength (SSW) array, covering 194 μm - 318 μm (944 GHz - 1568 GHz) and the spectrometer long wavelength (SLW) array, covering 294 μm - 671 μm (447 GHz - 1018 GHz). The two arrays have different responses on the sky with the full-width half-maximum (FWHM) of the SSW beam at 18" and the SLW beam varying from 30" to 42" with frequency [216]. The SPIRE/FTS data typically involves ~90-100 scans of the faint, high-redshift sources and about half as many scans for the lower-redshift sources. Total integration times for each source are presented in Table 9. Typical total integration times of order 5000 seconds achieve unresolved spectral line sensitivities down to $\sim 10^{-18}$ W m^{-2} (3σ).

Stacking Analysis

The Level-2 FTS spectral data are procured from the *Herschel* Science Archive (HSA) where they have already been reduced using version SPGv14.1.0 of the *Herschel* Interactive Processing Environment (HIPE, [169]) SPIRE spectrometer single pointing pipeline [80] with calibration tree SPIRE_CAL_14_2. We use the point-source calibrated spectra. Additional

steps are required to further reduce the data. An important step is the background subtraction. While *Herschel*/SPIRE-FTS observations include blank sky dark observations taken on or around the same observing day as the source observations are taken, they do not necessarily provide the best subtraction of the background [171]. The same study also showed that attempts to use a super-dark by combining many dark-sky observations into an average background do not always yield an acceptable removal of the background from science observations. Instead, the off-axis detectors present in each of the SPIRE arrays are used to construct a "dark" spectrum [177]. These off-axis detectors provide multiple measurements of the sky and telescope spectra simultaneous with the science observations and are more effective at correcting the central spectrum. The background is constructed by taking the average of the off-axis detector spectra, but only after visually checking the spectra via HIPE's background subtraction script [177] to ensure that the background detectors do not contain source emission. If any outliers are detected, they are removed from the analysis. Such outliers are mainly due to science observations that contain either an extended source or a random source that falls within the arrays. We use the average from all acceptable off-axis detectors from each science observation as the background to subtract from the central one. In a few unusual cases, a continuum bump from residual telescope emission in some spectra was better subtracted using a blank sky dark observation rather than an off-axis subtraction. In these cases, background subtraction was performed using the blank sky dark observation.

As part of the reduction, and similar to past analysis (e.g., [188, 171]), we found a sizable fraction of the sources to show a clear discontinuity in flux between the continuum levels of the central SLW and SSW detectors in the overlap frequency interval between 944

GHz and 1018 GHz. If this discontinuity is still visible after the background subtraction (off-axis detector background or blank sky observation background) as discussed above, then we considered this offset to be an indication of extended source emission. For extended sources, we subtract a blank sky dark (and not an off-axis dark, as off-axis detectors may contain source emission) and correct for the source's size with HIPE's semiExtendedCorrector tool (SECT, [246]), following the Rosenberg et al. 2015 [188] method of modeling the source as a Gaussian and normalizing the spectra for a Gaussian reference beam of 42''.

There are two other sources of discontinuity between the SLW and SSW detectors, one from a flux droop in the central SLW detector due to the recycling of the SPIRE cooler [171] and another due to potential pointing offsets [227]. Due to the differences in the size of the SLW and SSW SPIRE beams, a pointing offset can cause a larger loss of flux in the SSW beam than in the SLW beam. If an extended source correction was not able to fix the discontinuity between the SLW and SSW detectors, the discontinuity may likely be coming from the cooler recycling or from a pointing offset. We assume that these two effects are negligible, as we remove any continuum remaining after the application of SECT from the central SLW and SSW detectors by subtracting a second-order polynomial fit to the continuum.

Once the corrected individual spectra are obtained, the high-redshift lensed sample was corrected for lensing magnification. The magnification factors come from lens models based on Sub-millimeter Array (SMA) and Keck/NIRC2-LGS adaptive optics observations [33, 34]. Though these are mm-wave and optical magnifications while the present study involves far-IR observations, we ignore any effects of differential magnification [195]. We

simply make use of the best determined magnification factor, mainly from SMA analysis [33]. For the overlapping lensed source sample with PACS spectroscopy, the lensing magnification factor used here is consistent with values used in Wardlow et al. 2017 [237]. Sources with PACS spectroscopy that appear in Wardlow et al. 2017 are marked in Table 10.

To obtain the average stacked spectrum in each of the redshift bins or luminosity bins as we discuss later, we follow the stacking procedure outlined by Spilker et al. 2014 [203]. It involves scaling the flux densities in individual spectra in each redshift bin to the flux densities that the source would have were it located at some common redshift (which we take to be the mean redshift in each bin) and then scaling to a common luminosity so that we can present an average spectrum of the sample. For simplicity, we take the mean redshift and median infrared luminosity in each bin and both scale up and scale down individual galaxy spectra in both redshift and luminosity to avoid introducing biases in the average stacked spectrum; however, we note that the sample does contain biases associated with initial sample selections in the proposals that were accepted for *Herschel*/SPIRE-FTS observations. We discuss how such selections impact a precise interpretation of the spectra in the discussion. We now outline the process used in the scaling of spectra.

The background-subtracted flux densities of the spectra are scaled to the flux values that they would have at the common redshift, which was taken to be the mean redshift in each of the redshift categories; namely, $z_{com} = 0.02$ for the $0.005 < z < 0.05$ sources, $z_{com} = 0.1$ for $0.05 < z < 0.2$ sources, $z_{com} = 0.3$ for $0.2 < z < 0.5$ sources, $z_{com} = 1.4$ for $0.8 < z < 2$ sources, and $z_{com} = 2.8$ for $2 < z < 4$ sources. The choice between median or mean redshift

does not significantly affect the overall spectrum or line fluxes. The flux density and error values (error values are obtained from the error column of the level-2 spectrum products from the *Herschel* Science Archive) of each spectrum are multiplied by the scaling factor given in Spilker et al. 2014:

$$f = \left(\frac{D_L(z_{src})}{D_L(z_{com})}\right)^2 \times \left(\frac{1+z_{com}}{1+z_{src}}\right)$$

where D_L is the luminosity distance. The flux density and error values of each spectrum are then representative of the flux density and error values that the source would have were it located at z_{com}. The frequency axes of the scaled spectra are then converted from observed-frame frequencies to rest-frame frequencies. To normalize the spectra, all spectrum flux densities and errors are scaled by a factor such that each source will have the same total infrared luminosity (rest-frame 8-1000 μm); namely, $L_{IR} = 10^{11.35}\ L_\odot$, $10^{12.33}\ L_\odot$, $10^{11.89}\ L_\odot$, $10^{12.53}\ L_\odot$ and $10^{12.84}\ L_\odot$ in each of the five bins, respectively. In the two highest redshift bins, we calculate a total infrared luminosity by fitting a single-temperature, optically-thin, modified blackbody (i.e. greybody with $S(\nu) \propto \nu^\beta B_\nu(T)$ where $B_\nu(T)$ is the Planck function) spectral energy distribution (SED) (commonly used in the literature, e.g. [39, 33]) to the available photometry in the infrared from *Herschel* and public IRSA data. For this we use the publicly available code developed by Casey et al. 2012 [39] assuming a fixed emissivity ($\beta = 1.5$) (e.g. [33]). The resulting infrared luminosities are presented in Table 10, along with lensing magnification factors and references. Luminosities in the tables are corrected for lensing magnification (where applicable), and we ignore the uncertainty in magnification from existing lens models. Sources without a magnification of factor μ are not affected by gravitational lensing. After the spectra are scaled to a common IR luminosity, a

second-order polynomial is then fit to the continuum of each source and is subsequently subtracted from each source spectrum. Instrumental noise impacts the continuum subtraction and leads to residuals in the continuum-subtracted spectrum. These residuals in return impact the detection of faint lines.

Several objects have multiple FTS spectra, taken at multiple time intervals as part of the same program or observations conducted in different programs. Multiples of the same object are combined into a single average spectrum by calculating the mean flux density at each frequency for each of the repeats. This mean spectrum is what is used in the stacking procedure.

After the spectra are calibrated and scaled, the flux values at each frequency in the rest frame of the spectra are stacked using an inverse variance weighting scheme with the inverse of the square of the flux errors as weights. In the $0.005 < z < 0.05$ stack, a minority of the sources (though still a significant subset of the total) have high signal-to-noise ratios and thus dominate over the other sources when using the inverse variance weighting scheme. To avoid this bias without throwing out sources, we stack the $0.005 < z < 0.05$ bin by calculating the mean stack without inverse variance weighting. The unweighted mean stack is shown in Figure 3. The inverse variance weighted stack for this redshift bin is presented in the Appendix for comparison.

The noise level of the stacked spectrum in each of the five redshift bins is estimated using a jackknife technique in which we remove one source from the sample and then stack. The removed source is replaced, and this process is repeated for each source in the sample. The jackknife error in the mean of the flux densities at each frequency from the jackknifed stacks is taken to be the 1σ noise level in the overall stacked spectrum in each

redshift bin. The red curves in the upper panels of Figure 3 - Figure 7 are found by smoothing the jackknife error curve.

Stacking Results

The stacked spectra in each of the five redshift bins are shown in Figure 3 - Figure 7, while in Figure 8 we show the mean stacks (no inverse-variance weighting) for the $0.005 < z < 0.05$ bin by sub-dividing the sample into five luminosity bins given by $10^{11.0}\ L_\odot < L_{IR} < 10^{11.2}\ L_\odot$, $10^{11.2}\ L_\odot < L_{IR} < 10^{11.4}\ L_\odot$, $10^{11.4}\ L_\odot < L_{IR} < 10^{11.6}\ L_\odot$, $10^{11.6}\ L_\odot < L_{IR} < 10^{12.0}\ L_\odot$, and $L_{IR} > 10^{12.0}\ L_\odot$. For the purposes of this study and for PDR model interpretations, we concentrate on lines that are detected at a signal-to-noise ratio greater than 3.5. The stacks do reveal detections with a signal-to-noise ratios at the level of 2.5 to 3; we will return to those lines in future work.

The natural line shape of the SPIRE FTS is a sinc profile [216]. A sinc profile is typically used to fit unresolved spectral lines. However, a sinc profile may be too thin to fully capture the width of broad partially-resolved extragalactic spectral lines, in which case a sinc-Gauss (sinc convolved with a Gaussian) can provide a better fit (see http://*Herschel*.esac.esa.int/hcss-doc-15.0/index.jsp\#spire_drg:_start). For spectral lines with the same intrinsic line width, the sinc-Gauss fit gives a higher flux measurement than the sinc fit; the ratio of sinc-Gauss to sinc flux increases as a function of increasing spectral line frequency. For broad line-widths, the sinc-Gauss fit contains significantly more flux than the pure sinc fit. Because the stacked SPIRE/FTS spectra contain a variety of widths for each spectral line and because the width of each line is altered when scaling the frequency axis of the spectra to the common-redshift frame, the sinc profile appeared to

under-fit all of the spectral lines in the stacked spectra, so a sinc-Gauss profile was used for flux extraction. See Figure 9 - Figure 12. The width of the sinc component of the fit was fixed at the native SPIRE FTS resolution of 1.184 GHz, and the width of the Gaussian component was allowed to vary. The integral of the fitted sinc-Gauss profile was taken to be the measured flux. The fluxes from the fits are presented in Table 1 - Table 3. In the case of an undetected line (i.e., the feature has less than 3.5σ significance), we place an upper limit on its flux by injecting an artificial line with velocity width 300 km s^{-1} (a typical velocity width for these lines; e.g., [146]) into the stack at the expected frequency and varying the amplitude of this line until it is measured with 2σ significance. The flux of this artificial line is taken to be the upper limit on the flux of the undetected line.

The error on the fluxes includes a contribution from the uncertainty in the fits to the spectral lines as well as a 6% uncertainty from the absolute calibration of the FTS. The error due to the fit is estimated by measuring the "bin-to-bin" spectral noise of the residual spectrum in the region around the line of interest (see SPIRE Data Reduction Guide). The residual spectrum is divided into bins with widths of 30 GHz, and the standard deviation of the flux densities within each bin is taken to be the noise level in that bin. Additionally, we incorporate a 15% uncertainty for corrections to the spectra for (semi)-extended sources [188] in the lowest redshift stack. This 15% uncertainty is not included for sources with $z > 0.05$, as these are all point sources (as verified by inspection).

We now discuss the stacking results for the five redshift bins; for simplicity we define low-redshift as $0.005 < z < 0.2$, intermediate as $0.2 < z < 0.5$ and high-redshift as $0.8 < z < 4$; both low and high-redshift have two additional redshift bins. Within these bins we also consider luminosity bins when adequate statistics allow us to further divide

the samples.

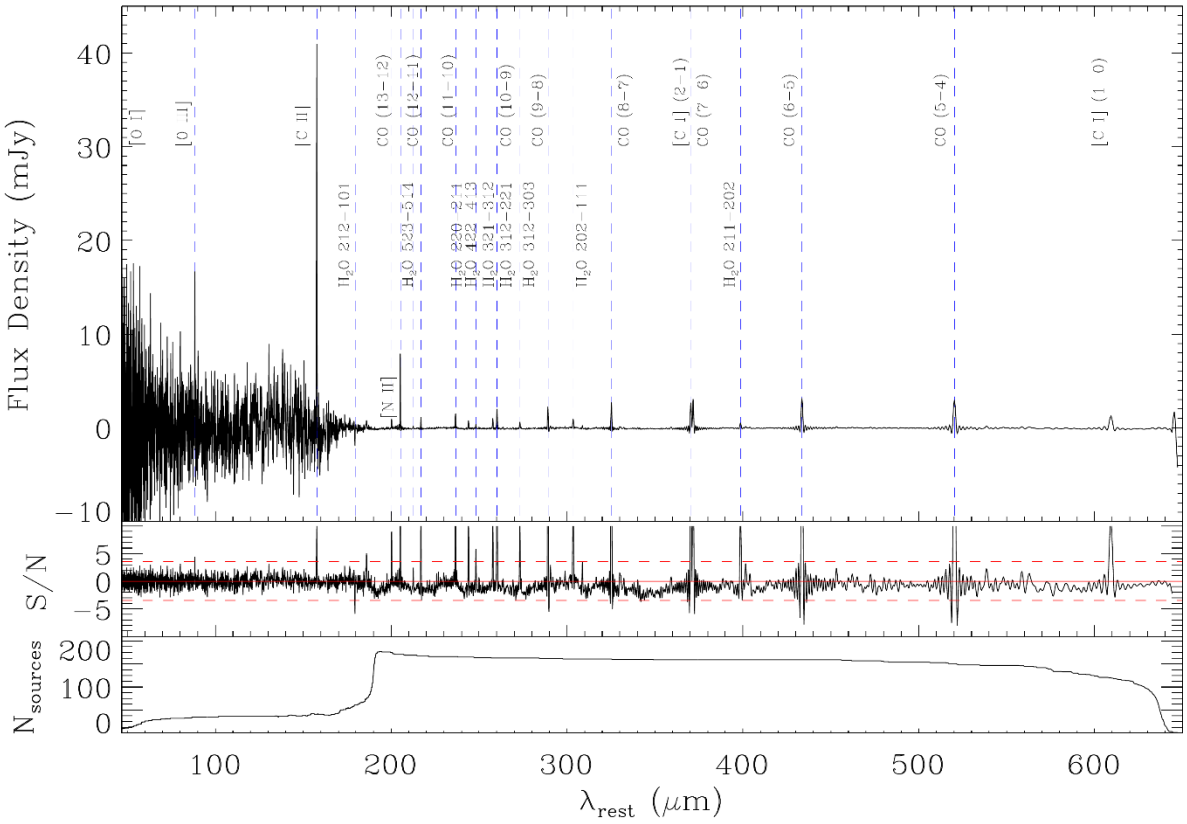

Figure 2: Stacked FTS spectra, all data

Top: Average far-infrared stacked spectrum containing all FTS data. Sources range in redshift from 0.005 < z < 4. This stack serves as a qualitative representation of the average spectrum of all of the *Herschel* spectra. For the purposes of analysis and interpretation, the dataset is split into redshift and luminosity bins for the remainder of this chapter. Dashed blue vertical lines indicate the locations of main molecular emission lines. We detect the fine-structure lines [C II], [O I], and [O III] as well as the CO emission line ladder from *J* = 13-12 to *J* = 5-4. Also detected are the two lowest [C I] emissions at 492 GHz (609 μm) and 809 GHz (370 μm), [N II] at 1461 GHz (205 μm) and the water lines within the frequency (wavelength) range covered in this stack from 50 μm to 652 μm). *Middle*: Signal-to-noise ratio. The horizontal dashed line indicates S/N = 3.5, and the solid red line represents S/N = 0. *Bottom*: The number of sources that contribute to the stack at each wavelength.

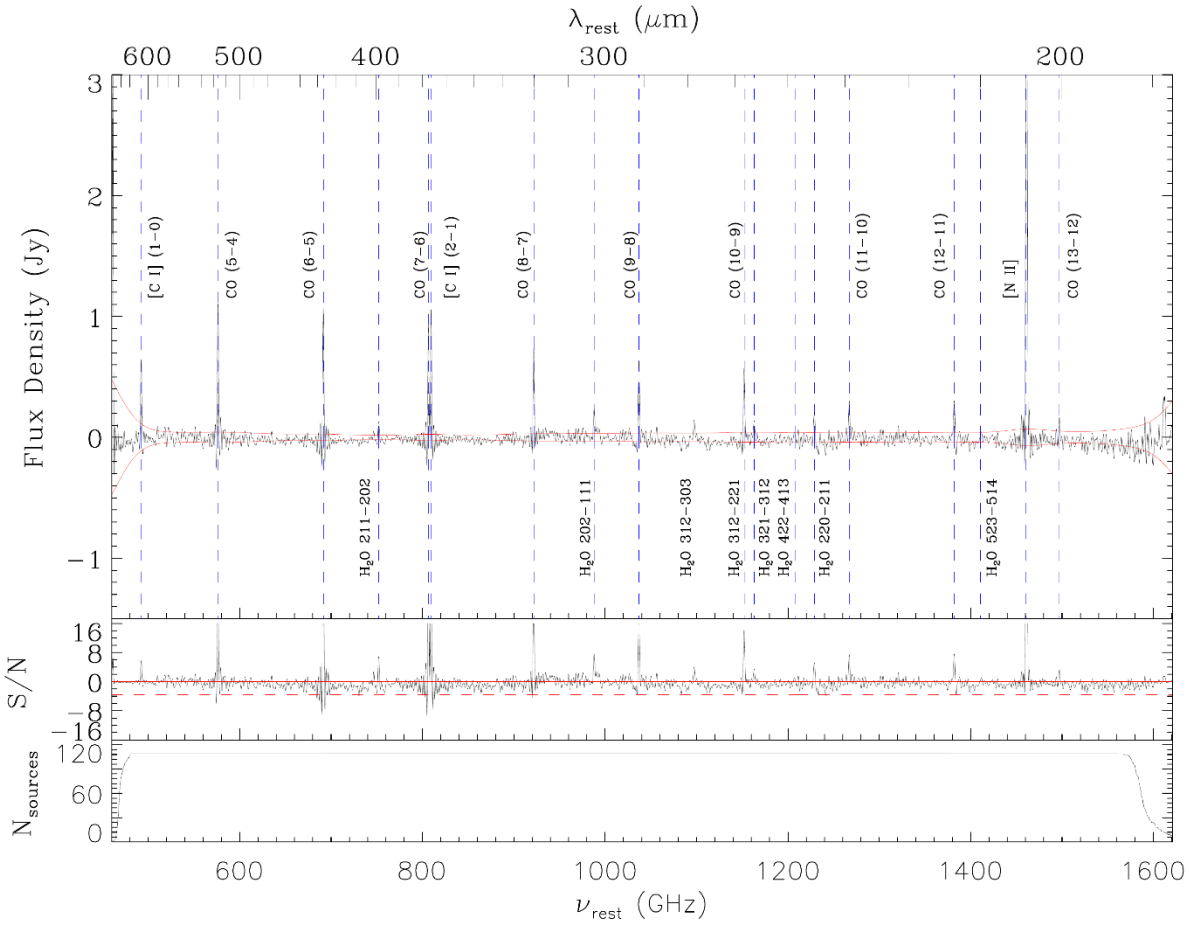

Figure 3: Stacked FTS spectra, 0.005 < z < 0.05

Top: Stacked SPIRE/FTS spectrum of archival sources with 0.005 < z < 0.05. Overlaid is the 1σ jackknifed noise level in red and dashed vertical lines showing the locations of main molecular emission lines. We detect the CO emission line ladder from J = 13-12 to J = 5-4, as well as the two lowest [C I] emissions at 492 GHz (609 μm) and 809 GHz (370 μm), [N II] at 1461 GHz (205 μm) and the water lines within the rest frequencies (wavelengths) covered in this stack from 460 GHz to 1620 GHz (185 μm to 652 μm). *Middle*: Signal-to-noise ratio. The horizontal dashed line indicates S/N = 3.5, and the solid red line indicates S/N = 0. Lines with S/N > 3.5 were considered detected. *Bottom*: The number of sources that contribute to the stack at each frequency.

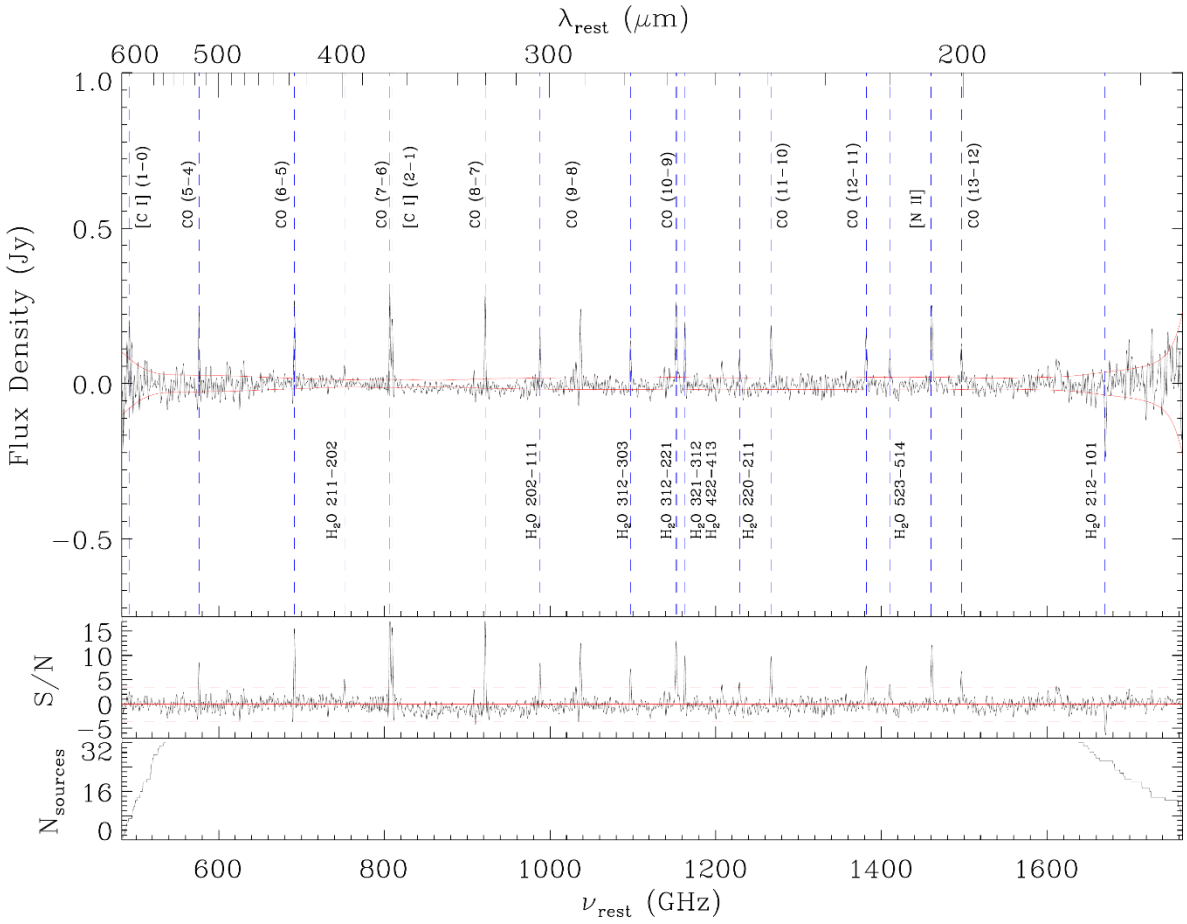

Figure 4: Stacked FTS spectra, 0.05 < z < 0.2

Same as Figure 3, but for the redshift range 0.05 < z < 0.2. We detect all the CO emission line ladder within the frequency (wavelength) covered by the stack from 480 GHz to 1760 GHz (170 μm to 625 μm). The stacked spectrum also shows 3.5σ detection for [C I](2-1) at 809 GHz (370 μm), [N II] at 1461 GHz (205 μm), and water lines.

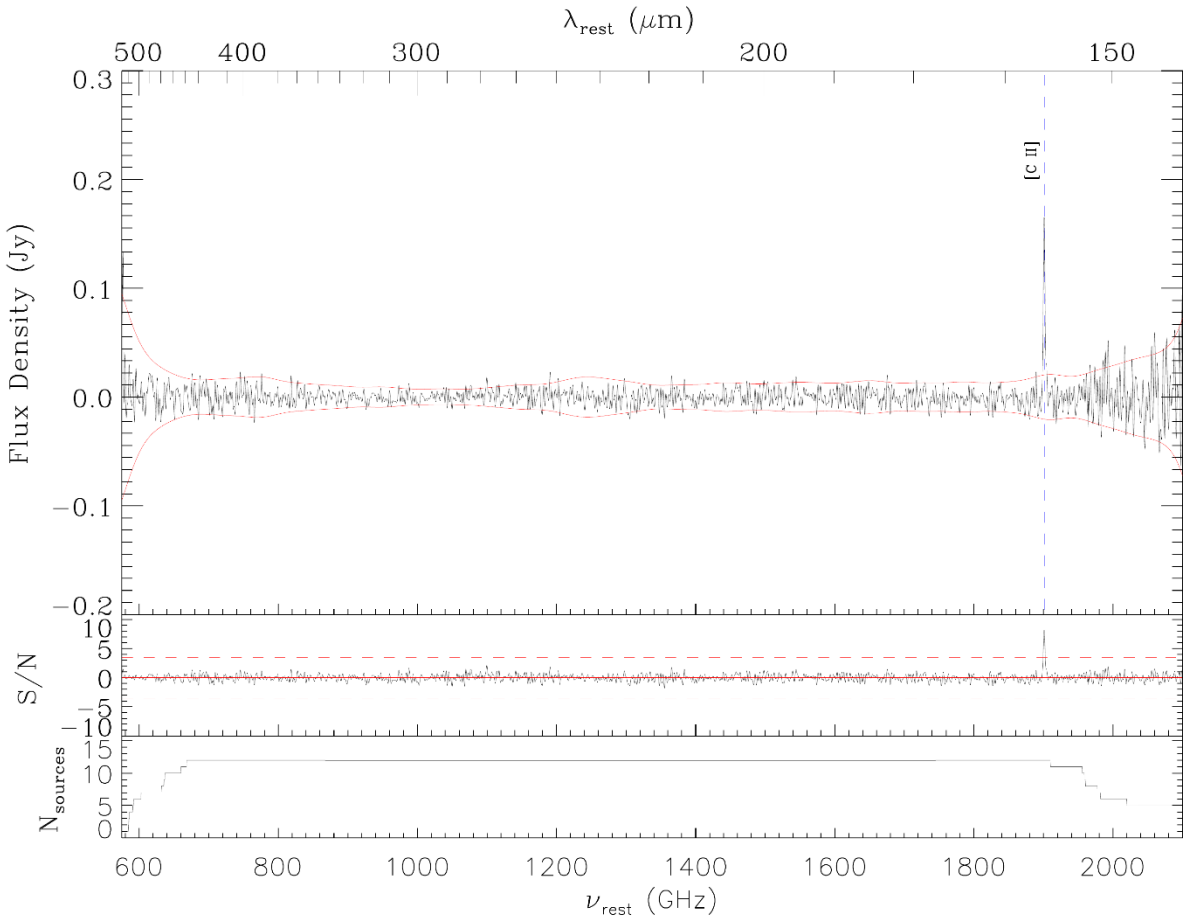

Figure 5: Stacked FTS spectra, 0.2 < z < 0.5

Same as Figure 3, but for the redshift range 0.2 < z < 0.5. We only detect the [C II] at 1901 GHz (158 μm) line in this stack with frequency (wavelength) coverage 580 GHz to 2100 GHz (143 μm to 517 μm).

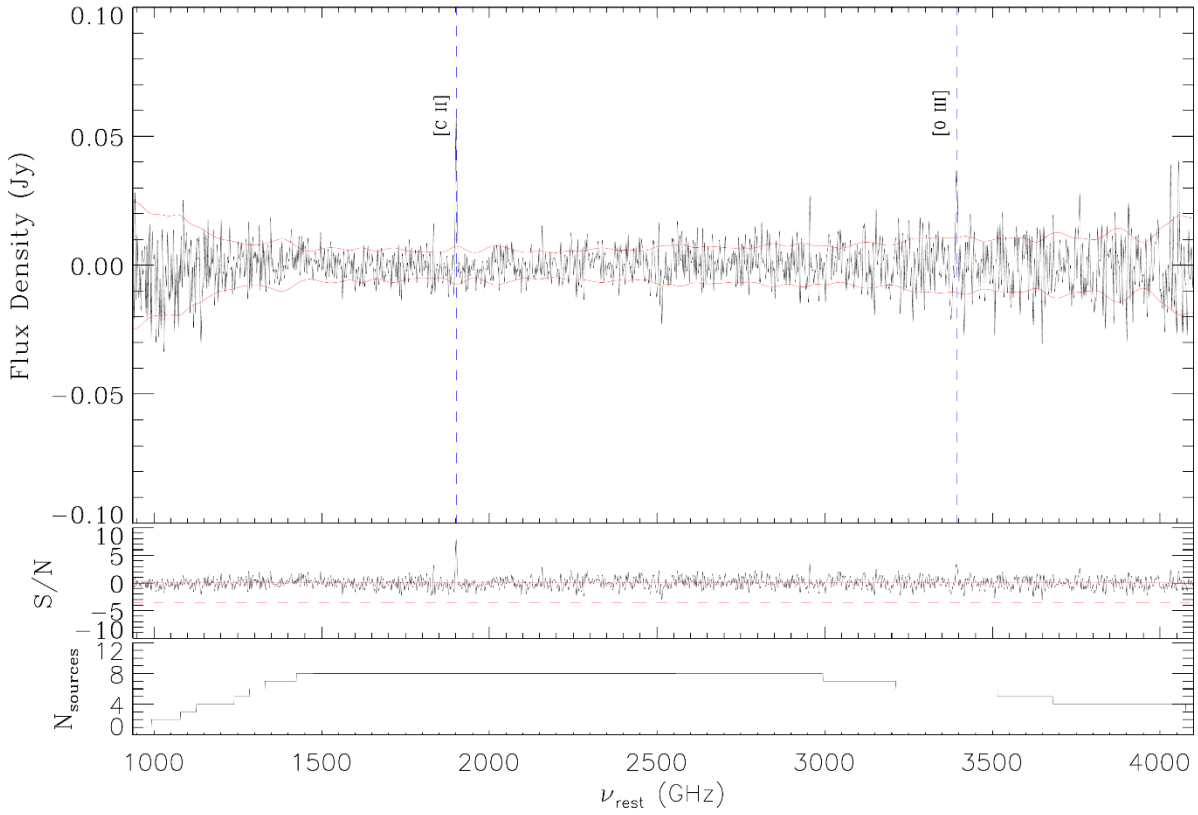

Figure 6: Stacked FTS spectra, 0.8 < z < 2

Same as Figure 3, but for the redshift range 0.8 < z < 2. We detect [N II] at 1461 GHz (205 μm), [C II] at 1901 GHz (158 μm) and [O III] at 3391 GHz (88 μm) in the frequency (wavelength) range of 950 GHz to 4100 GHz (70 μm to 316 μm) covered by the stack.

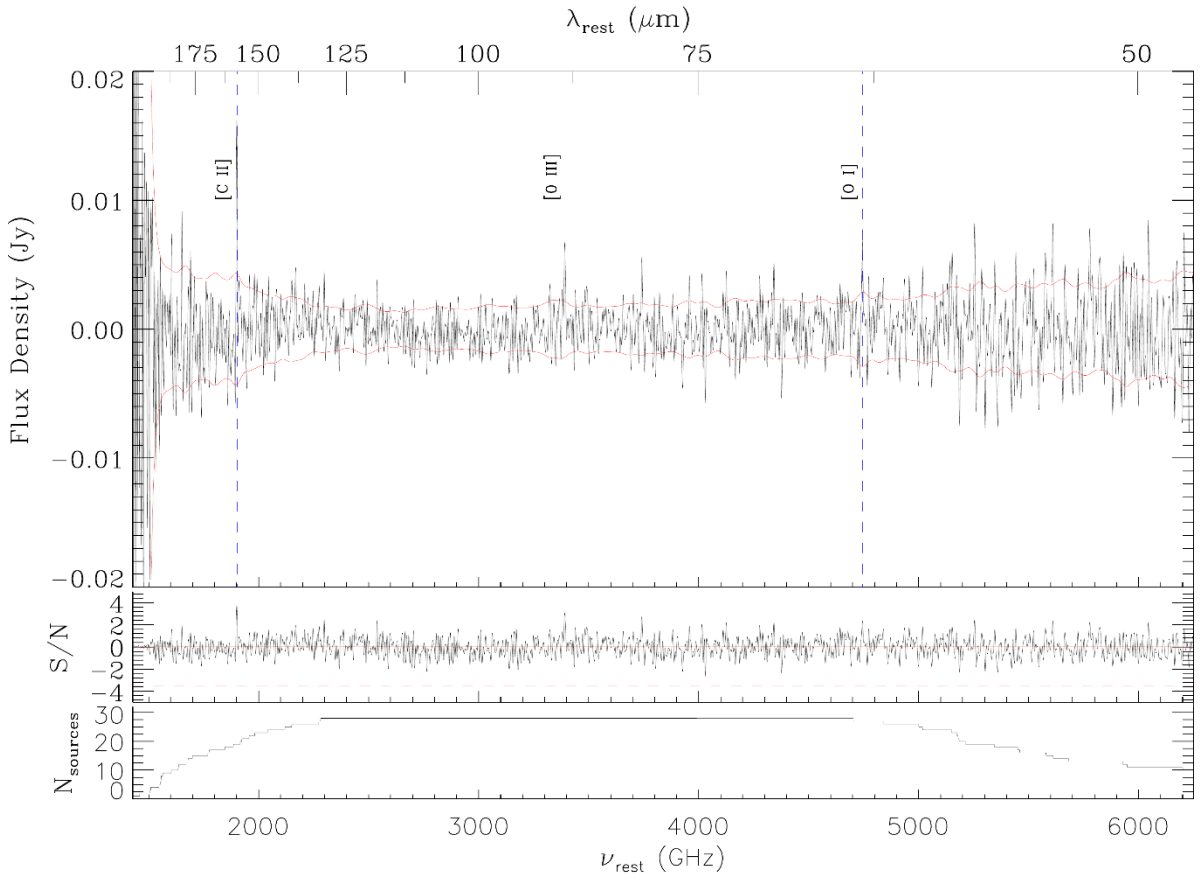

Figure 7: Stacked FTS spectra, 2 < z < 4

Same as Figure 3, but for the redshift range 2 < z < 4. We detect [C II] at 1901 GHz (158 μm) and [O III] at 3391 GHz (88 μm) in the frequency (wavelength) range of 1400 GHz to 6200 GHz (48 μm to 214 μm).

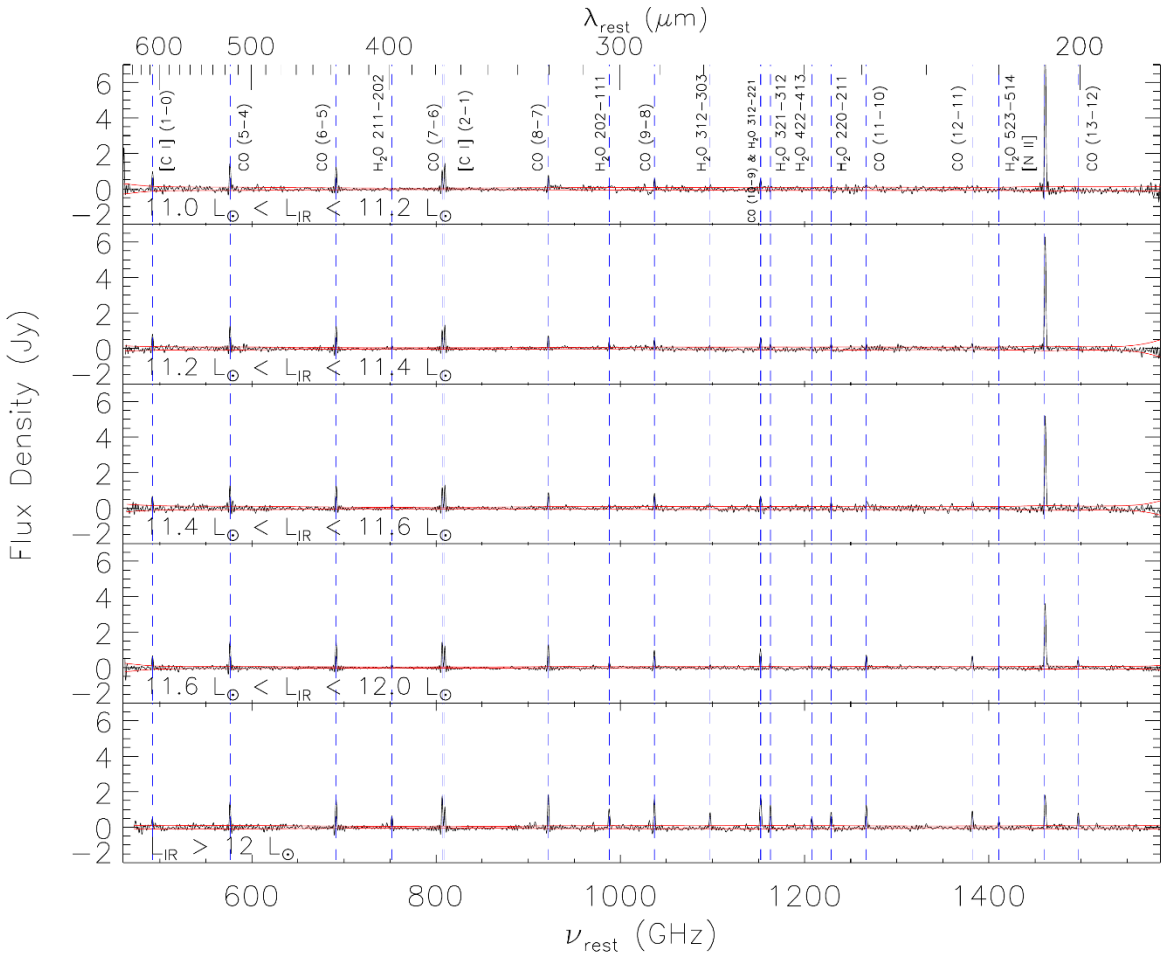

Figure 8: Stacked FTS spectra, in luminosity bins

The lowest redshift bin ($0.005 < z < 0.05$) is stacked using a straight mean (without inverse-variance weighting) in five luminosity bins as outlined in each panel. From top to bottom, the median luminosities in each bin are $10^{11.12}$ $L_\odot$, $10^{11.32}$ $L_\odot$, $10^{11.49}$ $L_\odot$, $10^{11.69}$ $L_\odot$, and $10^{12.21}$ $L_\odot$. The mean redshifts in each bin are 0.015, 0.018, 0.021, 0.027, and 0.038. The number of sources contributing to each bin are 37, 28, 17, 24, 9. and The CO molecular line excitations, [C I] atomic emissions, and [N II] at 205 μm are detected in all five luminosity bins.

Low-redshift stacks

Figure 3 and Figure 4 show the stacked FTS spectra and corresponding uncertainty along with major atomic and molecular emission and absorption lines for the $0.005 < z < 0.05$ and $0.05 < z < 0.2$ bins respectively. With the large number of galaxy samples, the far-IR spectrum of lowest redshift bin results in a highly reliable average spectrum showing a number of ISM atomic and molecular emission lines. In particular we detect all the CO lines with $J_{\rm upper} > 5$ out to the high excitation line of CO(13-12). This allows us to construct the CO spectral line energy distribution (SLED) and to explore the ISM excitation state in DSFGs in comparison with other starbursts and that of normal star-forming galaxies (see Section 5). We further detect multiple H_2O emission lines in these stacks which arise from the very dense regions in starbursts. The strength of the rotational water lines rivals that of the CO transition lines. we additionally detect the [C I] (1-0) at 609 μm and [C I] (2-1) at 370 μm along with [N II] at 205 μm in both redshift bins. We will use these measured line intensity ratios in Section 5 to construct photodissociation region models of the ISM and to study the density and ionizing photon intensities. We note here that the [C I] line ratios are very sensitive to the ISM conditions and would therefore not always agree with more simplistic models of the ISM. We will discuss these further in Section 5. For comparison to Figure 3, which is stacked using an unweighted mean, Figure 53 (see Appendix) shows the $0.005 < z < 0.05$ sources stacked with an inverse variance weighting. A few absorption lines also appear in the low-redshift stack. Despite Arp 220 [182] being the only individual source with strong absorption features, many of the absorption features are still present in the stack due to the high signal-to-noise ratio of Arp 220 in conjunction with an inverse variance weighting scheme for stacking. The SPIRE FTS spectrum of Arp 220 has been

studied in detail in Rangwala et al. 2011 [182] and is characterized by strong absorption features in water and related molecular ions OH^+ and H_2O^+ interpreted as a massive molecular outflow.

The best-fit profiles of the detected lines in the low-redshift stacks are shown in Figure 9 and Figure 10 for the $0.005 < z < 0.05$ and $0.05 < z < 0.2$ redshift bins, respectively. Fluxes in W m^{-2} are obtained by integrating the best-fit line profiles. Table 1 summarizes these line fluxes as well as velocity-integrated fluxes from the sinc-Gauss fits for detections with $S/N > 3.5$ in these stacks.

As discussed above, we further stack the lowest redshift bin ($0.005 < z < 0.05$) in five infrared luminosity bins. Figure 8 shows the stacked FTS spectra each of these luminosity bins. See the caption in Figure 8 for the redshift and luminosity breakdown of the sample. By comparing these stacks we can look at the effects of infrared luminosity on emission line strengths. It appears from these stacked spectra that the high-*J* CO lines are comparable in each of the luminosity bins. We explore the variation in the [N II] line in the discussion. Fluxes for the lines in each luminosity bin are tabulated in Table 2.

Intermediate-redshift stacks

We show the intermediate-redshift ($0.2 < z < 0.5$) stack in Figure 5. Due to the limited number of galaxies observed with SPIRE/FTS in this redshift range, we only detect a bright [C II] line with the threshold signal-to-noise ratio of 3.5. The [C II] 158 μm fine structure line is a main ISM cooling line and is the most pronounced ISM emission line detectable at high redshifts, when it moves into mm bands, revealing valuable information

on the state of the ISM. We further discuss these points in Section 5. Figure 11 shows the best-fit profile to the [C II] line in the intermediate redshift. The measured fluxes from this profile are reported in Table 1. The average [C II] flux from the stack is lower than the measurements reported in Magdis et al. 2014 [146] for individual sources (note that our $0.2 < z < 0.5$ bin is comprised almost entirely of the sources from Magdis et al. 2014, the exception being the source IRAS 00397-1312). Stacking without IRAS 00397-1312 leads to similar results. We attribute the deviation of the stack [C II] flux toward lower values to the scalings we apply when shifting spectra to a common redshift and common luminosity during the stacking process.

High-redshift stacks

The high redshift ($0.8 < z < 2$ and $2 < z < 4$) FTS stacks are shown in Figure 6 and Figure 7 consisting of 36 total individual spectra for sources in Table 10. The stack at $0.8 < z < 2$ also suffers from a limited number of galaxies observed with the FTS. At $0.8 < z < 2$, [C II] 158 μm and [O III] 88 μm appear. We detect [C II] at 158 μm, [O III] at 88 μm and [O I] at 63 μm atomic emission lines with S/N > 3.5 in the stacked spectra at $2 < z < 4$. The relative line ratios of these main atomic fine structure cooling lines will be used to construct the photodissociation region model of the ISM of DSFGs at these extreme redshifts to investigate the molecular density and radiation intensity.

To study the strengths of spectral lines at different luminosities, all sources with $z > 0.8$ were combined into a single sample and then divided into three luminosity bins with roughly the same number of sources in each bin. The average luminosities in the three bins are $10^{12.41}$ $L_{\odot}$, $10^{12.77}$ $L_{\odot}$, and $10^{13.24}$ $L_{\odot}$. See Table 3 and Table 4 for the precise breakdown

of the sample and measured fluxes. Each of the subsamples is separately stacked, and the line fluxes are measured as a function of far-infrared luminosity. Figure 12 shows the best-fit line profiles to the three main detected emission lines in the three infrared luminosity bins. The ISM emission lines are more pronounced with increasing infrared luminosity. This agrees with results of individual detected atomic emission lines at high redshifts [146, 185] although deviations from a main sequence are often observed depending on the physics of the ISM in the form of emission line deficits [210]. These are further discussed in the next section.

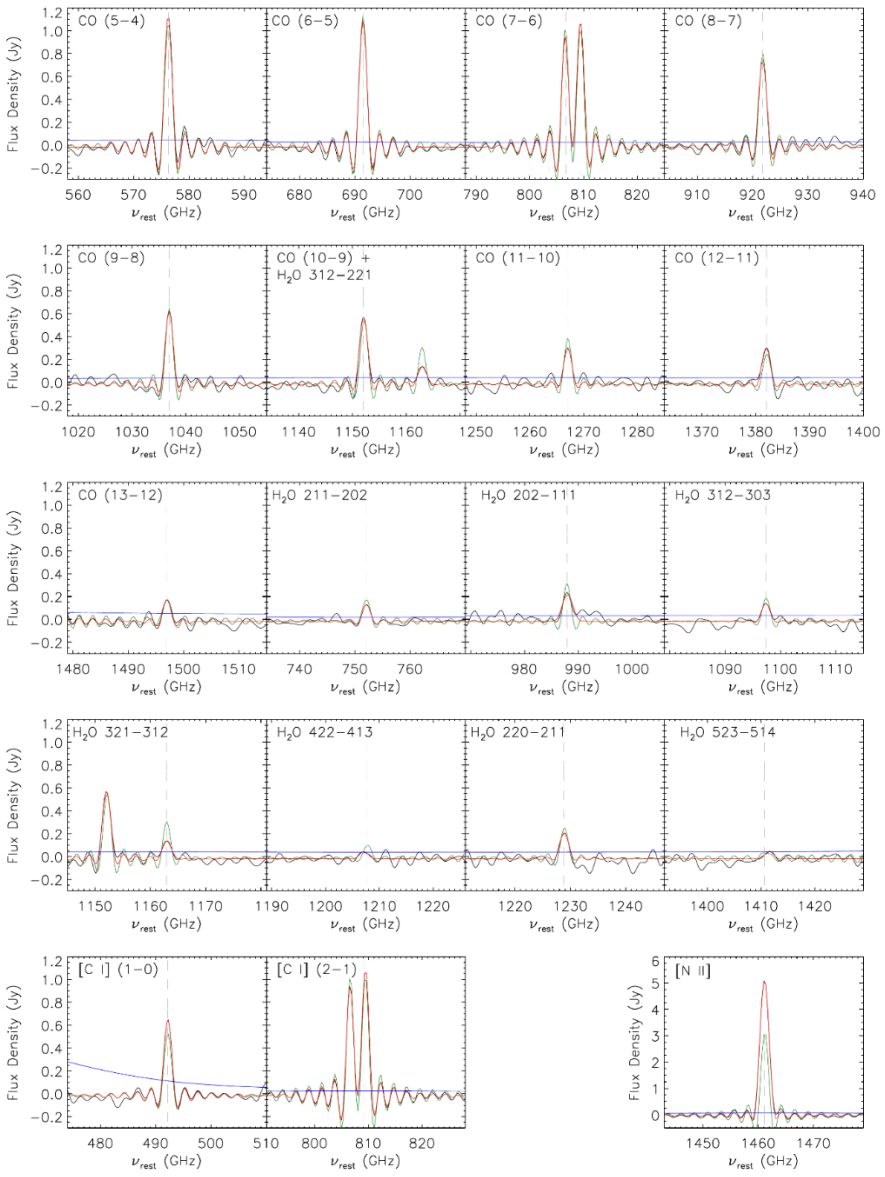

Figure 9: Fitting to atomic and molecular lines, 0.005 < z < 0.05

Sinc-Gauss and sinc fits to the detected atomic and molecular lines in the low-redshift stack at 0.005 < z < 0.05. The spectrum itself is shown in black. The green curve shows a sinc fit, red shows sinc-Gauss fit, and the blue curve is the 1σ jackknife noise level. The sinc fit is often too thin to capture the full width of the spectral lines. The lines are shifted to the rest-frame based on the public spectroscopic redshifts reported in the literature. Fluxes are measured from the best-fit models. The fluxes of the lines are reported in Table 2.

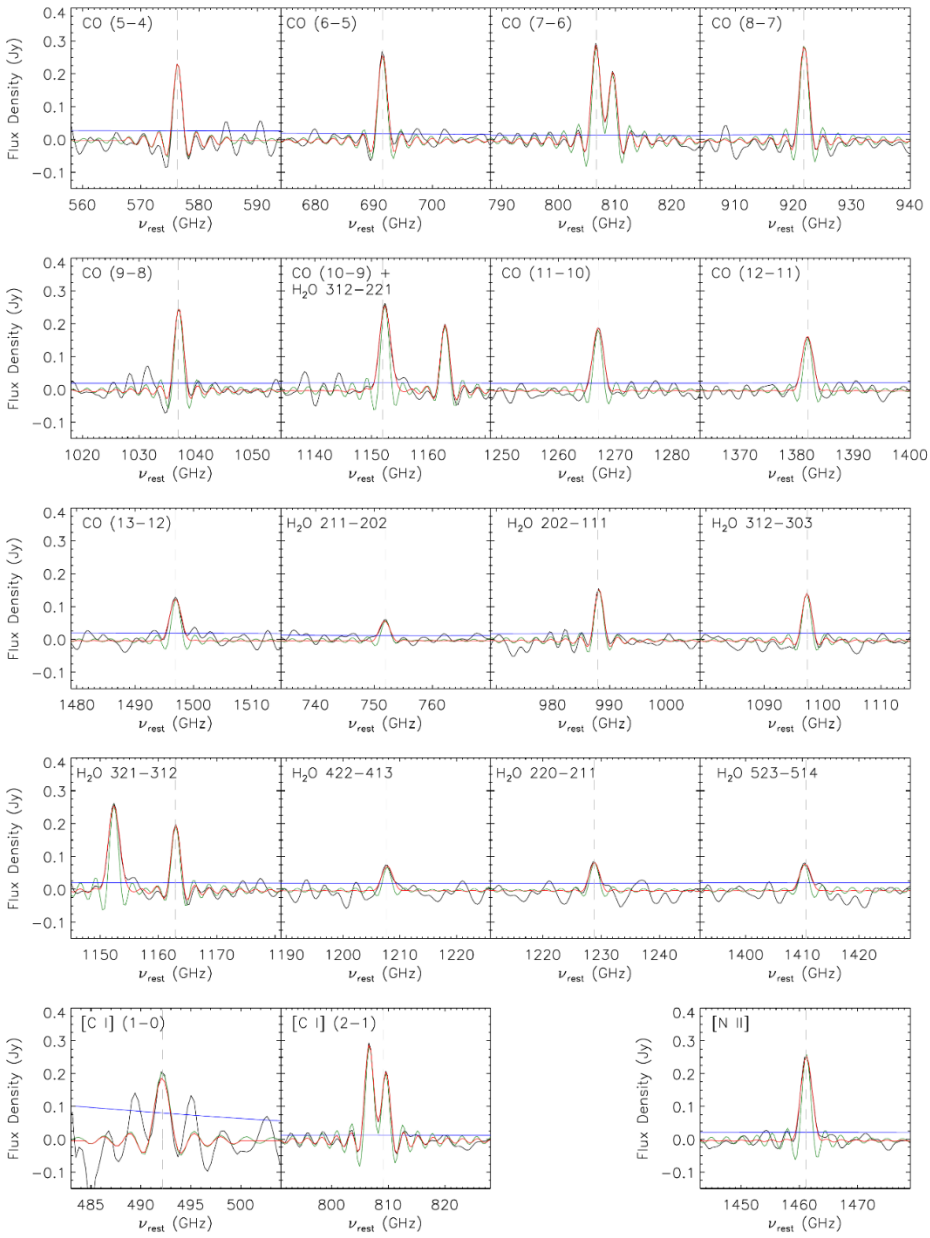

Figure 10: Fitting to atomic and molecular lines, 0.05 < z < 0.2

Sinc-Gauss (red) and sinc (green) fits to the detected atomic and molecular lines in the stack at 0.05 < z < 0.2, with the spectrum itself in black. We detect all the lines same as the low redshift stack (Figure 9) albeit with a different detection significance. In particular [C I] (1-0) is marginally detected in this redshift bin as fewer than ten sources contribute to the stack at this frequency, leading to a higher jackknife noise level. Fluxes of lines detected in this stack are also reported in Table 2.

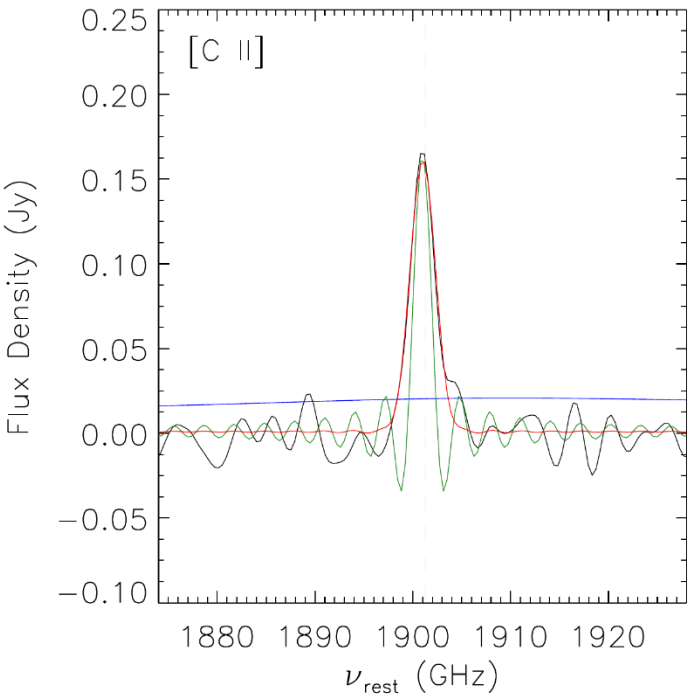

Figure 11: Fitting to [C II], 0.2 < z < 0.5.

Sinc-Gauss (red) and sinc (green) fits to the [C II] line in the 0.2 < z < 0.5 stack. The spectrum itself is shown in black with the 1σ noise level in blue.

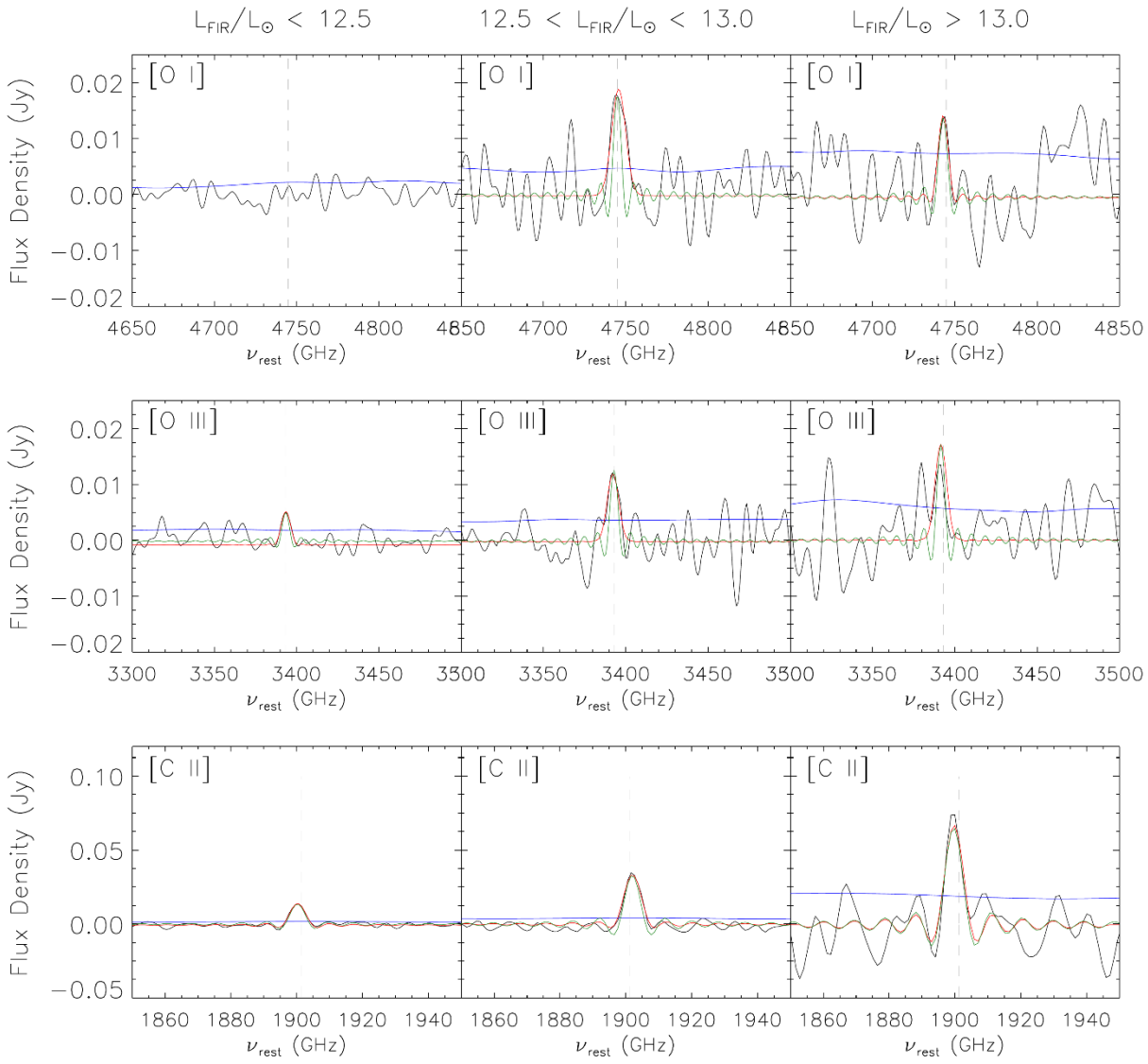

Figure 12: Fitting to atomic and molecular lines, z > 2

Fits to lines for the three luminosity bins of the high-redshift sources. The sinc-Gauss fit is shown in red, and the sinc-only fit is shown in green. The spectrum itself in black, and the 1σ jackknife noise level is in blue.

Discussion

The ISM atomic and molecular line emissions observed in the stacked spectra of DSFGs can be used to characterize the physical condition of the gas and radiation in the ISM across a wide redshift range. This involves investigating the CO and water molecular line transitions and the atomic line diagnostic ratios with respect to the underlying galaxy infrared luminosity for comparison to other populations and modeling of those line ratios to characterize the ISM.

The CO SLED

The CO molecular line emission intensity depends on the conditions in the ISM. Whereas the lower-*J* CO emission traces the more extended cold molecular ISM, the high-*J* emissions are observational evidence of ISM in more compact starburst clumps (e.g., [215]). In fact, observations of the relative strengths of the various CO lines have been attributed to a multi-phase ISM with different spatial extension and temperatures [118]. The CO spectral line energy distribution (SLED), plotted as the relative intensity of the CO emission lines as a function of the rotational quantum number, J, hence reveals valuable information on the ISM conditions (e.g., [143]).

Figure 13 shows the high-*J* CO SLED of the DSFGs for stacks in the two low redshift bins of $0.005 < z < 0.05$ and $0.05 < z < 0.2$. Here we are limited to the $J_{\rm upper} > 5$ CO SLED covered by the SPIRE/FTS in the redshift range probed. The CO SLED is normalized to CO (5-4) line flux density and plotted as a function of $J_{\rm upper}$. The background colored regions in Figure 13 are from Rosenberg et al. 2015 [188] in which they determined a range of CO flux

ratios for three classes of galaxies from the HerCULES sample: star-forming objects, starbursts and Seyferts, and ULIRGs and QSOs. The $0.005 < z < 0.05$ sample is consistent with the starbursts and Seyfert regions whereas line measurements from stacked spectra in $0.05 < z < 0.2$ redshift bin are more consistent with ULIRGs and QSO regions. Both measurements are higher than the expected region for normal star-forming galaxies which indicates a heightened excitation state in DSFGs specifically at the high-*J* lines linked to stronger radiation from starbursts and/or QSO activity.

Increased star-formation activity in galaxies is often accompanied by an increase in the molecular gas reservoirs. This is studied locally as a direct correlation between the observed infrared luminosity and CO molecular gas emission in individual LIRGs and ULIRGs [125]. To further investigate this correlation, we looked at the CO SLED in our low-z ($0.005 < z < 0.05$) sample in bins of infrared luminosity (Figure 8). Figure 13 further shows the CO SLED for the different luminosity bins. The stronger radiation present in the higher luminosity bin sample, as traced by the total infrared luminosity, is responsible for the increase in the CO line intensities. In the high luminosity bin sample, the excitation of the high-*J* lines could also partially be driven by AGN activity given the larger fraction of QSO host galaxies in the most IR luminous sources (e.g., [188]).

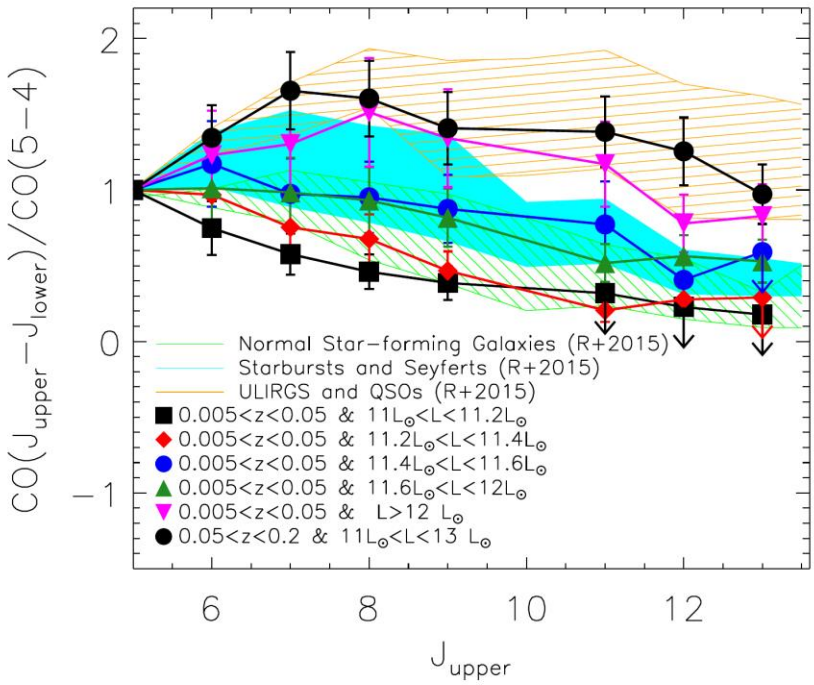

Figure 13: CO spectral line energy distribution

The carbon monoxide spectral line energy distribution for 0.005 < z < 0.05 in five luminosity bins as presented in Figure 8. The filled regions are taken from Rosenberg et al. 2015 [188] (see also Roberts-Borsani et al. 2017 [187]), and they correspond to the range of CO flux ratios in normal star-forming galaxies (green stripes), starbursts and Seyferts (solid cyan), and ULIRGs and QSOs (orange stripes).

Atomic and Molecular Line Ratios

We detect several H_2O emission lines in the two lowest redshift bins of 0.005 < z < 0.05 and 0.05 < z < 0.2. Fluxes from detected water rotational lines are plotted in Figure 14, along with data from fits made to individual spectra from the sample that exhibited strong water line emission. These include well-known sources such as Arp 220 at z = 0.0181 [182] and Mrk 231 at z = 0.0422 [231, 85]. H_20 lines are normally produced in the warm and

most dense regions of starbursts [57] and may indicate infrared pumping by AGN [86, 28]. Figure 13 also shows the different water emission lines and the ISM temperatures required for their production. As we see from the figure, at the highest temperature end the emission is more pronounced in galaxies in the $0.05 < z < 0.2$ redshift range. These systems tend to have a higher median infrared luminosity (Figure 1) and hence hotter ISM temperatures which are believed to drive the high temperature water emissions [218]. Figure 13 also shows the dependence of the water emission lines on the infrared luminosity for three of our five luminosity bins in the $0.005 < z < 0.05$ sample with the strongest H_2O detections. Using a sample of local *Herschel* FTS/SPIRE spectra with individual detections, Yang et al. 2013 [250] showed a close to linear relation between the strength of water lines and that of L_{IR}. We observe a similar relation in our stacked binned water spectra of DSFGs across all different transitions with higher water emission line intensities in the more IR-luminous sample.

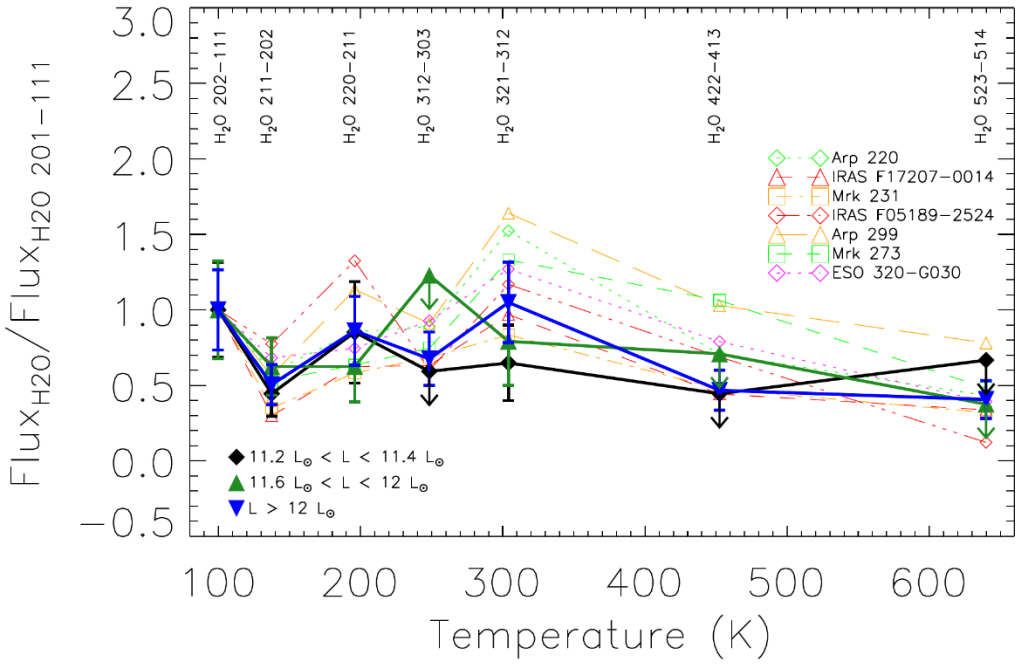

Figure 14: H_20 spectral line energy distribution

Spectral line energy distribution for transitions in water as a function of excitation temperature as in Yang et al. 2013 [250] at $0.005 < z < 0.05$ in the luminosity bins in which water lines were strongly detected. These detections are compared to the water spectral line energy distribution for individual sources fit using sinc-Gauss profiles.

The first two neutral [C I] transitions ([C I] (1-0) at 609 μm and [C I] (2-1) at 370 μm) are detected in both low-z stacks (see Figure 3 and Figure 4). We look at the [C I] line ratios in terms of gas density and kinetic temperature using the non-LTE radiative transfer code RADEX [228] (found at http://home.strw.leidenuniv.nl/~moldata/radex.html). To construct the RADEX models, we use the collisional rate coefficients by Schroder et al. 1991 [193] and use the same range of ISM physical conditions reported in Pereira et al. 2013

[172] (with T=10 - 1000 K, n_{H_2}=10 – 10^8 cm^{-3} and $N_C/\Delta v$=10^{12} – 10^{18} $cm^{-2}/(km\ s^{-1})$). Figure 15 shows the expected kinetic temperature and molecular hydrogen density derived by RADEX for the observed [C I] ratios in the low-z stacks for the different infrared luminosity bins with contours showing the different models. The [C I] emission is observed to originate from the colder ISM traced by CO (1-0) rather than the warm molecular gas component traced by the high-*J* CO lines [172] and in fact the temperature is well constrained from these diagrams for high gas densities.

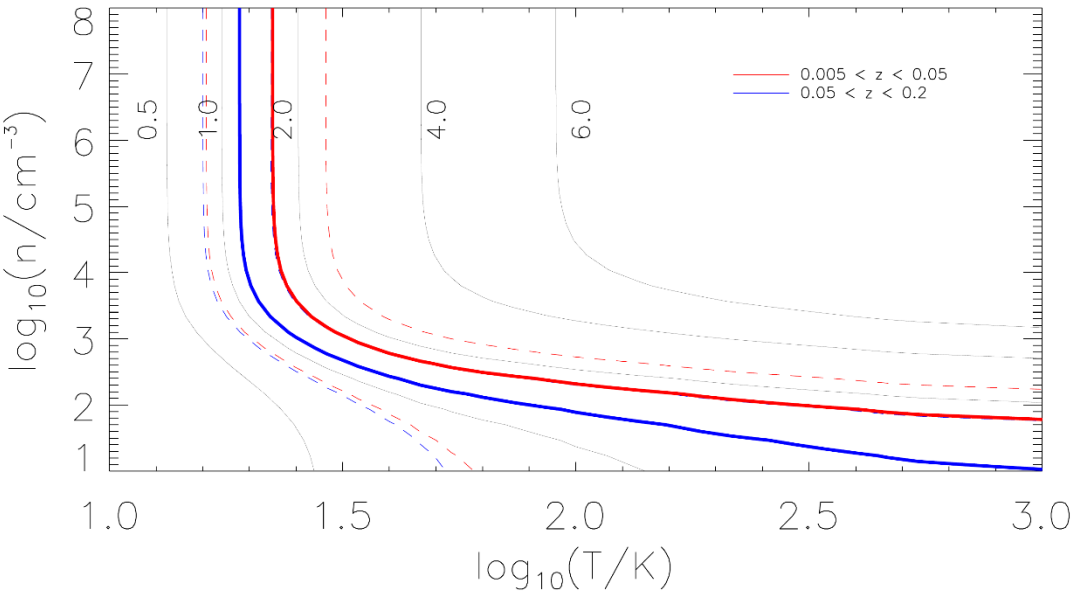

Figure 15: ISM conditions via neutral carbon ratios.

Conditions in the ISM as probed by neutral [C I] (2-1)/[C I] (1-0) line ratio for 0.005 < z < 0.05 and 0.05 < z < 0.2 redshift bins. RADEX contours for an array of theoretical [C I] (2-1)/[C I] (1-0) ratios are shown in black. The dashed lines represent the 1σ uncertainty.

The fine structure emission line relative strengths are important diagnostics of the physical conditions in the ISM. Here we focus on the three main atomic lines detected at z > 0.8 ([C II] at 158 μm, [O I] at 63 μm and [O III] at 88 μm) and study their relative strengths as well as their strength in comparison to the infrared luminosity of the galaxy. We break all sources with z > 0.8 into three smaller bins based on total infrared luminosity. Table 4 lists the infrared luminosity bins used. The [C II] line is detected in each subset of the high-redshift stack whereas [O I] and [O III] are only detected in the $10^{12.5}$ $L_{\odot}$ < 10^{13} $L_{\odot}$ infrared luminosity bin. Figure 16 shows the relation between emission line luminosity and total infrared luminosity. Total infrared luminosity is integrated in the rest-frame wavelength range 8-1000 μm. Luminosities in different wavelength ranges in the literature have been converted to L_{IR} using the mean factors derived from Table 7 of Brisbin et al. 2015 [31]:

$$\log(L_{IR}) = \log\big(L(42.5\mu m - 122.5\mu m)\big) + 0.30$$

$$\log(L_{IR}) = \log\big(L(40\mu m - 500\mu m)\big) + 0.145$$

$$\log(L_{IR}) = \log\big(L(30\mu m - 1000\mu m)\big) + 0.09$$

For the [C II] 158 μm line we used data from a compilation by Bonato et al. 2014 [24]; references therein, George 2015, Brisbin et al. 2015, Oteo et al. 2016, Gullberg et al. 2015, Schaerer et al. 2015, Yun et al. 2015, Magdis et al. 2014, Farrah et al. 2013, Stacey et al. 2010, Diaz et al. 2013 [81, 31, 168, 91, 192, 254, 146, 71, 210, 62], and a compilation of data from SHINING [212]. For the [O I] 63 μm line we used data from compilation by Bonato et al. 2014; references therein, Ferkinhoff et al. 2014, Brisbin et al. 2015, Farrah et al. 2013

[73, 31, 71], and SHINING. For the [O III] 88 μm line we used data from a compilation by Bonato et al. 2014; references therein, George 2015, and SHINING.

As in Bonato et al. 2014 [24], we excluded all objects for which there is evidence for a substantial AGN contribution. The line and continuum measurements of strongly lensed galaxies given by [81] were corrected using the gravitational magnifications, μ, estimated by Ferkinhoff et al. 2014 [73] while those by Gullberg et al. 2015 [91] were corrected using the magnification estimates from Hezaveh et al. 2013 [101] and Spilker et al. 2016 [204] available for 17 out of the 20 sources. For the other three sources we used the median value of $\mu_{med} = 7.4$.

The solid green lines in Figure 15 correspond to the average L_{line}/L_{IR} ratios of -3.03, -2.94 and -2.84 for the [O I] 63 μm, [O III] 88 μm and [C II] 158 μm lines from the literature, respectively. The [CII] line luminosity-to-IR luminosity ratio is at least an order of magnitude higher than the typical value of 10^{-4} quoted in the literature for local nuclear starburst ULIRGS and high-z QSOs. Since the data come from heterogeneous samples, a least square fitting is susceptible to selection effects that may bias the results. To address this issue, Bonato et al. 2014 [24] have carried out an extensive set of simulations of the expected emission line intensities as a function of infrared luminosity for different properties (density, metallicity, filling factor) of the emitting gas, different ages of the stellar populations and a range of dust obscuration. For a set of lines, including those considered in this chapter the simulations were consistent with a direct proportionality between L_{line} and L_{IR}. Based on this result, we have adopted a linear relation. The other lines show L_{line}-L_{IR} relations found in the literature, namely:

$$\log(\mathrm{L[OI]63\mu m}) = \log(\mathrm{L}_{IR}) - 2.99$$

$$\log(\mathrm{L[OIII]88\mu m}) = \log(\mathrm{L}_{IR}) - 2.87$$

$$\log(\mathrm{L[CII]158\mu m}) = \log(\mathrm{L}_{IR}) - 2.74$$

from Bonato et al. 2014 [24],

$$\log(\mathrm{L[OI]63\mu m}) = 0.98 \times \log(\mathrm{L_{IR}}) - 2.95$$

$$\log(\mathrm{L[OIII]88\mu m}) = 0.98 \times \log(\mathrm{L_{IR}}) - 3.11$$

$$\log(\mathrm{L[OIII]88\mu m}) = 0.98 \times \log(\mathrm{L_{IR}}) - 3.11$$

from Spinoglio et al. 2014 [206],

$$\log(\mathrm{L[OI]63\mu m}) = 0.70 \times \log(\mathrm{L_{IR}}) + 0.32$$

$$\log(\mathrm{L[OIII]88\mu m}) = 0.82 \times \log(\mathrm{L_{IR}}) - 1.40$$

$$\log(\mathrm{L[CII]158\mu m}) = 0.94 \times \log(\mathrm{L_{IR}}) - 2.39$$

from Gruppioni et al 2016 [90], and

$$\log(\mathrm{L[OI]63\mu m}) = 1.10 \times \log(\mathrm{L_{IR}}) - 4.70$$

$$\log(\mathrm{L[CII]158\mu m}) = 1.56 \times \log(\mathrm{L_{IR}}) - 10.52$$

from Farrah et al. 2013 [71], respectively.

In the high-z bin at z > 1, we find that [O III] and [O I] detections are limited to only one of the three luminosity bins. The ISM emission lines show a deficit (i.e. deviating from a one to one relation) compared to the infrared luminosity. This in particular is more pronounced in our stacked high-z DSFG sample compared to that of local starbursts and is similar to what is observed in local ULIRGs. This deficit further points towards an increase in the atomic ISM lines optical depth in these very dusty environments. There is no clear trend in the measured lines with the infrared luminosities, given the measured uncertainties, however there is some evidence pointing towards a further decrease with increasing IR luminosity. Figure 17Figure 19 shows the [O I]/[C II] line ratio for the stacks of DSFGs compared to Brauher et al. 2008 [29] and Cormier et al. 2015 [53]. Although both lines trace neutral gas, they have different excitation energies (with the [O I] being higher). Given the uncertainties, we do not see a significant trend in this line ratio with the infrared luminosity.

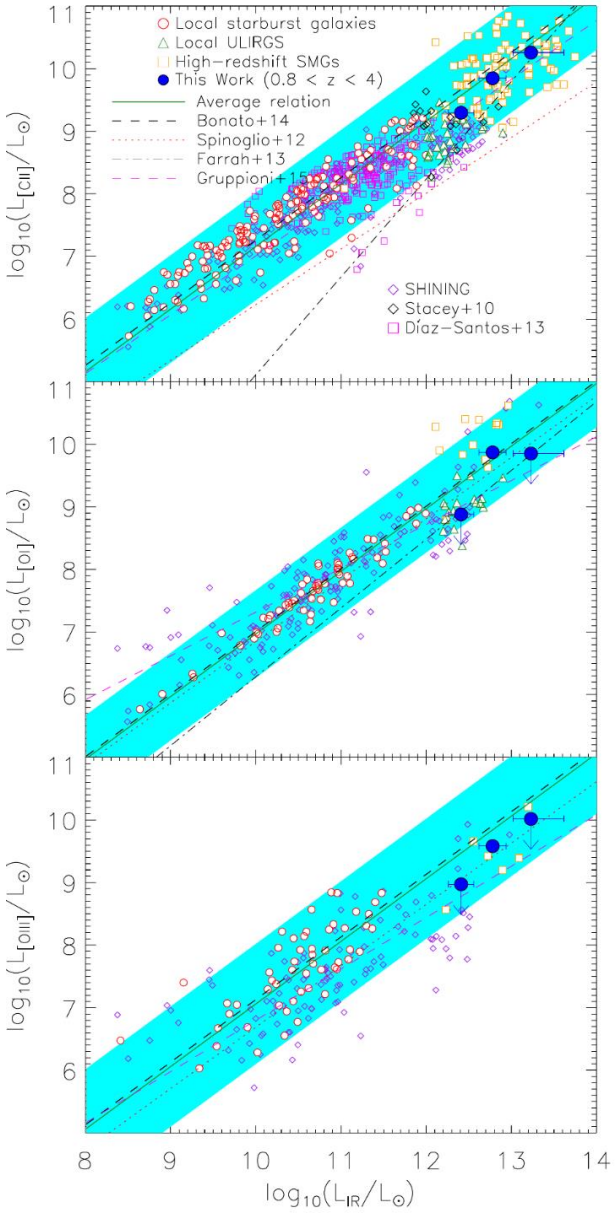

Figure 16: Line luminosity to total luminosity ratios.

Line versus infrared luminosity (rest-frame 8-1000 μm), L_{IR}, of star-forming galaxies for [C II], [O I], and [O III] fine-structure lines at high redshift. Background data are from the literature sources listed in the text. The solid green lines correspond to the average L_{line}/L_{IR} ratios (-3.03, -2.94 and -2.84) for the [O I] 63.18 μm, [O III] 88.36 μm, and [C II] 157.7 μm lines from the literature, respectively. The reason for the choice of a linear relation is explained in the main text. The cyan stripes correspond to two times the dispersion around the mean relation (σ = 0.35, 0.48 and 0.43, respectively). Also shown, for comparison, are the L_{line}/L_{IR} relations found in the literature.

Due to the wavelength coverage of SPIRE/FTS, we are unable to study the [N II] 205 μm line in the high-z bin. Instead, we concentrate on the luminosity dependence of the [N II] 205 μm line in the low-z bin. This [N II] ISM emission cooling line is usually optically thin, suffering less dust attenuation compared to optical lines and hence is a strong star-formation rate indicator [258, 99, 108, 259]. The [N II] line luminosity in fact shows a tight correlation with SFR for various samples of ULIRGs [258]. Given the ionization potential of [N II] at 14.53 eV, this line is also a good tracer of the warm ionized ISM regions [259]. Figure 20 shows the [N II] emission for our low-z stack ($0.005 < z < 0.05$) as a function of infrared luminosity for the five luminosity bins outlined in Figure 8. The [N II] line luminosity probes the same range as observed for other samples of ULIRGs and consistently increases with infrared luminosity (a proxy for star-formation) [258]. The [N II]/L_{IR} ratio is $\sim 10^{-5}$ compared to the [C II]/L_{IR} at $\sim 10^{-3}$ [62, 167, 100, 188].

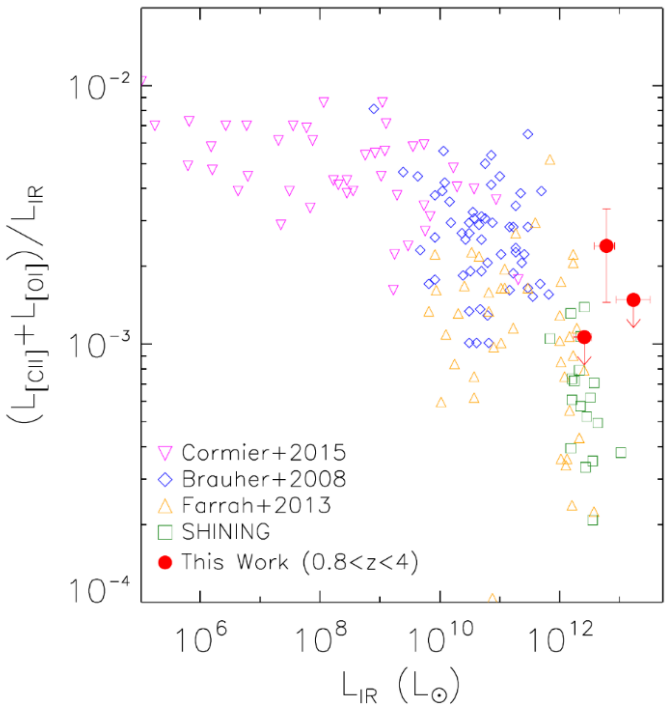

Figure 17: ($L_{[C\ II]}$ + $L_{[O\ I]}$) / L_{IR}

Ratio of ([C II]+[O I]) luminosity to total infrared luminosity (rest-frame 8-1000 μm) in three luminosity bins for sources with 0.8 < z < 4 as a function of total infrared luminosity. The breakdown of the three luminosity bins is as follows: $L_{IR} < 10^{12.5}\ L_{\odot}$, $10^{12.5}\ L_{\odot} < L_{IR} < 10^{13}\ L_{\odot}$, and $L_{IR} > 10^{13}\ L_{\odot}$; however, [O I] is only detected in the middle luminosity bin. For comparison, we show data from Cormier et al. 2015, Brauher et al. 2008, Farrah et al. 2013, the SHINING collaboration 2011 [53, 29, 71, 212].

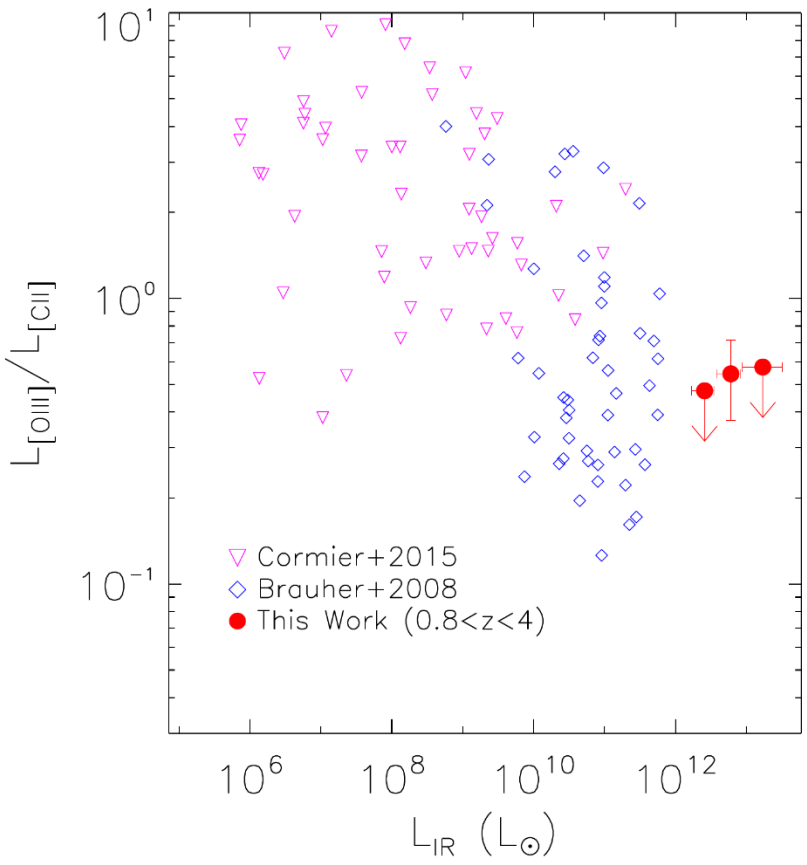

Figure 18: $L_{[O\ III]}$ / $L_{[C\ II]}$

Line ratios as a function of total infrared luminosity in three luminosity bins for sources with 0.8 < z < 4. For comparison, we show data from Cormier et al. 2015 [53] and Brauher et al. 2008 [29].

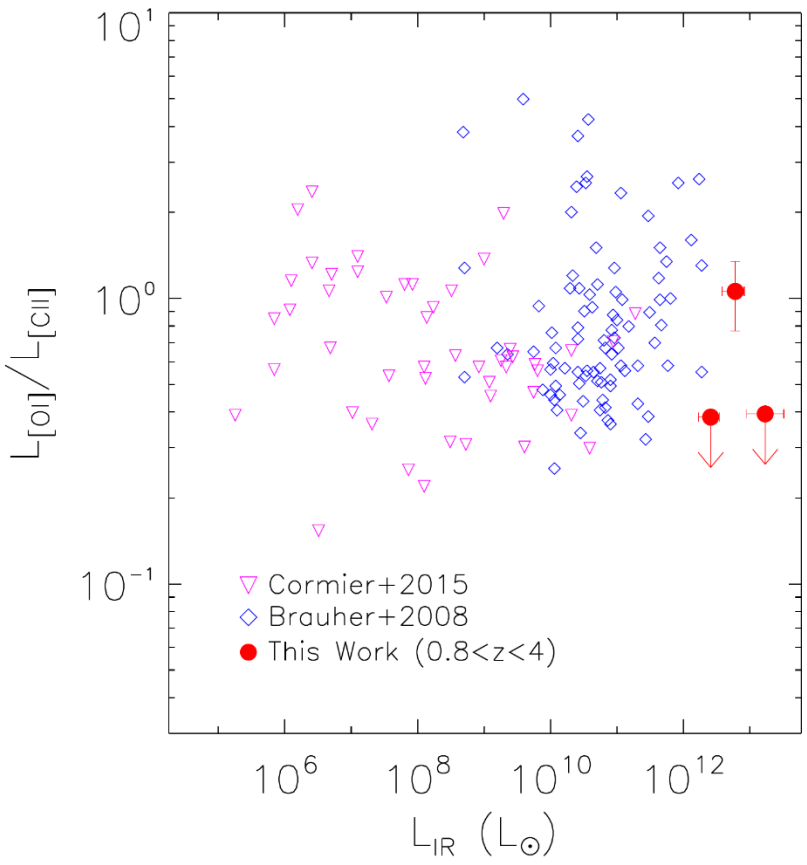

Figure 19: $L_{[O\ I]}$ / $L_{[C\ II]}$

Line ratios as a function of total infrared luminosity in three luminosity bins for sources with 0.8 < z < 4. For comparison, we show data from Cormier et al. 2015 [53] and Brauher et al. 2008 [29].

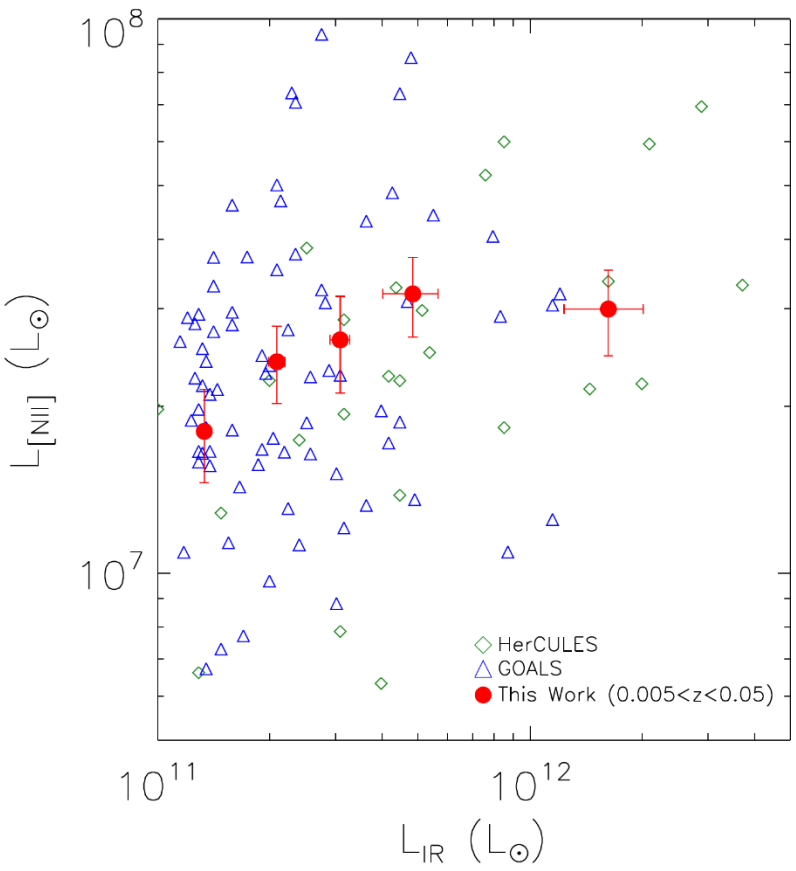

Figure 20: [N II] luminosity relative to total IR luminosity.

Line luminosity of the [N II] transition in luminosity bins for sources at $0.005 < z < 0.05$. Background data were produced by fitting to the [NII] lines in individual spectra in the HerCULES and GOALS samples.

Table 1: Fluxes of observed spectral lines in each redshift bin

		$0.005 < z < 0.05$		$0.05 < z < 0.2$		$0.2 < z < 0.5$		$0.8 < z < 2$		$2 < z < 4$	
Line	Rest Freq. [GHz]	Flux [10^{-18} Wm^{-2}]	Flux [Jy km s^{-1}]	Flux [10^{-18} Wm^{-2}]	Flux [Jy km s^{-1}]	Flux [10^{-18} Wm^{-2}]	Flux [Jy km s^{-1}]	Flux [10^{-18} Wm^{-2}]	Flux [Jy km s^{-1}]	Flux [10^{-18} Wm^{-2}]	Flux [Jy km s^{-1}]
CO (5-4)	576.268	15 ± 3	790 ± 130	2.8 ± 0.4	160 ± 30	-	-	-	-	-	-
CO (6-5)	691.473	14 ± 3	620 ± 100	3.8 ± 0.4	180 ± 20	< 0.40	< 23	-	-	-	-
CO (7-6)	806.653	12 ± 2	440 ± 80	4.7 ± 0.4	190 ± 20	< 0.38	< 19	-	-	-	-
CO (8-7)	921.800	11 ± 2	360 ± 60	4.5 ± 0.4	160 ± 20	< 0.24	< 10	-	-	-	-
CO (9-8)	1036.914	9.7 ± 1.7	280 ± 50	4.0 ± 0.5	130 ± 20	< 0.21	< 7.7	< 0.48	< 33	-	-
CO (10-9)	1151.985	9.6 ± 1.7	250 ± 50	5.7 ± 0.6	160 ± 20	< 0.32	< 11	< 0.34	< 21	-	-
CO (11-10)	1267.016	4.9 ± 1.0	120 ± 30	3.9 ± 0.4	100 ± 20	< 0.50	< 16	< 0.21	< 12	-	-
CO (12-11)	1381.997	5.4 ± 1.1	120 ± 30	3.5 ± 0.5	84 ± 10	< 0.34	< 9.5	< 0.26	< 14	-	-
CO (13-12)	1496.926	2.3 ± 0.6	54 ± 13	2.7 ± 0.5	60 ± 9	< 0.37	< 9.7	< 0.33	< 16	< 0.38	< 29
H_2O 211-202	752.032	1.9 ± 0.4	78 ± 17	1.1 ± 0.3	49 ± 9	< 0.49	< 26	-	-	-	-
H_2O 202-111	987.927	5.5 ± 1.2	170 ± 40	2.3 ± 0.3	78 ± 9	< 0.30	< 12	< 0.50	< 37	-	-
H_2O 312-303	1097.365	2.7 ± 0.7	75 ± 19	2.3 ± 0.3	70 ± 9	< 0.23	< 8.2	< 0.43	< 29	-	-
H_2O 312-221	1153.128	-	-	-	-	-	-	-	-	-	-
H_2O 321-312	1162.910	2.7 ± 0.7	72 ± 18	2.9 ± 0.3	82 ± 9	< 0.32	< 11	< 0.31	< 19	-	-
H_2O 422-413	1207.638	< 1.2	< 30	1.6 ± 0.5	44 ± 12	< 0.42	< 14	< 0.25	< 15	-	-
H_2O 220-211	1228.789	3.9 ± 1.0	96 ± 23	1.6 ± 0.4	43 ± 11	< 0.50	< 16	< 0.24	< 14	-	-
H_2O 523-514	1410.615	< 1.4	< 30	1.8 ± 0.4	41 ± 9	< 0.35	< 9.7	< 0.36	< 19	-	-
[C I] $(1-0)$	492.161	9.2 ± 4.1	570 ± 250	2.5 ± 0.8	170 ± 50	-	-	-	-	-	-
[C I] $(2-1)$	809.340	15 ± 3	570 ± 100	3.0 ± 0.3	120 ± 10	< 0.39	< 18	-	-	-	-
[N II]	1461.132	96 ± 16	2000 ± 400	5.4 ± 0.5	120 ± 10	< 0.39	< 11	< 0.14	< 6.9	< 0.52	< 41
[C II]	1901.128	-	-	-	-	4.0 ± 0.4	83 ± 7	1.3 ± 0.2	51 ± 5	0.22 ± 0.04	13 ± 2
[N II]	2461.250	-	-	-	-	-	-	< 0.17	< 4.8	< 0.048	< 2.2
[O III]	3393.006	-	-	-	-	-	-	1.1 ± 0.3	23 ± 6	0.14 ± 0.03	4.5 ± 1.0
[O I]	4744.678	-	-	-	-	-	-	-	-	0.14 ± 0.05	3.5 ± 1.1

Note. — CO$(10-9)$ is contaminated by emission from $H_2O\,312-221$, so we quote only the combined flux for the two emission lines in the CO$(10-9)$ row. In the five redshift bins ($0.005 < z < 0.05$, $0.05 < z < 0.2$, $0.2 < z < 0.5$, $0.8 < z < 2$, and $2 < z < 4$), the mean redshifts are $z = 0.02$, $z = 0.1$, $z = 0.3$, $z = 1.4$, $z = 2.8$, respectively, and the median IR luminosities are $10^{11.35}$ L$_\odot$, $10^{12.33}$ L$_\odot$, $10^{11.89}$ L$_\odot$, $10^{12.53}$ L$_\odot$, and $10^{12.84}$ L$_\odot$, respectively.

Table 2: Fluxes in luminosity bins at 0.005 < z < 0.05

		$10^{11.0}\,L_\odot < L < 10^{11.2}\,L_\odot$		$10^{11.2}\,L_\odot < L < 10^{11.4}\,L_\odot$		$10^{11.4}\,L_\odot < L < 10^{11.6}\,L_\odot$		$10^{11.6}\,L_\odot < L < 10^{12.0}\,L_\odot$		$L > 10^{12.0}\,L_\odot$	
Line	Rest Freq. [GHz]	Flux [10^{-18} Wm^{-2}]	Flux [Jy km s^{-1}]	Flux [10^{-18} Wm^{-2}]	Flux [Jy km s^{-1}]	Flux [10^{-18} Wm^{-2}]	Flux [Jy km s^{-1}]	Flux [10^{-18} Wm^{-2}]	Flux [Jy km s^{-1}]	Flux [10^{-18} Wm^{-2}]	Flux [Jy km s^{-1}]
CO (5-4)	576.268	22 ± 4	1200 ± 200	17 ± 3	880 ± 150	16 ± 3	840 ± 150	20 ± 4	1100 ± 200	18 ± 4	980 ± 170
CO (6-5)	691.473	16 ± 3	720 ± 120	16 ± 3	710 ± 120	18 ± 3	820 ± 150	20 ± 4	910 ± 200	22 ± 4	1000 ± 200
CO (7-6)	806.653	13 ± 3	480 ± 80	12 ± 3	470 ± 80	15 ± 3	580 ± 100	20 ± 4	760 ± 130	24 ± 4	910 ± 150
CO (8-7)	921.800	10 ± 2	330 ± 60	11 ± 2	370 ± 70	15 ± 3	500 ± 90	19 ± 3	630 ± 110	27 ± 5	930 ± 160
CO (9-8)	1036.914	8.5 ± 2.0	250 ± 60	7.7 ± 1.7	230 ± 50	14 ± 3	410 ± 80	16 ± 3	490 ± 90	24 ± 5	730 ± 130
CO (10-9)	1151.985	8.5 ± 1.9	230 ± 50	10 ± 2	260 ± 50	14 ± 4	380 ± 90	17 ± 3	460 ± 80	34 ± 6	930 ± 160
CO (11-10)	1267.016	< 7.0	< 170	3.4 ± 1.2	82 ± 27	12 ± 4	290 ± 100	10 ± 2	250 ± 50	21 ± 4	520 ± 90
CO (12-11)	1381.997	< 5.0	< 110	4.6 ± 1.5	100 ± 30	6.4 ± 1.9	140 ± 40	11 ± 2	250 ± 50	14 ± 3	320 ± 60
CO (13-12)	1496.926	< 3.9	< 80	< 4.8	< 97	< 9.3	< 190	11 ± 3	220 ± 50	15 ± 3	310 ± 60
H_2O 211-202	752.032	< 1.5	< 59	2.4 ± 0.6	97 ± 25	5.2 ± 1.4	210 ± 60	3.0 ± 0.6	120 ± 30	9.3 ± 1.7	390 ± 70
H_2O 202-111	987.927	< 3.2	< 99	5.4 ± 1.2	170 ± 40	< 6.1	< 190	4.8 ± 1.1	150 ± 40	18 ± 4	580 ± 110
H_2O 312-303	1097.365	< 6.1	< 170	< 3.2	< 88	< 5.9	< 170	< 4.8	< 140	12 ± 3	350 ± 70
H_2O 312-221	1153.128	-	-	-	-	-	-	-	-	-	-
H_2O 321-312	1162.910	< 2.7	< 69	3.5 ± 1.1	93 ± 28	< 5.0	< 140	3.8 ± 1.1	100 ± 30	19 ± 4	520 ± 90
H_2O 422-413	1207.638	< 2.7	< 67	< 2.4	< 60	< 2.7	< 68	< 3.4	< 87	8.6 ± 1.9	220 ± 50
H_2O 220-211	1228.789	< 4.6	< 120	4.6 ± 1.5	110 ± 37	6.1 ± 1.9	150 ± 50	3.0 ± 0.9	75 ± 22	16 ± 3	400 ± 80
H_2O 523-514	1410.615	< 3.0	< 65	< 3.6	< 77	< 2.8	< 61	< 1.8	< 40	7.5 ± 1.9	170 ± 40
[C I] (1 − 0)	492.161	14 ± 5	850 ± 250	11 ± 3	680 ± 140	10 ± 3	640 ± 150	9.6 ± 2.3	600 ± 140	8.8 ± 2.7	560 ± 170
[C I] (2 − 1)	809.340	21 ± 4	790 ± 130	19 ± 4	700 ± 120	20 ± 4	750 ± 130	17 ± 3	640 ± 110	16 ± 3	610 ± 110
[N II]	1461.132	160 ± 30	3300 ± 600	130 ± 20	2600 ± 500	100 ± 20	2100 ± 400	73 ± 12	1500 ± 300	34 ± 6	730 ± 120
[C II]	1901.128	-	-	-	-	-	-	-	-	-	-
[N II]	2461.250	-	-	-	-	-	-	-	-	-	-
[O III]	3393.006	-	-	-	-	-	-	-	-	-	-
[O I]	4744.678	-	-	-	-	-	-	-	-	-	-

Note. — CO(10 − 9) is contaminated by emission from H_2O 312 − 221, so we quote only the combined flux for the two emission lines in the CO(10 − 9) row. In the luminosity ranges $10^{11.0-11.2}L_\odot$, $10^{11.2-11.4}L_\odot$, $10^{11.4-11.6}L_\odot$, $10^{11.6-12.0}L_\odot$, and $L > 10^{12}$ $L_\odot$, the mean redshifts are $z = 0.015$, $z = 0.018$, $z = 0.021$, $z = 0.027$, and $z = 0.038$, respectively, and the median IR luminosities are $10^{11.12}$ $L_\odot$, $10^{11.32}$ $L_\odot$, $10^{11.49}$ $L_\odot$, $10^{11.69}$ $L_\odot$, and $10^{12.21}$ $L_\odot$, respectively.

Table 3: Fluxes in luminosity bins at 0.8 < z < 4

		$10^{11.5}\,L_\odot < L < 10^{12.5}\,L_\odot$		$10^{12.5}\,L_\odot < L < 10^{13.0}\,L_\odot$		$10^{13.0}\,L_\odot < L < 10^{14.5}\,L_\odot$	
Line	Rest Freq. [GHz]	Flux [10^{-18} Wm^{-2}]	Flux [Jy km s^{-1}]	Flux [10^{-18} Wm^{-2}]	Flux [Jy km s^{-1}]	Flux [10^{-18} Wm^{-2}]	Flux [Jy km s^{-1}]
CO (5-4)	576.268	-	-	-	-	-	-
CO (6-5)	691.473	-	-	-	-	-	-
CO (7-6)	806.653	-	-	-	-	-	-
CO (8-7)	921.800	-	-	-	-	-	-
CO (9-8)	1036.914	< 1.5	< 130	-	-	-	-
CO (10-9)	1151.985	< 1.1	< 89	< 0.51	< 46	-	-
CO (11-10)	1267.016	< 0.66	< 50	< 0.21	< 17	-	-
CO (12-11)	1381.997	< 0.18	< 12	< 0.20	< 15	-	-
CO (13-12)	1496.926	< 0.11	< 6.8	< 0.16	< 11	-	-
H_2O 211-202	752.032	-	-	-	-	-	-
H_2O 202-111	987.927	-	-	-	-	-	-
H_2O 312-303	1097.365	< 0.96	< 84	< 0.53	< 49	-	-
H_2O 312-221	1153.128	-	-	-	-	-	-
H_2O 321-312	1162.910	< 0.99	< 82	< 0.51	< 45	-	-
H_2O 422-413	1207.638	< 0.92	< 73	< 0.31	< 26	-	-
H_2O 220-211	1228.789	< 0.91	< 71	< 0.24	< 20	-	-
H_2O 523-514	1410.615	< 0.14	< 9.4	< 0.18	< 13	-	-
[C I] $(1-0)$	492.161	-	-	-	-	-	-
[C I] $(2-1)$	809.340	-	-	-	-	-	-
[N II]	1461.132	< 0.12	< 7.5	< 0.18	< 13	-	-
[C II]	1901.128	0.20 ± 0.02	10 ± 1	0.56 ± 0.06	30 ± 4	0.89 ± 0.25	55 ± 15
[N II]	2461.250	< 0.025	< 0.97	< 0.066	< 2.7	< 0.21	< 10
[O III]	3393.006	< 0.094	< 2.7	0.31 ± 0.09	9.2 ± 2.5	< 0.37	< 13
[O I]	4744.678	< 0.076	< 1.6	0.59 ± 0.15	13 ± 3	< 0.35	< 8.5

Note. — CO$(10-9)$ is contaminated by emission from H_2O 312 − 221, so we quote only the combined flux for the two emission lines in the CO$(10-9)$ row. In the luminosity ranges $10^{11.5-12.5}L_\odot$, $10^{12.5-13.0}L_\odot$, $10^{13.0-14.5}L_\odot$, the mean redshifts are $z = 2.19$, $z = 2.40$, and $z = 2.93$, respectively, and the median IR luminosities are $10^{12.41}$ $L_\odot$, $10^{12.77}$ $L_\odot$, and $10^{13.24}$ $L_\odot$, respectively.

Table 4: Uncorrected line ratios for high-redshift sources

Uncorrected line ratios used in PDR modeling for high-redshift sources in three luminosity bins based on lensing-corrected luminosity. The median luminosities in each bin are $10^{12.41}$ $L_\odot$, $10^{12.77}$ $L_\odot$, and $10^{13.24}$ $L_\odot$, and the mean redshifts are 2.19, 2.40, and 2.93. These ratios are uncorrected for [O I] optical thickness, filling factors, and non-PDR [C II] emission, or for a plane-parallel PDR model FIR. The total correction factor (i.e., $([A]/[B])_{corrected}/([A]/[B])_{uncorrected}$) for each ratio is given in brackets. The plots in Figure 22 do take these correction factors into account.

Range $[\log_{10}(L_\odot)]$	Median $[\log_{10}(L_\odot)]$	Number of Sources	[O I]/[C II]	[C II]/FIR $(\times 10^{-4})$	[O I]/FIR $(\times 10^{-4})$	([O I]+[C II])/FIR $(\times 10^{-4})$
11.5 - 12.5	12.41 ±0.12	11	< 0.38 [36]	7.8±2.3 [1]	< 3.0 [4]	< 11 [1.8]
12.5 - 13.0	12.77 ±0.17	15	1.1±0.3 [36]	12±5 [1]	13 ± 6 [4]	24±11 [2.6]
13.0 - 14.5	13.24 ±0.32	10	< 0.40 [36]	11±9 [1]	< 4.1 [4]	< 15 [1.8]

Table 5: Uncorrected line ratios for low-redshift sources

Uncorrected line ratios used in the PDR modeling of the observed lines in the 0.005 < z < 0.05 and 0.05 < z < 0.2 redshift bins. The median luminosities of sources in these bins are $L_{IR} = 10^{11.35}$ $L_\odot$ and $10^{12.33}$ $L_\odot$, and the mean redshifts are z = 0.02 and z = 0.1, respectively. These ratios do not account for the corrections given in the text. The total correction factor (i.e., $([A]/[B])_{corrected}/([A]/[B])_{uncorrected}$) for each ratio is given in brackets, where applicable. The large uncertainties reported in the 0.005 < z < 0.05 bin stem from the large standard deviation of source FIR luminosities.

Range	Median $[\log_{10}(L_\odot)]$	Number of Sources	$\frac{[C\,I](2-1)}{[C\,I](1-0)}$	$\frac{[C\,I](1-0)}{CO(7-6)}$	$\frac{[C\,I](2-1)}{CO(7-6)}$	$\frac{[C\,I](2-1)}{FIR}$ $(\times 10^{-5})$	$\frac{[C\,I](1-0)}{FIR}$ $(\times 10^{-5})$	$\frac{CO(7-6)}{FIR}$ $(\times 10^{-5})$
$0.005 < z < 0.05$	11.35 ±1.03	115	1.6±0.8 [1]	0.77±0.37 [1]	1.3±0.4 [1]	1.6±3.7 [0.5]	0.97±2.29 [0.5]	1.3 ± 2.9 [0.5]
$0.05 < z < 0.2$	12.33±0.23	34	1.2±0.4 [1]	0.53±0.18 [1]	0.63±0.09 [1]	0.93±0.51 [0.5]	0.78±0.48 [0.5]	1.5±0.8 [0.5]

PDR Modeling

The average gas number density and radiation field strength in the interstellar medium can be inferred using photodissociation regions (PDR) models. About 1% of far-ultraviolet (FUV) photons from young stars collide with neutral gas in the interstellar medium and strip electrons off of small dust grains and polycyclic aromatic hydrocarbons via the photoelectric effect. These electrons transfer some of their kinetic energy to the gas, heating it. The gas is subsequently cooled by the emission of the far-infrared lines that we observe. The remaining fraction of the UV light is reprocessed in the infrared by large dust grains via thermal continuum emission [105]. Understanding the balance between the input radiation source and the underlying atomic and molecular cooling mechanisms is essential in constraining the physical properties of the ISM.

We use the online PDR Toolbox [180, 123] (http://dustem.astro.umd.edu/pdrt/) to infer the average conditions in the interstellar medium that correspond to the measured fluxes of both the stacked low ($0.005 < z < 0.05$ and $0.05 < z < 0.2$) and high-redshift ($0.8 < z < 4$) spectra. The PDR toolbox uses the ratios between the fluxes of fine structure lines and of the FIR continuum to constrain the PDR gas density and strength of the incident FUV radiation (given in units of the Habing field, 1.6×10^{-3} erg cm^{-2} s^{-1}). At low redshifts, the PDR models take into account the lines [C I] (1-0), [C I] (2-1), CO (7-6), and the FIR continuum; at high redshifts, the models use [C II] 158 μm, [O I] 63 μm, and the FIR continuum. We do not attempt PDR models of the intermediate redshift sample as we only detect the [C II] line in that redshift bin which would not allow us to constrain the

parameters characterizing the ISM (in particular constraining the radiation field-gas density parameter space).

As previously discussed, all sources with $z > 0.8$ are divided into three smaller bins based on total infrared luminosity. The [C II] line is detected in each subset of the high-redshift stack. In the high-redshift stacks, we observed emission from singly-ionized carbon ([C II] at 158 μm) as well as some weak emission from neutral oxygen ([O I] at 63 μm). We perform PDR modeling for only one of three luminosity bins. In this bin ($12.5\ L_{\odot} < L < 13.0\ L_{\odot}$), the [C II] and [O I] detections were the strongest, while in the other two bins, the detections were either too weak or nonexistent.

Before applying measured line ratios to the PDR toolbox, we must make a number of corrections to the measured fluxes. First, the PDR models of Kaufman et al. 1999 [124] and Kaufman et al. 2006 [123] assume a single, plane-parallel, face-on PDR. However, if there are multiple clouds in the beam or if the clouds are in the active regions of galaxies, there can be emission from the front and back sides of the clouds, requiring the total infrared flux to be cut in half in order to be consistent with the models (e.g., [124, 60]). Second, [O I] can be optically thick and suffers from self-absorption, so the measured [O I] is assumed to be only half of the true [O I] flux; i.e., we multiply the measured [O I] flux by two (e.g., [60, 49]). [C II] is assumed to be optically thin, so no correction is applied. Similarly, no correction is applied for [C I] and CO at low redshifts. Third, the different line species considered will have different beam filling factors for the SPIRE beam. We follow the method used in Wardlow et al. 2017 [237] and apply a correction to only the [O I]/[C II] ratio using a relative filling factor for M82 from the literature. Since the large SPIRE beam size prevents measurement of the relative filling factors, the [O I]/[C II] ratio is corrected by a factor of

1/0.112, which is the measured relative filling factor for [O I] and [C II] in M82 [209, 139, 124, 49]. Wardlow et al. 2017 [237] note that the M82 correction factor is large, so the corrected [O I]/[C II] ratio represents an approximate upper bound. Lastly, it is possible that a significant fraction of the [C II] flux can come from ionized gas in the ISM and not purely from the neutral gas in PDRs (e.g., [1, 49]). As a limiting case, we assume that 50% of the [C II] emission comes from ionized regions. This correction factor is equivalent to the correction for ionized gas emission used in Wardlow et al. 2017 and is consistent with the results of Abel et al. 2006, who finds that the ionized gas component makes up between 10-50% of [C II] emission.

To summarize: a factor of 0.5 is applied to the FIR flux to account for the plane-parallel model of the PDR Toolbox, a factor of 2 is applied to the [O I] flux to account for optical thickness, a factor of 0.5 is applied to the [C II] flux to account for ionized gas emission, and lastly, a correction factor of 1/0.112 is applied to the [O I]/[C II] ratio to account for relative filling factors. we do not apply any corrections to the [C I] (1-0), [C I] (2-1), or CO (7-6) fluxes used in the PDR modeling of the lower-redshift stacks. These correction factors can significantly alter the flux ratios; for example, the ratio $([\mathrm{O\ I}]/[\mathrm{C\ II}])_{\mathrm{corrected}} = 36 \times ([\mathrm{O\ I}]/[\mathrm{C\ II}])_{\mathrm{uncorrected}}$. Table 4 and Table 5 contain the uncorrected line ratios with the total correction factor for each ratio given in brackets. Naturally, these corrections introduce a large amount of uncertainty into our estimated line ratios. To demonstrate the effects that these corrections have on the results, we include contours from uncorrected and corrected line ratios in Figure 21 and Figure 22. In Figure 21 (low redshifts), the only flux correction carried out is the correction to the FIR flux. This correction is indicated by the dashed line in each of the plots. In Figure 22, the lefthand-

side plot displays the constraints on gas density and radiation field intensity (n, G_0) for high-redshift sources in the luminosity bin 12.5 $L_\odot$ < L < 13.0 $L_\odot$ determined from the uncorrected line ratios. The righthand-side plot shows the same contours but with the aforementioned correction factors taken into account. Clearly, the corrections can shift the intersection locus (the gray regions) to very different parts of n-G_0 parameter space. However, the correction factors should be treated with caution and represent limiting cases. The most variation is observed in the [O I]/[C II] ratio (shown in red), so the [O I]/[C II] contours on the lefthand and righthand plots in Figure 22 represent the two extreme locations that this contour can occupy. The uncorrected line ratios are summarized in Table 4 and Table 5. These tables include line ratios that are not included in Figure 21 and Figure 22 (for example, Table 4 contains the ratio [O I]/FIR, which does not appear in Figure 22). The figures contain only the independent ratios; the tables contain more (though not all independent ratios) for completeness.

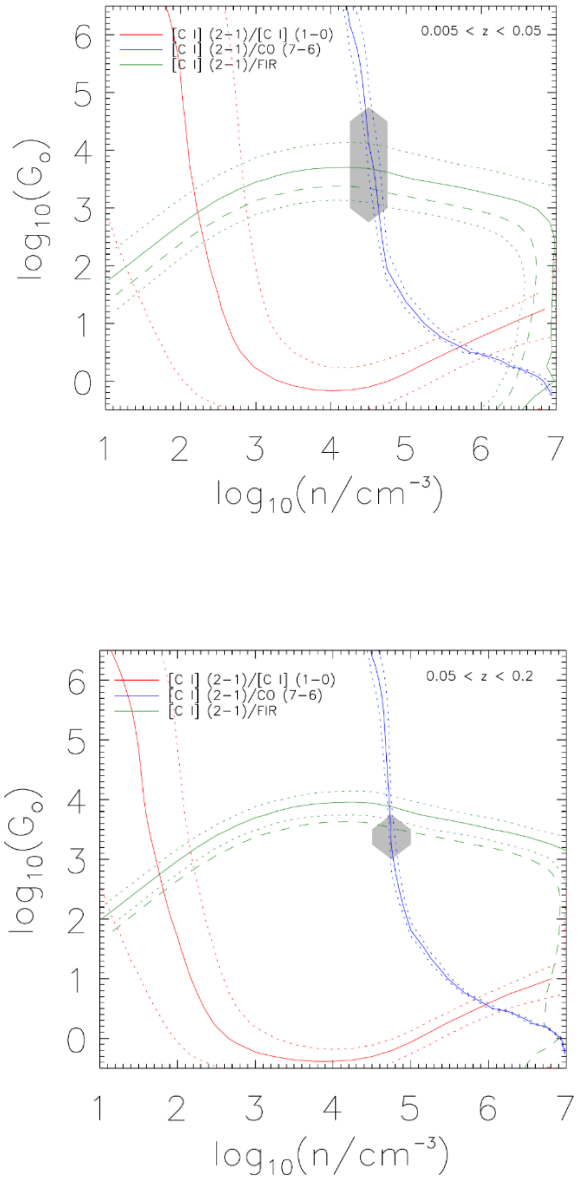

Figure 21: PDR modelling at low redshifts

PDR modeling of observed fluxes in 0.005 < z < 0.05 bin (top) and 0.05 < z < 0.2 (bottom). The solid lines are constraint contours determined from modeling, and the dotted lines are the 1σ uncertainties. The dashed lines indicate the changes in line flux ratios when the FIR correction (see main text) is applied. The gray regions indicate the most likely values of *n* and G_0 determined from a likelihood analysis using the corrected flux values of FIR. Table 5 lists the flux values for these two redshift bins before FIR corrections were applied. The line fluxes are in units of W m^{-2}, and the L_{IR} is the far-infrared flux, where the wavelength range that defines L_{IR} is converted to 30-1000 μm (See Farrah et al. 2013 [71]).

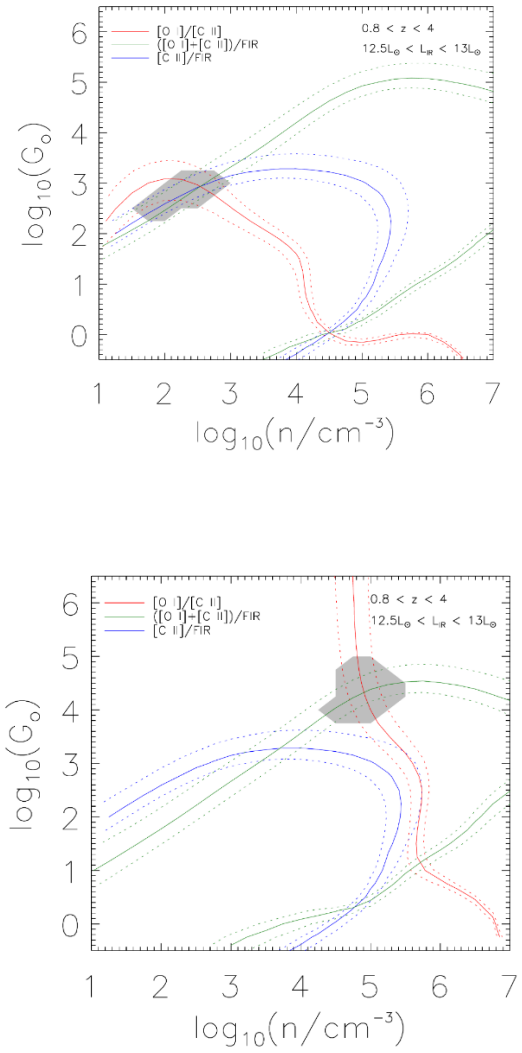

Figure 22: PDR modelling at high redshifts

Top: PDR modeling of observed fluxes for sources with $0.8 < z < 4$ in the luminosity bin $10^{12.5}\ L_\odot < L^{IR} < 10^{13}\ L_\odot$. No correction factors (see text) are applied to the line and line-FIR ratios in this plot. The gray regions indicate the most likely values of n and G_0 determined from a likelihood analysis. The uncorrected ratios used for PDR modeling are given in Table 4. The line fluxes are in units of W m^{-2}, and the FIR is the far-infrared flux, where the wavelength range that defines L_{IR} is converted to 30-1000 μm [71]. Though sources in this redshift range are split into three bins based on total infrared luminosity in the text ($L_{IR} < 10^{12.5}\ L_\odot$, $10^{12.5}\ L_\odot < L_{IR} < 10^{13}\ L_\odot$, and $L_{IR} > 10^{13}\ L_\odot$), the lack of [O I] detections in the first and third bins mean that PDR models for only the second bin are presented. Bottom: Same PDR model as on the left but with the correction factors discussed in the text taken into account. The most variation appears in the [O I]/[C II] ratio, which shifts the intersection region from $\log(n) \sim 2.5$ and $\log(G_0) \sim 2.5$ to $\log(n) \sim 5$ and $\log(G_0) \sim 4$.

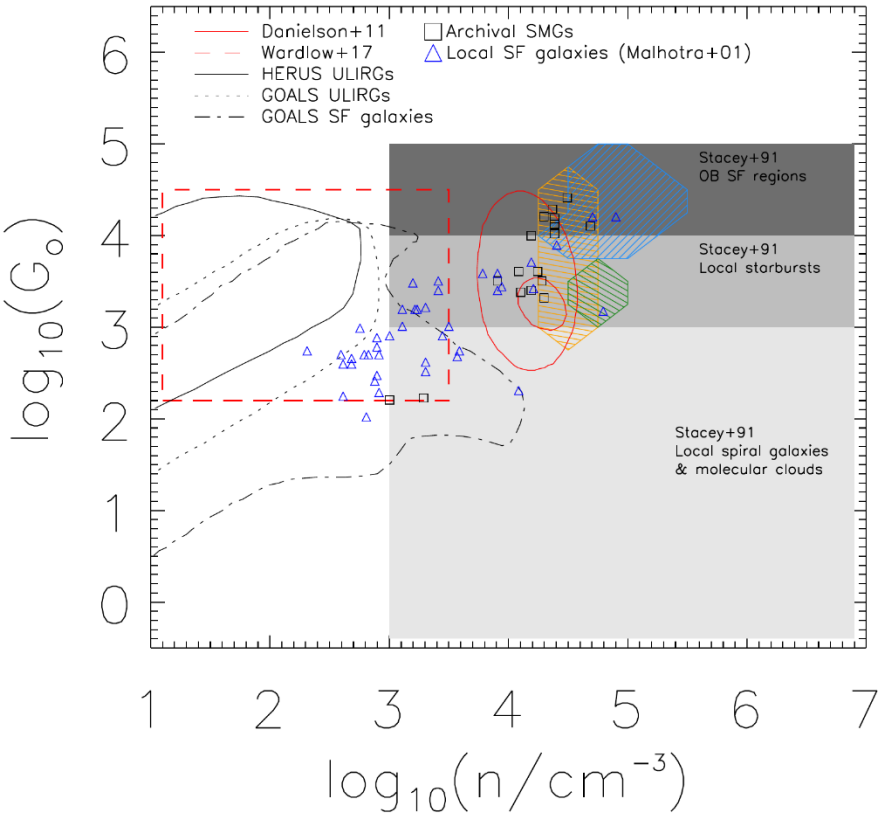

Figure 23: PDR modeling results compared to the literature.

The light blue region represents the derived n-G_0 for sources with $0.8 < z < 4$ and $12.5 < L/L_{\odot} < 13.0$. The orange and green regions represent the derived quantities for $0.005 < z < 0.05$ and $0.05 < z < 0.2$ subsamples, respectively. The regions shown here take into the account the correction factors discussed in the text. For comparison, the conditions for local spiral galaxies, molecular clouds, local starbursts, and galactic OB star-forming regions from Stacey et al. 1991 [209] are shown, as well as data points for local star-forming galaxies from Malhotra et al. 2001 [148] and for SMGs come from [237, 213, 54, 57, 226, 4, 111, 183].

The gray shaded regions in Figure 21 and Figure 22 represent the most likely values of n and G_0 given the measured line flux ratios. To generate these regions, we perform a likelihood analysis using a method adapted from Ward et al. 2003 [236]. The density n and radiation field strength G_0 are taken as free parameters. For measured line ratios $\vec{R}$ with errors $\vec{\sigma}$, we take a Gaussian form for the probability distribution; namely,

$$P\left(\vec{R} \mid n, G_0, \vec{\sigma}\right) = \prod_{i=1}^{N} \frac{1}{\sqrt{2\pi}\sigma_i} e^{\left\{-\frac{1}{2}\left[\frac{R_i - M_i}{\sigma_i}\right]^2\right\}}$$

where the R_i are the measured line ratios (i.e., [O I]/[C II], [C II]/FIR, etc.), N is the number of independent line ratios, and the M_i are the theoretical line ratio plots from the PDR toolbox. A grid of discrete points in n, G_0-space ranging from $1 < \log_{10}(n) < 7$ and $-0.5 < \log_{10}(G_0) < 6.5$ is constructed. To compute the most likely values of n and G_0, we use Bayes' theorem:

$$\mathrm{P}\left(\mathrm{n}, G_0 \middle| \vec{R}, \vec{\sigma}\right) = \frac{\mathrm{P}(\mathrm{n}, G_0) P\left(\vec{R} \mid n, G_0, \vec{\sigma}\right)}{\sum_{n, G_0} \mathrm{P}(\mathrm{n}, G_0) P\left(\vec{R} \mid n, G_0, \vec{\sigma}\right)}$$

The prior probability density function, P(n, G_0), is set equal to 1 for all points in the grid with $G_0 > 10^2$. Points with $G_0 < 10^2$ are given a prior probability of 0. The reason for this choice of prior stems from the argument that, given the intrinsic luminosities of our sources ($\sim 10^{11.5 - 13.5}$ $L_\odot$), low values of G_0 (which include, for example, the value of G_0 at the line convergence in the high-z PDR plot at $\log(n/cm^{-3}) \sim 4.5$ and $\log(G_0) \sim 0.2$) would correspond to galaxies with sizes on the order of hundreds of kpc or greater [237]. Such sizes are expected to be unphysical, as typical measurements put galaxy sizes with these luminosities at ~0.5-10 kpc (see [237] and references therein). P(n, $G_0 \mid \vec{R}, \vec{\sigma}$) gives the

probability for each point in the n-G_0 grid that that point represents the actual conditions in the PDR, given the measured flux ratios. The gray regions in Figure 21 and Figure 22 are 68.2% confidence regions. The relative likelihoods of each of the points in the grid are sorted from highest to lowest, and the cumulative sum for each grid point (the likelihood associated with that grid point summed with the likelihoods of the points preceding it in the high-to-low ordering) is computed. Grid points with a cumulative sum less than 0.682 represent the most likely values of density n and UV radiation intensity G_0, given the measured fluxes, with a total combined likelihood of 68.2%. These points constitute the gray regions.

The data constrain the interstellar gas density to be in the range $\log(n/cm^{-3}) \sim 4.5$ - 5.5 for both low-z and high-z, where these values are estimated from the PDR models with correction factors taken into account. The FUV radiation is constrained to be in the range of $\log(G_0) \sim 3$ - 4 and $\log(G_0) \sim 3$ - 5 for low-z and high-z, respectively.

The [C I] (2-1)/[C I] (1-0) line ratio is observed to deviate from the region of maximum likelihood on the G_0-density diagram (Figure 21). The region of maximum likelihood is shaded in gray in the figure. In fact, this ratio is very sensitive to the conditions in the ISM, such that a modest change in the radiation strength or density would shift the line towards the expected locus [57]. The PDR models also constrain the assumption for the production of [C I] to that of a thin layer on the surface of far-UV heated molecular ISM whereas several studies [170] point to the coexistence of neutral [C I] along CO in the same volume. These assumptions could also result in the deviations observed in the PDR models.

Figure 23 summarizes our main results of the PDR modeling based on the low and high redshift ISM emission lines from the stacked FTS spectra. We compare these

measurements with that of local star-forming galaxies [148], local starbursts [209] and archival SMGs. We see from Figure 23 that local DSFGs are on average subject to stronger UV radiation than that of local star-forming galaxies and are more consistent with local starbursts. Our measured density and radiation field strengths are further in agreement with results reported in Danielson et al. 2001 [57] for a single DSFG at $z \sim 2$. Given the uncertainty in filling factors and in the fraction of non-PDR [C II] emission, the [O I]/[C II] ratio contour in Figure 22 may shift downward and to the left toward smaller density and radiation field strength where it would be more consistent with the results in Wardlow et al. 2017 for *Herschel*/PACS stacked spectra of DSFGs.

Summary

We have stacked a diverse sample of *Herschel* dusty, star-forming galaxies from redshifts $0.005 < z < 4$ and with total infrared luminosities from LIRG levels up to luminosities in excess of 10^{13} $L_{\odot}$. The sample is heterogeneous, consisting of starbursts, QSOs, and AGN, among other galaxy types. With this large sample, we presented a stacked statistical analysis of the archival spectra in redshift and luminosity bins. We also presented the CO and H_2O spectral line energy distributions for the stacked spectra. Radiative transfer modeling with RADEX places constraints on the gas density and temperature based on [C I] (2-1) 370 μm and [C I] (1-0) 609 μm measurements. We use PDR modeling in conjunction with measured average fluxes to constrain the interstellar gas density to be in the range $\log(n/cm^{-3})$ 4.5 - 5.5 for stacks at low and high redshifts. The FUV radiation is constrained to be in the range of $\log(G_0) \sim 3$ - 4 and $\log(G_0) \sim 3$ - 5, for low redshifts and high redshifts, respectively. Large uncertainties are present, especially due to

effects such as contributions to the [C II] line flux due to non-PDR emission for which we can only estimate the correction factors to the observed line fluxes. Such uncertainties may lead to further discrepancies between the gas conditions at high- and low-redshifts, which may be understood in terms of nuclear starbursts of local DSFGs and luminous and ultra-luminous infrared galaxies compared to $\sim$ 10 kpc-scale massive starbursts of high-z DSFGs.

Chapter 2: Photometric Redshift Estimation with Galaxy Morphology using Self-Organizing Maps

Introduction

Photometric redshift (photo-z) estimation is crucial for astrophysical applications as obtaining spectroscopic redshifts for large samples of distant galaxies is oftentimes infeasible. Physical properties of extragalactic sources further depend on accurate redshift measurements. The photometric redshift can also be used as a good proxy for distance for mapping the large-scale structure and performing weak lensing studies [161].

Unfortunately, due to selective sampling of the galaxy SED, photometric redshifts suffer from much higher uncertainties than spectroscopic redshifts. Errors in photometric redshifts can significantly affect cosmological parameter measurements in, for example, weak lensing studies (e.g., [110, 144, 21]) and baryon acoustic oscillation studies (e.g., [257, 44]).

The observable quantity available for photo-z estimation is galaxy photometry in multiple wavelength bands, and a large number of techniques have been developed to estimate redshift while trying to minimize z_{phot} - z_{spec}. Photometric redshift estimation is primarily done via template fitting (e.g., [134, 75]) and/or statistical (e.g., [46]) and machine learning techniques. As surveys grow ever larger, machine learning techniques that can process enormous amounts of data with minimal human input are becoming increasingly important.

Some techniques for photo-*z* estimation involve using artificial neural networks with photometry and/or morphology data (e.g., [76, 15, 45, 232, 25, 198]), support vector

machines (e.g., [235, 117]), the Multi-Layer Perceptron with Quasi Newton Algorithm (MLPQNA, [30]), and the conditional density estimator FLEXCODE [116]. Statistical models have also been developed, such as the surface brightness and photometry model of Kurtz et al. 2007 [133], the algorithm based on surface brightness, Sérsic index and photometry developed in Wray & Gunn 2008 [244], and the Gaussian process regression models [239, 238, 25, 6, 7], which also appears in Gomes et al. 2018 [84] when applied to infrared- and visible-band photometry in conjunction with angular size. Wadadekar et al. 2005 [235] use support vector machines to estimate redshifts from photometric data as well as the 50% and 90% Petrosian radii for their sources. They observe a 15% increase in accuracy when they use the two Petrosian radii with photometry than when photometry alone was used. The empirical techniques in Vince & Csabai 2006 [234] use photometry and morphological data from SDSS, and they find that the weak correlation between morphology and redshift leads to only negligible gains in photo-z estimation accuracy. Singal et al. 2011 [197] use a principal component analysis including morphological parameters to estimate photometric redshifts for the All-wavelength Extended Groth Strip International Survey (AEGIS; [58]). They conclude that the additional noise added to the data set by including morphological parameters will offset any of the gains coming from correlations between redshift and morphology. Jones & Singal 2017 [117] use a support vector machine to estimate photometric redshifts. Their work includes principal components of eight morphological parameters; however, they observe no significant decrease in the RMS error or in the number of outliers (i.e., the number of galaxies with $(z_{phot} - z_{spec})/(1 + z_{spec})$ greater than some value, such as the value of 0.15 in Hildebrandt et al. 2010 [102]) when using morphological data. Machine learning models are trained on photometric and/or

morphological features that have been derived from the galaxy images. Hoyle et al. 2016 [107] develops a deep neural network that is trained directly on galaxy images, so the network itself decides which parts of the image are important. The paper does not note a significant improvement in redshift accuracy. A similar approach is found in Menou et al. 2018 [155], which uses a multi-layer perceptron/convolutional neural network (MLP-convnet) architecture that analyzes galaxy-integrated features such as fluxes and colors using the MLP framework while adding in morphological information found by analyzing images directly with the convnet framework. They find that the MLP-convnet architecture does lead to a significant improvement in accuracy but has no effect on the number of outliers.

We now focus on the use of a machine learning technique known as a self-organizing map (SOM; [130, 131]) has increased in the last decade. An SOM is an artificial neural network whose main advantage is its ability to reduce the dimensionality of input data while preserving the relationships between data points, thus making those relationships easier to visualize. We use the SOM to characterize the multi-dimensional space of observed galaxy Spectral Energy Distributions (SEDs). In the literature, Tagliaferri et al. 2003 [217] combine multilayer perceptrons with self-organizing maps to analyze photometric data from SDSS. There is also MLZ (Machine Learning and photo-*z*, [37, 38] which performs two regression algorithms for computing photo-zs: TPZ, which uses prediction trees and random forests, and SOMZ, which uses self-organizing maps. SOMs are also used by Masters et al. 2015 [151] to estimate redshifts and identify regions in galaxy color space where spectroscopic redshifts have not been obtained in past surveys. If these gaps could be filled in by future surveys, such a complete training set would be a powerful

tool for photo-z estimation using machine learning. Recent work by Speagle & Eisenstein 2017 [200, 201] develop a photo-z technique that combines template-fitting methods with self-organizing maps. When trained on mock LSST and *Euclid* data, they find that their technique can predict redshifts to the accuracy required for *Euclid* weak lensing measurements [200, 201].

In this chapter, we explore the effect that the addition of galaxy morphology to SOM training data has on redshift estimation accuracy. This chapter is organized as follows: Section 2 describes the catalog data from GOODS-S used in our study. In Section 3, we summarize the self-organizing map algorithm. Sections 4 and 5 discuss the performance of the self-organizing maps when photometry alone and photometry plus morphology, respectively, are used for training. The AB magnitude system is used, and a flat-ΛCDM cosmology of $\Omega_{m,0} = 0.27$, $\Omega_{\Lambda,0} = 0.73$, and $H_0 = 70$ km s^{-1} Mpc^{-1} is assumed. The code developed herein will be made publicly available at https://github.com/derkwilson/PhotSOM.

Data

We use publicly available data from the GOODS-S field (centered at R.A. = $03^h32^m30^s$, Decl. = $-27^d48^m20^s$) which covers an area of approximately 150 $arcmin^2$. Our training and testing catalogs are pulled from the Cosmic Assembly Near-Infrared Deep Extragalactic Legacy Survey (CANDELS; [89, 129], https://archive.stsci.edu/prepds/candels/). The full CANDELS GOODS-S catalog [93]

includes optical, near-, and mid-infrared photometry from the *Hubble* Space Telescope (HST), the Very Large Telescope (VLT), and the *Spitzer* Infrared Array Camera (IRAC). Our primary training and testing catalogs each consist of 506 galaxies in the GOODS-S field with colors computed from the 15 bands listed in Table 1, comparable to the training and testing sets of Dahlen et al. 2013 [56]. We have an additional training set with about 1360 sources, and the results using this training set do not differ significantly from the 506-source training set, so we will focus on the results from the 506-source set. We note that Bonfield et al. 2010 [25] find that photo-z estimates deteriorate with fewer than 2000 training objects when using artificial neural networks and Gaussian process regression, but that the size and architecture of the network may permit reasonable results with fewer training objects. All sources in the training and testing sets have $z_{spec} < 2$, and the distribution of redshifts is shown in Figure 24. Dahlen et al. 2013 [56] previously released a training/testing catalog set with photometry in the same bands (except ACS F814W) extending up to $z \sim 5$ in redshift, so we also test our SOMs with these catalogs for comparison.

The full CANDELS GOODS-S catalog [93] includes mid-infrared photometry from Wide Field Camera 3 (WFC3) F105W, F125W, and F160W on the *Hubble* Space Telescope as well as public U band CTIO/MOSAIC and VLT/VIMOS data, optical HST/ACS F435W, F606W, F775W, F814W, F850LP data, and near-infrared HST/WFC3 F098M, VLT/ISAAC Ks, VLT/HAWK-I Ks, *Spitzer*/IRAC 3.6, 4.5, 5.8, and 8 μm data.

In addition to the photometry, we use half-light radii (from Häußler et al. 2013 [94]) and concentration, asymmetry, and smoothness data from Peth et al. 2016 [173] (see Table 6). In total, we use 15 photometric features and 4 morphological features when training

and testing our SOMs. Half-light radii come from a single-Sérsic fit to sources extracted from H-band images. Peth et al. 2016 [173] extract morphological quantities from the WFC3 F125W and F160W images obtained by CANDELS. We use the H-band morphologies from the Peth et al. 2016 catalog. Training data consists of the colors [93] and sizes/morphologies [173, 94] for ~500 galaxies with known spectroscopic redshifts. We match the size/morphology data to the photometry for each of the sources in these catalogs based on sky coordinates.

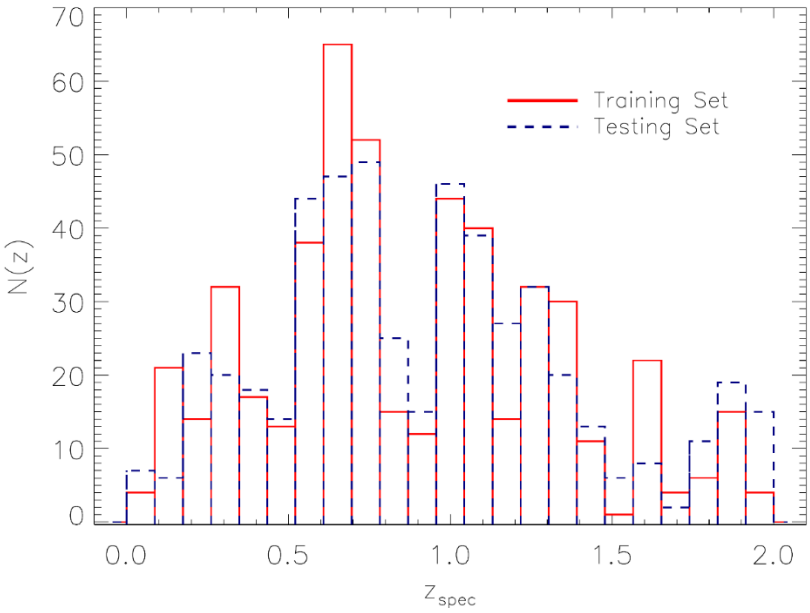

Figure 24: Spectroscopic redshift sample for SOMs

Histograms of the galaxy spectroscopic redshifts comprising the training (red) and testing (blue dashed) sets. The training and testing sets each contain 506 individual galaxies up to a redshift of 2.

Table 6: Features used for SOM training

The 19 features used in the training and testing of the SOMs. The first 15 lines of the table are the photometry, showing the instrument and filter used as well as the central wavelength of the filter. The bottom 4 lines of the table show the morphological quantities used and the corresponding wavelengths. References: G04: Giavalisco et al. 2004 [83], N09: Nonino et al. 2009 [165], R10: Retzlaff et al. 2010 [184], K11: Koekemoer et al. 2011 [129], W11: Windhorst et al. 2011 [240], A13: Ashby et al. 2013 [13], G13: Guo et al. 2013 [93], H13: H*ä*ußler et al. 2013 [94], P16: Peth et al. 2016 [173]

Feature	Wavelength (μm)	Refs.
VLT/VIMOS U	$\sim$0.36	N09,G13
HST/ACS F435W	0.4320	G04,K11,G13
HST/ACS F606W	0.5956	G04,K11,G13
HST/ACS F775W	0.7760	G04,K11,G13
HST/ACS F814W	0.8353	G04,K11,G13
HST/ACS F850LP	0.8320	G04,K11,G13
HST/WFC3 F098M	0.985	W11,G13
HST/WFC3 F105W	1.045	K11,G13
HST/WFC3 F125W	1.250	K11,G13
HST/WFC3 F160W	1.545	K11,G13
VLT/ISAAC Ks	2.16	R10,G13
Spitzer/IRAC 3.6	3.6	A13,G13
Spitzer/IRAC 4.5	4.5	A13,G13
Spitzer/IRAC 5.8	5.8	G13
Spitzer/IRAC 8.0	8.0	G13
R_{50}	0.4320	H13
Concentration (C)	1.250	P16
Asymmetry (A)	1.250	P16
Smoothness (S)	1.250	P16

Galaxy morphologies are captured by a number of quantities; for example, radius, concentration, asymmetry, smoothness, Sérsic index, axis ratio, Gini coefficient, and second order moment (e.g., [48, 47, 141, 173]). A galaxy's spatial extent can be characterized through measurements of half-light radius (hereafter R_{50}), which is the radius at which 50% of the galaxy's total flux falls. Concentration [127, 22, 47] describes the extent to which a galaxy's light is concentrated toward the center. The concentration is taken to be the ratio between the radii containing 80% and 20% of the galaxy's light within 1.5 Petrosian [174] radii (e.g., [173]). Large scale asymmetries in the light distribution of the source are described by the asymmetry statistic [48]. High asymmetry is typical for blue, star forming galaxies and can be indicative of systems that have undergone mergers [48, 47]. Smoothness [47], also known as clumpiness, traces structures with high spatial frequencies, such as star forming regions. In contrast, objects like elliptical galaxies consist primarily of low spatial frequencies, due to their smooth light distributions. Conselice et al. 2003 [47] define clumpiness as the ratio between the flux in high frequency spatial structures and the total flux of the galaxy. There are alternative methods for identifying clumps, such as resolved rest-frame *(U-V)* color selections [97], see also [247, 92] which yield comparable results.

Together, concentration, asymmetry, and smoothness make the CAS structural parameter system [47]. The CAS parameters form a three-dimensional volume that can be used to classify galaxies into elliptical, spiral, dwarf irregular, dwarf elliptical and merger classes. We include the CAS system in our analysis to see if the evolution of morphological parameters correlates strongly enough with redshift in order to improve photo-*z* estimates.

We provide a brief summary of other interesting morphological quantities that could also potentially be used in training the self-organizing maps, though were not used in this study. The Gini coefficient [140, 2, 141] is a quantity used to measure how equally light is distributed amongst pixels in a galaxy image. The Gini coefficient is also correlated with concentration [2]. The second-order moment [141] measures the flux in pixels weighted by their squared distance from the galaxy center. This statistic is sensitive to bright features like galactic nuclei, bars, spiral arms, and star clusters [141].

Redshift Measurement Algorithm

We use the self-organizing map to identify correlations between redshift and observed galaxy colors as measured from the multi-band optical and near-infrared data. Galaxy morphological information is included in the self-organizing map algorithm in a later section. When the SOM is given the color/morphology data of a test galaxy, it searches for the node that is closest in color-morphology space to that test galaxy and makes an approximation of its redshift based on the location of the node within the map. In theory, we could supply the self-organizing map with any observable quantity (photometric or morphological; such as color, half-light radius, Sérsic index, asymmetry, concentration, Gini coefficient, etc.), and the SOM would cluster the input data according to the correlations that it locates in the data. For galaxy SED studies, this means that we can explore any of the mapped properties and associate those with a measured value given the clustered information.

The construction of the self-organizing map is similar to the self-organizing map association network (SOMA) from Yamakawa 2001 [249], though our method of association differs. A SOMA infers a set of perfect (complete) information from a set of incomplete information. For the case presented here, we take the perfect information to be a vector of data points consisting of galaxy photometry, morphology, and spectroscopic redshift, and the incomplete information would be a vector of photometric and morphological data points, without a redshift. The SOMs are constructed and organized from a set of training samples consisting of perfect information; subsequently, samples composed of incomplete information and unknown spectroscopic redshift can be presented to the map for redshift classification. Note that *perfect* in this sense does not mean without error, but rather that the data *exists*.

The self-organizing map is initialized to an $m \times n$ array of nodes. Each node contains a weight vector that covers the attribute (e.g., color, size, spectroscopic redshift) space of the input data. This weight vector is initialized to random values, and, as the map is trained, these weight vectors will update themselves to be more representative of the data. This training process is repeated for each galaxy in the training sample. The map as a whole has a topology which we take to be toroidal. Various works in the literature (e.g., [249, 151]) describe the training process in detail. We summarize the same process here and borrow their notation. One training iteration begins with the selection of a random training sample with feature vector $\vec{x}$ containing photometric and morphological data as well as a spectroscopic redshift. Next is the identification of the Best-Matching Unit (BMU), the node which is closest in attribute space to the training sample according to the reduced-χ^2 distance given by:

$$d_k^2(\vec{x}, \overrightarrow{w_k}) = \frac{1}{m}\sum_{i=1}^{m}\frac{\left(x_i - w_{k,i}\right)^2}{\sigma_{xi}^2}$$

where d_k is the reduced-χ^2 distance, m is the length of the feature vector $\vec{x}$, x_i is the i^{th} component of $\vec{x}$, σ_{xi} is the uncertainty associated with x_i, and $\overrightarrow{w_k}$ is the k^{th} weight vector in the SOM. In the cases in which a training object or testing object was missing a data feature (i.e., a value of -99 for flux in some band), the reduced χ^2 distances for each node were computed by taking the missing feature to be exactly equal to the node weight that corresponded to the missing feature; i.e., setting x_i equal to $w_{k,i}$ for that feature. This means that only the non-missing data will contribute to the sum in the equation above. In this way, the incomplete training/testing vector can still exist in the *m*-dimensional feature space, but its reduced χ^2 distance will only depend on the features that are not missing. This technique also works if more than one feature are missing.

The goal is to have nodes with similar weights located near each other in the map. The nodes in the "neighborhood" of the BMU are determined by the neighborhood function H_k, which we take to be Gaussian:

$$H_k(\mathrm{t}) = e^{-d_k^2/\sigma^2(t)}$$

where the standard deviation $\sigma^2(\mathrm{t})$ of the neighborhood function is:

$$\sigma(\mathrm{t}) = \sigma_0\left(\frac{1}{\sigma_0}\right)^{(\mathrm{t}/\mathrm{N_{iters}})}$$

where σ_0 is an arbitrary initial value, and *t* is an integer ranging from 1 to the total number of training iterations, N_{iters}.

The BMU and surrounding nodes are then rewarded for being nearest to the training sample and are allowed to update their weights according to the relation:

$$\overrightarrow{w_k}(t+1) = \overrightarrow{w_k}(t) + a(t)H_k(t)[\vec{x}(t) - \overrightarrow{w_k}(t)]$$

where we adopt the learning function a(t):

$$a(t) = e^{-t/N_{iters}}$$

While other learning functions exist in the literature (e.g., [151]), we selected this one because it gave the lowest outlier fraction. The learning function decreases monotonically and is intended to de-sensitize the SOM to new training data as time progresses, allowing it to converge to a stable solution.

The multitude of SOM parameters (e.g., number of nodes, number of training iterations, learning rate, neighborhood function) affect the performance of the SOM as a whole. The number of nodes and training iterations used will depend on the total number of training samples available. A larger training set will require more training iterations to fully capture the data; however, it is possible to over-train a map with too many training iterations, where the SOM learns the training data well but does not generalize to data it has not seen before.

The number of nodes affects the number and size of clusters that form in the trained map. If the number of nodes is too small, the map may not capture the full set of relations present in the data. Increasing the number of nodes and training iterations comes at a cost in computing time as well. We determined by cross-validation that a map size of 150 pixels by 150 pixels had optimal predictive ability. Cross-validation involves removing a subset of samples (the validation set) from the training set, training the map on the remaining samples, and then using the validation set as testing samples. The grid size of the map is

varied, and the optimal value of the grid size hyperparameter is selected based on performance on the validation set.

To extract a redshift prediction from the SOM, it is presented with a test vector that contains the same photometric and morphological attributes as the training vectors, but without the spectroscopic redshift. While ignoring the redshift attribute of the SOM nodes, the reduced-χ^2 distance is computed between the test vector and each node in the map, identifying the best-matching unit (node). The redshift of the best-matching unit becomes the redshift associated with the test vector and represents the best prediction of the redshift of the test source. An example SOM is shown in Figure 25.

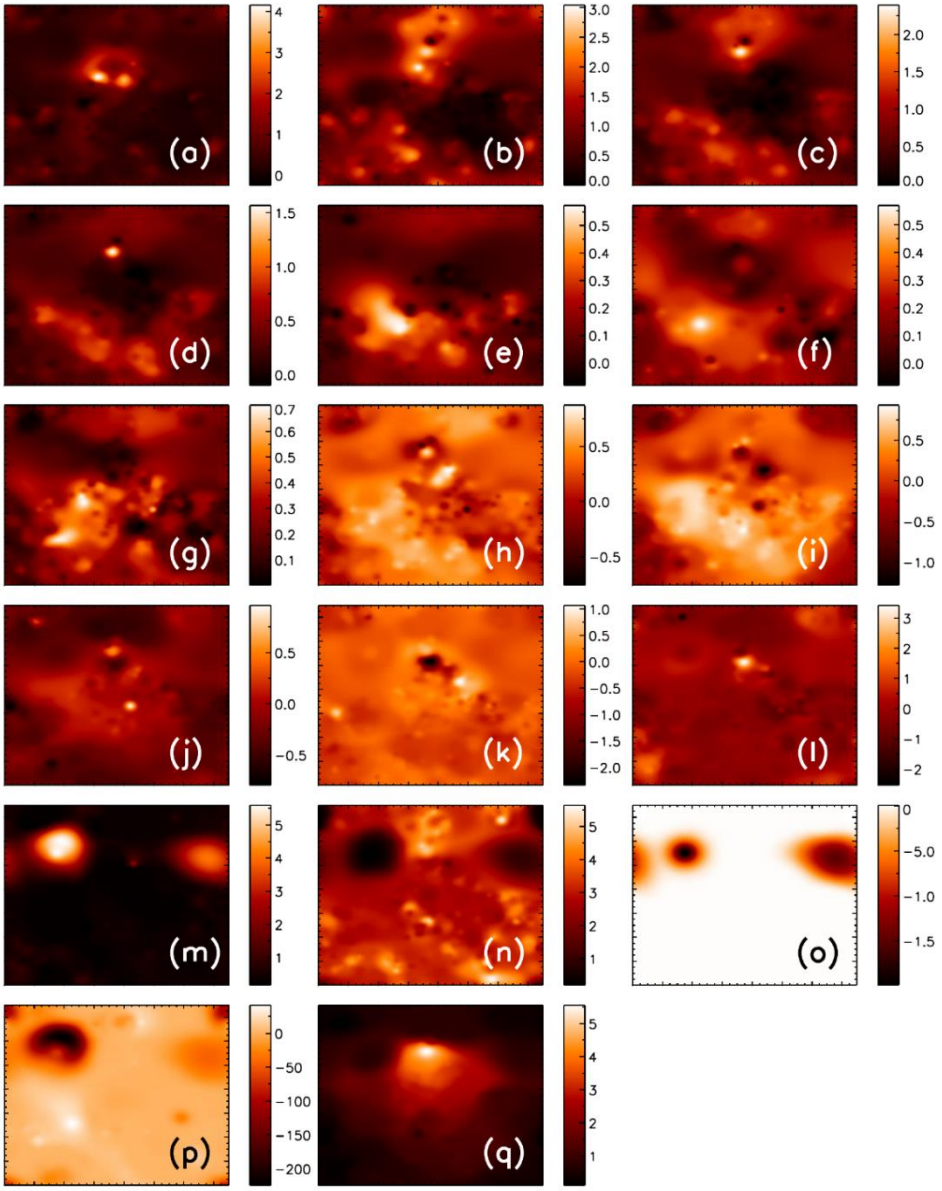

Figure 25: Example self-organizing map decomposition

Decomposition of a self-organizing map into its component planes for the GOODS-S field. Each pixel in the 150-pixel-by-150-pixel (corresponding to the x- and y-axes in the figure) self-organizing map contains a vector of weights corresponding to each of the input data features. For each data feature, there exists a component plant, which shows the value for that particular data feature at each pixel in the map. For each of the component planes shown above, we show the values of the individual weights. Maps (a)-(l) correspond to the various galaxy colors. Map (m) shows the weights corresponding to redshift. Maps (n), (o), (p), and (q) correspond to half-light radius, concentration, asymmetry, and clumpiness, respectively.

SOMs on Galaxies

In order to test the SOM, the known spectroscopic redshifts of galaxies must be compared to the predictions of the map. However, the galaxies used to test the map must not be sources that the map has seen before; that is, they cannot appear in the training set. A study of several photometric redshift codes was performed by Dahlen et al. 2013 [56], and they have released the training and control catalogs based on GOODS-S data that was used in the study. As a first test, our SOMs were trained and tested using this training/control set, which contained only photometric data. For each source, the quantity $\sigma = \Delta z/(1 + z_{spec})$, where $\Delta z = z_{BMU} - z_{spec}$, is determined. There are several measures of performance (e.g., [56]), denoted by σ_F (= rms[$\Delta z / (1 + z_{spec})$]), σ_O (the same as σ_F but has sources with $\sigma > 0.15$ removed), and the outlier fraction (OLF) specifying the fraction of sources with $\sigma > 0.15$). Individual SOMs were trained using the training/testing set from Dahlen et al. 2013, and the performance of individual maps was found to be $\sigma_F \sim 0.17$, $\sigma_O \sim$ 0.042 - 0.044, and OLF $\sim$ 9% - 10%. To obtain a slight improvement in accuracy, the median of the results of 500 SOMs was found (since each self-organizing map will be slightly different as the initial node weights are random and the training samples may be presented in different orders), giving $\sigma_F \sim 0.15$, $\sigma_O \sim$ 0.036 - 0.038, and OLF $\sim$ 6% - 8%.

Next, we trained and tested the SOMs using three training/testing set pairs each composed of ~500 sources with $z < 2$ The first training/testing set contained only 13 colors (computed from 14 photometric bands), the second set contains R_{50} from a single-Sérsic fit in addition to the colors, and the third set contains the colors as well as concentration, asymmetry, and clumpiness (CAS) data. We select sources with $z < 2$ because

morphological measurements for higher redshift sources will be inherently less precise. A single self-organizing map trained and tested with our training set of z < 2 sources produced a typical σ_F in the range 0.14 - 0.16 and σ_0 in the range 0.048 - 0.052 with outlier fractions of ~10% - 12%. By computing the median of multiple SOMs, we produced slightly lower values of σ_0. By averaging the SOM outputs in this way, we obtained the results in Table 2 when using photometry alone, and photometry with either R_{50} or CAS. An example of typical results is shown in Figure 26.

Table 7: SOM performance metrics

Summary of performance when using the median of multiple SOM predictions after training was done with photometry alone, photometry plus half-light radius, and photometry plus concentration, asymmetry, and smoothness. The addition of morphological parameters had an insignificant effect on photometric redshift estimation.
[1]OLF: Outlier fraction, the fraction of sources with σ > 0.15.

	σ_F	σ_o	OLF[1]
photometry only	~0.14	~0.05	10% - 11%
with R_{50}	~0.14	~0.06	12% - 14%
with CAS	~0.13	~0.05	10% - 12%

For comparison, we run several public photo-*z* codes on the three training/testing set pairs. The photo-*z* codes used were PhotoRApToR using MLPQNA [30], FLEXCODE [116], and TPZ and SOMz from the MLZ package [37, 38]. Here we will only give a brief summary of these algorithms. MLPQNA uses a supervised learning technique involving multi-layer perceptrons, a network of neurons that is trained by minimizing a loss function. The loss function is minimized by iteratively updating the weights in the neural network. The Quasi-Newton Algorithm is used to compute the Hessian of second derivatives, which is necessary for computing the amount by which the network weights are updated. We use a three-layer network with 15, 16, or 18 neurons in the first layer (if the training set contains just photometry, phot + R_{50}, or phot + CAS, respectively), 64 neuron in the second layer, and 1 neuron in the final layer. We set a decay rate of 0.001 and use 10000 max iterations.

FLEXCODE employs a conditional density estimator method which seeks to improve photo-zs by constructing a full conditional density distribution from the data. This is done using an orthogonal series formulation, with the series coefficients determined by regression. The result is a conditional probability distribution that is useful for handling the multi-modality in a photo-z prediction. When running FLEXCODE, we use the XGBoost regression method with a cosine basis system.

MLZ can perform regression using two different methods: a prediction tree and random forest algorithm and a self-organizing map algorithm. Prediction trees work by splitting the data into multiple branches based on some attribute. This process is repeated recursively until a stopping criterion is met, at which point a photo-z prediction can be made. A random forest is a collection of prediction trees whose predictions can be combined to produce more accurate results. The SOM component of MLZ works similarly to

the SOM algorithm described in this work. The main difference between the SOM algorithms is the way in which spectroscopic redshift is used to train the SOM. In the MLZ SOMz, the spectroscopic redshift does not enter in the training of the SOM. Only after the map has been trained are the spectroscopic redshifts from the training sample associated with the nodes in the map, with the mean redshift of the sources associated with each node becoming the final redshift of that node. For our study with TPZ, we set the MinLeaf parameter to 10. For SOMz, we use a periodic grid with a size of 64 nodes and 3000 training iterations.

Our implementation of the SOM algorithm uses a supervised approach. The spectroscopic redshift is included during the training process, and the final trained map will contain weights corresponding to the final redshift associated with each node. Overall, the performances of our SOM algorithm and the other photo-z codes were comparable, though missing data negatively affected the performance of some of the codes. As almost every source was missing photometry in one band or another, the replacement of the missing value with -99 may not allow the codes to perform optimally, while at the same time, removal of all data points with a missing value was not possible. The results from the photo-z codes are shown in Figure 27, and the corresponding metrics are listed in Table 3. FLEXCODE returned similar results for all three testing sets. The TPZ algorithm from MLZ was generally less accurate for the testing sets that included morphological data. We note that it is possible that there may exist hyperparameters for the FLEXCODE and TPZ algorithms that may improve their predictions but which we may have missed while tuning these models, despite our best efforts to find the optimal hyperparameters. MLPQNA and the SOMz algorithm had large outlier fractions, with the number of outliers increasing when

morphological data was used in training. It is likely that the large outlier fractions may be caused by missing data.

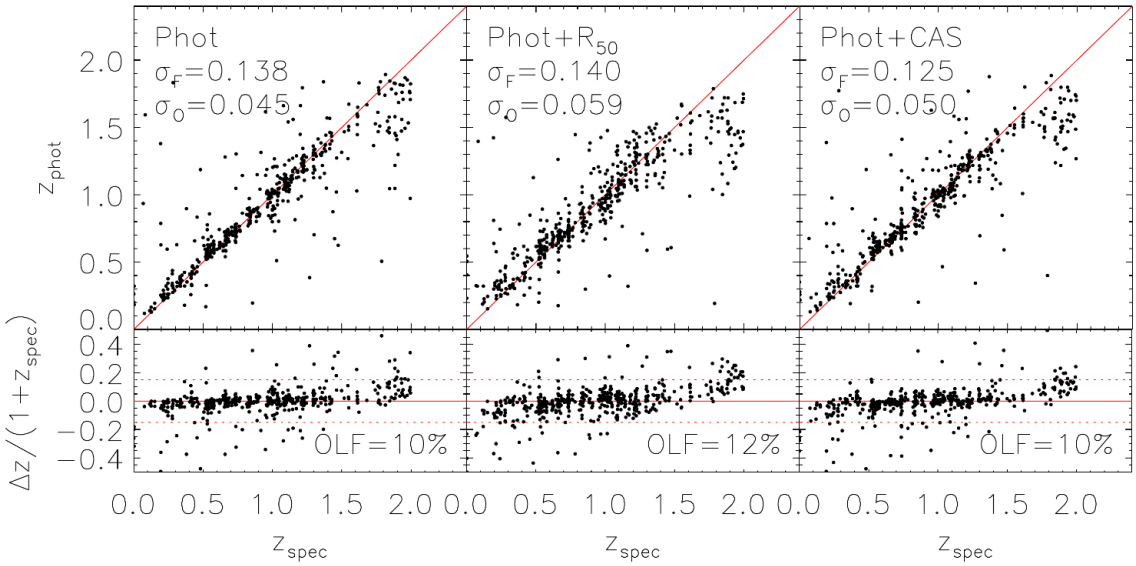

Figure 26: Photo-z predictions using SOMs

The top row shows a comparison of photo-z to spec-z for GOODS-S field using different subsets of data features. The bottom shows the normalized residuals given by (z_{phot} - z_{spec})/(1 + z_{spec}). Left: SOM predictions using only photometric data. Middle: Using photometry and half-light radius. Right: Using photometry and concentration-asymmetry-smoothness (CAS) data.

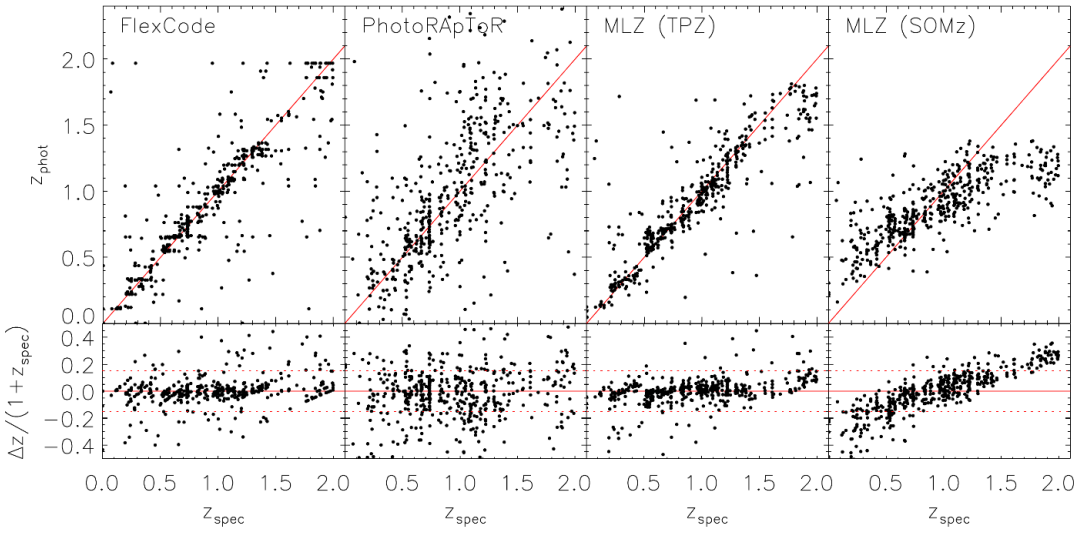

Figure 27: Comparison of photo-z codes

An example of the results from the literature photo-z codes when applied to our training/testing set containing photometry and R_{50}. See text for references and Table 3 for quantitative metrics of the results. We find that our SOM implementation produces results that are similar in dispersion and outlier fraction. PhotoRApToR and SOMz had unusually large outlier fractions, which we attribute to the effects of missing data in the training/testing sets. It is possible that a more extensive search over hyperparameter space may yield better results.

Table 8: Photo-z code performance metrics

Typical results obtained by running photo-z codes from the literature on our training/testing sets including photometry and morphologies. The results from our SOM implementation are about the same as the results from these other software packages.

	σ_F	σ_o	OLF
FlexCode	∼0.15	∼0.05	11% - 13%
PhotoRApToR (MLPQNA)	∼0.44	∼0.07	21% - 27%
MLZ (TPZ)	∼0.12	∼0.05	9% - 10%
MLZ (SOM)	∼0.16	∼0.07	24% - 28%

Probability Distributions

Many photo-*z* methods return a probability distribution in redshift space (e.g., LEPHARE [12, 112], PROBWTS [55]) as methods that only give point estimates can miss important information; e.g., a probability distribution may be double-peaked, but a point estimate may only see the larger peak and miss the information in the secondary peak [150, 55, 241, 26, 3, 196]. By using an ensemble of SOMs, the algorithm that we employ can be extended to return a probability distribution. Each individual SOM in the ensemble is initialized randomly, with no two SOMs having the same starting parameters. The different initializations will lead each map to converge to different weights after the training process is completed, and thus each map will predict a different photometric redshift for a test source. The results from the ensemble of SOMs are histogram-ed with a bin size of $\Delta z = 0.01$ to form the final probability distribution function (see Figure 28), and the median of the distribution is taken to be the final point estimate of the redshift.

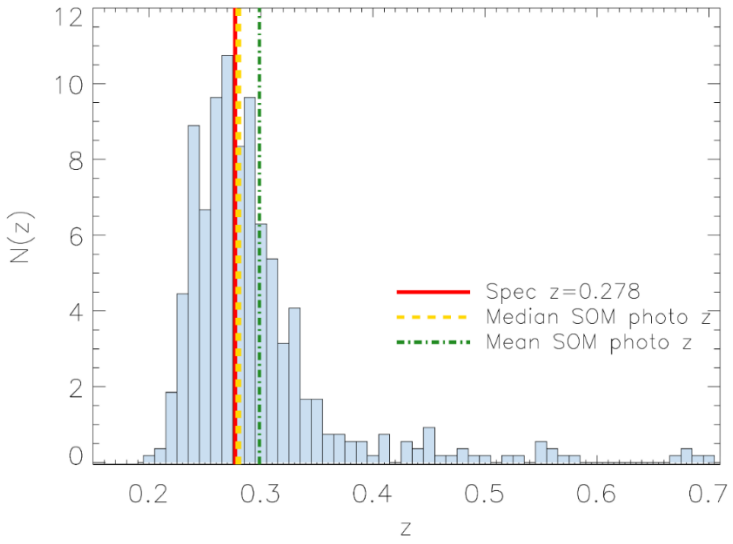

Figure 28: Estimated redshift probabilities

Example of a redshift probability distribution generated using 500 different SOMs. The spectroscopic redshift for this source is z = 0.278. Since each of the 500 SOMs is initialized with a different random set of parameters, each will converge to its own estimate of the redshift. The median of multiple SOMs provided measurements that were more closely aligned with the spectroscopic redshifts, due to its insensitivity to outliers.

The quality of the probability distribution functions (PDFs) is tested using the probability integral transform (PIT) described in Polsterer et al. 2016 [178] and the confidence test from Wittman et al. 2016 [242]. The probability integral transform (PIT, [59]) is given by the histogram of the cumulative probabilities of each redshift PDF computed at the value of the spectroscopic redshift. The PIT histogram serves as a visual guide for how well-calibrated the probability distribution is [178]. Figure 29 shows an

example derived from the SOM distribution functions. Ideally, the PIT should be nearly uniform if the PDFs are well-calibrated. The U-shape of the histogram in Figure 29 indicates that our PDFs are under-dispersed, i.e., that the dispersion in the redshift PDFs predicted by the SOMs is too small and the spectroscopic redshifts are too often ending up in the tails of the PDFs. As such, it appears that there is an overabundance of PDFs in which the statistical likelihood is very low for the spectroscopic redshift associated with the galaxy for that PDF. This means that the PDFs do not adequately represent the spectroscopic redshifts, and more work is required to make them more accurate.

The second metric used to test the SOM PDFs is the test developed by Wittman et al. 2016 [242] to determine whether the widths of probability distribution functions are over- or under-confident. We refer readers to the original paper for a more in-depth explanation of the test but provide a brief summary here. This confidence test is based on the principle that, ideally, a sample of galaxies should have 1% of its spectroscopic redshifts fall in the 1% credibility intervals (CI) of the corresponding PDFs, 2% of spectroscopic redshifts fall in the 2% CI, 50% of spectroscopic redshifts fall in the 50% CI, and so on. To perform the test, the threshold credibility, c_i, is computed for each galaxy in the testing set. The cumulative probability function F(c) is then found from the distribution of the c_i. This cumulative distribution function is plotted in Figure 30. Ideally, the curve should lie on the red dashed line, if 1% of z_{spec} fall in the 1% CI, etc. In our case, the black curve lies below the ideal case, indicating that our redshift PDFs are overconfident, i.e., that the confidence intervals are too narrow, and the uncertainties are underestimated. Again, more work is needed to improve the PDFs.

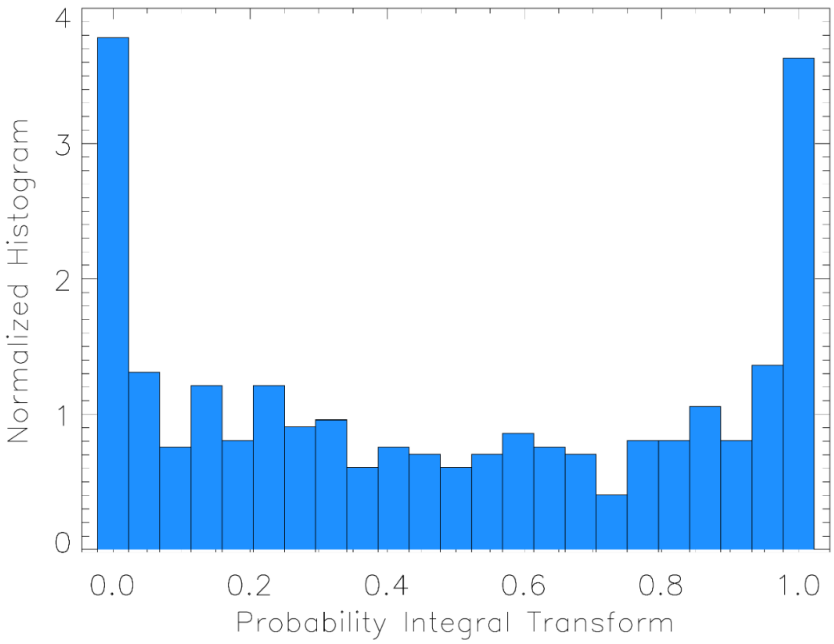

Figure 29: Probability Integral Transform

The probability integral transform (e.g., [178]) from a set of redshift probability distribution functions. A set of well-calibrated PDFs will have a near uniform PIT. The U-shape of our PIT indicates that our redshift PDFs are under-dispersed.

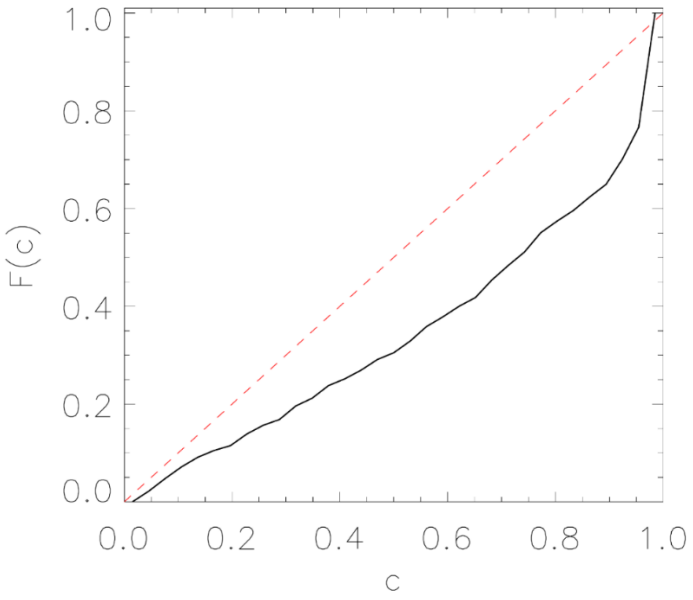

Figure 30: Quantile-Quantile plot confidence test

The confidence test from Wittman et al. 2016 [242]. Shown in black is the cumulative distribution function, F(c), of the binned threshold credibilities, c. The red dashed line represents the case in which the redshift probability distribution functions have a well-calibrated width. The plot indicates that at least some of our redshift PDFs are overconfident, i.e., that their widths are too narrow.

Discussion

Figure 31 shows the difference between the SOM photo-z using photometry alone and the SOM photo-z using photometry in conjunction with R_{50}. For each galaxy in the test sample, we calculate its redshift with and without R_{50} as input data and then determine the absolute difference between the two photo-zs (σ_{phot} and $\sigma_{phot+size}$, or equivalently, $|\Delta z_{phot}|$ and $|\Delta z_{phot+size}|$ up to a normalization factor of $1 + z_{spec}$) and the spectroscopic redshift. If R_{50} had no effect on the redshift determination, then $|\Delta z_{phot}| - |\Delta z_{phot+size}|$ should be zero. If, however, R_{50} led to some improvement, then $|\Delta z_{phot}| - |\Delta z_{phot+size}|$ would be positive, since the deviation of z_{phot} from z_{spec} would be larger than the deviation of $z_{phot+size}$ from z_{spec}. Negative values would indicate that R_{50} had a detrimental effect. In Figure 31, 67% of data points lie below zero, indicating that half-light radius did not improve photo-z estimation.

We find that the addition of galaxy morphological data does not significantly improve the redshift estimation from the self-organizing maps. The scatter introduced by the morphological data most likely dominates any benefit coming from the correlation between redshift and morphology. These results appear to be in line with the results from Soo et al. 2018 [198], who find that adding morphological quantities such as galaxy size, Sérsic index, surface brightness, and ellipticity do not significantly improve photo-z estimates when combined with a complete set of good photometry (in their case, full it *ugriz* photometry). Soo et al. 2018 conclude that including a full set of photometric bands may saturate the amount of redshift information available, which is reasonable given that they find improvement in photo-z estimates when morphology is used in conjunction with sub-optimal photometry or photometry in fewer than all five *ugriz* bands. Similarly, we

conclude that our use of morphology, at its present precision, may not be providing any new information that is not already contained in our 15 bands of photometry. Soo et al. 2018 also compare the effects of low-quality versus high-quality morphology by studying galaxy radii measured by the Sloan Digital Sky Survey (SDSS) Stripe-82 survey and by the Canada-France-Hawaii Telescope (CFHT) in Stripe 82 (CS82), the latter of which they assume to be of higher quality due to its 0.6 arcsecond seeing. However, they do not find any improvement in photo-zs when using the CS82 data over the SDSS data. In comparison, we find that improvement might be possible if the scatter in radii is less than 0.05 arcseconds (Figure 33), which is well below the CS82 seeing.

While morphological parameters did not lead to significant increases in accuracy, we would like to see if future morphological measurements with increased precision may lead to better SOM predictions. To do this, we pass simulated R_{50} data to the SOMs during training and testing. The mock size data is generated by taking the power law fits for $\log(r_e)$ as a function of redshift for Lyman-break galaxies in Mosleh et al. 2012 [160] to be the true relation between size and redshift (see also, [229]). The simulated R_{50} are drawn from a Gaussian distribution with a variable standard deviation (scatter) and mean equal to the half-light radius at each redshift from the "true relation". Figure 32 shows a comparison of the simulated R_{50} with the actual R_{50} from the data. In Figure 33, we examine the effect that increased precision in R_{50} has on σ_0 for a sample of galaxies. As the amount of scatter (black points) is lowered, improvement to photo-*z* estimation is achieved when the deviation in half-light radius from the theoretical relation is less than ~0.05 arcseconds. Even with next generation space telescopes such as the James Webb Space Telescope (JWST) and the Wide Field Infrared Survey Telescope (WFIRST) with diameters of 6.5 m

and 2.4 m, respectively, the best angular resolution possible would be ~0".05 and ~0".15 for H band at ~1.65 μm. Improvement to photo-z estimation using half-light radius may not be viable in the near future. It may also be the case that the intrinsic scatter in radii at the same redshift may be too large (i.e., greater than 0".03) for any correlation to improve redshift estimates.

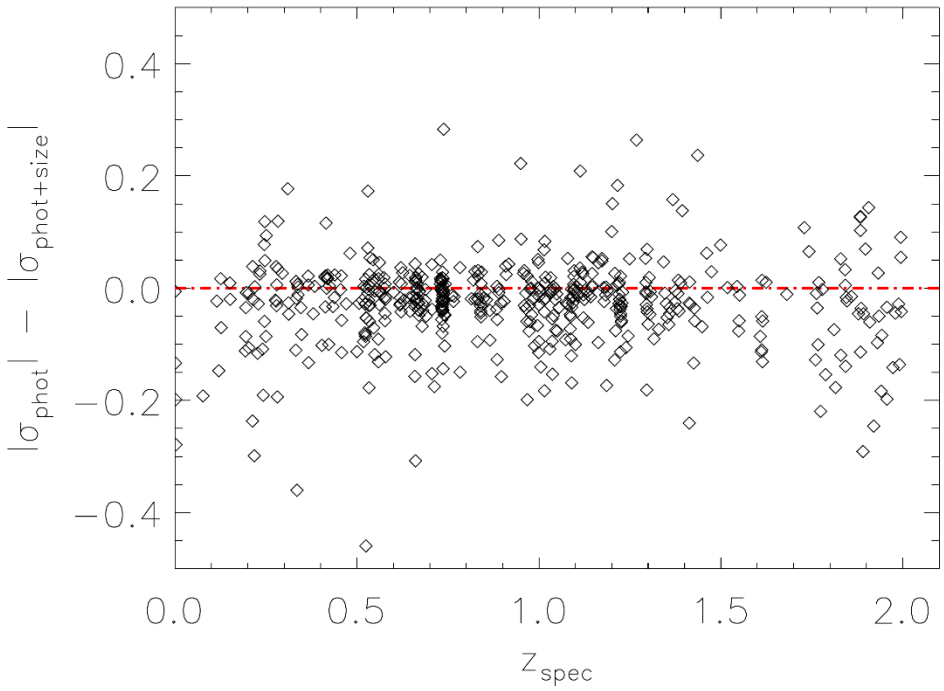

Figure 31: SOM predictions with and without R_{50}

Comparison of SOM predictions for each test source with and without half-light radius. The quantity Δz is given by $z_{spec} - z_{phot}$. We show $\sigma_{phot} = \Delta z_{phot}/(1 + z_{spec})$ calculated with photometry alone (Δz_{phot}) minus $\sigma_{phot+size} = \Delta z_{phot+size}/(1 + z_{spec})$ calculated with photometry and size ($\Delta z_{phot+size}$). Positive values indicate that use of half-light radius increased the accuracy of the SOM, while negative values indicate a decrease in accuracy.

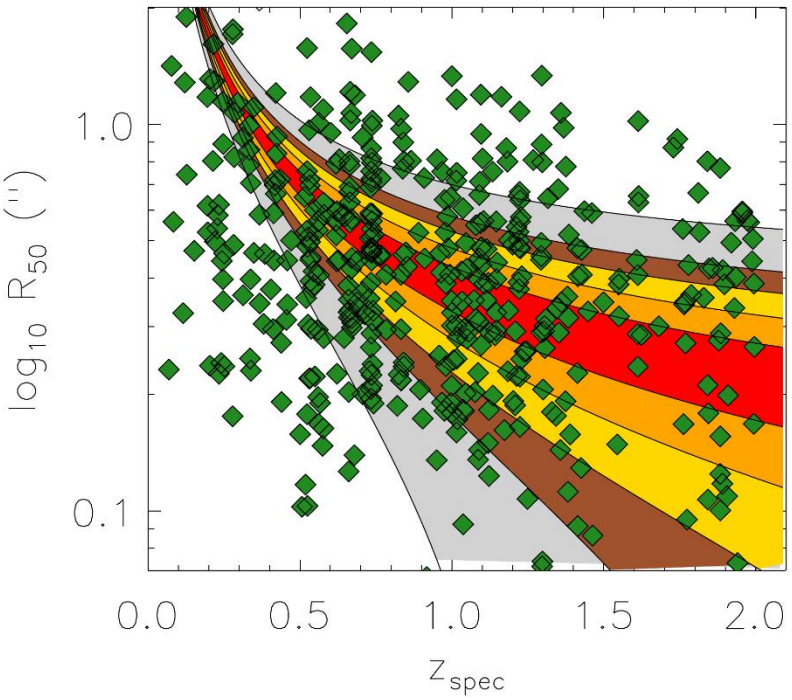

Figure 32: Comparison of simulated R_{50} with real R_{50} data

Comparison of simulated R_{50} with real R_{50} data (green diamonds). The regions correspond to simulated R_{50} with different Gaussian spreads around a presumed average trend; red: σ = 0.05 arcseconds, orange: σ = 0.1 arcseconds, yellow: σ = 0.15 arcseconds, brown: σ = 0.2 arcseconds, and gray: σ = 0.32 arcseconds. The scatter of the real R_{50} is ~0.32 arcseconds, with approximately 68% of data points falling within the gray region. We find improvement in photo-z estimates that include R_{50} only when the spread in R_{50} is smaller than 0.05 arcseconds. Such a spread in real data may be impossible to achieve due to the intrinsic variation in R_{50}, even with increased telescopic precision.

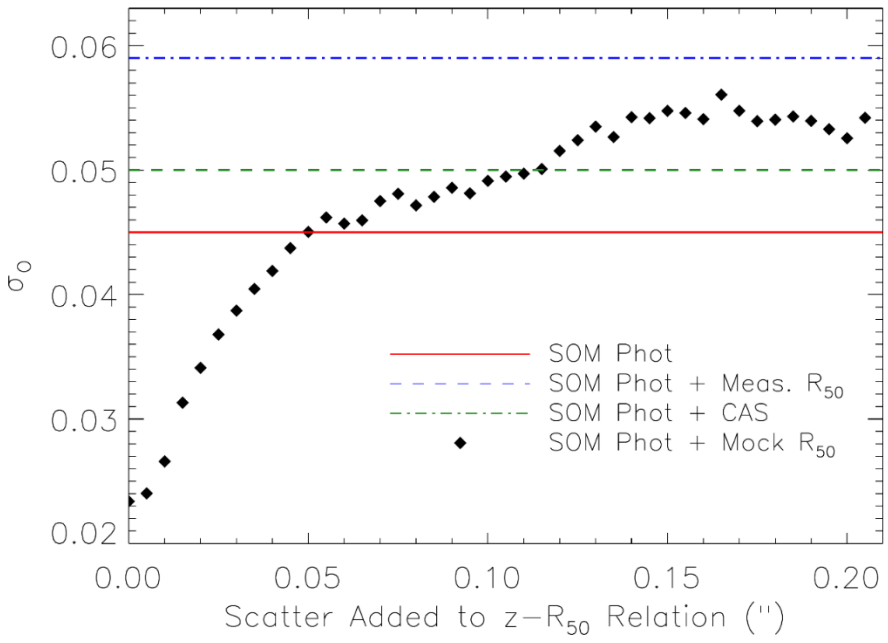

Figure 33: Redshift uncertainty as a function of scatter in R_{50}

Redshift uncertainty as a function of the scatter added to the theoretical size relation for the GOODS-S field (black dots). The training data for the SOM results given by the black dots consist of photometry and size (half-light radius, computed according to the relation in Mosleh et al. 2012 [160] (see also Van der Wel et al. 2014 [229]). For comparison, we show the performance of the SOM when using photometry alone (red line), photometry and half-light radius from GALFIT (blue line), and the existing precision of photo-zs in the CANDELS catalog. The SOMs with photometry+size would perform better than with photometry alone if the variation in size at a particular redshift was less than about 0".02. If future surveys with higher precision instruments could measure half-light radii to this precision, the SOM networks presented here may offer improvement to photo-z estimates.

Summary

We apply the self-organizing map algorithm to photometric and morphological data in the GOODS-S field to study the effect that morphological parameters have on estimating photometric redshifts. The self-organizing maps are trained on photometry in 15 wavelength bands and on half-light radius, concentration, asymmetry, and smoothness for about 500 galaxies with known spectroscopic redshifts up to $z \sim 2$. The SOMs make predictions for the redshifts of about 500 galaxies in a separate testing set and are compared to the spectroscopic redshifts of those sources. The results indicate no significant improvement in the accuracy of the SOM redshift predictions when using morphology plus photometry, in comparison to photometry alone. Similar results are obtained after cursory studies using our training and testing data on other photo-z codes, leading to typical results of $\sigma_F \sim 0.13$ - 0.16, $\sigma_0 \sim 0.05$ - 0.07, and OLF $\sim 10\%$ - 14% in the best cases. We attribute this result to the large scatter in the morphological data and the possibility that morphology is not introducing any new information that is not already contained in the photometry.

Redshift probability distribution functions are produced by the SOMs in addition to point estimates. Probability distribution functions are more sensitive to multi-modality in the SOM prediction results. At the present, tests of our redshift pdfs show that they are under-dispersed as well as overconfident (or too narrow in width), and more work is required to improve their accuracy.

Lastly, we explore the effect that a strong radius-redshift relation would have on the SOM predictions. The goal was to identify how tight a radius-redshift relation would have

to be in order to give improvement in photo-z estimation. This was done by simulating half-light radii with varying levels of scatter around a theoretical radius-redshift relation. The simulated radii were used along with photometry to train and test a group of SOMs. Improvement was found only for very small scatter less than ~0.05 arcseconds around a theoretical radius-redshift relation.

Chapter 3: Near- and Far-IR Cross-Power Spectra in the North Ecliptic Pole region with *Spitzer* and *Herschel*

Introduction

The near-infrared wavelengths (between approximately 1 – 10 μm, with a peak at ~ 1 μm) of the cosmic infrared background (CIB) light can be traced back to faint, dwarf galaxies at low and intermediate redshifts [52, 214, 221, 43, 95] and to early Population III stars and galaxies [121, 122, 152] from the epoch of reionization (EOR). The epoch of reionization was a period in cosmic history between redshifts of ~ 6 – 1000 in which the first stars and galaxies started to form and undergo nucleosynthesis, thus emitting radiation that would ionize the intergalactic medium. In addition to Pop III stars and faint, low-redshift galaxies, early direct collapse black holes are also thought to contribute to the CIB, as their UV emissions have been redshifted into the infrared [252, 251, 253].

Of importance to this work is the idea that the near-IR can also be used to probe the intrahalo light (IHL, [52, 256]) of galaxies at redshifts of z ~ 1 – 3. The IHL is caused by stars that have been tidally stripped during galaxy mergers and collisions and flung out into the dark matter halos of their galaxies [181]. These stars form a diffuse source of infrared radiation that is thought to explain the CIB excess above the contributions of faint, low-redshift galaxies and Pop III stars [52].

The CIB also contains a peak at far-infrared wavelengths, at 250 μm, in particular, which is caused by the reprocessing of UV photons by dust [63, 41]. Unlike at near-infrared wavelengths, far-infrared observations are limited by the large aperture sizes of telescopes such as *Herschel* SPIRE, and thus have not been well-resolved. In this work, we aim to study

the correlation of the far-infrared light measured with *Herschel* SPIRE with the near-infrared light measured with *Spitzer.*

In order to measure the faint signature of the IHL, we employ the angular power spectrum of CIB fluctuations, as it is sensitive to confused, unresolved sources and to faint sources below the telescope's sensitivity [120]. The angular power spectrum provides statistical information about the distribution of the faint, unresolved source population. By masking bright foreground galaxies and stars in our data, we are left with the background on which to perform our analysis. However, we must also make corrections for the shuffling of power caused by the masking and mosaicking steps in the data reduction, as well as a correction for the telescope beams. The final power spectrum can then be compared to a theoretical power spectrum calculated via a halo model approach [50]. Halo modeling studies the way in which large-scale density and velocity fields evolve due to nonlinear gravitational clustering by modeling the "number and spatial distribution of halos, and the distribution of dark matter within the halos" [50].

Data

The North Ecliptic Pole (NEP) is centered at R.A = $18^h00^m00^s$, Decl. = $66^d33^m38^s.552$. In this analysis, we use data from the *Spitzer* Infrared Array Camera (IRAC, [72]) and the *Herschel* Spectral and Photometric Imaging Receiver (SPIRE, [175, 88]), centered at the NEP. The *Spitzer* data were taken during *Spitzer*'s Warm Mission as part of program 10147 with Principal Investigator J. Bock. The data cover about 7.04 deg^2 and span three epochs in the 3.6 μm wavelength channel and two epochs at 4.5 μm. Three epochs are available at 4.5

μm, but due to striping in one of the epochs (pattern noise in the bias for readout electronics, an issue highlighted by the *Spitzer* Science Center, discussed later), that epoch is omitted from our analysis. An in-depth discussion of the data and acquisition methods can be found in Nayyeri et al. 2017 [163]. The observations were made using an observing/dithering pattern that maximized inter-pixel correlations in order to optimize the data for self-calibration. Each IRAC image consists of 256 × 256 pixels, with a pixel scale of 1.22 arcseconds [72]. Each epoch at 3.6 μm and 4.5 μm contains 3936 individual tiles, with the exception of epoch 2 at 3.6 μm, which contains only 3854 tiles [163]. Integration times were 23.6 seconds and 26.8 seconds at 3.6 μm and 4.5 μm, respectively.

The corrected-Basic Calibrated Data (cBDCs) are downloaded from the *Spitzer* Heritage archive (https://sha.ipac.caltech.edu/applications/*Spitzer*/SHA/). These data have undergone artifact-mitigation processing by the archive, including corrections for stray light and muxstriping (see *Spitzer* IRAC Instrument Handbook, https://irsa.ipac.caltech.edu/data/*SPITZER*/docs/irac/iracinstrumenthandbook/2/). We did note that some pattern noise remained in some of the cBCDs. Pattern noise is a "horizontal striping" in the BCDs most likely caused by an electronic "interference modulation of the signal across the array" which is more noticeable at 4.5 μm than at 3.6 μm (https://irachpp.*Spitzer*.caltech.edu/page/patternnoise). The pattern noise was so strong in the first epoch at 4.5 μm that we dropped that epoch from our analysis.

In addition to *Spitzer* NEP data, we also use observations made by the *Herschel* SPIRE photometer. There exists a skymap of the NEP in each of the three SPIRE photometer bands, PSW (Photometer Short Wavelength), PMW (Photometer Medium Wavelength), and PLW (Photometer Long Wavelength), corresponding to 250 μm, 350 μm, and 500 μm,

respectively. The pixel scales for 250 μm, 350 μm, and 500 μm maps are 6", 10", and 14", respectively. Each skymap covers an area of approximately 7.7 deg^2. The maps are publicly available and were downloaded from the *Herschel* Science Archive (http://archives.esac.esa.int/hsa/whsa). They were taken in "Large Map" mode by the program OT2_sserje01_2 and have observation ID 1342239959.

In order to probe large-scale angular fluctuations, the individual *Spitzer* cBCD frames are tiled into a mosaic. The mosaicking is done using the self-calibration algorithm of Arendt et al. 2000 and Fixsen et al. 2000 [9, 78, 10]. The self-calibration algorithm uses a least-squares method to model out offsets in the cBCDs caused by foreground emissions and zodiacal light (e.g., [157]). The mosaics in each band and epoch are reprojected to the astrometry of epoch 1 of the 3.6 μm band. The final mosaics are shown in Figure 34. The *Herschel* maps were downloaded as "Large Maps" from the *Herschel* Science Archive and thus did not need any further mosaicking or processing. *Herschel* Large Maps are made using an observing mode in which the SPIRE photometer repeatedly scans the area of interest and by subsequent processing by the *Herschel* Science Archive (see *Herschel* SPIRE Quick Start Guide: https://www.cosmos.esa.int/documents/12133/1035800/QUICK-START+GUIDE+TO+*HERSCHEL*-SPIRE).

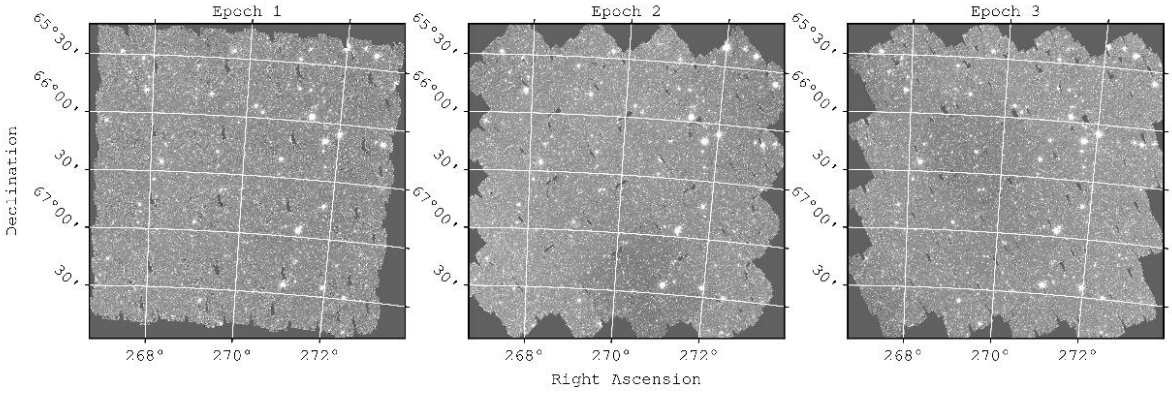

Figure 34: Self-calibrated mosaics for each epoch taken with IRAC at 3.6 μm

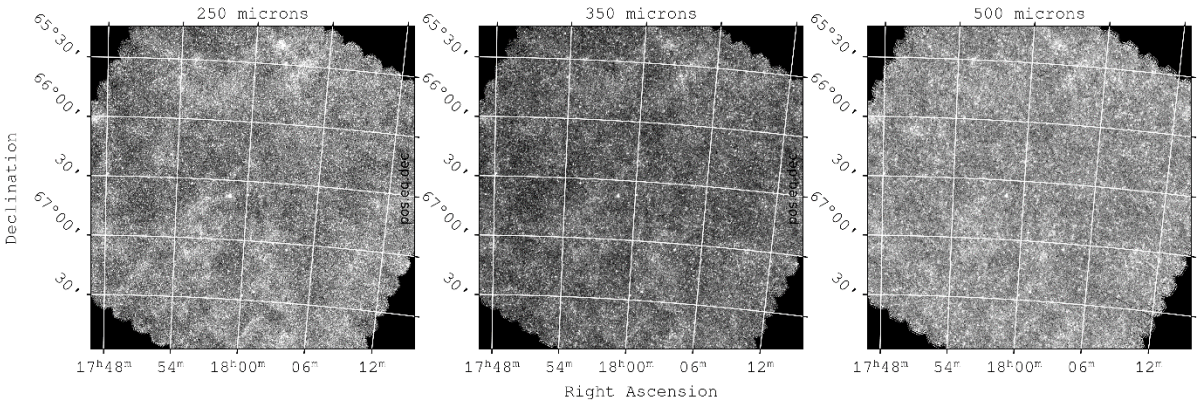

Figure 35: *Herschel* NEP maps from the *Herschel* Science Archive

Masking Point Sources

In order to measure the faint CIB light, we must remove bright stars and galaxies from the foreground of our images. We do this by applying a source mask on all pixels above about 0.035 MJy/sr. However, the mask is not as simple as just eliminating the brightest pixels, as the point spread function of the instrument contaminates surrounding pixels. The point-source mask is generated using the method in Cooray et al. 2012 [51], as follows. A mask is created using this procedure for each epoch in *Spitzer* IRAC 3.6 μm and 4.5 μm mosaics and for each *Herschel* wavelength. At the end, all of the masks were combined to create one all-encompassing mask. SourceExtractor [23] was used to extract all sources with a detection threshold of 3σ with a minimum area of one pixel. A blank, artificial map is created, to which we add the sources identified by SourceExtractor. Each source is given a size in pixels equal to the elliptical size parameters determined by SourceExtractor for that particular source. The corresponding flux values from the data mosaic are transferred to the map. The source map is then convolved with the normalized PSF for each map, shown in Figure 36. The pixels in the map with a flux above a certain cutoff are set to a value of zero. The map is then histogram-ed, and any pixels with fluxes more than 5σ from the median were rejected. The remaining pixels in the artificial source map were set to a value of 1, with all other pixels set to 0. This mask is then applied to the real NEP skymap. An additional flux cut is made on the masked skymap to remove any pixels that may have escaped masking from the previous procedure. All zeroed pixels in this final map constitute the final mask. The union of these masks is shown in Figure 38.

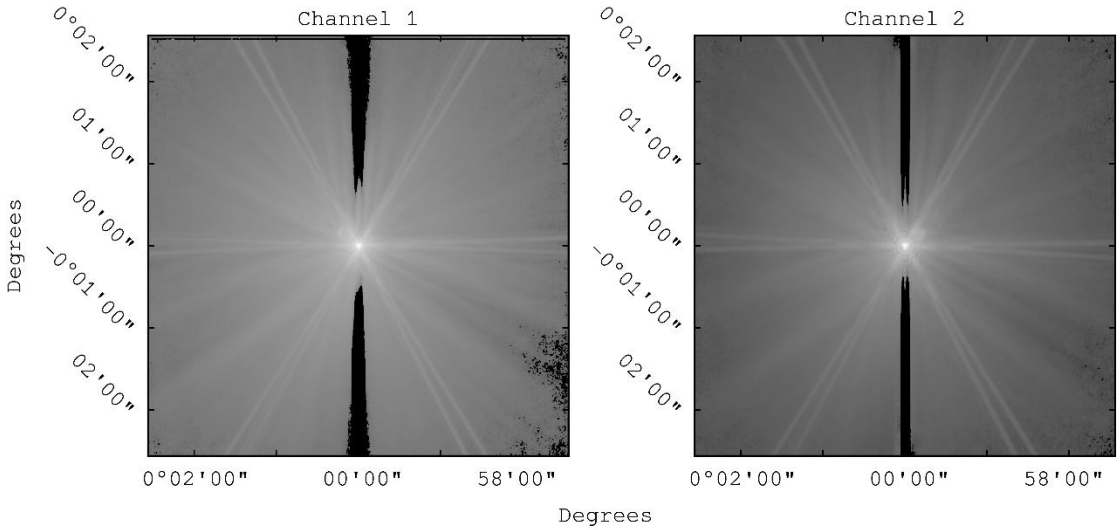

Figure 36: IRAC point-spread functions

The IRAC 3.6 μm (left) and 4.5 μm (right) point-spread functions.

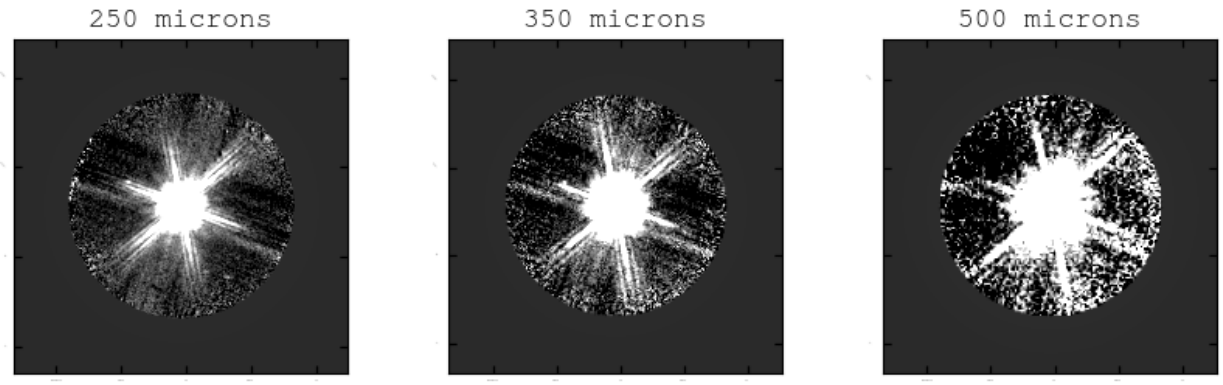

Figure 37: *Herschel* SPIRE photometer point-spread functions

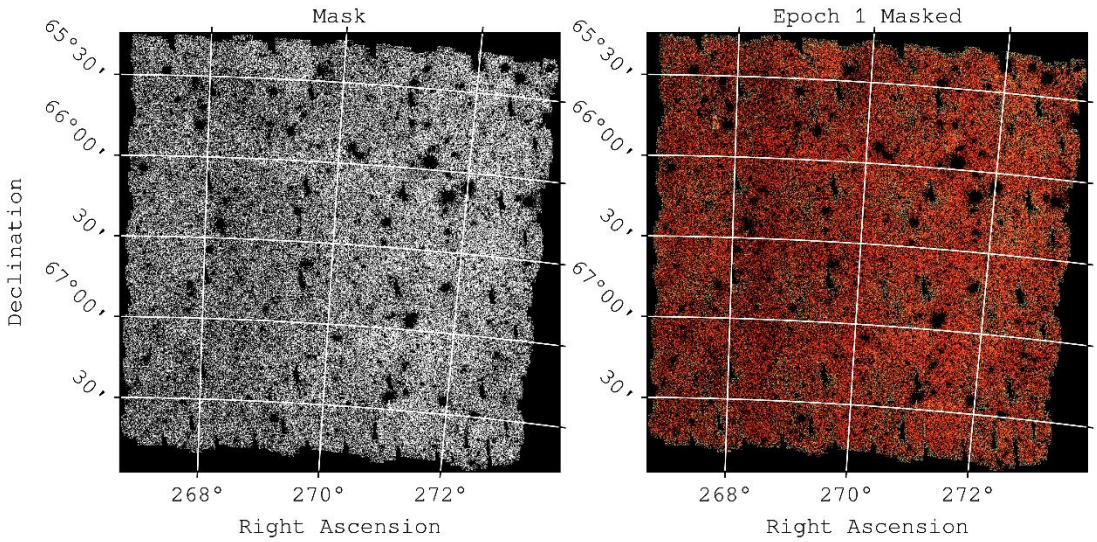

Figure 38: Masked *Spitzer* skymap

Left: The point-source mask. Right: The point-source mask applied to the *Spitzer* 3.6 μm sky map in the first epoch.

Angular Power Spectra

The angular power spectrum is a tool for measuring the extent to which fluctuations in two sky maps correlate with each other. Fluctuations on the sky are composed of different spherical harmonic functions with multipole moments, ℓ, which the power spectrum can isolate. The spherical harmonic functions are typically used when computing power spectra of the full sky. However, for small angular extents, such as the maps used in this work, a flat-sky approximation has been developed [103] that takes advantage of the Fast Fourier transform (FFT). In the flat-sky approximation, where it is assumed that the

angular extent of the maps is much less than 1 radian and $\ell >> 1$, it can be shown [103, 219] that the 2D power spectrum can be reduced to a 2D Fourier transform. This method is applied to the masked *Spitzer* and *Herschel* sky maps. When the power spectrum of a sky map is computed with itself, this is called the auto-spectrum, and when the power spectrum of two different maps is computed, this is referred to as a cross-spectrum. We compute the auto-spectrum of the *Spitzer* maps at 3.6 μm and 4.5 μm, the cross-spectrum of *Spitzer* 3.6 μm with 4.5 μm (3.6 μm × 4.5 μm), and the cross-spectrum of each *Spitzer* wavelength with each *Herschel* wavelength; that is, 3.6 μm × 250 μm, 3.6 μm × 350 μm, 3.6 μm × 500 μm, 4.5 μm × 250 μm, 4.5 μm × 350 μm, and 4.5 μm × 500 μm. Since we have multiple observation epochs at each of the *Spitzer* wavelengths, we take the auto-spectrum to be the mean spectrum of various cross-spectra between epochs. For example, at 3.6 μm, we computed Epoch 1 × Epoch 2, Epoch 2 × Epoch 3, and Epoch 1 × Epoch 3, and take the average of these cross-spectra to be the 3.6 μm auto-spectrum. In this case, we are not computing the auto-spectrum by Epoch 1 × Epoch 1, etc. The crossing of different epochs is done in order to reduce and/or eliminate the contribution to the final power spectrum from uncorrelated noise between different epochs. For cross-spectra between different wavelengths, such as for *Spitzer*-*Herschel* crosses, we use a similar technique and cross each *Spitzer* epoch with the relevant *Herschel* map and then take the average between the various power spectrum measurements to be the final cross-power spectrum measurement.

The raw, uncorrected auto- and cross-power spectra are computed as follows. To compute the ℓ-modes for an $N_x \times N_y$ pixels sky map, we employ the equation from Ponthieu et al. 2011 [179]:

$$\ell_{mn} = \left(\frac{2\pi}{\Delta\theta}\right)\sqrt{\left(\frac{m'}{N_x}\right)^2 + \left(\frac{n'}{N_y}\right)^2}$$

where $\Delta\theta$ is the pixel scale (1.2'' for the *Spitzer* maps and 6'', 10'', and 14'' for the *Herschel* PSW, PMW, and PLW maps respectively and m' and n' integers with m' = m if $m \leq N_x/2$ and m' = N_x - m if $m > N_x/2$ (same for n' with respect to N_y). We drop all modes that are larger than the Nyquist mode $\pi/\Delta\theta$.

The point source mask is applied to each of the sky maps to eliminate the foreground stars and galaxies. The mean value of each map is then subtracted, and the 2D Fourier transform of each map, denoted $\widetilde{M}$, is taken.

We then compute the C_ℓ, using the equation from Cooray et al. 2012 [51]:

$$C_{\ell_i} = \frac{\sum_{\ell_x^2+\ell_y^2\geq\ell_1^2}^{\ell_x^2+\ell_y^2\leq\ell_2^2} w[\ell_x,\ell_y]\,\widetilde{M}_1[\ell_x,\ell_y]\widetilde{M}_2^*[\ell_x,\ell_y]}{\sum_{\ell_x^2+\ell_y^2\geq\ell_1^2}^{\ell_x^2+\ell_y^2\leq\ell_2^2} w[\ell_x,\ell_y]}$$

where ℓ_x and ℓ_y are the ℓ-coordinates along the dimensions of the Fourier transformed image, ℓ_1 and ℓ_2 are the minimum and maximum value in each ℓ bin, respectively, $\widetilde{M}_1$and $\widetilde{M}_2$ are the Fourier transformed images, and w is a weight function used to remove unwanted ℓ-modes. We set w to be 1 for all ℓ-modes except those above $\pi/\Delta\theta$, which we set to 0. The above equation for the C_ℓ amounts to radially averaging the product of the 2D Fourier transforms in ℓ bins (see [51]) for each pair of epochs; i.e., 1×2, 2×3, and 1×3. A related quantity used for plotting is D_ℓ, given by:

$$D_\ell = \left(\frac{\ell(\ell+1)C_\ell}{2\pi}\right)^{\frac{1}{2}}$$

With the raw C_ℓ in hand, we apply three corrections to the raw cross spectra: the mode-coupling correction, the beam correction, and the transfer function correction [51] to account for various systematic effects in our analysis.

Mode-Coupling Matrix

The point-source mask can redistribute power between ℓ-modes by breaking up large scale fluctuations into smaller ones. To correct for this effect, a mode-coupling matrix can be applied to the power spectrum of a masked mosaic in order to undo this redistribution of power. Cooray et al. 2012 [51] develops an empirical method for calculating the mode-coupling matrix. This is done by generating a series of simulated sky maps containing only the tones in a single ℓ bin. We use 100 simulated maps for each ℓ bin in the final power spectrum. Each of these simulated maps is masked, and its auto-spectrum is calculated. The auto-spectrum for each single-ℓ bin becomes a column in the mode-coupling matrix. The inverse of the mode-coupling matrix represents a transformation from a masked sky map to an unmasked sky map.

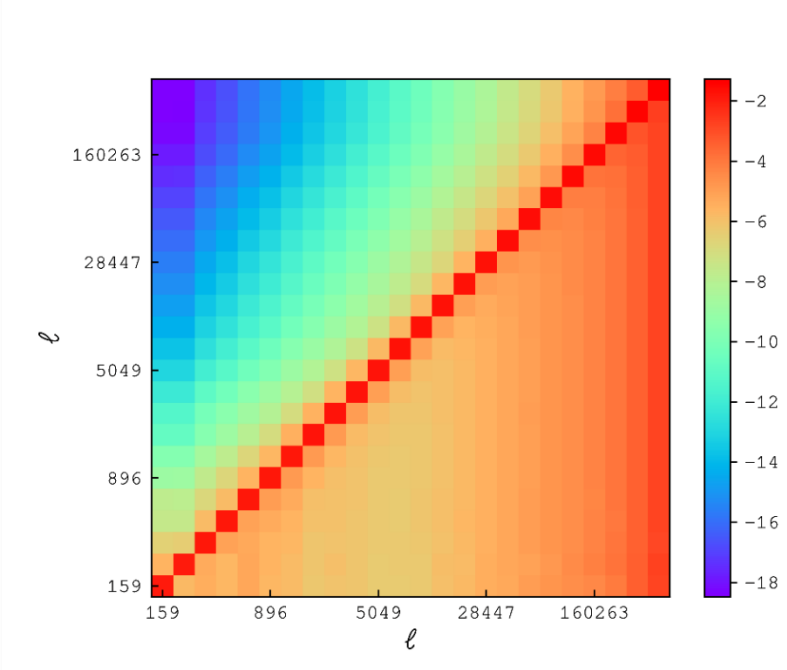

Figure 39: Mode-coupling matrix on a logarithmic scale

To verify that the mode-coupling matrix is working, a simulated sky map with an arbitrary power spectrum similar to that in Cooray et al. 2012 [52] is created and masked. The mode-coupling matrix is then applied to the auto-spectrum of the masked map to see if it recovers the unmasked power spectrum. The results are shown in Figure 40. We estimate the uncertainty in the mode-coupling correction by computing the relative error between the unmasked power spectrum and the mode-coupling corrected power spectrum for several simulated sky maps.

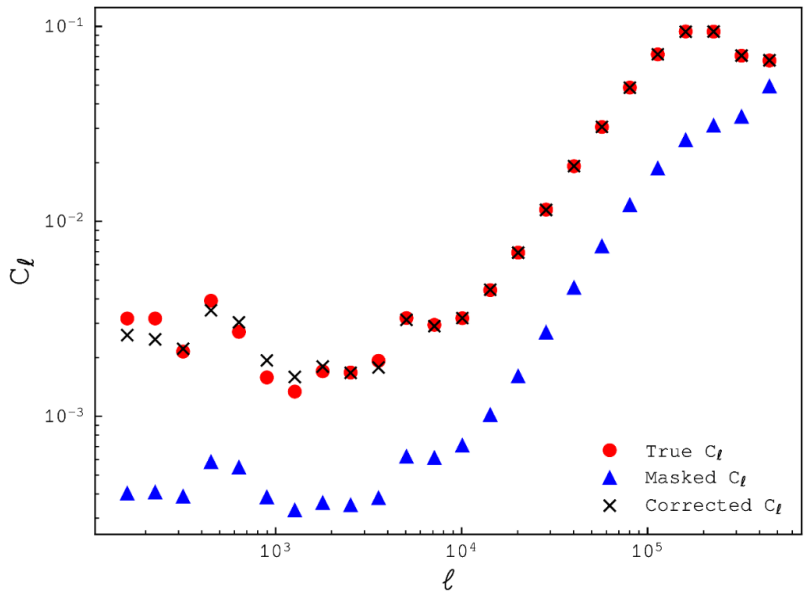

Figure 40: Testing the mode-coupling matrix

Beam Correction

The limited resolving power of the *Spitzer* and *Herschel* telescopes causes a drop in power at high multipoles or small angular scales [52]. The effect of the beam on the power spectrum can be estimated using the point-spread function (PSF). A point-like source on the sky would ideally be detected as a single point, illuminating only a single pixel on the detector. However, the limited resolution of a telescope causes the light of a point source to be smeared out, covering a larger area than just a single pixel. To correct for this effect, we compute the auto-spectrum of the PSF, divided by the auto-spectrum of a single pixel. See

Figure 41. This is equivalent to computing the auto-spectrum of the normalized instrument PSF. To compute the final beam correction, b_ℓ^2, for a cross-spectrum between two images, we use the geometric mean $b_\ell = \sqrt{b_1 b_2}$ or $b_\ell^2 = b_1 b_2$. The beam correction is divided out of the raw C$_\ell$.

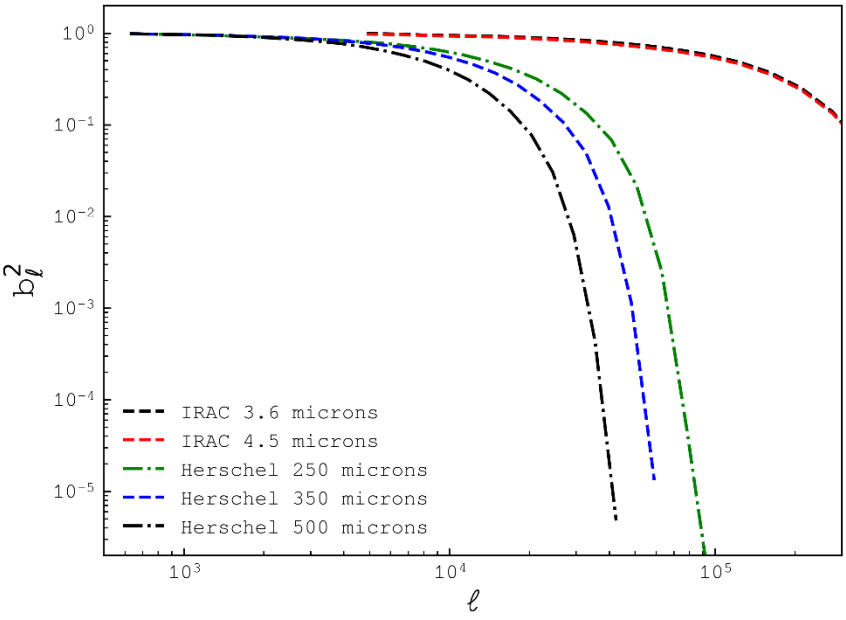

Figure 41: Beam correction for each PSF

Transfer Function

To produce the map-making transfer function, we follow the procedure from the supplement section of [51]. The process begins with the creation of a simulated map of the infrared background sky. This simulated map is generated from an arbitrary power spectrum, which we take to be flat spectrum. Cooray et al. 2012 found that the final transfer function is insensitive to the shape or amplitude of this initial, arbitrary spectrum. An estimate of the instrumental noise is then added to the simulated map, which is then broken up into tiles with the same astrometry as the data tiles for re-mosaicking. The tiles are mosaicked using SelfCal, and the resulting map shows the changes to the original, pure signal that the mosaicking procedure induces. The transfer function is divided out of the raw C_ℓ. The entire procedure was repeated for 10 simulated maps, and the final transfer function was taken to be the mean of the 10 simulations. The number of simulations would ideally be higher, but computational power and run-time put limits on the number of simulations that could be run. The standard deviation of the multiple transfer function estimates was taken to be the uncertainty in the transfer function.

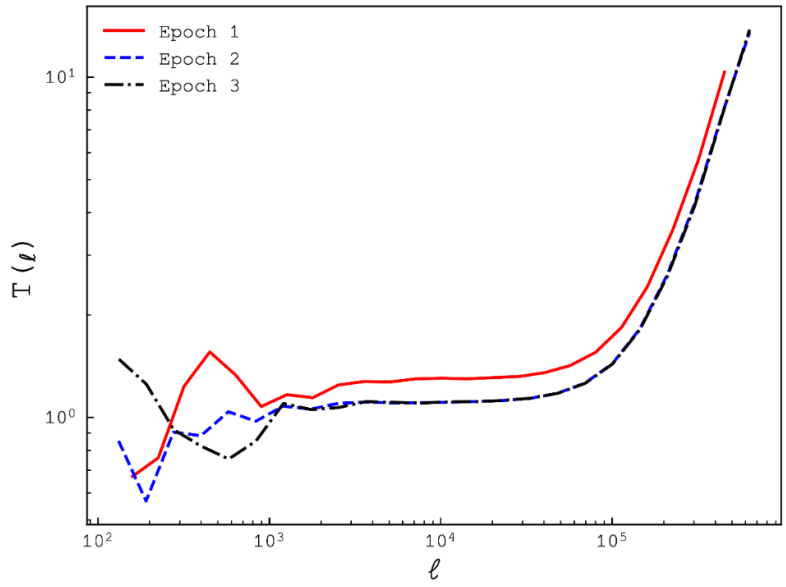

Figure 42: Mosaicking transfer functions for each *Spitzer* image at 3.6 μm

Noise Estimate

Cross-power spectra are used because they help to eliminate uncorrelated noise. This is demonstrated in Cooray et al. 2012 [52], and we briefly recount the process here. First, assume the noise is uncorrelated with the signal, and assume that image pixels, M_i, take the form $M_i = S_i + N_i$, where S is the signal and N is the uncorrelated noise. For a cross-spectrum, $M_1 \times M_2 = (S_1 + N_1) \times (S_2 + N_2) = (S_1 \times S_2) + (S_1 \times N_2) + (S_2 \times N_1) + (N_1 \times N_2) = S^2$, assuming $S_1 = S_2$. We are thus left with the task of estimating correlated noise that may still remain between two images when computing the power spectrum. This is done using the combination $(M_1 - M_2) \times (M_3)$, which, using the formalism from above

but now assuming that N_ℓ is correlated noise, leads to $(M_1 - M_2) \times (M_3) = (S_1 + N_1 - S_2 - N_2) \times (S_3 + N_3) = (N_1 - N_2) \times (S_3 - N_3)$, which does not completely eliminate a contribution from the signal from the noise estimate, but represents our current best estimate. The indices run up to 3 for *Spitzer* maps, since we have three epochs available. At 4.5 μm, we do not compute power spectra using one of the three epochs due to pattern noise, but we do use this epoch to help estimate the noise. As we had only one image at each *Herschel* wavelength, we did not estimate the correlated noise for the *Herschel* maps. The estimated noise for each cross- or auto-spectrum is subtracted from the raw spectrum before the mode-coupling, beam, and transfer function corrections are applied.

Error Estimation

As stated previously, the uncertainty in the transfer function was estimated as the standard deviation of transfer function estimates from multiple simulated sky maps, and the uncertainty in the mode-coupling correction was found by computing the relative error between the unmasked power spectrum and the mode-coupling corrected power spectrum for several simulated sky maps. There is one more source of error that we account for, the cosmic variance. Cosmic variance is a statistical uncertainty that accounts for the fact that the general fluctuations on the sky and thus the power spectrum can vary depending on which patch of sky we happen to be looking at. Different patches of sky will have slightly different power spectra, and thus, our measurement represents one measurement from an ensemble of possible power spectra.

The cosmic variance, δC_ℓ, for an auto-spectrum is given by (e.g., [157]):

$$\delta C_\ell = \sqrt{\frac{2}{f_{sky}(2\ell+1)\Delta\ell}}(C_\ell^{auto} + N_\ell)$$

and for a cross-spectrum, it is:

$$\delta C_\ell = \sqrt{\frac{1}{f_{sky}(2\ell+1)\Delta\ell}\left[\left(C_{\ell,m}^{auto} + N_{\ell,m}\right)\left(C_{\ell,n}^{auto} + N_{\ell,n}\right) + \left(C_\ell^{m\times n}\right)^2\right]}$$

where f_{sky} is the fraction of total sky that is unmasked in each sky map, $\Delta\ell$ is the width of the ℓ-bins, C_ℓ^{auto} refers to the auto-spectrum measurement, and $C_\ell^{m\times n}$ refers to the cross-spectrum measurement between maps m and n.

Finally, since we cross multiple epochs of *Spitzer* maps with each *Herschel* map, we take the mean and standard deviation between the results for each epoch (e.g., mean and standard deviation of the C_ℓ for *Spitzer* 3.6 μm Epoch 1 × *Herschel* 250 μm, *Spitzer* 3.6 μm Epoch 2 × *Herschel* 250 μm, and *Spitzer* 3.6 μm Epoch 3 × *Herschel* 250 μm.) See Figure 43. The standard deviation of the measurements is added to the total error budget. Uncertainties from the transfer function, mode-coupling correction, cosmic variance, and standard deviation between measurements with different epochs are combined to produce the error bars shown in the final power spectra in the next section.

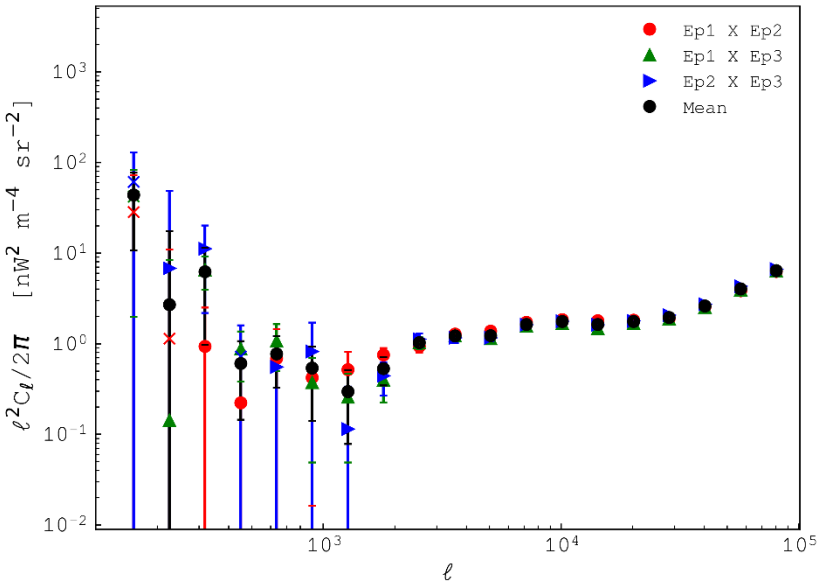

Figure 43: Combining multiple power spectra

Example of multiple power spectrum measurements averaged to get the mean power spectrum in black.

Final Power Spectra

The measured auto- and cross-spectra for the *Spitzer* maps are shown in Figure 44. We find an offset of a couple of orders of magnitude between our measurements and those of Cooray et al. 2012 [52]. The offset may be due to differences in masking depth. If there are remnants from bright sources in our maps that were not fully masked, they might raise the measured power. There is a trade-off between masking more pixels in order to remove bright sources and having to have enough pixels remaining to do a proper analysis. Kashlinsky et al. 2005 [121] (also [10, 119]) find that Fourier analysis becomes unreliable as more of the map pixels are masked, and they mask only around 25% of the pixels in their

analyses. In this work, we have masked 40-50% of the pixels, which may be too many. However, masking fewer pixels leaves brighter sources still in the maps. Due to this uncertainty, we are unable to draw strong conclusions from our results.

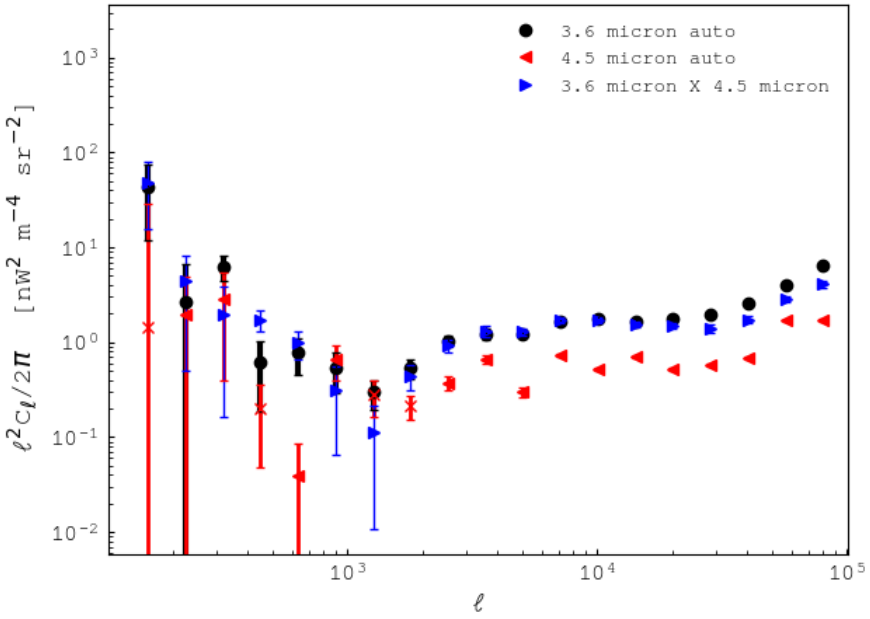

Figure 44: *Spitzer* auto- and cross-spectra

Cross-power spectra of *Herschel* 250 μm, 350 μm, and 500 μm crossed with *Spitzer* 3.6 μm and 4.5 μm are shown in Figure 45 and Figure 46, respectively. The error-bars at large angular scales (low ℓ) are large, even given the logarithmic scale. The overall curve disagrees with the measurements made in Figure 9 of Thacker et al. 2015 [220] by a couple of orders of magnitude, similar to the offset seen in the *Spitzer* power spectra.

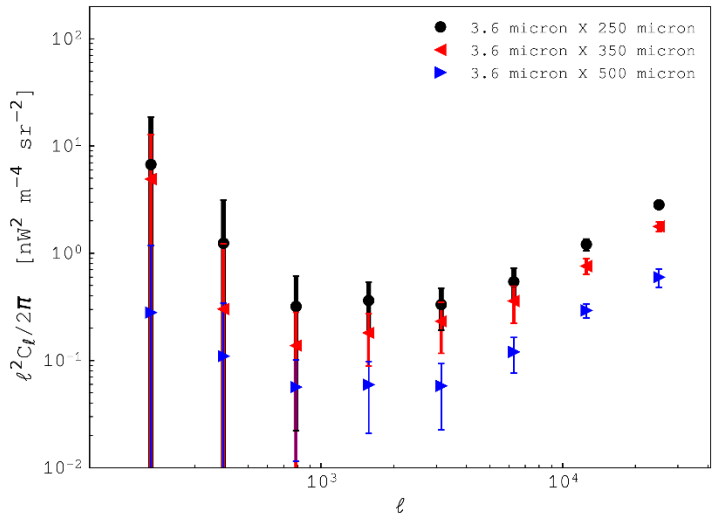

Figure 45: Cross-power spectra of *Spitzer* 3.6 μm × *Herschel* 250, 350, and 500 μm

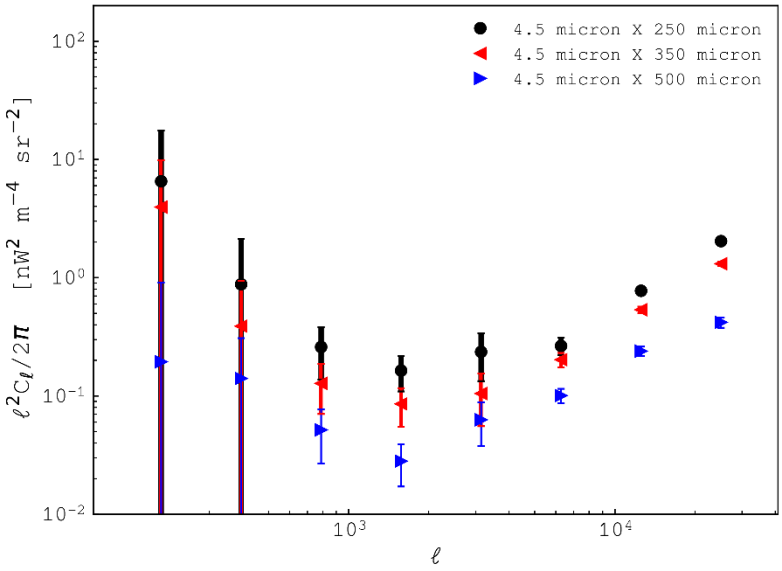

Figure 46: Cross-power spectra of *Spitzer* 4.5 μm × *Herschel* 250, 350, and 500 μm

Finally, we report the correlation coefficients, also known as coherence, for each cross-wavelength pair, defined as (e.g., [119, 52, 157]):

$$r_\ell = \frac{|C_\ell^{n \times m}|}{\sqrt{C_{\ell,n}^{auto} C_{\ell,m}^{auto}}}$$

where $C_\ell^{n \times m}$ is the cross-spectrum between wavelengths *n* and *m,* and $C_{\ell,n}^{auto}$ and $C_{\ell,m}^{auto}$ are the auto-spectra for each wavelength. The correlation coefficient represents the fraction of diffuse emission from a common population between the two wavelengths, *n* and *m* (e.g., [35, 157]). It is usually assumed either that the physical source of the common emission is the same in both wavelengths or that the sources have an angular separation less than the point-spread-function [157]. A correlation coefficient of order 1 indicates that the same source population is causing the diffuse signal in both wavelengths [119], and a value near 0 indicates that the sources contributing to the signal at wavelength *n* are not the same sources contributing to the signal at wavelength *m.*

We report two sets of correlation coefficients; one computed with the corrections applied to the power spectra and one without corrections applied. Ideally, a correlation coefficient should always be less than 1; however, the corrections for noise and other systematics that we apply to each power spectrum can change the ratios between the cross- and auto-spectra in the equation for the correlation coefficient relative to what the ratios would be if no corrections were applied. For example, when we compute the auto-spectrum for 3.6 μm, we are not computing a "true" auto-spectrum, but rather the cross-spectrum between multiple epochs at the same wavelength. Subtracting noise estimates

and using the mode-coupling correction can also skew the ratios. These effects can result in some values of the correlation coefficient that are larger than 1. The correlation coefficients with no corrections applied to the power spectra are shown in Figure 47, Figure 48, and Figure 49. The curves in these figures were made without subtracting a noise estimate and without applying mode-coupling, beam, or transfer function corrections. We also used a true auto-spectrum to compute these coefficients, instead of an "auto-spectrum" that is the cross-spectrum between two epochs at the same wavelength. In the uncorrected case, all values of the correlation coefficient lie below 1. The raw correlation coefficients between *Spitzer* 3.6 μm and 4.5 μm vary from 0.15 up to about 0.4, with one point at low ℓ up near 0.75. The raw *Herschel* correlation coefficients are also low, with most of the coefficients between 0.1 and 0.3 for the *Herschel* wavelengths crossed with 3.6 μm. When crossing *Herschel* with *Spitzer* 4.5 microns, we find correlation coefficients between about 0.2 and 0.3 (except for the point at lowest ℓ) for wavelengths 250 μm and 350 μm. The 4.5 μm × 500 μm curve is slightly lower, ranging from about 0.1 to 0.2. Overall, the raw correlation coefficients show low correlations.

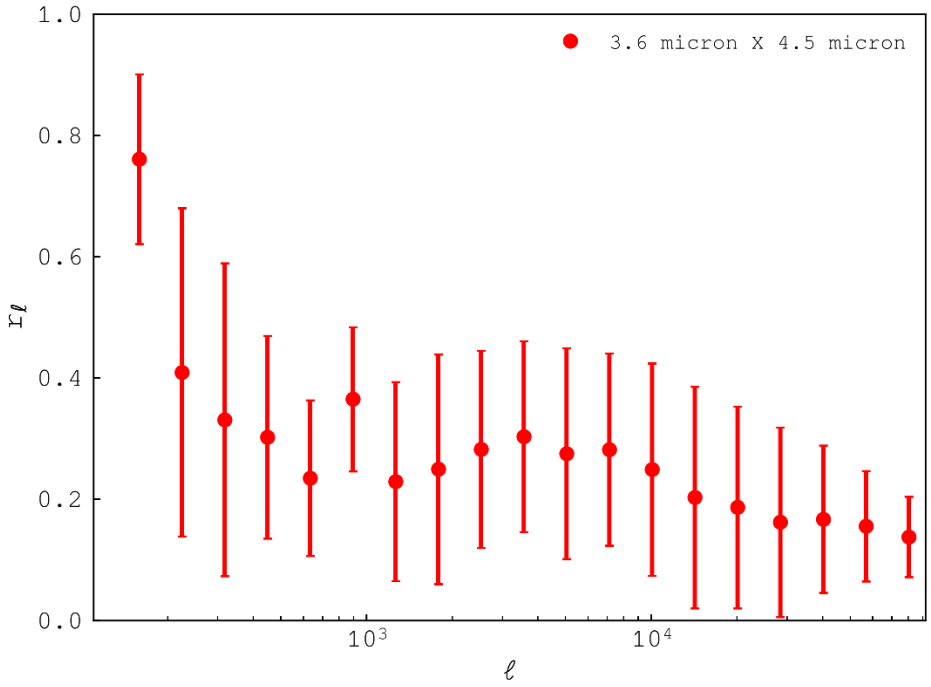

Figure 47: Uncorrected correlation coefficients for *Spitzer* 3.6 μm × 4.5 μm.

No corrections have been applied to the power spectra used to compute these correlation coefficients.

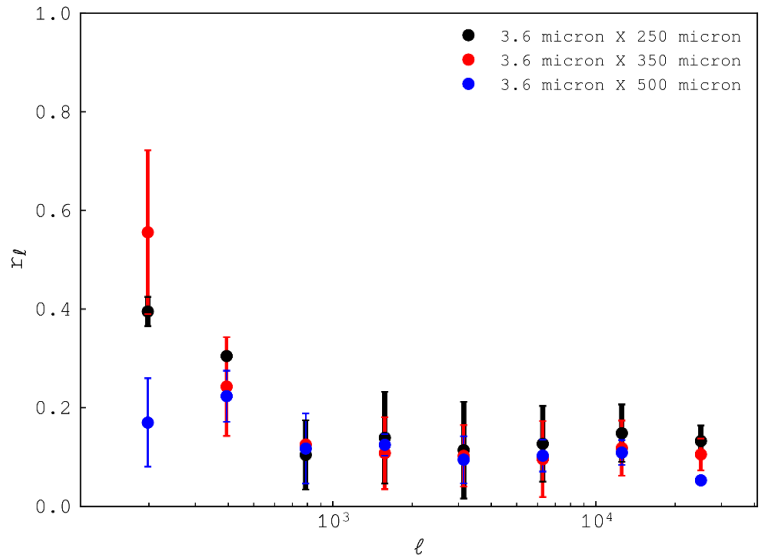

Figure 48: Uncorrected correlation coefficients for *Spitzer* 3.6 μm × *Herschel* 250, 350, and 500 μm.

No corrections have been applied to the power spectra used to compute these correlation coefficients.

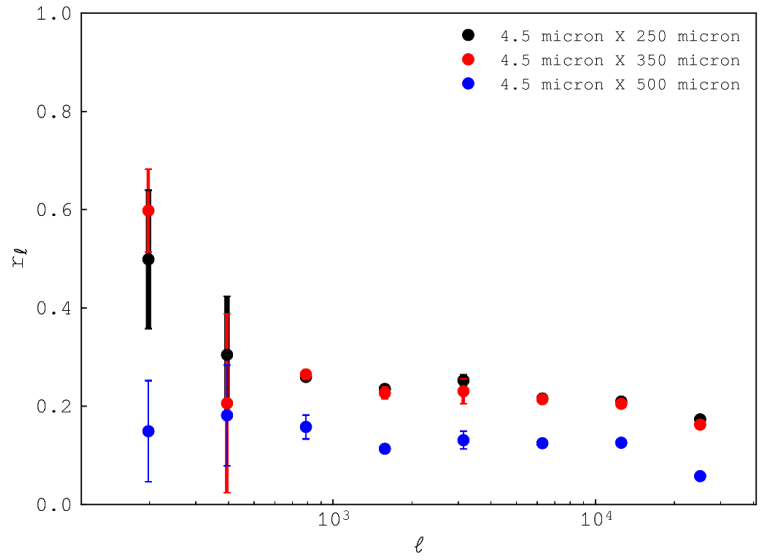

Figure 49: Uncorrected correlation coefficients for *Spitzer* 4.5 μm × *Herschel* 250, 350, and 500 μm.

No corrections have been applied to the power spectra used to compute these correlation coefficients.

The measured correlation coefficients with all corrections applied to the power spectra for *Spitzer* 3.6 μm × 4.5 μm are shown in Figure 50. The coefficients are of order unity, roughly consistent with the correlation coefficients found in [52], despite the offset of the power spectra between [52] and this work. If we take the correlation coefficients at face-value, then values of order unity suggests that the same source population is creating most of the signal at 3.6 μm and 4.5 μm. Without further modeling of different source populations, we cannot specify what this source population is, possible sources could include faint, unresolved galaxies, Galactic dust, intrahalo dust, or the intrahalo light suggested by Cooray et al. 2012.

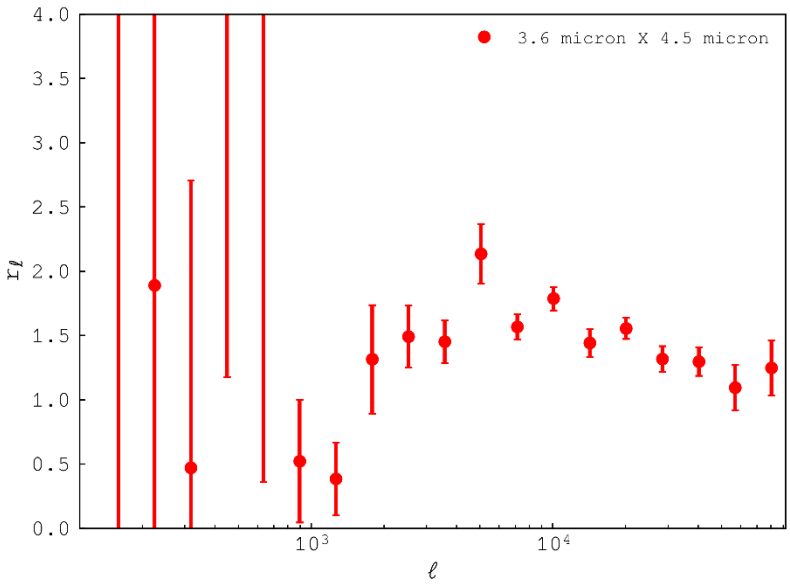

Figure 50: Corrected correlation coefficients for *Spitzer* 3.6 μm × 4.5 μm. Corrections have been applied to the power spectra.

The *Spitzer-Herschel* correlation coefficients are shown in Figure 51 and Figure 52. The correlation coefficients for each combination of wavelengths vary from 0.05 up to about 0.3 at smaller angular scales and is nearly the same at 250 μm, 350 μm, and 500 μm. The values of the coefficients are a bit higher at the lowest ℓ data points, but the uncertainties are also very high at these points.

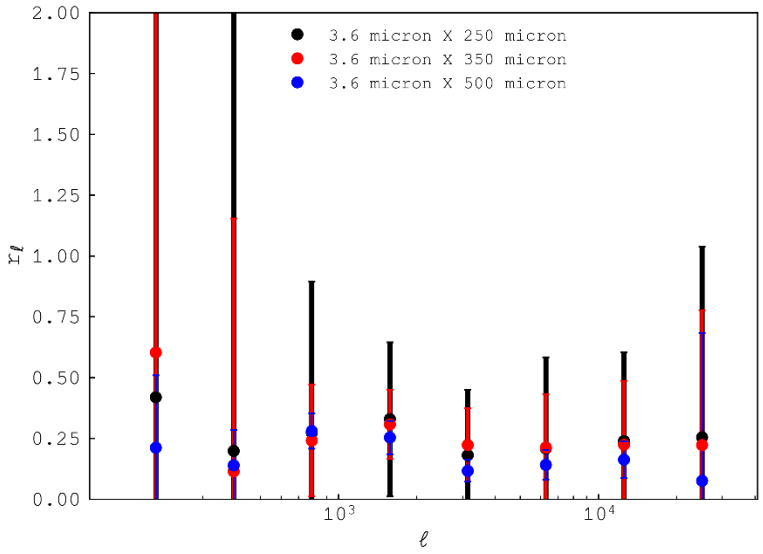

Figure 51: Corrected correlation coefficients for *Spitzer* 3.6 μm × *Herschel* 250, 350, and 500 μm.

Corrections have been applied to the power spectra.

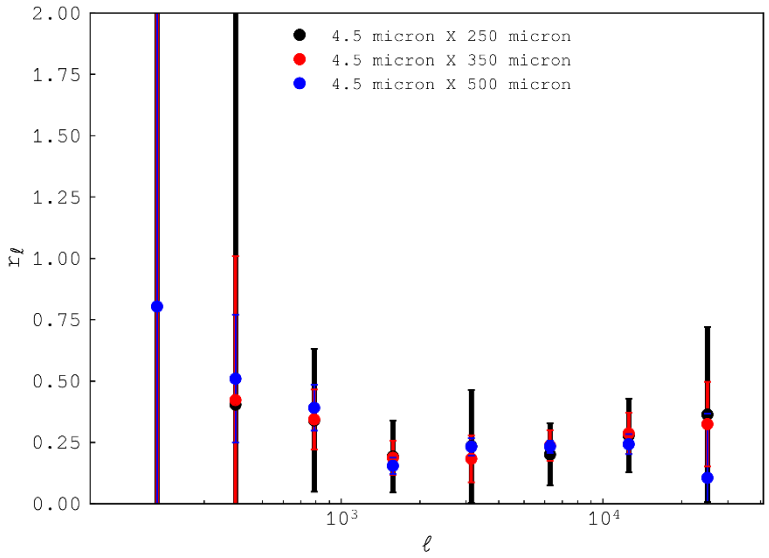

Figure 52: Corrected correlation coefficients for *Spitzer* 4.5 μm × *Herschel* 250, 350, and 500 μm.

Corrections have been applied to the power spectra.

The *Herschel* result is roughly in agreement with the result from Thacker et al. 2015 [220], which found that the correlation coefficients for *Spitzer* 3.6 μm crossed with *Herschel* decreased from about 0.3 to about 0.1 with increasing *Herschel* wavelength. If we take our *Herschel* results at face-value, the correlation coefficients suggest that *Spitzer* and *Herschel* are weakly correlated. Thacker et al. 2015 similarly found little correlation between *Spitzer* and *Herschel*, meaning that they are likely tracing different populations. After modeling, Thacker et al. 2015 concluded that the small correlation they did observe is likely due to faint far-IR and near-IR galaxies originating from the same halo. If we are observing a real correlation in our work, then it may be originating from those same galaxies, but without further analysis, we cannot make any strong claims for any particular source population.

Summary

We study the cosmic infrared background fluctuations via their cross-power spectra between near- and far-infrared wavelengths. To eliminate systematic errors, a beam correction, mode-coupling correction, and mosaicking transfer function correction are applied. The errors at large scales are still rather large and preclude any statistically significant detection of intrahalo light. The measure power spectra are found to be a couple of orders of magnitude larger than other works in the literature. The correlation coefficients do show a positive correlation between *Spitzer-Spitzer* maps that is relatively independent of scale, and a positive correlation between *Spitzer-Herschel* maps that is also relatively independent of scale. This suggests that *Spitzer* and *Herschel* may be tracing the same source populations, but it is difficult to make any strong conclusions.

Appendix to Chapter 1

Figure 53 shows the stack at 0.005 < z < 0.05 resulting from an inverse variance weighting scheme. In the main text, an unweighted average is used for this redshift bin. In Figure 53, sources with low signal-to-noise, such as Arp 220, dominate the stack. Notable in this stack are the absorption features, which are present primarily in Arp 220 and survive the stacking process. Table 9 and Table 10 enumerate the sources and source properties used in this work.

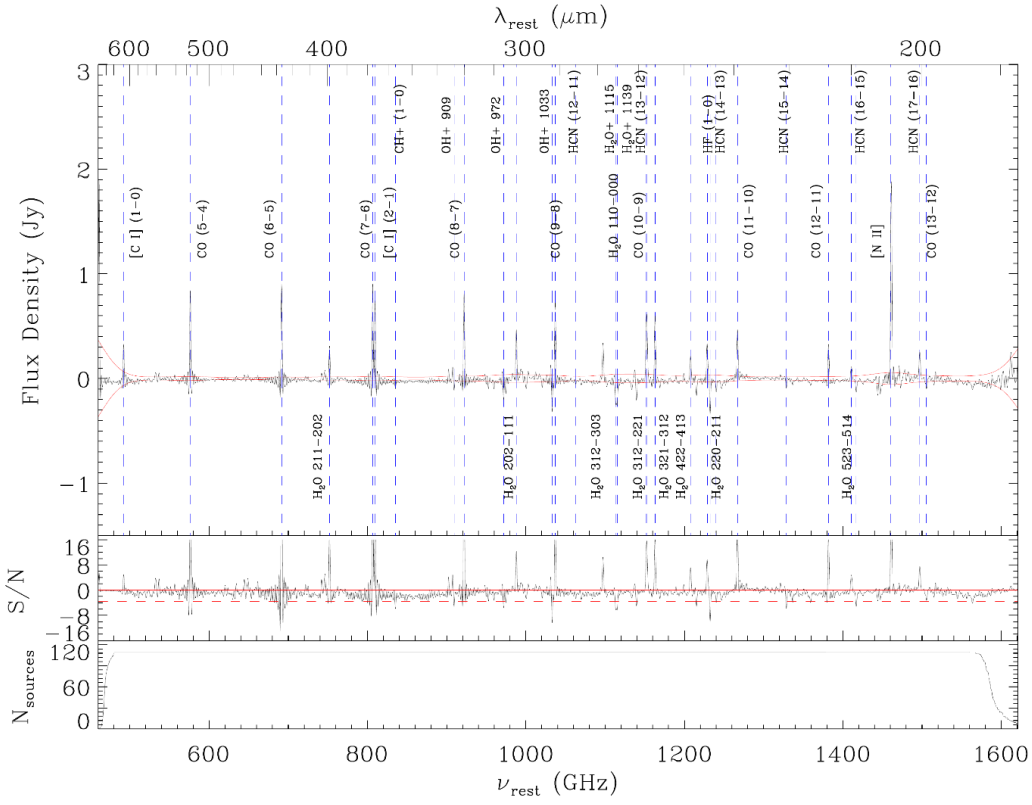

Figure 53: Stacked spectra, 0.005 < z < 0.05 with inverse variance weighting

Top: Stacked SPIRE/FTS spectrum of archival sources with 0.005 < z < 0.05 when stacked according to an inverse variance weighting scheme, unlike Figure *3* which is an unweighted mean stack. We present this stack to show how sources such as Arp 220 that were

measured with high signal-to-noise can dominate the stack if an inverse variance weighting scheme is used. In particular, strong absorption features from Arp 220 are still identifiable even after stacking. Fluxes from the emission lines in this figure can differ from the fluxes from Figure 3 by as little as 10% or up to a few hundred percent. Large differences in flux are apparent in the H_2O lines, which are significant in the Arp 220 spectrum, but which are reduced in significance when domination of the stack by sources like Arp 220 is removed. Overlaid is the 1σ jackknifed noise level in red and dashed vertical lines showing the locations of main molecular emission lines. Middle: Signal-to-noise ratio. The horizontal dashed line indicates S/N = 3.5, and the solid red line indicates S/N = 0. Lines with S/N > 3.5 were considered detected. Bottom: The number of sources that contribute to the stack at each wavelength.

Table 9: Observation IDs and Integration Times

Target	Obs. ID	Program	Int. Time [s]
Mrk 231	1342187893	SDP_pvanderw_3	6601
	1342210493	SDP_pvanderw_3	13722
Arp 220	1342190674	KPGT_wilso01_1	9772
IRAS F17207-0014	1342192829	SDP_pvanderw_3	6334
IRAS F18293-3413	1342192830	SDP_pvanderw_3	5279
NGC 1614	1342192831	SDP_pvanderw_3	6334
IRAS F05189-2524	1342192832	SDP_pvanderw_3	16360
	1342192833	SDP_pvanderw_3	16360
IC 4687	1342192993	SDP_pvanderw_3	13986
SDP.81	1342197467	GT1_ivaltcha_1	13194
SDP.130	1342197469	GT1_ivaltcha_1	13194

NGC 7552	1342198428	SDP_pvanderw_3	1717
Arp 299	1342199248	SDP_pvanderw_3	4620
	1342199249	SDP_pvanderw_3	4620
NGC 7469	1342199252	SDP_pvanderw_3	11875
NGC 34	1342199253	SDP_pvanderw_3	14249
NGC 3256	1342201201	SDP_pvanderw_3	4883
ESO 173-G015	1342202268	SDP_pvanderw_3	1717
NGC 1365	1342204020	SDP_pvanderw_3	3168
	1342204021	SDP_pvanderw_3	5279
Mrk 273	1342209850	SDP_pvanderw_3	13062
Arp 193	1342209853	SDP_pvanderw_3	14249
ESO 320-G030	1342210861	SDP_pvanderw_3	5675
IC 1623	1342212314	SDP_pvanderw_3	12799
Mrk 331	1342212316	SDP_pvanderw_3	13061
NGC 7771	1342212317	SDP_pvanderw_3	14249
IRAS 13120-5453	1342212342	SDP_pvanderw_3	3828
NGC 5135	1342212344	SDP_pvanderw_3	14250
CGCG 049-057	1342212346	SDP_pvanderw_3	14250
NGC 6052	1342212347	OT1_nlu_1	2641
MCG +12-02-001	1342213377	SDP_pvanderw_3	1385
MCG-03-04-014	1342213442	OT1_nlu_1	5279
CGCG 436-030	1342213443	OT1_nlu_1	5280
NGC 6240	1342214831	SDP_pvanderw_3	12798
ESO 286-G035	1342216901	OT1_nlu_1	2640
NGC 2623	1342219553	SDP_pvanderw_3	12007
SMMJ2135-0102	1342219562	OT1_rivison_1	13194
GOODS-N07	1342219575	OT1_apope_1	9237
CGCG 448-020	1342221679	OT1_nlu_1	2641
MCG+04-48-002	1342221682	OT1_nlu_1	1321
UGC 12150	1342221699	OT1_nlu_1	2640
IC 5298	1342221700	OT1_nlu_1	2640
NGC 7679	1342221701	OT1_nlu_1	2640
NGC 7592	1342221702	OT1_nlu_1	2641
NGC 0232	1342221707	OT1_nlu_1	2641
ESO 244-G012	1342221708	OT1_nlu_1	2641
NGC 3221	1342221714	OT1_nlu_1	1322
NGC 6286	1342221715	OT1_nlu_1	1322
NGC 6621	1342221716	OT1_nlu_1	2641
IRAS 03158+4227	1342224764	OT1_dfarrah_1	9237
NGC 0695	1342224767	OT1_nlu_1	5279
IRAS 23365+3604	1342224768	OT1_dfarrah_1	5279
IRAS 14378-3651	1342227456	OT1_dfarrah_1	5939
UGC 03094	1342227522	OT1_nlu_1	2641
IRAS 04271+3849	1342227786	OT1_nlu_1	2641
NGC 1961	1342228708	OT1_nlu_1	1321
MCG+02-20-003	1342228728	OT1_nlu_1	2641
NGC 2342	1342228729	OT1_nlu_1	2641
IRAS 05223+1908	1342228738	OT1_nlu_1	2641
UGC 03608	1342228744	OT1_nlu_1	2641
IRAS 05442+1732	1342230413	OT1_nlu_1	1322
MCG+08-11-002	1342230414	OT1_nlu_1	1322
UGC 03351	1342230415	OT1_nlu_1	1322
IRAS F17138-1017	1342230418	OT1_nlu_1	1321
ESO 099-G004	1342230419	OT1_nlu_1	5279
IRAS 06035-7102	1342230420	OT1_dfarrah_1	7258
IRAS 08311-2459	1342230421	OT1_dfarrah_1	7258
IRAS 06206-6315	1342231038	OT1_dfarrah_1	9237
IRAS 19254-6315	1342231039	OT1_dfarrah_1	7258
ESO 069-IG006	1342231040	OT1_nlu_1	7918
NGC 6156	1342231041	OT1_nlu_1	1322
ESO 138-G027	1342231042	OT1_nlu_1	2641
IRAS 17578-0400	1342231047	OT1_nlu_1	1322
IRAS 20087-0308	1342231049	OT1_dfarrah_1	9237
NGC 6926	1342231050	OT1_nlu_1	2640
UGC 11041	1342231061	OT1_nlu_1	2640
IRAS 09022-3615	1342231063	OT1_nlu_1	7917
NGC 4194	1342231069	OT1_nlu_1	1321
NGC 2388	1342231071	OT1_nlu_1	1321
UGC 03410	1342231072	OT1_nlu_1	1321
IRAS 19297-0406	1342231078	OT1_dfarrah_1	5279
NGC 2369	1342231083	OT1_nlu_1	1322
ESO 255-IG007	1342231084	OT1_nlu_1	5279
NGC 3110	1342231971	OT1_nlu_1	1321
IRAS 08355-4944	1342231975	OT1_nlu_1	2641
G09v1.40	1342231977	OT1_rivison_1	13194
IRAS 08572+3915	1342231978	OT1_dfarrah_1	5279
HerMES-Lock01	1342231980	OT2_rivison_2	13195
G09v1.326	1342231985	OT1_rivison_1	13195
SDP.9	1342231986	OT1_rivison_1	13195
G09v1.97	1342231988	OT1_rivison_1	13194

SPT0538-50	1342231989	OT1_dmarrone_1	13194
ESO 339-G011	1342231990	OT1_nlu_1	2640
NGC 6701	1342231994	OT1_nlu_1	1321
NGC 5010	1342236996	OT1_nlu_1	1321
VV 340	1342238241	OT1_nlu_1	5279
UGC 545	1342238246	SDP_pvanderw_3	15042
IRAS 16090-0139	1342238699	OT1_dfarrah_1	10556
G15v2.235	1342238700	OT1_rivison_1	13194
G15v2.19	1342238701	OT1_rivison_1	13194
IRAS 03521+0028	1342238704	OT1_dfarrah_1	11875
HXMM02	1342238706	OT2_rivison_2	13195
Mrk 1014	1342238707	SDP_pvanderw_3	13495
HBootes03	1342238709	OT2_rivison_2	13195
Mrk 478	1342238710	SDP_pvanderw_3	5279
IRAS 15250+3609	1342238711	OT1_dfarrah_1	5279
VV 705	1342238712	OT1_nlu_1	5279
NGC 0958	1342239339	OT1_nlu_1	2641
UGC 02238	1342239340	OT1_nlu_1	2641
UGC 02369	1342239341	OT1_nlu_1	5279
NGC 0877	1342239342	OT1_nlu_1	1322
IRAS F01417+1651	1342239343	OT1_nlu_1	2641
UGC 02608	1342239356	OT1_nlu_1	2641
NGC 0828	1342239357	OT1_nlu_1	1321
NGC 0317B	1342239358	OT1_nlu_1	2641
IC 4734	1342240013	OT1_nlu_1	1322
NGC 5990	1342240016	OT1_nlu_1	1323
UGC 02982	1342240021	OT1_nlu_1	1322
UGC 01845	1342240022	OT1_nlu_1	1322
NGC 1572	1342242588	OT1_nlu_1	2640
MCG-05-12-006	1342242589	OT1_nlu_1	2640
ESO 420-G013	1342242590	OT1_nlu_1	1321
PG 1613+658	1342242593	SDP_pvanderw_3	13194
FLS02	1342242594	OT2_drigopou_3	13194
	1342259071	OT2_drigopou_3	13195
IRAS 20414-1651	1342243623	OT1_dfarrah_1	9237
IRAS 22491-1808	1342245082	OT1_dfarrah_1	7258
IRAS 01003-2238	1342246256	OT1_dfarrah_1	11875
IRAS 20100-4156	1342245106	OT1_dfarrah_1	7258
ESO 286-IG019	1342245107	OT1_nlu_1	5279
ESO 467-G027	1342245108	OT1_nlu_1	2641
IC 5179	1342245109	OT1_nlu_1	1322
ESO 148-IG002	1342245110	OT1_nlu_1	6994
NGC 7674	1342245858	OT1_nlu_1	5279
IRAS 00397-1312	1342246257	OT1_dfarrah_1	13194
IRAS 00188-0856	1342246259	OT1_dfarrah_1	11875
SWIRE05	1342246268	OT2_drigopou_3	13194
IRAS 23230-6926	1342246276	OT1_dfarrah_1	10555
IRAS 23253-5415	1342246277	OT1_dfarrah_1	11875
ESO 350-IG038	1342246978	OT1_nlu_1	2641
DAN03	1342246979	OT2_drigopou_3	13194
IRAS F10565+2448	1342247096	OT1_nlu_1	5279
BOOTES01	1342247113	OT2_drigopou_3	13194
IRAS 10378+1109	1342247118	OT1_dfarrah_1	11875
UGC 08739	1342247123	OT1_nlu_1	2641
NGC 5653	1342247565	OT1_nlu_1	1322
NGC 5104	1342247566	OT1_nlu_1	2641
MCG-02-33-098	1342247567	OT1_nlu_1	2641
ESO 353-G020	1342247615	OT1_nlu_1	2641
MCG-02-01-051	1342247617	OT1_nlu_1	2641
NGC 0023	1342247622	OT1_nlu_1	1322
G12v2.43	1342247744	OT1_rivison_1	13194
G12v2.30	1342247758	OT1_rivison_1	13195
G12v2.257	1342247759	OT1_rivison_1	13195
IRAS 11095-0238	1342247760	OT1_dfarrah_1	10556
IRAS 12071-0444	1342248239	OT1_dfarrah_1	11875
NGP-NC.v1.143	1342248412	OT1_rivison_1	13194
NGP-NA.v1.56	1342248416	OT1_rivison_1	13194
NGC 5734	1342248417	OT1_nlu_1	1321
ESO 507-G070	1342248421	OT1_nlu_1	2641
MCG-03-34-064	1342249041	OT1_nlu_1	2640
IC 4280	1342249042	OT1_nlu_1	2640
ESO 264-G057	1342249043	OT1_nlu_1	2640
ESO 264-G036	1342249044	OT1_nlu_1	2640
IRAS 15462-0450	1342249045	OT1_dfarrah_1	11875
NGC 5936	1342249046	OT1_nlu_1	1321
Mrk 463	1342249047	OT1_dfarrah_1	11875
NGP-NB.v1.78	1342249063	OT1_rivison_1	13194
NGP-NB.v1.43	1342249064	OT1_rivison_1	13194
NGP-NA.v1.144	1342249066	OT1_rivison_1	13195
IRAS 14348-1447	1342249457	OT1_dfarrah_1	5939

ESO 221-IG010	1342249461	OT1_nlu_1	1322
IRAS 12116-5615	1342249462	OT1_nlu_1	5279
IC 4518AB	1342250514	OT1_nlu_1	2641
CGCG 052-037	1342251284	OT1_nlu_1	5279
IRAS F16399-0937	1342251334	OT1_nlu_1	5279
IRAS F16516-0948	1342251335	OT1_nlu_1	5279
SWIRE04	1342253658	OT2_drigopou_3	13194
IRAS 07598+6508	1342253659	OT1_dfarrah_1	11875
MM J18423+5938	1342253672	OT2_maravena_2	15833
	1342255798	OT2_maravena_2	17152
	1342255810	OT2_maravena_2	17152
	1342255811	OT2_maravena_2	17152
	1342255812	OT2_maravena_2	17152
	1342256357	OT2_maravena_2	17152
MG 0751+2716	1342253966	OT1_mbradfor_1	21110
APM 08279+5255	1342253967	OT1_mbradfor_1	21110
SWIRE01	1342254034	OT2_drigopou_3	13194
SWIRE03	1342254035	OT2_drigopou_3	13194
SWIRE02	1342255265	OT2_drigopou_3	13195
SDP.17	1342255280	OT1_rivison_1	13194
SDP.11	1342255281	OT1_rivison_1	13194
G09v1.124	1342255282	OT1_rivison_1	13194
IRAS FSC10214+4724	1342255799	OT1_mbradfor_1	21110
GOODS-N26	1342256083	OT1_apope_1	9236
GOODS-N19	1342256358	OT1_apope_1	9236
GOODS-NC1	1342256359	OT1_apope_1	9236
NGC 7591	1342257346	OT1_nlu_1	2640
BOOTES03	1342257936	OT2_drigopou_3	13195
HXMM01	1342258698	OT2_drigopou_3	13194
FLS01	1342258701	OT2_drigopou_3	13194
BOOTES02	1342259073	OT2_drigopou_3	13195
Cloverleaf	1342259573	OT1_mbradfor_1	21110
CDFS01	1342259582	OT2_drigopou_3	13195
CDFS02	1342259583	OT2_drigopou_3	13194
CDFS04	1342259584	OT2_drigopou_3	13195
SMMJ02399-0136	1342262900	OT2_cferkinh_1	17811

Table 10: Properties of sources in the stacks

Target	R.A.	DEC.	z_{spec}	μ	L_{IR}	Refs.
NGC 7552	23:16:10.80	-42:35:04.65	0.0054	-	11.11	R15,G14,A09
NGC 1365	03:33:36.61	-36:08:18.05	0.00546	-	11.00	R15,A09
NGC 4194	12:14:09.78	+54:31:34.36	0.008342	-	11.10	A09,L17
NGC 3256	10:27:51.18	-43:54:14.21	0.0094	-	11.64	R15,G14,A09
ESO 173-G015	13:27:23.73	-57:29:22.96	0.0097	-	11.38	R15,G14,A09
NGC 5010	13:12:26.52	-15:47:51.75	0.009924	-	11.50	A09,L17
ESO 221-IG010	13:50:56.87	-49:03:18.66	0.010337	-	11.22	A09,L17
Arp 299	11:28:33.31	+58:33:44.89	0.0104	-	11.93	R15,NED,A09
ESO 320-G030	11:53:11.63	-39:07:49.34	0.0108	-	11.17	R15,G14,A09
NGC 2369	07:16:37.96	-62:20:35.71	0.010807	-	11.16	A09,L17
NGC 6156	16:34:52.26	-60:37:06.06	0.010885	-	11.14	A09,L17
IC 5179	22:16:09.08	-36:50:36.54	0.011415	-	11.24	A09,L17
NGC 5653	14:30:09.89	+31:12:56.97	0.011881	-	11.13	A09,L17
ESO 420-G013	04:13:49.69	-32:00:24.34	0.011908	-	11.07	A09,L17
NGC 5990	15:46:16.41	+02:24:54.68	0.012806	-	11.13	A09,L17
CGCG 049-057	15:13:13.18	+07:13:30.24	0.013	-	11.35	R15,A09
NGC 0877	02:18:00.12	+14:32:34.34	0.013052	-	11.10	A09,L17
UGC 03410	06:14:30.27	+80:27:00.89	0.013079	-	11.10	A09,L17
NGC 1961	05:42:04.67	+69:22:42.69	0.013122	-	11.06	A09,L17
NGC 6701	18:43:12.47	+60:39:09.42	0.013226	-	11.12	A09,L17
NGC 5936	15:30:00.76	+12:59:20.78	0.013356	-	11.14	A09,L17
NGC 5135	13:25:44.09	-29:49:59.51	0.0137	-	11.30	R15,G14,A09
NGC 3221	10:22:20.36	+21:34:21.41	0.013709	-	11.09	A09,L17
NGC 5734	14:45:09.02	-20:52:13.17	0.013746	-	11.15	A09,L17
NGC 2388	07:28:53.51	+33:49:08.56	0.01379	-	11.28	A09,L17
MCG+04-48-002	20:28:35.15	+25:44:03.27	0.0139	-	11.11	A09,L17
IRAS 17578-0400	18:00:31.78	-04:00:54.86	0.014043	-	11.48	A09,L17
NGC 7771	23:51:24.67	+20:06:40.24	0.0143	-	11.40	R15,G14,A09
UGC 03351	05:45:48.22	+58:42:05.69	0.01486	-	11.28	A09,L17
NGC 0023	00:09:53.39	+25:55:25.98	0.015231	-	11.12	A09,L17
UGC 01845	02:24:07.87	+47:58:11.61	0.015607	-	11.12	A09,L17
IC 4734	18:38:25.65	-57:29:25.01	0.015611	-	11.35	A09,L17
MCG+12-02-001	00:54:03.47	+73:05:10.14	0.0157	-	11.50	R15,G14,A09
IC 4518AB	14:57:41.12	-43:07:56.00	0.015728	-	11.23	A09,L17

NGC 6052	16:05:12.93	+20:32:36.42	0.015808	-	11.09	A09,L17
NGC 1614	04:33:59.75	-08:34:44.84	0.0159	-	11.65	R15,G14,A09
ESO 353-G020	01:34:51.30	-36:08:14.57	0.015921	-	11.06	A09,L17
MCG-02-33-098	13:02:19.78	-15:46:03.69	0.015921	-	11.17	A09,L17
MCG+02-20-003	07:35:43.63	+11:42:36.02	0.016255	-	11.13	A09,L17
UGC 11041	17:54:51.76	+34:46:32.76	0.016281	-	11.11	A09,L17
NGC 7469	23:03:15.79	+08:52:28.62	0.0163	-	11.65	R15,G14,A09
IC 4280	13:32:53.31	-24:12:25.81	0.016331	-	11.15	A09,L17
NGC 7591	23:18:16.34	+06:35:09.43	0.016531	-	11.12	A09,L17
MCG-03-34-064	13:22:24.43	-16:43:42.76	0.016541	-	11.28	A09,L17
UGC 08739	13:49:14.26	+35:15:19.63	0.016785	-	11.15	A09,L17
NGC 3110	10:04:02.20	-06:28:28.08	0.016858	-	11.37	A09,L17
NGC 7679	23:28:46.63	+03:30:43.34	0.017139	-	11.11	A09,L17
ESO 264-G057	10:59:01.79	-43:26:25.61	0.017199	-	11.14	A09,L17
IC 4687	18:13:39.82	-57:43:30.54	0.0173	-	11.62	R15,G14,A09
IRAS F17138-1017	17:16:35.74	-10:20:41.31	0.017335	-	11.49	A09,L17
ESO 286-G035	21:04:11.06	-43:35:30.24	0.017361	-	11.20	A09,L17
ESO 467-G027	22:14:39.81	-27:27:50.32	0.017401	-	11.08	A09,L17
NGC 2342	07:09:18.22	+20:38:11.26	0.017599	-	11.31	A09,L17
UGC 02982	04:12:22.51	+05:32:49.65	0.017696	-	11.20	A09,L17
NGC 0828	02:10:09.45	+39:11:25.50	0.017926	-	11.36	A09,L17
Arp 220	15:34:57.22	+23:30:12.34	0.0181	-	12.28	R11,R15,A09
NGC 0317B	00:57:40.32	+43:47:31.94	0.018109	-	11.19	A09,L17
IRAS F18293-3413	18:32:41.36	-34:11:25.88	0.0182	-	11.88	R15,A09
NGC 6286	16:58:31.38	+58:56:15.38	0.018349	-	11.37	A09,L17
NGC 2623	08:38:24.06	+25:45:17.00	0.0185	-	11.60	R15,G14,A09
Mrk 331	23:51:26.53	+20:35:09.12	0.0185	-	11.50	R15,G14,A09
NGC 5104	13:21:22.99	+00:20:33.32	0.018606	-	11.27	A09,L17
IRAS 05442+1732	05:47:11.24	+17:33:47.37	0.01862	-	11.30	A09,L17
MCG-05-12-006	04:52:04.97	-32:59:25.66	0.018753	-	11.17	A09,L17
IRAS 04271+3849	04:30:33.23	+38:55:48.62	0.018813	-	11.11	A09,L17
NGC 0958	02:30:42.79	-02:56:23.96	0.01914	-	11.20	A09,L17
MCG+08-11-002	05:40:43.73	+49:41:41.58	0.019157	-	11.46	A09,L17
ESO 339-G011	19:57:37.37	-37:56:08.47	0.0192	-	11.20	A09,L17
NGC 34	00:11:06.54	-12:06:23.70	0.0196	-	11.49	R15,G14,A09
NGC 6926	20:33:06.02	-02:01:40.02	0.019613	-	11.32	A09,L17
IC 1623	01:07:46.72	-17:30:27.31	0.0201	-	11.71	R15,G14,A09
NGC 1572	04:22:42.75	-40:36:03.31	0.020384	-	11.30	A09,L17
ESO 350-IG038	00:36:52.39	-33:33:17.36	0.020598	-	11.28	A09,L17
NGC 6621	18:12:55.21	+68:21:46.48	0.020652	-	11.29	A09,L17
ESO 138-G027	17:26:43.00	-59:55:54.34	0.020781	-	11.41	A09,L17
ESO 264-G036	10:43:07.67	-46:12:44.83	0.021065	-	11.32	A09,L17
UGC 03608	06:57:34.59	+46:24:11.62	0.021351	-	11.34	A09,L17
UGC 12150	22:41:12.20	+34:14:53.38	0.021391	-	11.35	A09,L17
ESO 507-G070	13:02:52.32	-23:55:17.90	0.021702	-	11.56	A09,L17
UGC 02238	02:46:17.42	+13:05:45.17	0.021883	-	11.33	A09,L17
NGC 0232	00:42:45.76	-23:33:39.06	0.022639	-	11.44	A09,L17
IRAS F16516-0948	16:54:23.78	-09:53:21.05	0.022706	-	11.32	A09,L17
ESO 244-G012	01:18:08.31	-44:27:38.75	0.022903	-	11.38	A09,L17
Arp 193	13:20:35.49	+34:08:22.52	0.0233	-	11.73	R15,G14,A09
UGC 02608	03:15:01.23	+42:02:08.76	0.023343	-	11.41	A09,L17
NGC 7592	23:18:22.22	-04:24:56.56	0.024444	-	11.40	A09,L17
UGC 03094	04:35:33.85	+19:10:18.51	0.02471	-	11.44	A09,L17
CGCG 052-037	16:30:56.58	+04:04:58.99	0.02449	-	11.45	A09,L17
NGC 6240	16:52:59.10	+02:24:04.07	0.0245	-	11.93	R15,G14,A09
IRAS 08355-4944	08:37:02.00	-49:54:29.02	0.025898	-	11.62	A09,L17
IRAS F16399-0937	16:42:40.11	-09:43:13.41	0.027012	-	11.63	A09,L17
IRAS 12116-5615	12:14:22.18	-56:32:32.78	0.027102	-	11.65	A09,L17
MCG-02-01-051	00:18:50.85	-10:22:37.73	0.027299	-	11.48	A09,L17
IRAS F01417+1651	01:44:30.50	+17:06:08.40	0.027399	-	11.64	A09,L17
IC 5298	23:16:00.62	+25:33:22.03	0.027422	-	11.60	A09,L17
NGC 7674	23:27:56.74	+08:46:43.49	0.028924	-	11.56	A09,L17
ESO 099-G004	15:24:57.73	-63:07:30.44	0.029284	-	11.74	A09,L17
IRAS 05223+1908	05:25:16.75	+19:10:49.25	0.029577	-	11.65	A09,L17
IRAS 13120-5453	13:15:06.42	-55:09:21.22	0.0308	-	12.34	R15,G14
UGC 02369	02:54:01.75	+14:58:13.49	0.031202	-	11.67	A09,L17
CGCG 436-030	01:20:02.47	+14:21:40.61	0.031229	-	11.69	A09,L17
NGC 0695	01:51:14.37	+22:34:55.81	0.032472	-	11.68	A09,L17
VV 340	14:57:00.78	+24:37:04.37	0.033669	-	11.74	A09,L17
MCG-03-04-014	01:10:08.85	-16:51:11.29	0.035144	-	11.65	A09,L17
CGCG 448-020	20:57:24.32	+17:07:37.28	0.036098	-	11.94	A09,L17
Mrk 273	13:44:42.42	+55:53:11.78	0.0378	-	12.21	R15,G14,A09
ESO 255-IG007	06:27:21.68	-47:10:36.83	0.03879	-	11.90	A09,L17
VV 705	15:18:06.26	+42:44:43.68	0.040191	-	11.92	A09,L17
Mrk 231	12:56:14.46	+56:52:24.92	0.0422	-	12.57	R15,G14,A09,V10
IRAS F05189-2524	05:21:01.29	-25:21:45.21	0.0426	-	12.16	R15,G14,A09
IRAS F17207-0014	17:23:21.98	-00:17:00.96	0.0428	-	12.46	R15,A09
ESO 286-IG019	20:58:26.81	-42:38:59.71	0.042996	-	12.06	A09,L17
IRAS F10565+2448	10:59:18.17	+24:32:34.26	0.0431	-	12.08	A09,L17
ESO 148-IG002	23:15:46.70	-59:03:14.91	0.044601	-	12.06	A09,L17

ESO 069-IG006	16:38:11.46	-68:26:07.94	0.046972	-	11.98	A09,L17
Mrk 463	13:56:02.86	+18:22:20.05	0.051	-	11.79	M90,F07,F13
IRAS 15250+3609	15:26:59.56	+35:58:37.63	0.055	-	12.00	M90,F07,I11
IRAS 08572+3915	09:00:25.70	+39:03:54.83	0.058	-	12.11	M90,F07,G14
UGC 545	00:53:34.86	+12:41:34.87	0.0589	-	11.93	S11,E06,NED
IRAS 09022-3615	09:04:12.87	-36:27:00.14	0.059641	-	12.31	A09,L17
IRAS 19254-6315	19:31:20.23	-72:39:22.89	0.063	-	12.09	M90,F07,F13
IRAS 23365+3604	23:39:01.08	+36:21:09.28	0.064	-	12.15	M90,F07,G14
IRAS 14378-3651	14:40:58.89	-37:04:32.47	0.068	-	12.23	HW88,F07,I11
IRAS 22491-1808	22:51:49.20	-17:52:23.62	0.078	-	11.65	M90,F07,F13
IRAS 06035-7102	06:02:54.36	-71:03:08.81	0.079	-	12.22	M90,F07 ,F13
Mrk 478	14:42:07.61	+35:26:23.22	0.0791	-	11.52	E06,S11,NED
IRAS 14348-1447	14:37:38.29	-15:00:24.75	0.083	-	12.42	HW88,F07,G14
IRAS 19297-0406	19:32:21.84	-04:00:02.83	0.086	-	12.45	HW88,F07,I11
IRAS 20414-1651	20:44:18.25	-16:40:16.02	0.087	-	12.22	HW88,F07,F13
IRAS 06206-6315	06:21:01.47	-63:17:23.12	0.092	-	12.23	M90,F07,F13
IRAS 08311-2459	08:33:20.65	-25:09:32.20	0.100	-	12.50	HW88,F07 ,F13
IRAS 15462-0450	15:48:56.83	-04:59:33.71	0.100	-	12.24	M90,F07,F13
IRAS 20087-0308	20:11:23.73	-02:59:50.82	0.106	-	12.42	HW88,F07,F13
IRAS 11095-0238	11:12:03.35	-02:54:23.93	0.107	-	12.28	HW88,F07,F13
IRAS 23230-6926	23:26:03.52	-69:10:19.11	0.107	-	12.37	M90,F07,F13
IRAS 01003-2238	01:02:49.92	-22:21:56.47	0.118	-	12.32	HW88,F07,F13
IRAS 00188-0856	00:21:26.52	-08:39:26.86	0.128	-	12.39	M90,F07 ,F13
IRAS 12071-0444	12:09:45.13	-05:01:13.46	0.128	-	12.41	M90,F07,F13
PG 1613+658	16:13:57.15	+65:43:09.19	0.129	-	11.88	NED,E06
IRAS 20100-4156	20:13:29.68	-41:47:34.68	0.13	-	12.67	HW88,F07,F13
IRAS 23253-5415	23:28:06.15	-53:58:30.96	0.13	-	12.36	M90,F07,F13
IRAS 03158+4227	03:19:12.50	+42:38:28.37	0.134	-	12.63	HW88,F07,F13
IRAS 16090-0139	16:11:40.61	-01:47:05.86	0.134	-	12.55	M90,F07,F13
IRAS 10378+1109	10:40:29.13	+10:53:18.36	0.136	-	12.31	HW88,F07,F13
SWIRE03	10:40:43.66	+59:34:09.66	0.148	-	12.25	M90,H03,Y13
IRAS 07598+6508	08:04:30.36	+64:59:52.76	0.148	-	12.50	M90,F07,F13
IRAS 03521+0028	03:54:42.10	+00:37:00.71	0.152	-	12.52	HW88,F07 ,F13
Mrk 1014	01:59:50.10	+00:23:39.10	0.1631	-	12.62	F13,NED
CDFS04	03:35:49.16	-27:49:18.29	0.168	-	11.80	E09,D09,M90,M11
BOOTES03	14:28:49.80	+34:32:39.81	0.219	-	11.87	M14
CDFS02	03:28:18.03	-27:43:08.25	0.248	-	11.82	M14
BOOTES02	14:32:34.88	+33:28:32.25	0.25	-	11.91	M14
SWIRE04	10:32:37.47	+58:08:45.75	0.251	-	11.80	M14
IRAS 00397-1312	00:42:15.50	-12:56:03.17	0.262	-	12.90	HW88,F07
DAN03	00:40:14.68	-43:20:10.81	0.265	-	11.59	M14
CDFS01	03:29:04.38	-28:47:52.52	0.289	-	11.79	M14
BOOTES01	14:36:31.97	+34:38:29.60	0.354	-	12.69	M14
SWIRE02	10:51:13.42	+57:14:25.79	0.362	-	11.90	M14
SWIRE05	10:35:58.01	+58:58:46.17	0.366	-	12.06	M14
FLS01	17:20:17.08	+59:16:37.47	0.417	-	11.86	M14
FLS02	17:13:31.69	+58:58:04.60	0.436	-	12.41	M14
SWIRE01	10:47:53.34	+58:21:05.99	0.887	-	12.92	M14
G15v2.19*	14:29:35.27	-00:28:36.23	1.027	9.7 ± 0.7	12.42	ME14,W17
GOODS-N26	12:36:34.53	+62:12:39.74	1.219	-	12.26	G14,M12
HBootes03	14:28:24.16	+35:26:19.84	1.326	3.0 ± 1.5	12.69	B13
SDP.9	09:07:40.22	-00:41:59.03	1.577	8.8 ± 2.2	12.58	B13
NGP-NB.v1.43	13:24:27.23	+28:44:50.37	1.68	2.8 ± 0.4	12.92	B13,T16
SDP.11	09:10:43.04	-00:03:22.72	1.784	10.9 ± 1.3	12.48	B13
GOODS-N07	12:36:21.22	+62:17:10.32	1.9924	-	12.42	M12
GOODS-NC1	12:36:00.25	+62:10:47.13	2.0017	-	12.22	G14
G09v1.40*	08:53:59.04	+01:55:38.05	2.0894	15.3 ± 3.5	12.45	B13,W17
G12v2.257*	11:58:20.06	-01:37:52.10	2.191	13.0 ± 7.0	12.04	W17
NGP-NA.v1.144*	13:36:49.88	+29:18:00.95	2.202	4.4 ± 0.8	12.95	B13,W17
IRAS FSC10214+4724	10:24:34.58	+47:09:10.11	2.286	50	12.46	BL95,RR93,B99
NGP-NA.v1.56*	13:44:29.41	+30:30:36.10	2.301	11.7 ± 0.9	12.77	B13,W17
SDP.17	09:03:02.83	-01:41:25.84	2.3051	4.9 ± 0.7	13.00	B13
HXMM01*	02:20:16.53	-06:01:43.67	2.308	1.5 ± 0.3	13.30	B13,W17
SMMJ2135-0102	21:35:11.60	-01:02:52.16	2.326	37.5 ± 4.5	12.41	I10b,SW11
G09v1.124*	08:49:33.31	+02:14:42.61	2.410	2.8 ± 0.2	13.14	B13,W17
G15v2.235*	14:13:52.18	-00:00:23.84	2.478	1.8 ± 0.3	13.26	B13,W17
GOODS-N19	12:37:07.26	+62:14:07.55	2.484	-	12.57	M12
Cloverleaf	14:15:46.26	+11:29:43.45	2.56	11	12.78	B92,B99,VS03,U16
G09v1.326*	09:18:40.85	+02:30:47.37	2.581	-	12.76	B13,W17
SDP.130	09:13:05.30	-00:53:42.80	2.626	2.1 ± 0.3	13.30	B13
SMMJ02399-0136	02:39:51.89	-01:35:58.56	2.795	2.38 ± 0.08	12.73	G14,I10a,T12
SPT0538-50	05:38:16.77	-50:30:53.66	2.782	21 ± 4	12.54	BW13
HerMES-Lock01	10:57:51.21	+57:30:27.83	2.956	9.2 ± 0.4	13.06	B13
SDP.81	09:03:11.50	+00:39:06.70	3.043	11.1 ± 1.1	12.57	B13
NGP-NB.v1.78*	13:30:08.34	+24:59:00.07	3.111	13.0 ± 1.5	12.78	B13,W17
G12v2.43*	11:35:26.16	-01:46:06.84	3.127	2.8 ± 0.4	12.70	B13,W17
MG 0751+2716	07:51:41.62	+27:16:32.67	3.2	16	11.77	A07,BI02,B02,WU09
G12v2.30*	11:46:37.96	-00:11:32.89	3.259	9.5 ± 0.6	13.06	B13,W17
HXMM02	02:18:30.56	-05:31:31.85	3.39	4.4 ± 1.0	12.90	B13
NGP-NC.v1.143	12:56:32.65	+23:36:25.55	3.565	11.3 ± 1.7	12.91	B13

G09v1.97	08:30:51.12	+01:32:26.00	3.634	6.9 ± 0.6	13.20	B13
APM 08279+5255	08:31:41.59	+52:45:17.81	3.91	4	13.78	E00,R09,B06,K07,LI11,V11
MM J18423+5938	18:42:22.50	+59:38:29.81	3.926	12	12.13	L11,D12

Unused Spectra						
HATLAS 090302-014226†	09:03:02.95	-01:42:26.30				
SF.V1.88†	23:26:23.03	-34:26:40.34				
SF.V1.100†	01:24:07.35	-28:14:35.78				
SG.V1.22†	01:37:19.98	-33:19:49.54				
SG.V1.29†	01:40:31.14	-32:42:03.51				
SG.V1.77†	01:48:34.68	-30:35:32.05				
SA.V1.44†	22:38:29.06	-30:41:48.86				
SC.V1.128†	23:24:19.84	-32:39:23.71				
SD.V1.70†	00:09:12.62	-30:08:09.16				
SD.V1.133†	00:07:22.37	-35:20:15.57				
SB.V1.143†	23:25:55.44	-30:22:34.89				
SGP-B-202†	23:26:23.03	-34:26:40.34				
SGP-D-328†	00:26:25.11	-34:17:38.13				
SGP-E-165†	00:47:36.05	-27:29:54.03				
SGP-A-53†	22:25:36.37	-29:56:46.03				
MACS J2043-2144‡	20:43:14.17	-21:44:38.80				
MMJ0107†	01:07:02.35	-73:01:59.80				
SWIRE 07†	11:02:05.80	+57:57:40.75				
XMM 02†	02:19:57.26	-05:23:48.81				
DAN 02†	17:20:17.08	+53:12:43.41				
Locke 01†	10:45:30.42	+58:12:32.86				
HeLMS 44†	23:32:55.44	-03:11:34.34				
HeLMS 45†	23:24:39.55	-04:39:36.18				
SPT 0551-50††	05:51:39.41	-50:58:02.36	3.164			
SPT 0512-59††	05:12:57.93	-59:35:41.87	2.2331			
NGC 2146‡‡	06:18:38.91	+78:21:25.37	0.00298			
NGC 1068‡‡	02:42:40.82	-00:00:47:56	0.00379			
NGC 4151‡‡	12:10:32.88	+39:24:18.55	0.00332			
NGC 5128‡‡	13:25:27.55	-43:01:09.79	0.00183			
M81‡‡	09:55:32.78	+69:03:57.05	-0.000113			
M82‡‡	09:55:51.67	+69:40:48.20	0.000677			
NGC 2403‡‡	07:36:49.82	+65:36:12.27	0.000445			
NGC 205‡‡	00:40:24.03	+41:41:50.39	-0.000768			
MCG 604†	01:34:33.46	+30:46:47.59				

Notes: L_{IR} values for sources with z < 1 are taken from the literature. The given values of L_{IR} for sources with z > 1 are computed from fits to continuum photometry and are corrected for lensing magnification. Sources marked with * have PACS spectroscopy and appear in Wardlow et al. 2017 [237]. References: A07: Alloin et al. 2007 [5], A09: Armus et al. 2009 [11], B92: Barvainis et al. 1992 [17], B99: Benford 1999 [20], B02: Barvainis et al. 2002 [16], B06: Beelen et al. 2006 [19], B13: Bussmann et al. 2013 [33], BI02: Barvainis & Ivison 2002 [18], BL95: Broadhurst & Lehar 1995 [32], BW13: Bothwell et al. 2013 [27], D09: Dye et al. 2009 [64], D12: Decarli et al. 2012 [61], E00: Egami et al. 2000 [67], E06: Evans et al. 2006 [69], E09: Eales et al. 2009 [65], F07: Farrah et al. 2007 [70], F13: Farrah et al. 2013 [71], G14: Greve et al. 2014 [87], H03: Hutchings et al. 2003 [109], HW88: Helou & Walker 1988 [96], I10a: Ivison et al. 2010a [113], I10b: Ivison et al. 2010b [114], V10: Van der Werf et al. 2010 [231], I11: Iwasawa et al. 2011 [115], K07: Krips et al. 2007 [132], L11: Lestrade et al. 2011 [137], L17: Lu et al. 2017 [142], LI11: Lis et al. 2011 [138], M90: Moshir et al. 1990 [159], M11: Moncelsi et al. 2011 [158], M12: Magnelli et al. 2012 [147], M14: Magdis et al. 2014 [146], ME14: Messias et al. 2014 [156], NED: NASA/IPAC Extragalactic Database, R09: Riechers et al. 2009 [186], R11: Rangwala et al. 2011 [182], R15: Rosenberg et al. 2015 [188], RR93: Rowan-Robinson et al. 1993 [189], S11: Sargsyan et al. 2011 [191], S14: Spilker et al. 2014 [203], SW11: Swinbank et al. 2011 [215], T12:

Thomson et al. 2012 [222], T16: Timmons et al. 2016 [224], U16: Uzgil et al. 2016 [225], V11: Van der Werf et al. 2011 [230], VS03: Venturini & Solomon et al. 2003 [233], W17: Wardlow et al. 2017 [237], WU09: Wu et al. 2009 [245], Y13: Yamada et al. 2013 [248].

For unused spectra: †No spectroscopic redshift and/or magnification factor. ‡Multiple objects within beam. ††No magnification factor. ‡‡Redshift less than 0.005.

Bibliography

[1] N. P. Abel. The H^+ region contribution to [CII] 158-μm emission. , 368:1949–1958, June 2006.

[2] R. G. Abraham, S. van den Bergh, and P. Nair. A New Approach to Galaxy Morphology. I. Analysis of the Sloan Digital Sky Survey Early Data Release. , 588:218–229, May 2003.

[3] A. Abrahamse, L. Knox, S. Schmidt, P. Thorman, J. A. Tyson, and H. Zhan. Characterizing and Propagating Modeling Uncertainties in Photometrically Derived Redshift Distributions. , 734:36, June 2011.

[4] S. Alaghband-Zadeh, S. C. Chapman, A. M. Swinbank, I. Smail, A. L. R. Danielson, R. Decarli, R. J. Ivison, R. Meijerink, A. Weiss, and P. P. van der Werf. Using [C I] to probe the interstellar medium in z 2.5 sub-millimeter galaxies. , 435:1493–1510, October 2013.

[5] D. Alloin, J.-P. Kneib, S. Guilloteau, and M. Bremer. Dust and molecular content of the lensed quasar, MG0751+2716, at z = 3.2. , 470:53–60, July 2007.

[6] Ibrahim A. Almosallam, Matt J. Jarvis, and Stephen J. Roberts. GPZ: non-stationary sparse Gaussian processes for heteroscedastic uncertainty estimation in photometric redshifts. , 462(1):726–739, Oct 2016.

[7] Ibrahim A. Almosallam, Sam N. Lindsay, Matt J. Jarvis, and Stephen J. Roberts. A sparse Gaussian process framework for photometric redshift estimation. , 455(3):2387–2401, Jan 2016.

[8] M. Aravena, R. Decarli, F. Walter, R. Bouwens, P. A. Oesch, C. L. Carilli, F. E. Bauer, E. Da Cunha, E. Daddi, J. Gónzalez-López, R. J. Ivison, D. A. Riechers, I. Smail, A. M. Swinbank, A. Weiss, T. Anguita, R. Bacon, E. Bell, F. Bertoldi, P. Cortes, P. Cox, J. Hodge, E. Ibar, H. Inami,

L. Infante, A. Karim, B. Magnelli, K. Ota, G. Popping, P. van der Werf, J. Wagg, and Y. Fudamoto. The ALMA Spectroscopic Survey in the Hubble Ultra Deep Field: Search for [CII] Line and Dust Emission in 6. , 833:71, December 2016.

[9] R. G. Arendt, D. J. Fixsen, and S. H. Moseley. Dithering Strategies for Efficient Self-Calibration of Imaging Arrays. , 536:500–512, June 2000.

[10] Richard G. Arendt, A. Kashlinsky, S. H. Moseley, and J. Mather. Cosmic Infrared Background Fluctuations in Deep *Spitzer* Infrared Array Camera Images: Data Processing and Analysis. , 186(1):10–47, January 2010.

[11] L. Armus, J. M. Mazzarella, A. S. Evans, J. A. Surace, D. B. Sanders, K. Iwasawa, D. T. Frayer, J. H. Howell, B. Chan, A. Petric, T. Vavilkin, D. C. Kim, S. Haan, H. Inami, E. J. Murphy, P. N. Appleton, J. E. Barnes, G. Bothun, C. R. Bridge, V. Charmandaris, J. B. Jensen, L. J. Kewley, S. Lord, B. F. Madore, J. A. Marshall, J. E. Melbourne, J. Rich, S. Satyapal, B. Schulz, H. W. W. Spoon, E. Sturm, V. U, S. Veilleux, and K. Xu. GOALS: The Great Observatories All-Sky LIRG Survey. , 121:559, June 2009.

[12] S. Arnouts, S. Cristiani, L. Moscardini, S. Matarrese, F. Lucchin, A. Fontana, and E. Giallongo. Measuring and modelling the redshift evolution of clustering: the Hubble Deep Field North. , 310:540–556, December 1999.

[13] M. L. N. Ashby, S. P. Willner, G. G. Fazio, J. S. Huang, R. Arendt, P. Barmby, G. Barro, E. F. Bell, R. Bouwens, A. Cattaneo, D. Croton, R. Davé, J. S. Dunlop, E. Egami, S. Faber, K. Finlator, N. A. Grogin, P. Guhathakurta, L. Hernquist, J. L. Hora, G. Illingworth, A. Kashlinsky, A. M. Koekemoer, D. C. Koo, I. Labbé, Y. Li, L. Lin, H. Moseley, K. Nand ra, J. Newman, K. Noeske, M. Ouchi, M. Peth, D. Rigopoulou, B. Robertson, V. Sarajedini, L. Simard, H. A. Smith, Z. Wang, R. Wechsler, B. Weiner, G. Wilson, S. Wuyts, T. Yamada, and

H. Yan. SEDS: The *Spitzer* Extended Deep Survey. Survey Design, Photometry, and Deep IRAC Source Counts. , 769(1):80, May 2013.

[14] E. L. O. Bakes and A. G. G. M. Tielens. The photoelectric heating mechanism for very small graphitic grains and polycyclic aromatic hydrocarbons. , 427:822–838, June 1994.

[15] N. M. Ball, J. Loveday, M. Fukugita, O. Nakamura, S. Okamura, J. Brinkmann, and R. J. Brunner. Galaxy types in the Sloan Digital Sky Survey using supervised artificial neural networks. , 348:1038–1046, March 2004.

[16] R. Barvainis, D. Alloin, and M. Bremer. A CO survey of gravitationally lensed quasars with the IRAM interferometer. , 385:399–403, April 2002.

[17] R. Barvainis, R. Antonucci, and P. Coleman. Submillimeter observations of radio-quiet quasars and a luminous Seyfert 1 galaxy including the first detections. , 399:L19–L22, November 1992.

[18] R. Barvainis and R. Ivison. A Submillimeter Survey of Gravitationally Lensed Quasars. , 571:712–720, June 2002.

[19] A. Beelen, P. Cox, D. J. Benford, C. D. Dowell, A. Kovács, F. Bertoldi, A. Omont, and C. L. Carilli. 350 μm Dust Emission from High-Redshift Quasars. , 642:694–701, May 2006.

[20] D. J. Benford. *Broadband submillimeter instrumentation for the detection of distant galaxies*. PhD thesis, CALIFORNIA INSTITUTE OF TECHNOLOGY, 1999.

[21] G. Bernstein and D. Huterer. Catastrophic photometric redshift errors: weak-lensing survey requirements. , 401:1399–1408, January 2010.

[22] M. A. Bershady, A. Jangren, and C. J. Conselice. Structural and Photometric Classification of Galaxies. I. Calibration Based on a Nearby Galaxy Sample. , 119:2645–2663, June 2000.

[23] E. Bertin and S. Arnouts. SExtractor: Software for source extraction. , 117:393–404, June 1996.

[24] M. Bonato, M. Negrello, Z.-Y. Cai, G. De Zotti, A. Bressan, A. Lapi, C. Gruppioni, L. Spinoglio, and L. Danese. Exploring the early dust-obscured phase of galaxy formation with blind mid-/far-infrared spectroscopic surveys. , 438:2547–2564, March 2014.

[25] D. G. Bonfield, Y. Sun, N. Davey, M. J. Jarvis, F. B. Abdalla, M. Banerji, and R. G. Adams. Photometric redshift estimation using Gaussian processes. , 405(2):987–994, Jun 2010.

[26] R. Bordoloi, S. J. Lilly, and A. Amara. Photo-z performance for precision cosmology. , 406:881–895, August 2010.

[27] M. S. Bothwell, J. E. Aguirre, S. C. Chapman, D. P. Marrone, J. D. Vieira, M. L. N. Ashby, M. Aravena, B. A. Benson, J. J. Bock, C. M. Bradford, M. Brodwin, J. E. Carlstrom, T. M. Crawford, C. de Breuck, T. P. Downes, C. D. Fassnacht, A. H. Gonzalez, T. R. Greve, B. Gullberg, Y. Hezaveh, G. P. Holder, W. L. Holzapfel, E. Ibar, R. Ivison, J. Kamenetzky, R. Keisler, R. E. Lupu, J. Ma, M. Malkan, V. McIntyre, E. J. Murphy, H. T. Nguyen, C. L. Reichardt, M. Rosenman, J. S. Spilker, B. Stalder, A. A. Stark, M. Strandet, J. Vernet, A. Weiß, and N. Welikala. SPT 0538-50: Physical Conditions in the Interstellar Medium of a Strongly Lensed Dusty Star-forming Galaxy at z = 2.8. , 779:67, December 2013.

[28] C. M. Bradford, A. D. Bolatto, P. R. Maloney, J. E. Aguirre, J. J. Bock, J. Glenn, J. Kamenetzky, R. Lupu, H. Matsuhara, E. J. Murphy, B. J. Naylor, H. T. Nguyen, K. Scott, and J. Zmuidzinas. The Water Vapor Spectrum of APM 08279+5255: X-Ray Heating and Infrared Pumping over Hundreds of Parsecs. , 741:L37, November 2011.

[29] J. R. Brauher, D. A. Dale, and G. Helou. A Compendium of Far-Infrared Line and Continuum Emission for 227 Galaxies Observed by the Infrared Space Observatory. , 178:280–301, October 2008.

[30] M. Brescia, S. Cavuoti, R. D'Abrusco, G. Longo, and A. Mercurio. Photometric redshifts for quasars in multi-band surveys. *The Astrophysical Journal*, 772(2):140, 2013.

[31] D. Brisbin, C. Ferkinhoff, T. Nikola, S. Parshley, G. J. Stacey, H. Spoon, S. Hailey-Dunsheath, and A. Verma. Strong C^+ Emission in Galaxies at z 1-2: Evidence for Cold Flow Accretion Powered Star Formation in the Early Universe. , 799:13, January 2015.

[32] T. Broadhurst and J. Lehar. A Gravitational Lens Solution for the IRAS Galaxy FSC 10214+4724. , 450:L41, September 1995.

[33] R. S. Bussmann, I. Pérez-Fournon, S. Amber, J. Calanog, M. A. Gurwell, H. Dannerbauer, F. De Bernardis, H. Fu, A. I. Harris, M. Krips, A. Lapi, R. Maiolino, A. Omont, D. Riechers, J. Wardlow, A. J. Baker, M. Birkinshaw, J. Bock, N. Bourne, D. L. Clements, A. Cooray, G. De Zotti, L. Dunne, S. Dye, S. Eales, D. Farrah, R. Gavazzi, J. González Nuevo, R. Hopwood, E. Ibar, R. J. Ivison, N. Laporte, S. Maddox, P. Martnez-Navajas, M. Michalowski, M. Negrello, S. J. Óliver, I. G. Roseboom, D. Scott, S. Serjeant, A. J. Smith, M. Smith, A. Streblyanska, E. Valiante, P. van der Werf, A. Verma, J. D. Vieira, L. Wang, and D. Wilner. Gravitational Lens Models Based on Submillimeter Array Imaging of *Herschel*-selected Strongly Lensed Sub-millimeter Galaxies at z 1.5. , 779:25, December 2013.

[34] J. A. Calanog, H. Fu, A. Cooray, J. Wardlow, B. Ma, S. Amber, A. J. Baker, M. Baes, J. Bock, N. Bourne, R. S. Bussmann, C. M. Casey, S. C. Chapman, D. L. Clements, A. Conley, H. Dannerbauer, G. De Zotti, L. Dunne, S. Dye, S. Eales, D. Farrah, C. Furlanetto, A. I. Harris, R. J. Ivison, S. Kim, S. J. Maddox, G. Magdis, H. Messias, M. J. Michaowski, M. Negrello,

J. Nightingale, J. M. O'Bryan, S. J. Oliver, D. Riechers, D. Scott, S. Serjeant, J. Simpson, M. Smith, N. Timmons, C. Thacker, E. Valiante, and J. D. Vieira. Lens Models of *Herschel*-selected Galaxies from High-resolution Near-IR Observations. , 797:138, December 2014.

[35] N. Cappelluti, A. Kashlinsky, R. G. Arendt, A. Comastri, G. G. Fazio, A. Finoguenov, G. Hasinger, J. C. Mather, T. Miyaji, and S. H. Moseley. Cross-correlating Cosmic Infrared and X-Ray Background Fluctuations: Evidence of Significant Black Hole Populations among the CIB Sources. , 769(1):68, May 2013.

[36] C. L. Carilli and F. Walter. Cool Gas in High-Redshift Galaxies. , 51:105–161, August 2013.

[37] M. Carrasco Kind and R. J. Brunner. TPZ: photometric redshift PDFs and ancillary information by using prediction trees and random forests. , 432:1483–1501, June 2013.

[38] M. Carrasco Kind and R. J. Brunner. SOMz: photometric redshift PDFs with self-organizing maps and random atlas. , 438:3409–3421, March 2014.

[39] C. M. Casey. Far-infrared spectral energy distribution fitting for galaxies near and far. , 425:3094–3103, October 2012.

[40] C. M. Casey, D. Narayanan, and A. Cooray. Dusty star-forming galaxies at high redshift. , 541:45–161, August 2014.

[41] C. M. Casey, D. Narayanan, and A. Cooray. Dusty star-forming galaxies at high redshift. , 541:45–161, August 2014.

[42] R. Chary and D. Elbaz. Interpreting the Cosmic Infrared Background: Constraints on the Evolution of the Dust-enshrouded Star Formation Rate. , 556:562–581, August 2001.

[43] Ranga-Ram Chary, Asantha Cooray, and Ian Sullivan. Contribution to Unresolved Infrared Fluctuations from Dwarf Galaxies at Redshifts of 2-3. , 681(1):53–57, July 2008.

[44] J. Chaves-Montero, R. E. Angulo, and C. Hernández-Monteagudo. The effect of photometric redshift uncertainties on galaxy clustering and baryonic acoustic oscillations. , 477:3892–3909, July 2018.

[45] A. A. Collister and O. Lahav. ANNz: Estimating Photometric Redshifts Using Artificial Neural Networks. , 116:345–351, April 2004.

[46] A. J. Connolly, I. Csabai, A. S. Szalay, D. C. Koo, R. G. Kron, and J. A. Munn. Slicing Through Multicolor Space: Galaxy Redshifts from Broadband Photometry. , 110:2655, December 1995.

[47] C. J. Conselice. The Relationship between Stellar Light Distributions of Galaxies and Their Formation Histories. , 147:1–28, July 2003.

[48] C. J. Conselice, M. A. Bershady, and A. Jangren. The Asymmetry of Galaxies: Physical Morphology for Nearby and High-Redshift Galaxies. , 529:886–910, February 2000.

[49] A. Contursi, A. Poglitsch, J. Grácia Carpio, S. Veilleux, E. Sturm, J. Fischer, A. Verma, S. Hailey-Dunsheath, D. Lutz, R. Davies, E. González-Alfonso, A. Sternberg, R. Genzel, and L. Tacconi. Spectroscopic FIR mapping of the disk and galactic wind of M 82 with *Herschel*-PACS. , 549:A118, January 2013.

[50] Asantha Cooray and Ravi Sheth. Halo models of large scale structure. , 372(1):1–129, December 2002.

[51] Asantha Cooray, Joseph Smidt, Francesco De Bernardis, Yan Gong, Daniel Stern, Matthew L. N. Ashby, Peter R. Eisenhardt, Christopher C. Frazer, Anthony H. Gonzalez, Christopher S. Kochanek, Szymon Kozlowski, and Edward L. Wright. A measurement of the intrahalo light fraction with near-infrared background anisotropies. *arXiv e-prints*, page arXiv:1210.6031, Oct 2012.

[52] Asantha Cooray, Joseph Smidt, Francesco de Bernardis, Yan Gong, Daniel Stern, Matthew L. N. Ashby, Peter R. Eisenhardt, Christopher C. Frazer, Anthony H. Gonzalez, Christopher S. Kochanek, Szymon Kozowski, and Edward L. Wright. Near-infrared background anisotropies from diffuse intrahalo light of galaxies. , 490(7421):514–516, Oct 2012.

[53] D. Cormier, S. C. Madden, V. Lebouteiller, N. Abel, S. Hony, F. Galliano, A. Rémy-Ruyer, F. Bigiel, M. Baes, A. Boselli, M. Chevance, A. Cooray, I. De Looze, V. Doublier, M. Galametz, T. Hughes, O. . Karczewski, M.-Y. Lee, N. Lu, and L. Spinoglio. The *Herschel* Dwarf Galaxy Survey. I. Properties of the low-metallicity ISM from PACS spectroscopy. , 578:A53, June 2015.

[54] P. Cox, M. Krips, R. Neri, A. Omont, R. Güsten, K. M. Menten, F. Wyrowski, A. Weiß, A. Beelen, M. A. Gurwell, H. Dannerbauer, R. J. Ivison, M. Negrello, I. Aretxaga, D. H. Hughes, R. Auld, M. Baes, R. Blundell, S. Buttiglione, A. Cava, A. Cooray, A. Dariush, L. Dunne, S. Dye, S. A. Eales, D. Frayer, J. Fritz, R. Gavazzi, R. Hopwood, E. Ibar, M. Jarvis, S. Maddox, M. Michaowski, E. Pascale, M. Pohlen, E. Rigby, D. J. B. Smith, A. M. Swinbank, P. Temi, I. Valtchanov, P. van der Werf, and G. de Zotti. Gas and Dust in a Submillimeter Galaxy at z = 4.24 from the *Herschel* Atlas. , 740:63, October 2011.

[55] C. E. Cunha, M. Lima, H. Oyaizu, J. Frieman, and H. Lin. Estimating the redshift distribution of photometric galaxy samples - II. Applications and tests of a new method. , 396:2379–2398, July 2009.

[56] T. Dahlen, B. Mobasher, S. M. Faber, H. C. Ferguson, G. Barro, S. L. Finkelstein, K. Finlator, A. Fontana, R. Gruetzbauch, S. Johnson, J. Pforr, M. Salvato, T. Wiklind, S. Wuyts, V. Acquaviva, M. E. Dickinson, Y. Guo, J. Huang, K.-H. Huang, J. A. Newman, E. F. Bell, C. J.

Conselice, A. Galametz, E. Gawiser, M. Giavalisco, N. A. Grogin, N. Hathi, D. Kocevski, A. M. Koekemoer, D. C. Koo, K.-S. Lee, E. J. McGrath, C. Papovich, M. Peth, R. Ryan, R. Somerville, B. Weiner, and G. Wilson. A Critical Assessment of Photometric Redshift Methods: A CANDELS Investigation. , 775:93, October 2013.

[57] A. L. R. Danielson, A. M. Swinbank, I. Smail, P. Cox, A. C. Edge, A. Weiss, A. I. Harris, A. J. Baker, C. De Breuck, J. E. Geach, R. J. Ivison, M. Krips, A. Lundgren, S. Longmore, R. Neri, and B. O. Flaquer. The properties of the interstellar medium within a star-forming galaxy at z= 2.3. , 410:1687–1702, January 2011.

[58] M. Davis, P. Guhathakurta, N. P. Konidaris, J. A. Newman, M. L. N. Ashby, A. D. Biggs, P. Barmby, K. Bundy, S. C. Chapman, A. L. Coil, C. J. Conselice, M. C. Cooper, D. J. Croton, P. R. M. Eisenhardt, R. S. Ellis, S. M. Faber, T. Fang, G. G. Fazio, A. Georgakakis, B. F. Gerke, W. M. Goss, S. Gwyn, J. Harker, A. M. Hopkins, J.-S. Huang, R. J. Ivison, S. A. Kassin, E. N. Kirby, A. M. Koekemoer, D. C. Koo, E. S. Laird, E. Le Floc'h, L. Lin, J. M. Lotz, P. J. Marshall, D. C. Martin, A. J. Metevier, L. A. Moustakas, K. Nandra, K. G. Noeske, C. Papovich, A. C. Phillips, R. M. Rich, G. H. Rieke, D. Rigopoulou, S. Salim, D. Schiminovich, L. Simard, I. Smail, T. A. Small, B. J. Weiner, C. N. A. Willmer, S. P. Willner, G. Wilson, E. L. Wright, and R. Yan. The All-Wavelength Extended Groth Strip International Survey (AEGIS) Data Sets. , 660:L1–L6, May 2007.

[59] A. P. Dawid. Present position and potential developments: Some personal views: Statistical theory: The prequential approach. *Journal of the Royal Statistical Society. Series A (General)*, 147(2):278–292, 1984.

[60] Ilse De Looze, Maarten Baes, Diane Cormier, Hiroyuki Kaneko, Nario Kuno, Lisa Young, George J. Bendo, MÃ©dÃ©ric Boquien, Jacopo Fritz, Gianfranco Gentile, Robert C.

Kennicutt, Suzanne C. Madden, Matthew W. L. Smith, and Christine D. Wilson. The interstellar medium in andromeda's dwarf spheroidal galaxies â€“ ii. multiphase gas content and ism conditions. *Monthly Notices of the Royal Astronomical Society*, 465(3):3741, 2017.

[61] R. Decarli, F. Walter, R. Neri, F. Bertoldi, C. Carilli, P. Cox, J. P. Kneib, J. F. Lestrade, R. Maiolino, A. Omont, J. Richard, D. Riechers, K. Thanjavur, and A. Weiss. Ionized Nitrogen at High Redshift. , 752:2, June 2012.

[62] T. Dáz-Santos, L. Armus, V. Charmandaris, S. Stierwalt, E. J. Murphy, S. Haan, H. Inami, S. Malhotra, R. Meijerink, G. Stacey, A. O. Petric, A. S. Evans, S. Veilleux, P. P. van der Werf, S. Lord, N. Lu, J. H. Howell, P. Appleton, J. M. Mazzarella, J. A. Surace, C. K. Xu, B. Schulz, D. B. Sanders, C. Bridge, B. H. P. Chan, D. T. Frayer, K. Iwasawa, J. Melbourne, and E. Sturm. Explaining the [C II]157.7 μm Deficit in Luminous Infrared GalaxiesFirst Results from a *Herschel*/PACS Study of the GOALS Sample. , 774:68, September 2013.

[63] H. Dole, G. Lagache, J. L. Puget, K. I. Caputi, N. Fernández-Conde, E. Le Floc'h, C. Papovich, P. G. Pérez-González, G. H. Rieke, and M. Blaylock. The cosmic infrared background resolved by *Spitzer*. Contributions of mid-infrared galaxies to the far-infrared background. , 451(2):417–429, May 2006.

[64] S. Dye, P. A. R. Ade, J. J. Bock, E. L. Chapin, M. J. Devlin, J. S. Dunlop, S. A. Eales, M. Griffin, J. O. Gundersen, M. Halpern, P. C. Hargrave, D. H. Hughes, J. Klein, B. Magnelli, G. Marsden, P. Mauskopf, L. Moncelsi, C. B. Netterfield, L. Olmi, E. Pascale, G. Patanchon, M. Rex, D. Scott, C. Semisch, T. Targett, N. Thomas, M. D. P. Truch, C. Tucker, G. S. Tucker, M. P. Viero, and D. V. Wiebe. Radio and Mid-Infrared Identification of Blast Source Counterparts in the Chandra Deep Field South. , 703:285–299, September 2009.

[65] S. Eales, E. L. Chapin, M. J. Devlin, S. Dye, M. Halpern, D. H. Hughes, G. Marsden, P. Mauskopf, L. Moncelsi, C. B. Netterfield, E. Pascale, G. Patanchon, G. Raymond, M. Rex, D. Scott, C. Semisch, B. Siana, M. D. P. Truch, and M. P. Viero. BLAST: The Redshift Survey. , 707:1779–1808, December 2009.

[66] S. A. Eales, M. W. L. Smith, C. D. Wilson, G. J. Bendo, L. Cortese, M. Pohlen, A. Boselli, H. L. Gomez, R. Auld, M. Baes, M. J. Barlow, J. J. Bock, M. Bradford, V. Buat, N. Castro-Rodrguez, P. Chanial, S. Charlot, L. Ciesla, D. L. Clements, A. Cooray, D. Cormier, J. I. Davies, E. Dwek, D. Élbaz, M. Galametz, F. Galliano, W. K. Gear, J. Glenn, M. Griffin, S. Hony, K. G. Isaak, L. R. Levenson, N. Lu, S. Madden, B. O'Halloran, K. Okumura, S. Oliver, M. J. Page, P. Panuzzo, A. Papageorgiou, T. J. Parkin, I. Pérez-Fournon, N. Rangwala, E. E. Rigby, H. Roussel, A. Rykala, N. Sacchi, M. Sauvage, B. Schulz, M. R. P. Schirm, L. Spinoglio, S. Srinivasan, J. A. Stevens, M. Symeonidis, M. Trichas, M. Vaccari, L. Vigroux, H. Wozniak, G. S. Wright, and W. W. Zeilinger. Mapping the interstellar medium in galaxies with *Herschel*/SPIRE. , 518:L62, July 2010.

[67] E. Egami, G. Neugebauer, B. T. Soifer, K. Matthews, M. Ressler, E. E. Becklin, T. W. Murphy, Jr., and D. A. Dale. APM 08279+5255: Keck Near- and Mid-Infrared High-Resolution Imaging. , 535:561–574, June 2000.

[68] D. Elbaz, M. Dickinson, H. S. Hwang, T. Dáz-Santos, G. Magdis, B. Magnelli, D. Le Borgne, F. Galliano, M. Pannella, P. Chanial, L. Armus, V. Charmandaris, E. Daddi, H. Aussel, P. Popesso, J. Kartaltepe, B. Altieri, I. Valtchanov, D. Coia, H. Dannerbauer, K. Dasyra, R. Leiton, J. Mazzarella, D. M. Alexander, V. Buat, D. Burgarella, R.-R. Chary, R. Gilli, R. J. Ivison, S. Juneau, E. Le Floc'h, D. Lutz, G. E. Morrison, J. R. Mullaney, E. Murphy, A. Pope, D. Scott, M. Brodwin, D. Calzetti, C. Cesarsky, S. Charlot, H. Dole, P. Eisenhardt, H. C.

Ferguson, N. Förster Schreiber, D. Frayer, M. Giavalisco, M. Huynh, A. M. Koekemoer, C. Papovich, N. Reddy, C. Surace, H. Teplitz, M. S. Yun, and G. Wilson. GOODS-*Herschel*: an infrared main sequence for star-forming galaxies. , 533:A119, September 2011.

[69] A. S. Evans, P. M. Solomon, L. J. Tacconi, T. Vavilkin, and D. Downes. Dense Molecular Gas and the Role of Star Formation in the Host Galaxies of Quasi-stellar Objects. , 132:2398–2408, December 2006.

[70] D. Farrah, J. Bernard-Salas, H. W. W. Spoon, B. T. Soifer, L. Armus, B. Brandl, V. Charmandaris, V. Desai, S. Higdon, D. Devost, and J. Houck. High-Resolution Mid-Infrared Spectroscopy of Ultraluminous Infrared Galaxies. , 667:149–169, September 2007.

[71] D. Farrah, V. Lebouteiller, H. W. W. Spoon, J. Bernard-Salas, C. Pearson, D. Rigopoulou, H. A. Smith, E. González-Alfonso, D. L. Clements, A. Efstathiou, D. Cormier, J. Afonso, S. M. Petty, K. Harris, P. Hurley, C. Borys, A. Verma, A. Cooray, and V. Salvatelli. Far-infrared Fine-structure Line Diagnostics of Ultraluminous Infrared Galaxies. , 776:38, October 2013.

[72] G. G. Fazio, J. L. Hora, L. E. Allen, M. L. N. Ashby, P. Barmby, L. K. Deutsch, J. S. Huang, S. Kleiner, M. Marengo, S. T. Megeath, G. J. Melnick, M. A. Pahre, B. M. Patten, J. Polizotti, H. A. Smith, R. S. Taylor, Z. Wang, S. P. Willner, W. F. Hoffmann, J. L. Pipher, W. J. Forrest, C. W. McMurty, C. R. McCreight, M. E. McKelvey, R. E. McMurray, D. G. Koch, S. H. Moseley, R. G. Arendt, J. E. Mentzell, C. T. Marx, P. Losch, P. Mayman, W. Eichhorn, D. Krebs, M. Jhabvala, D. Y. Gezari, D. J. Fixsen, J. Flores, K. Shakoorzadeh, R. Jungo, C. Hakun, L. Workman, G. Karpati, R. Kichak, R. Whitley, S. Mann, E. V. Tollestrup, P. Eisenhardt, D. Stern, V. Gorjian, B. Bhattacharya, S. Carey, B. O. Nelson, W. J. Glaccum, M. Lacy, P. J. Lowrance, S. Laine, W. T. Reach, J. A. Stauffer, J. A. Surace, G. Wilson, E. L. Wright, A. Hoffman, G. Domingo, and

M. Cohen. The Infrared Array Camera (IRAC) for the *Spitzer* Space Telescope. , 154(1):10–17, September 2004.

[73] C. Ferkinhoff, D. Brisbin, S. Parshley, T. Nikola, G. J. Stacey, J. Schoenwald, J. L. Higdon, S. J. U. Higdon, A. Verma, D. Riechers, S. Hailey-Dunsheath, K. M. Menten, R. Güsten, A. Weiß, K. Irwin, H. M. Cho, M. Niemack, M. Halpern, M. Amiri, M. Hasselfield, D. V. Wiebe, P. A. R. Ade, and C. E. Tucker. The Second-generation z (Redshift) and Early Universe Spectrometer. I. First-light Observation of a Highly Lensed Local-ulirg Analog at High-z. , 780:142, January 2014.

[74] J. A. Fernández-Ontiveros, L. Spinoglio, M. Pereira-Santaella, M. A. Malkan, P. Andreani, and K. M. Dasyra. Far-infrared Line Spectra of Active Galaxies from the *Herschel*/PACS Spectrometer: The Complete Database. , 226:19, October 2016.

[75] A. Fernández-Soto, K. M. Lanzetta, and A. Yahil. A New Catalog of Photometric Redshifts in the Hubble Deep Field. , 513:34–50, March 1999.

[76] A. E. Firth, O. Lahav, and R. S. Somerville. Estimating photometric redshifts with artificial neural networks. , 339:1195–1202, March 2003.

[77] J. Fischer, M. L. Luhman, S. Satyapal, M. A. Greenhouse, G. J. Stacey, C. M. Bradford, S. D. Lord, J. R. Brauher, S. J. Unger, P. E. Clegg, H. A. Smith, G. Melnick, J. W. Colbert, M. A. Malkan, L. Spinoglio, P. Cox, V. Harvey, J.-P. Suter, and V. Strelnitski. ISO FAR-IR spectroscopy of IR-bright galaxies and ULIRGs. , 266:91–98, 1999.

[78] D. J. Fixsen, S. H. Moseley, and R. G. Arendt. Calibrating Array Detectors. , 128(2):651–658, June 2000.

[79] D. R. Flower and G. Pineau Des Forêts. Excitation and emission of H2, CO and H2O molecules in interstellar shock waves. , 406:1745–1758, August 2010.

[80] T. Fulton, D. A. Naylor, E. T. Polehampton, I. Valtchanov, R. Hopwood, N. Lu, J.-P. Baluteau, G. Mainetti, C. Pearson, A. Papageorgiou, S. Guest, L. Zhang, P. Imhof, B. M. Swinyard, M. J. Griffin, and T. L. Lim. The data processing pipeline for the *Herschel* SPIRE Fourier Transform Spectrometer. , 458:1977–1989, May 2016.

[81] R. D. George. *State of the gas in intense lensed starbursts*. PhD thesis, University of Edinburgh, November 2015.

[82] R. D. George, R. J. Ivison, R. Hopwood, D. A. Riechers, R. S. Bussmann, P. Cox, S. Dye, M. Krips, M. Negrello, R. Neri, S. Serjeant, I. Valtchanov, M. Baes, N. Bourne, D. L. Clements, G. De Zotti, L. Dunne, S. A. Eales, E. Ibar, S. Maddox, M. W. L. Smith, E. Valiante, and P. van der Werf. Far-infrared spectroscopy of a lensed starburst: a blind redshift from *Herschel*. , 436:L99–L103, November 2013.

[83] M. Giavalisco, H. C. Ferguson, A. M. Koekemoer, M. Dickinson, D. M. Alexander, F. E. Bauer, J. Bergeron, C. Biagetti, W. N. Brandt, S. Casertano, C. Cesarsky, E. Chatzichristou, C. Conselice, S. Cristiani, L. Da Costa, T. Dahlen, D. de Mello, P. Eisenhardt, T. Erben, S. M. Fall, C. Fassnacht, R. Fosbury, A. Fruchter, J. P. Gardner, N. Grogin, R. N. Hook, A. E. Hornschemeier, R. Idzi, S. Jogee, C. Kretchmer, V. Laidler, K. S. Lee, M. Livio, R. Lucas, P. Madau, B. Mobasher, L. A. Moustakas, M. Nonino, P. Padovani, C. Papovich, Y. Park, S. Ravindranath, A. Renzini, M. Richardson, A. Riess, P. Rosati, M. Schirmer, E. Schreier, R. S. Somerville, H. Spinrad, D. Stern, M. Stiavelli, L. Strolger, C. M. Urry, B. Vandame, R. Williams, and C. Wolf. The Great Observatories Origins Deep Survey: Initial Results from Optical and Near-Infrared Imaging. , 600(2):L93–L98, Jan 2004.

[84] Zahra Gomes, Matt J. Jarvis, Ibrahim A. Almosallam, and Stephen J. Roberts. Improving photometric redshift estimation using GPZ: size information, post processing, and improved photometry. , 475(1):331–342, Mar 2018.

[85] E. González-Alfonso, J. Fischer, K. Isaak, A. Rykala, G. Savini, M. Spaans, P. van der Werf, R. Meijerink, F. P. Israel, A. F. Loenen, C. Vlahakis, H. A. Smith, V. Charmandaris, S. Aalto, C. Henkel, A. Weiß, F. Walter, T. R. Greve, J. Martn-Pintado, D. A. Naylor, L. Spinoglio, S. Veilleux, A. I. Harris, L. Ármus, S. Lord, J. Mazzarella, E. M. Xilouris, D. B. Sanders, K. M. Dasyra, M. C. Wiedner, C. Kramer, P. P. Papadopoulos, G. J. Stacey, A. S. Evans, and Y. Gao. *Herschel* observations of water vapour in Markarian 231. , 518:L43, July 2010.

[86] E. González-Alfonso, J. Fischer, K. Isaak, A. Rykala, G. Savini, M. Spaans, P. van der Werf, R. Meijerink, F. P. Israel, A. F. Loenen, C. Vlahakis, H. A. Smith, V. Charmandaris, S. Aalto, C. Henkel, A. Weiß, F. Walter, T. R. Greve, J. Martn-Pintado, D. A. Naylor, L. Spinoglio, S. Veilleux, A. I. Harris, L. Ármus, S. Lord, J. Mazzarella, E. M. Xilouris, D. B. Sanders, K. M. Dasyra, M. C. Wiedner, C. Kramer, P. P. Papadopoulos, G. J. Stacey, A. S. Evans, and Y. Gao. *Herschel* observations of water vapour in Markarian 231. , 518:L43, July 2010.

[87] T. R. Greve, I. Leonidaki, E. M. Xilouris, A. Weiß, Z.-Y. Zhang, P. van der Werf, S. Aalto, L. Armus, T. Dáz-Santos, A. S. Evans, J. Fischer, Y. Gao, E. González-Alfonso, A. Harris, C. Henkel, R. Meijerink, D. A. Naylor, H. A. Smith, M. Spaans, G. J. Stacey, S. Veilleux, and F. Walter. Star Formation Relations and CO Spectral Line Energy Distributions across the J-ladder and Redshift. , 794:142, October 2014.

[88] M. J. Griffin, A. Abergel, A. Abreu, P. A. R. Ade, P. André, J.-L. Augueres, T. Babbedge, Y. Bae, T. Baillie, J.-P. Baluteau, M. J. Barlow, G. Bendo, D. Benielli, J. J. Bock, P. Bonhomme, D. Brisbin, C. Brockley-Blatt, M. Caldwell, C. Cara, N. Castro-Rodriguez, R. Cerulli, P. Chanial,

S. Chen, E. Clark, D. L. Clements, L. Clerc, J. Coker, D. Communal, L. Conversi, P. Cox, D. Crumb, C. Cunningham, F. Daly, G. R. Davis, P. de Antoni, J. Delderfield, N. Devin, A. di Giorgio, I. Didschuns, K. Dohlen, M. Donati, A. Dowell, C. D. Dowell, L. Duband, L. Dumaye, R. J. Emery, M. Ferlet, D. Ferrand, J. Fontignie, M. Fox, A. Franceschini, M. Frerking, T. Fulton, J. Garcia, R. Gastaud, W. K. Gear, J. Glenn, A. Goizel, D. K. Griffin, T. Grundy, S. Guest, L. Guillemet, P. C. Hargrave, M. Harwit, P. Hastings, E. Hatziminaoglou, M. Herman, B. Hinde, V. Hristov, M. Huang, P. Imhof, K. J. Isaak, U. Israelsson, R. J. Ivison, D. Jennings, B. Kiernan, K. J. King, A. E. Lange, W. Latter, G. Laurent, P. Laurent, S. J. Leeks, E. Lellouch, L. Levenson, B. Li, J. Li, J. Lilienthal, T. Lim, S. J. Liu, N. Lu, S. Madden, G. Mainetti, P. Marliani, D. McKay, K. Mercier, S. Molinari, H. Morris, H. Moseley, J. Mulder, M. Mur, D. A. Naylor, H. Nguyen, B. O'Halloran, S. Oliver, G. Olofsson, H.-G. Olofsson, R. Orfei, M. J. Page, I. Pain, P. Panuzzo, A. Papageorgiou, G. Parks, P. Parr-Burman, A. Pearce, C. Pearson, I. Pérez-Fournon, F. Pinsard, G. Pisano, J. Podosek, M. Pohlen, E. T. Polehampton, D. Pouliquen, D. Rigopoulou, D. Rizzo, I. G. Roseboom, H. Roussel, M. Rowan-Robinson, B. Rownd, P. Saraceno, M. Sauvage, R. Savage, G. Savini, E. Sawyer, C. Scharmberg, D. Schmitt, N. Schneider, B. Schulz, A. Schwartz, R. Shafer, D. L. Shupe, B. Sibthorpe, S. Sidher, A. Smith, A. J. Smith, D. Smith, L. Spencer, B. Stobie, R. Sudiwala, K. Sukhatme, C. Surace, J. A. Stevens, B. M. Swinyard, M. Trichas, T. Tourette, H. Triou, S. Tseng, C. Tucker, A. Turner, M. Vaccari, I. Valtchanov, L. Vigroux, E. Virique, G. Voellmer, H. Walker, R. Ward, T. Waskett, M. Weilert, R. Wesson, G. J. White, N. Whitehouse, C. D. Wilson, B. Winter, A. L. Woodcraft, G. S. Wright, C. K. Xu, A. Zavagno, M. Zemcov, L. Zhang, and E. Zonca. The *Herschel*-SPIRE instrument and its in-flight performance. , 518:L3, July 2010.

[89] N. A. Grogin, D. D. Kocevski, S. M. Faber, H. C. Ferguson, A. M. Koekemoer, A. G. Riess, V. Acquaviva, D. M. Alexander, O. Almaini, M. L. N. Ashby, M. Barden, E. F. Bell, F. Bournaud, T. M. Brown, K. I. Caputi, S. Casertano, P. Cassata, M. Castellano, P. Challis, R.-R. Chary, E. Cheung, M. Cirasuolo, C. J. Conselice, A. Roshan Cooray, D. J. Croton, E. Daddi, T. Dahlen, R. Davé, D. F. de Mello, A. Dekel, M. Dickinson, T. Dolch, J. L. Donley, J. S. Dunlop, A. A. Dutton, D. Elbaz, G. G. Fazio, A. V. Filippenko, S. L. Finkelstein, A. Fontana, J. P. Gardner, P. M. Garnavich, E. Gawiser, M. Giavalisco, A. Grazian, Y. Guo, N. P. Hathi, B. Häussler, P. F. Hopkins, J.-S. Huang, K.-H. Huang, S. W. Jha, J. S. Kartaltepe, R. P. Kirshner, D. C. Koo, K. Lai, K.-S. Lee, W. Li, J. M. Lotz, R. A. Lucas, P. Madau, P. J. McCarthy, E. J. McGrath, D. H. McIntosh, R. J. McLure, B. Mobasher, L. A. Moustakas, M. Mozena, K. Nandra, J. A. Newman, S.-M. Niemi, K. G. Noeske, C. J. Papovich, L. Pentericci, A. Pope, J. R. Primack, A. Rajan, S. Ravindranath, N. A. Reddy, A. Renzini, H.-W. Rix, A. R. Robaina, S. A. Rodney, D. J. Rosario, P. Rosati, S. Salimbeni, C. Scarlata, B. Siana, L. Simard, J. Smidt, R. S. Somerville, H. Spinrad, A. N. Straughn, L.-G. Strolger, O. Telford, H. I. Teplitz, J. R. Trump, A. van der Wel, C. Villforth, R. H. Wechsler, B. J. Weiner, T. Wiklind, V. Wild, G. Wilson, S. Wuyts, H.-J. Yan, and M. S. Yun. CANDELS: The Cosmic Assembly Near-infrared Deep Extragalactic Legacy Survey. , 197:35, December 2011.

[90] C. Gruppioni, S. Berta, L. Spinoglio, M. Pereira-Santaella, F. Pozzi, P. Andreani, M. Bonato, G. De Zotti, M. Malkan, M. Negrello, L. Vallini, and C. Vignali. Tracing black hole accretion with SED decomposition and IR lines: from local galaxies to the high-z Universe. , 458:4297–4320, June 2016.

[91] B. Gullberg, C. De Breuck, J. D. Vieira, A. Weiß, J. E. Aguirre, M. Aravena, M. Béthermin, C. M. Bradford, M. S. Bothwell, J. E. Carlstrom, S. C. Chapman, C. D. Fassnacht,

A. H. Gonzalez, T. R. Greve, Y. Hezaveh, W. L. Holzapfel, K. Husband, J. Ma, M. Malkan, D. P. Marrone, K. Menten, E. J. Murphy, C. L. Reichardt, J. S. Spilker, A. A. Stark, M. Strandet, and N. Welikala. The nature of the [C II] emission in dusty star-forming galaxies from the SPT survey. , 449:2883–2900, May 2015.

[92] Y. Guo, H. C. Ferguson, E. F. Bell, D. C. Koo, C. J. Conselice, M. Giavalisco, S. Kassin, Y. Lu, R. Lucas, N. Mandelker, D. M. McIntosh, J. R. Primack, S. Ravindranath, G. Barro, D. Ceverino, A. Dekel, S. M. Faber, J. J. Fang, A. M. Koekemoer, K. Noeske, M. Rafelski, and A. Straughn. Clumpy Galaxies in CANDELS. I. The Definition of UV Clumps and the Fraction of Clumpy Galaxies at 0.5 z 3. , 800:39, February 2015.

[93] Y. Guo, H. C. Ferguson, M. Giavalisco, G. Barro, S. P. Willner, M. L. N. Ashby, T. Dahlen, J. L. Donley, S. M. Faber, A. Fontana, A. Galametz, A. Grazian, K.-H. Huang, D. D. Kocevski, A. M. Koekemoer, D. C. Koo, E. J. McGrath, M. Peth, M. Salvato, S. Wuyts, M. Castellano, A. R. Cooray, M. E. Dickinson, J. S. Dunlop, G. G. Fazio, J. P. Gardner, E. Gawiser, N. A. Grogin, N. P. Hathi, L.-T. Hsu, K.-S. Lee, R. A. Lucas, B. Mobasher, K. Nandra, J. A. Newman, and A. van der Wel. CANDELS Multi-wavelength Catalogs: Source Detection and Photometry in the GOODS-South Field. , 207:24, August 2013.

[94] B. Häußler, S. P. Bamford, M. Vika, A. L. Rojas, M. Barden, L. S. Kelvin, M. Alpaslan, A. S. G. Robotham, S. P. Driver, I. K. Baldry, S. Brough, A. M. Hopkins, J. Liske, R. C. Nichol, C. C. Popescu, and R. J. Tuffs. MegaMorph - multiwavelength measurement of galaxy structure: complete Sérsic profile information from modern surveys. , 430:330–369, March 2013.

[95] Kari Helgason, Massimo Ricotti, and Alexander Kashlinsky. Reconstructing the Near-infrared Background Fluctuations from Known Galaxy Populations Using Multiband Measurements of Luminosity Functions. , 752(2):113, June 2012.

[96] G. Helou and D. W. Walker, editors. *Infrared astronomical satellite (IRAS) catalogs and atlases. Volume 7: The small scale structure catalog*, volume 7, 1988.

[97] S. Hemmati, S. H. Miller, B. Mobasher, H. Nayyeri, H. C. Ferguson, Y. Guo, A. M. Koekemoer, D. C. Koo, and C. Papovich. Kiloparsec-scale Properties of Emission-line Galaxies. , 797:108, December 2014.

[98] S. Hemmati, L. Yan, T. Diaz-Santos, L. Armus, P. Capak, A. Faisst, and D. Masters. The Local [C ii] 158 μm Emission Line Luminosity Function. , 834:36, January 2017.

[99] R. Herrera-Camus, A. Bolatto, J. D. Smith, B. Draine, E. Pellegrini, M. Wolfire, K. Croxall, I. de Looze, D. Calzetti, R. Kennicutt, A. Crocker, L. Armus, P. van der Werf, K. Sandstrom, M. Galametz, B. Brandl, B. Groves, D. Rigopoulou, F. Walter, A. Leroy, M. Boquien, F. S. Tabatabaei, and P. Beirao. The Ionized Gas in Nearby Galaxies as Traced by the [N II] 122 and 205 μm Transitions. , 826:175, August 2016.

[100] R. Herrera-Camus, A. D. Bolatto, M. G. Wolfire, J. D. Smith, K. V. Croxall, R. C. Kennicutt, D. Calzetti, G. Helou, F. Walter, A. K. Leroy, B. Draine, B. R. Brandl, L. Armus, K. M. Sandstrom, D. A. Dale, G. Aniano, S. E. Meidt, M. Boquien, L. K. Hunt, M. Galametz, F. S. Tabatabaei, E. J. Murphy, P. Appleton, H. Roussel, C. Engelbracht, and P. Beirao. [C II] 158 μm Emission as a Star Formation Tracer. , 800:1, February 2015.

[101] Y. D. Hezaveh, D. P. Marrone, C. D. Fassnacht, J. S. Spilker, J. D. Vieira, J. E. Aguirre, K. A. Aird, M. Aravena, M. L. N. Ashby, M. Bayliss, B. A. Benson, L. E. Bleem, M. Bothwell, M. Brodwin, J. E. Carlstrom, C. L. Chang, S. C. Chapman, T. M. Crawford, A. T. Crites, C. De

Breuck, T. de Haan, M. A. Dobbs, E. B. Fomalont, E. M. George, M. D. Gladders, A. H. Gonzalez, T. R. Greve, N. W. Halverson, F. W. High, G. P. Holder, W. L. Holzapfel, S. Hoover, J. D. Hrubes, K. Husband, T. R. Hunter, R. Keisler, A. T. Lee, E. M. Leitch, M. Lueker, D. Luong-Van, M. Malkan, V. McIntyre, J. J. McMahon, J. Mehl, K. M. Menten, S. S. Meyer, L. M. Mocanu, E. J. Murphy, T. Natoli, S. Padin, T. Plagge, C. L. Reichardt, A. Rest, J. Ruel, J. E. Ruhl, K. Sharon, K. K. Schaffer, L. Shaw, E. Shirokoff, B. Stalder, Z. Staniszewski, A. A. Stark, K. Story, K. Vanderlinde, A. Weiß, N. Welikala, and R. Williamson. ALMA Observations of SPT-discovered, Strongly Lensed, Dusty, Star-forming Galaxies. , 767:132, April 2013.

[102] H. Hildebrandt, S. Arnouts, P. Capak, L. A. Moustakas, C. Wolf, F. B. Abdalla, R. J. Assef, M. Banerji, N. Bentez, G. B. Brammer, T. Budavári, S. Carliles, D. Coe, T. Dahlen, R. Feldmann, D. Gerdes, B. Gillis, O. Ilbert, R. Kotulla, O. Lahav, I. H. Li, J. M. Miralles, N. Purger, S. Schmidt, and J. Singal. PHAT: PHoto-z Accuracy Testing. , 523:A31, Nov 2010.

[103] Eric Hivon, Krzysztof M. Górski, C. Barth Netterfield, Brendan P. Crill, Simon Prunet, and Frode Hansen. MASTER of the Cosmic Microwave Background Anisotropy Power Spectrum: A Fast Method for Statistical Analysis of Large and Complex Cosmic Microwave Background Data Sets. , 567(1):2–17, March 2002.

[104] D. J. Hollenbach and A. G. G. M. Tielens. Dense Photodissociation Regions (PDRs). , 35:179–216, 1997.

[105] D. J. Hollenbach and A. G. G. M. Tielens. Photodissociation regions in the interstellar medium of galaxies. *Reviews of Modern Physics*, 71:173–230, January 1999.

[106] P. F. Hopkins, E. Quataert, and N. Murray. The structure of the interstellar medium of star-forming galaxies. , 421:3488–3521, April 2012.

[107] B. Hoyle. Measuring photometric redshifts using galaxy images and Deep Neural Networks. *Astronomy and Computing*, 16:34–40, Jul 2016.

[108] T. M. Hughes, M. Baes, M. R. P. Schirm, T. J. Parkin, R. Wu, I. De Looze, C. D. Wilson, S. Viaene, G. J. Bendo, A. Boselli, D. Cormier, E. Ibar, O. . Karczewski, N. Lu, and L. Spinoglio. The spatially resolved correlation between [NII] 205 μm line emission and the 24 μm continuum in nearby galaxies. , 587:A45, March 2016.

[109] J. B. Hutchings, N. Maddox, R. M. Cutri, and B. O. Nelson. Host Galaxies of 2MASS-Selected QSOs to Redshift 0.3. , 126:63–72, July 2003.

[110] D. Huterer, M. Takada, G. Bernstein, and B. Jain. Systematic errors in future weak-lensing surveys: requirements and prospects for self-calibration. , 366:101–114, February 2006.

[111] M. T. Huynh, A. E. Kimball, R. P. Norris, I. Smail, K. E. Chow, K. E. K. Coppin, B. H. C. Emonts, R. J. Ivison, V. Smolcic, and A. M. Swinbank. Detection of molecular gas in an ALMA [C II]-identified submillimetre galaxy at z = 4.44. , 443:L54–L58, September 2014.

[112] O. Ilbert, S. Arnouts, H. J. McCracken, M. Bolzonella, E. Bertin, O. Le Fèvre, Y. Mellier, G. Zamorani, R. Pellò, A. Iovino, L. Tresse, V. Le Brun, D. Bottini, B. Garilli, D. Maccagni, J. P. Picat, R. Scaramella, M. Scodeggio, G. Vettolani, A. Zanichelli, C. Adami, S. Bardelli, A. Cappi, S. Charlot, P. Ciliegi, T. Contini, O. Cucciati, S. Foucaud, P. Franzetti, I. Gavignaud, L. Guzzo, B. Marano, C. Marinoni, A. Mazure, B. Meneux, R. Merighi, S. Paltani, A. Pollo, L. Pozzetti, M. Radovich, E. Zucca, M. Bondi, A. Bongiorno, G. Busarello, S. de La Torre, L. Gregorini, F. Lamareille, G. Mathez, P. Merluzzi, V. Ripepi, D. Rizzo, and D. Vergani. Accurate photometric redshifts for the CFHT legacy survey calibrated using the VIMOS VLT deep survey. , 457:841–856, October 2006.

[113] R. J. Ivison, I. Smail, P. P. Papadopoulos, I. Wold, J. Richard, A. M. Swinbank, J.-P. Kneib, and F. N. Owen. Gas, dust and stars in the SCUBA galaxy, SMMJ02399-0136: the EVLA reveals a colossal galactic nursery. , 404:198–205, May 2010.

[114] R. J. Ivison, A. M. Swinbank, B. Swinyard, I. Smail, C. P. Pearson, D. Rigopoulou, E. Polehampton, J.-P. Baluteau, M. J. Barlow, A. W. Blain, J. Bock, D. L. Clements, K. Coppin, A. Cooray, A. Danielson, E. Dwek, A. C. Edge, A. Franceschini, T. Fulton, J. Glenn, M. Griffin, K. Isaak, S. Leeks, T. Lim, D. Naylor, S. J. Oliver, M. J. Page, I. Pérez Fournon, M. Rowan-Robinson, G. Savini, D. Scott, L. Spencer, I. Valtchanov, L. Vigroux, and G. S. Wright. *Herschel* and SCUBA-2 imaging and spectroscopy of a bright, lensed submillimetre galaxy at z = 2.3. , 518:L35, July 2010.

[115] K. Iwasawa, D. B. Sanders, S. H. Teng, V. U, L. Armus, A. S. Evans, J. H. Howell, S. Komossa, J. M. Mazzarella, A. O. Petric, J. A. Surace, T. Vavilkin, S. Veilleux, and N. Trentham. C-GOALS: Chandra observations of a complete sample of luminous infrared galaxies from the IRAS Revised Bright Galaxy Survey. , 529:A106, May 2011.

[116] Rafael Izbicki and Ann B. Lee. Converting high-dimensional regression to high-dimensional conditional density estimation. *Electron. J. Statist.*, 11(2):2800–2831, 2017.

[117] E. Jones and J. Singal. Analysis of a custom support vector machine for photometric redshift estimation and the inclusion of galaxy shape information. , 600:A113, Apr 2017.

[118] J. Kamenetzky, N. Rangwala, J. Glenn, P. R. Maloney, and A. Conley. L'_{CO}/L_{FIR} Relations with CO Rotational Ladders of Galaxies Across the *Herschel* SPIRE Archive. , 829:93, October 2016.

[119] A. Kashlinsky, R. G. Arendt, M. L. N. Ashby, G. G. Fazio, J. Mather, and S. H. Moseley. New Measurements of the Cosmic Infrared Background Fluctuations in Deep *Spitzer*/IRAC Survey Data and Their Cosmological Implications. , 753(1):63, July 2012.

[120] A. Kashlinsky, R. G. Arendt, F. Atrio-Barandela, N. Cappelluti, A. Ferrara, and G. Hasinger. Looking at cosmic near-infrared background radiation anisotropies. *Reviews of Modern Physics*, 90(2):025006, April 2018.

[121] A. Kashlinsky, R. G. Arendt, J. Mather, and S. H. Moseley. Tracing the first stars with fluctuations of the cosmic infrared background. , 438(7064):45–50, November 2005.

[122] A. Kashlinsky, R. G. Arendt, J. Mather, and S. H. Moseley. New Measurements of Cosmic Infrared Background Fluctuations from Early Epochs. , 654(1):L5–L8, January 2007.

[123] M. J. Kaufman, M. G. Wolfire, and D. J. Hollenbach. [Si II], [Fe II], [C II], and H_2 Emission from Massive Star-forming Regions. , 644:283–299, June 2006.

[124] M. J. Kaufman, M. G. Wolfire, D. J. Hollenbach, and M. L. Luhman. Far-Infrared and Submillimeter Emission from Galactic and Extragalactic Photodissociation Regions. , 527:795–813, December 1999.

[125] R. C. Kennicutt and N. J. Evans. Star Formation in the Milky Way and Nearby Galaxies. , 50:531–608, September 2012.

[126] R. C. Kennicutt, Jr. Star Formation in Galaxies Along the Hubble Sequence. , 36:189–232, 1998.

[127] S. M. Kent. CCD surface photometry of field Galaxies. II - Bulge/disk decompositions. , 59:115–159, October 1985.

[128] A. Kirkpatrick, A. Pope, D. M. Alexander, V. Charmandaris, E. Daddi, M. Dickinson, D. Elbaz, J. Gabor, H. S. Hwang, R. Ivison, J. Mullaney, M. Pannella, D. Scott, B. Altieri,

H. Aussel, F. Bournaud, V. Buat, D. Coia, H. Dannerbauer, K. Dasyra, J. Kartaltepe, R. Leiton, L. Lin, G. Magdis, B. Magnelli, G. Morrison, P. Popesso, and I. Valtchanov. GOODS-*Herschel*: Impact of Active Galactic Nuclei and Star Formation Activity on Infrared Spectral Energy Distributions at High Redshift. , 759:139, November 2012.

[129] Anton M. Koekemoer, S. M. Faber, Henry C. Ferguson, Norman A. Grogin, Dale D. Kocevski, David C. Koo, Kamson Lai, Jennifer M. Lotz, Ray A. Lucas, Elizabeth J. McGrath, Sara Ogaz, Abhijith Rajan, Adam G. Riess, Steve A. Rodney, Louis Strolger, Stefano Casertano, Marco Castellano, Tomas Dahlen, Mark Dickinson, Timothy Dolch, Adriano Fontana, Mauro Giavalisco, Andrea Grazian, Yicheng Guo, Nimish P. Hathi, Kuang-Han Huang, Arjen van der Wel, Hao-Jing Yan, Viviana Acquaviva, David M. Alexander, Omar Almaini, Matthew L. N. Ashby, Marco Barden, Eric F. Bell, Frédéric Bournaud, Thomas M. Brown, Karina I. Caputi, Paolo Cassata, Peter J. Challis, Ranga-Ram Chary, Edmond Cheung, Michele Cirasuolo, Christopher J. Conselice, Asantha Roshan Cooray, Darren J. Croton, Emanuele Daddi, Romeel Davé, Duilia F. de Mello, Loic de Ravel, Avishai Dekel, Jennifer L. Donley, James S. Dunlop, Aaron A. Dutton, David Elbaz, Giovanni G. Fazio, Alexei V. Filippenko, Steven L. Finkelstein, Chris Frazer, Jonathan P. Gardner, Peter M. Garnavich, Eric Gawiser, Ruth Gruetzbauch, Will G. Hartley, Boris Häussler, Jessica Herrington, Philip F. Hopkins, Jia-Sheng Huang, Saurabh W. Jha, Andrew Johnson, Jeyhan S. Kartaltepe, Ali A. Khostovan, Robert P. Kirshner, Caterina Lani, Kyoung-Soo Lee, Weidong Li, Piero Madau, Patrick J. McCarthy, Daniel H. McIntosh, Ross J. McLure, Conor McPartland, Bahram Mobasher, Heidi Moreira, Alice Mortlock, Leonidas A. Moustakas, Mark Mozena, Kirpal Nandra, Jeffrey A. Newman, Jennifer L. Nielsen, Sami Niemi, Kai G. Noeske, Casey J. Papovich, Laura Pentericci, Alexandra Pope, Joel R. Primack, Swara Ravindranath,

Naveen A. Reddy, Alvio Renzini, Hans-Walter Rix, Aday R. Robaina, David J. Rosario, Piero Rosati, Sara Salimbeni, Claudia Scarlata, Brian Siana, Luc Simard, Joseph Smidt, Diana Snyder, Rachel S. Somerville, Hyron Spinrad, Amber N. Straughn, Olivia Telford, Harry I. Teplitz, Jonathan R. Trump, Carlos Vargas, Carolin Villforth, Cory R. Wagner, Pat Wand ro, Risa H. Wechsler, Benjamin J. Weiner, Tommy Wiklind, Vivienne Wild, Grant Wilson, Stijn Wuyts, and Min S. Yun. CANDELS: The Cosmic Assembly Near-infrared Deep Extragalactic Legacy SurveyThe Hubble Space Telescope Observations, Imaging Data Products, and Mosaics. , 197(2):36, Dec 2011.

[130] Teuvo Kohonen. Self-organized formation of topologically correct feature maps. *Biological cybernetics*, 43(1):59–69, 1982.

[131] Teuvo Kohonen. The self-organizing map. *Proceedings of the IEEE*, 78(9):1464–1480, 1990.

[132] M. Krips, A. B. Peck, K. Sakamoto, G. B. Petitpas, D. J. Wilner, S. Matsushita, and D. Iono. Sma high angular resolution imaging of the lensed quasar apm 08279+5255. *The Astrophysical Journal Letters*, 671(1):L5, 2007.

[133] M. J. Kurtz, M. J. Geller, D. G. Fabricant, W. F. Wyatt, and I. P. Dell'Antonio. μ-PhotoZ: Photometric Redshifts by Inverting the Tolman Surface Brightness Test. , 134:1360–1367, October 2007.

[134] K. M. Lanzetta, A. Yahil, and A. Fernández-Soto. Star-forming galaxies at very high redshifts. , 381:759–763, June 1996.

[135] S. Lepp and A. Dalgarno. Heating of interstellar gas by large molecules or small grains. , 335:769–773, December 1988.

[136] A. K. Leroy, F. Walter, E. Brinks, F. Bigiel, W. J. G. de Blok, B. Madore, and M. D. Thornley. The Star Formation Efficiency in Nearby Galaxies: Measuring Where Gas Forms Stars Effectively. , 136:2782–2845, December 2008.

[137] J.-F. Lestrade, C. L. Carilli, K. Thanjavur, J.-P. Kneib, D. A. Riechers, F. Bertoldi, F. Walter, and A. Omont. A Molecular Einstein Ring Toward the z = 3.93 Submillimeter Galaxy MM18423+5938. , 739:L30, September 2011.

[138] D. C. Lis, D. A. Neufeld, T. G. Phillips, M. Gerin, and R. Neri. Discovery of Water Vapor in the High-redshift Quasar APM 08279+5255 at z = 3.91. , 738:L6, September 2011.

[139] S. D. Lord, D. J. Hollenbach, M. R. Haas, R. H. Rubin, S. W. J. Colgan, and E. F. Erickson. Interstellar Properties of a Dual Nuclear Starburst: Far-Infrared Spectroscopy of M82. , 465:703, July 1996.

[140] M. O. Lorenz. Methods of measuring the concentration of wealth. *Publications of the American Statistical Association*, 9(70):209–219, 1905.

[141] J. M. Lotz, J. Primack, and P. Madau. A New Nonparametric Approach to Galaxy Morphological Classification. , 128:163–182, July 2004.

[142] N. Lu, Y. Zhao, T. Dáz-Santos, C. K. Xu, Y. Gao, L. Armus, K. G. Isaak, J. M. Mazzarella, P. P. van der Werf, P. N. Appleton, V. Charmandaris, A. S. Evans, J. Howell, K. Iwasawa, J. Leech, S. Lord, A. O. Petric, G. C. Privon, D. B. Sanders, B. Schulz, and J. A. Surace. A *Herschel* Space Observatory Spectral Line Survey of Local Luminous Infrared Galaxies from 194 to 671 Microns. *ArXiv e-prints*, February 2017.

[143] N. Lu, Y. Zhao, C. K. Xu, Y. Gao, L. Armus, J. M. Mazzarella, K. G. Isaak, A. O. Petric, V. Charmandaris, T. Dáz-Santos, A. S. Evans, J. Howell, P. Appleton, H. Inami, K. Iwasawa,

J. Leech, S. Lord, D. B. Sanders, B. Schulz, J. Surace, and P. P. van der Werf. Warm Molecular Gas in Luminous Infrared Galaxies. , 787:L23, June 2014.

[144] Z. Ma, W. Hu, and D. Huterer. Effects of Photometric Redshift Uncertainties on Weak-Lensing Tomography. , 636:21–29, January 2006.

[145] G. E. Magdis, E. Daddi, M. Béthermin, M. Sargent, D. Elbaz, M. Pannella, M. Dickinson, H. Dannerbauer, E. da Cunha, F. Walter, D. Rigopoulou, V. Charmandaris, H. S. Hwang, and J. Kartaltepe. The Evolving Interstellar Medium of Star-forming Galaxies since z = 2 as Probed by Their Infrared Spectral Energy Distributions. , 760:6, November 2012.

[146] G. E. Magdis, D. Rigopoulou, R. Hopwood, J.-S. Huang, D. Farrah, C. Pearson, A. Alonso-Herrero, J. J. Bock, D. Clements, A. Cooray, M. J. Griffin, S. Oliver, I. Perez Fournon, D. Riechers, B. M. Swinyard, D. Scott, N. Thatte, I. Valtchanov, and M. Vaccari. A Far-infrared Spectroscopic Survey of Intermediate Redshift (Ultra) Luminous Infrared Galaxies. , 796:63, November 2014.

[147] B. Magnelli, D. Lutz, P. Santini, A. Saintonge, S. Berta, M. Albrecht, B. Altieri, P. Andreani, H. Aussel, F. Bertoldi, M. Béthermin, A. Bongiovanni, P. Capak, S. Chapman, J. Cepa, A. Cimatti, A. Cooray, E. Daddi, A. L. R. Danielson, H. Dannerbauer, J. S. Dunlop, D. Elbaz, D. Farrah, N. M. Förster Schreiber, R. Genzel, H. S. Hwang, E. Ibar, R. J. Ivison, E. Le Floc'h, G. Magdis, R. Maiolino, R. Nordon, S. J. Oliver, A. Pérez Garcá, A. Poglitsch, P. Popesso, F. Pozzi, L. Riguccini, G. Rodighiero, D. Rosario, I. Roseboom, M. Salvato, M. Sanchez-Portal, D. Scott, I. Smail, E. Sturm, A. M. Swinbank, L. J. Tacconi, I. Valtchanov, L. Wang, and S. Wuyts. A *Herschel* view of the far-infrared properties of submillimetre galaxies. , 539:A155, March 2012.

[148] S. Malhotra. Far Infrared Spectroscopy of Star-Forming Galaxies: Expectations for the *Herschel* Space Observatory. In G. L. Pilbratt, J. Cernicharo, A. M. Heras, T. Prusti, and R. Harris, editors, *The Promise of the Herschel Space Observatory*, volume 460 of *ESA Special Publication*, page 155, July 2001.

[149] P. R. Maloney, D. J. Hollenbach, and A. G. G. M. Tielens. X-Ray–irradiated Molecular Gas. I. Physical Processes and General Results. , 466:561, July 1996.

[150] R. Mandelbaum, U. Seljak, C. M. Hirata, S. Bardelli, M. Bolzonella, A. Bongiorno, M. Carollo, T. Contini, C. E. Cunha, B. Garilli, A. Iovino, P. Kampczyk, J.-P. Kneib, C. Knobel, D. C. Koo, F. Lamareille, O. Le Fèvre, J.-F. Le Borgne, S. J. Lilly, C. Maier, V. Mainieri, M. Mignoli, J. A. Newman, P. A. Oesch, E. Perez-Montero, E. Ricciardelli, M. Scodeggio, J. Silverman, and L. Tasca. Precision photometric redshift calibration for galaxy-galaxy weak lensing. , 386:781–806, May 2008.

[151] D. Masters, P. Capak, D. Stern, O. Ilbert, M. Salvato, S. Schmidt, G. Longo, J. Rhodes, S. Paltani, B. Mobasher, H. Hoekstra, H. Hildebrandt, J. Coupon, C. Steinhardt, J. Speagle, A. Faisst, A. Kalinich, M. Brodwin, M. Brescia, and S. Cavuoti. Mapping the Galaxy Color-Redshift Relation: Optimal Photometric Redshift Calibration Strategies for Cosmology Surveys. , 813:53, November 2015.

[152] T. Matsumoto, H. J. Seo, W. S. Jeong, H. M. Lee, S. Matsuura, H. Matsuhara, S. Oyabu, J. Pyo, and T. Wada. AKARI Observation of the Fluctuation of the Near-infrared Background. , 742(2):124, December 2011.

[153] R. Meijerink and M. Spaans. Diagnostics of irradiated gas in galaxy nuclei. I. A far-ultraviolet and X-ray dominated region code. , 436:397–409, June 2005.

[154] M. Meixner, A. Cooray, R. Carter, M. DiPirro, A. Flores, D. Leisawitz, L. Armus, C. Battersby, E. Bergin, C. M. Bradford, K. Ennico, G. J. Melnick, S. Milam, D. Narayanan, K. Pontoppidan, A. Pope, T. Roellig, K. Sandstrom, K. Y. L. Su, J. Vieira, E. Wright, J. Zmuidzinas, S. Alato, S. Carey, M. Gerin, F. Helmich, K. Menten, D. Scott, I. Sakon, and R. Vavrek. The Far-Infrared Surveyor Mission study: paper I, the genesis. In *Society of Photo-Optical Instrumentation Engineers (SPIE) Conference Series*, volume 9904 of , page 99040K, July 2016.

[155] Kristen Menou. Morpho-Photometric Redshifts. *arXiv e-prints*, page arXiv:1811.06374, Nov 2018.

[156] H. Messias, S. Dye, N. Nagar, G. Orellana, R. S. Bussmann, J. Calanog, H. Dannerbauer, H. Fu, E. Ibar, A. Inohara, R. J. Ivison, M. Negrello, D. A. Riechers, Y.-K. Sheen, J. E. Aguirre, S. Amber, M. Birkinshaw, N. Bourne, C. M. Bradford, D. L. Clements, A. Cooray, G. De Zotti, R. Demarco, L. Dunne, S. Eales, S. Fleuren, J. Kamenetzky, R. E. Lupu, S. J. Maddox, D. P. Marrone, M. J. Michaowski, E. J. Murphy, H. T. Nguyen, A. Omont, K. Rowlands, D. Smith, M. Smith, E. Valiante, and J. D. Vieira. *Herschel*-ATLAS and ALMA. HATLAS J142935.3-002836, a lensed major merger at redshift 1.027. , 568:A92, August 2014.

[157] Ketron Mitchell-Wynne, Asantha Cooray, Yongquan Xue, Bin Luo, William Brandt, and Anton Koekemoer. Cross-correlation between X-Ray and Optical/Near-infrared Background Intensity Fluctuations. , 832(2):104, December 2016.

[158] L. Moncelsi, P. A. R. Ade, E. L. Chapin, L. Cortese, M. J. Devlin, S. Dye, S. Eales, M. Griffin, M. Halpern, P. C. Hargrave, G. Marsden, P. Mauskopf, C. B. Netterfield, E. Pascale, D. Scott, M. D. P. Truch, C. Tucker, M. P. Viero, and D. V. Wiebe. A Panchromatic Study of

BLAST Counterparts: Total Star Formation Rate, Morphology, Active Galactic Nucleus Fraction, and Stellar Mass. , 727:83, February 2011.

[159] M. Moshir and et al. IRAS Faint Source Catalogue, version 2.0. In *IRAS Faint Source Catalogue, version 2.0 (1990)*, 1990.

[160] M. Mosleh, R. J. Williams, M. Franx, V. Gonzalez, R. J. Bouwens, P. Oesch, I. Labbe, G. D. Illingworth, and M. Trenti. The Evolution of Mass-Size Relation for Lyman Break Galaxies from z = 1 to z = 7. , 756:L12, September 2012.

[161] Dipak Munshi, Patrick Valageas, Ludovic van Waerbeke, and Alan Heavens. Cosmology with weak lensing surveys. , 462(3):67–121, Jun 2008.

[162] D. A. Naylor, J.-P. Baluteau, M. J. Barlow, D. Benielli, M. Ferlet, T. R. Fulton, M. J. Griffin, T. Grundy, P. Imhof, S. Jones, K. King, S. J. Leeks, T. L. Lim, N. Lu, G. Makiwa, E. T. Polehampton, G. Savini, S. D. Sidher, L. D. Spencer, C. Surace, B. M. Swinyard, and R. Wesson. In-orbit performance of the *Herschel*/SPIRE imaging Fourier transform spectrometer. In *Space Telescopes and Instrumentation 2010: Optical, Infrared, and Millimeter Wave*, volume 7731 of , page 773116, July 2010.

[163] H. Nayyeri, S. Hemmati, B. Mobasher, H. C. Ferguson, A. Cooray, G. Barro, S. M. Faber, M. Dickinson, A. M. Koekemoer, M. Peth, M. Salvato, M. L. N. Ashby, B. Darvish, J. Donley, M. Durbin, S. Finkelstein, A. Fontana, N. A. Grogin, R. Gruetzbauch, K. Huang, A. A. Khostovan, D. Kocevski, D. Kodra, B. Lee, J. Newman, C. Pacifici, J. Pforr, M. Stefanon, T. Wiklind, S. P. Willner, S. Wuyts, M. Castellano, C. Conselice, T. Dolch, J. S. Dunlop, A. Galametz, N. P. Hathi, R. A. Lucas, and H. Yan. CANDELS Multi-wavelength Catalogs: Source Identification and Photometry in the CANDELS COSMOS Survey Field. , 228:7, January 2017.

[164] M. Negrello, R. Hopwood, S. Dye, E. d. Cunha, S. Serjeant, J. Fritz, K. Rowlands, S. Fleuren, R. S. Bussmann, A. Cooray, H. Dannerbauer, J. Gonzalez-Nuevo, A. Lapi, A. Omont, S. Amber, R. Auld, M. Baes, S. Buttiglione, A. Cava, L. Danese, A. Dariush, G. De Zotti, L. Dunne, S. Eales, E. Ibar, R. J. Ivison, S. Kim, L. Leeuw, S. Maddox, M. J. Michaowski, M. Massardi, E. Pascale, M. Pohlen, E. Rigby, D. J. B. Smith, W. Sutherland, P. Temi, and J. Wardlow. *Herschel* *-ATLAS: deep HST/WFC3 imaging of strongly lensed submillimetre galaxies. , 440:1999–2012, May 2014.

[165] M. Nonino, M. Dickinson, P. Rosati, A. Grazian, N. Reddy, S. Cristiani, M. Giavalisco, H. Kuntschner, E. Vanzella, E. Daddi, R. A. E. Fosbury, and C. Cesarsky. Deep U Band and R Imaging of Goods-South: Observations, Data Reduction and First Results. , 183(2):244–260, Aug 2009.

[166] S. J. Oliver, J. Bock, B. Altieri, A. Amblard, V. Arumugam, H. Aussel, T. Babbedge, A. Beelen, M. Béthermin, A. Blain, A. Boselli, C. Bridge, D. Brisbin, V. Buat, D. Burgarella, N. Castro-Rodrguez, A. Cava, P. Chanial, M. Cirasuolo, D. L. Clements, A. Conley, L. Conversi, A. Cooray, C. D. Dowell, E. N. Dubois, E. Dwek, S. Dye, S. Éales, D. Elbaz, D. Farrah, A. Feltre, P. Ferrero, N. Fiolet, M. Fox, A. Franceschini, W. Gear, E. Giovannoli, J. Glenn, Y. Gong, E. A. González Solares, M. Griffin, M. Halpern, M. Harwit, E. Hatziminaoglou, S. Heinis, P. Hurley, H. S. Hwang, A. Hyde, E. Ibar, O. Ilbert, K. Isaak, R. J. Ivison, G. Lagache, E. Le Floc'h, L. Levenson, B. L. Faro, N. Lu, S. Madden, B. Maffei, G. Magdis, G. Mainetti, L. Marchetti, G. Marsden, J. Marshall, A. M. J. Mortier, H. T. Nguyen, B. O'Halloran, A. Omont, M. J. Page, P. Panuzzo, A. Papageorgiou, H. Patel, C. P. Pearson, I. Pérez-Fournon, M. Pohlen, J. I. Rawlings, G. Raymond, D. Rigopoulou, L. Riguccini, D. Rizzo, G. Rodighiero, I. G. Roseboom, M. Rowan-Robinson, M. Sánchez Portal, B. Schulz, D. Scott, N. Seymour, D. L. Shupe, A. J.

Smith, J. A. Stevens, M. Symeonidis, M. Trichas, K. E. Tugwell, M. Vaccari, I. Valtchanov, J. D. Vieira, M. Viero, L. Vigroux, L. Wang, R. Ward, J. Wardlow, G. Wright, C. K. Xu, and M. Zemcov. The *Herschel* Multi-tiered Extragalactic Survey: HerMES. , 424:1614–1635, August 2012.

[167] K. Ota, F. Walter, K. Ohta, B. Hatsukade, C. L. Carilli, E. da Cunha, J. González-López, R. Decarli, J. A. Hodge, H. Nagai, E. Egami, L. Jiang, M. Iye, N. Kashikawa, D. A. Riechers, F. Bertoldi, P. Cox, R. Neri, and A. Weiss. ALMA Observation of 158 μm [C II] Line and Dust Continuum of a z = 7 Normally Star-forming Galaxy in the Epoch of Reionization. , 792:34, September 2014.

[168] I. Oteo, R. J. Ivison, L. Dunne, I. Smail, A. M. Swinbank, Z.-Y. Zhang, A. Lewis, S. Maddox, D. Riechers, S. Serjeant, P. Van der Werf, A. D. Biggs, M. Bremer, P. Cigan, D. L. Clements, A. Cooray, H. Dannerbauer, S. Eales, E. Ibar, H. Messias, M. J. Michaowski, I. Pérez-Fournon, and E. van Kampen. Witnessing the Birth of the Red Sequence: ALMA High-resolution Imaging of [C II] and Dust in Two Interacting Ultra-red Starbursts at z = 4.425. , 827:34, August 2016.

[169] S. Ott. The *Herschel* Data Processing System HIPE and Pipelines Up and Running Since the Start of the Mission. In Y. Mizumoto, K.-I. Morita, and M. Ohishi, editors, *Astronomical Data Analysis Software and Systems XIX*, volume 434 of *Astronomical Society of the Pacific Conference Series*, page 139, December 2010.

[170] P. P. Papadopoulos, W.-F. Thi, and S. Viti. CI lines as tracers of molecular gas, and their prospects at high redshifts. , 351:147–160, June 2004.

[171] C. Pearson, D. Rigopoulou, P. Hurley, D. Farrah, J. Afonso, J. Bernard-Salas, C. Borys, D. L. Clements, D. Cormier, A. Efstathiou, E. Gonzalez-Alfonso, V. Lebouteiller, and H. Spoon. HERUS: A CO Atlas from SPIRE Spectroscopy of Local ULIRGs. , 227:9, November 2016.

[172] M. Pereira-Santaella, L. Spinoglio, G. Busquet, C. D. Wilson, J. Glenn, K. G. Isaak, J. Kamenetzky, N. Rangwala, M. R. P. Schirm, M. Baes, M. J. Barlow, A. Boselli, A. Cooray, and D. Cormier. *Herschel*/SPIRE Submillimeter Spectra of Local Active Galaxies. , 768:55, May 2013.

[173] M. A. Peth, J. M. Lotz, P. E. Freeman, C. McPartland, S. A. Mortazavi, G. F. Snyder, G. Barro, N. A. Grogin, Y. Guo, S. Hemmati, J. S. Kartaltepe, D. D. Kocevski, A. M. Koekemoer, D. H. McIntosh, H. Nayyeri, C. Papovich, J. R. Primack, and R. C. Simons. Beyond spheroids and discs: classifications of CANDELS galaxy structure at 1.4 z 2 via principal component analysis. , 458:963–987, May 2016.

[174] V. Petrosian. Surface brightness and evolution of galaxies. , 209:L1–L5, October 1976.

[175] G. L. Pilbratt, J. R. Riedinger, T. Passvogel, G. Crone, D. Doyle, U. Gageur, A. M. Heras, C. Jewell, L. Metcalfe, S. Ott, and M. Schmidt. *Herschel* Space Observatory. An ESA facility for far-infrared and submillimetre astronomy. , 518:L1, July 2010.

[176] A. Poglitsch, C. Waelkens, N. Geis, H. Feuchtgruber, B. Vandenbussche, L. Rodriguez, O. Krause, E. Renotte, C. van Hoof, P. Saraceno, J. Cepa, F. Kerschbaum, P. Agnèse, B. Ali, B. Altieri, P. Andreani, J.-L. Augueres, Z. Balog, L. Barl, O. H. Bauer, N. Belbachir, M. Benedettini, N. Billot, O. Boulade, H. Bischof, J. Blommaert, E. Callut, C. Cara, R. Cerulli, D. Cesarsky, A. Contursi, Y. Creten, W. De Meester, V. Doublier, E. Doumayrou, L. Duband, K. Exter, R. Genzel, J.-M. Gillis, U. Grözinger, T. Henning, J. Herreros, R. Huygen, M. Inguscio,

G. Jakob, C. Jamar, C. Jean, J. de Jong, R. Katterloher, C. Kiss, U. Klaas, D. Lemke, D. Lutz, S. Madden, B. Marquet, J. Martignac, A. Mazy, P. Merken, F. Montfort, L. Morbidelli, T. Müller, M. Nielbock, K. Okumura, R. Orfei, R. Ottensamer, S. Pezzuto, P. Popesso, J. Putzeys, S. Regibo, V. Reveret, P. Royer, M. Sauvage, J. Schreiber, J. Stegmaier, D. Schmitt, J. Schubert, E. Sturm, M. Thiel, G. Tofani, R. Vavrek, M. Wetzstein, E. Wieprecht, and E. Wiezorrek. The Photodetector Array Camera and Spectrometer (PACS) on the *Herschel* Space Observatory. , 518:L2, July 2010.

[177] E. Polehampton, R. Hopwood, I. Valtchanov, N. Lu, N. Marchili, D. Naylor, M. van der Wiel, and T. Fulton. The *Herschel*/SPIRE Spectrometer Useful Scripts. In A. R. Taylor and E. Rosolowsky, editors, *Astronomical Data Analysis Software an Systems XXIV (ADASS XXIV)*, volume 495 of *Astronomical Society of the Pacific Conference Series*, page 339, September 2015.

[178] Kai Lars Polsterer, Antonio D'Isanto, and Fabian Gieseke. Uncertain Photometric Redshifts. *arXiv e-prints*, page arXiv:1608.08016, Aug 2016.

[179] N. Ponthieu, J. Grain, and G. Lagache. POKER: estimating the power spectrum of diffuse emission with complex masks and at high angular resolution. , 535:A90, Nov 2011.

[180] M. W. Pound and M. G. Wolfire. The Photo Dissociation Region Toolbox. In R. W. Argyle, P. S. Bunclark, and J. R. Lewis, editors, *Astronomical Data Analysis Software and Systems XVII*, volume 394 of *Astronomical Society of the Pacific Conference Series*, page 654, August 2008.

[181] Chris W. Purcell, James S. Bullock, and Andrew R. Zentner. Shredded Galaxies as the Source of Diffuse Intrahalo Light on Varying Scales. , 666(1):20–33, September 2007.

[182] N. Rangwala, P. R. Maloney, J. Glenn, C. D. Wilson, A. Rykala, K. Isaak, M. Baes, G. J. Bendo, A. Boselli, C. M. Bradford, D. L. Clements, A. Cooray, T. Fulton, P. Imhof, J. Kamenetzky, S. C. Madden, E. Mentuch, N. Sacchi, M. Sauvage, M. R. P. Schirm, M. W. L. Smith, L. Spinoglio, and M. Wolfire. Observations of Arp 220 Using *Herschel*-SPIRE: An Unprecedented View of the Molecular Gas in an Extreme Star Formation Environment. , 743:94, December 2011.

[183] T. D. Rawle, E. Egami, R. S. Bussmann, M. Gurwell, R. J. Ivison, F. Boone, F. Combes, A. L. R. Danielson, M. Rex, J. Richard, I. Smail, A. M. Swinbank, B. Altieri, A. W. Blain, B. Clement, M. Dessauges-Zavadsky, A. C. Edge, G. G. Fazio, T. Jones, J.-P. Kneib, A. Omont, P. G. Pérez-González, D. Schaerer, I. Valtchanov, P. P. van der Werf, G. Walth, M. Zamojski, and M. Zemcov. [C II] and ^{12}CO(1-0) Emission Maps in HLSJ091828.6+514223: A Strongly Lensed Interacting System at z = 5.24. , 783:59, March 2014.

[184] J. Retzlaff, P. Rosati, M. Dickinson, B. Vandame, C. Rité, M. Nonino, C. Cesarsky, and GOODS Team. The Great Observatories Origins Deep Survey. VLT/ISAAC near-infrared imaging of the GOODS-South field. , 511:A50, Feb 2010.

[185] D. A. Riechers, C. L. Carilli, P. L. Capak, N. Z. Scoville, V. Smolcic, E. Schinnerer, M. Ýun, P. Cox, F. Bertoldi, A. Karim, and L. Yan. ALMA Imaging of Gas and Dust in a Galaxy Protocluster at Redshift 5.3: [C II] Emission in "Typical" Galaxies and Dusty Starbursts 1 Billion Years after the Big Bang. , 796:84, December 2014.

[186] D. A. Riechers, F. Walter, C. L. Carilli, and G. F. Lewis. Imaging The Molecular Gas in a z = 3.9 Quasar Host Galaxy at 0farcs3 Resolution: A Central, Sub-Kiloparsec Scale Star Formation Reservoir in APM 08279+5255. , 690:463–485, January 2009.

[187] G. W. Roberts-Borsani, M. J. Jiménez-Donaire, M. Daprà, K. Alatalo, I. Aretxaga, J. Álvarez-Márquez, A. J. Baker, S. Fujimoto, P. A. Gallardo, M. Gralla, M. Hilton, J. P. Hughes, C. Jiménez, N. Laporte, T. A. Marriage, F. Nati, J. Rivera, A. Sievers, A. Weiß, G. W. Wilson, E. J. Wollack, and M. S. Yun. Multiwavelength characterisation of an ACT-selected, lensed dusty star-forming galaxy at z=2.64. *ArXiv e-prints*, June 2017.

[188] M. J. F. Rosenberg, P. P. van der Werf, S. Aalto, L. Armus, V. Charmandaris, T. Díaz-Santos, A. S. Evans, J. Fischer, Y. Gao, E. González-Alfonso, T. R. Greve, A. I. Harris, C. Henkel, F. P. Israel, K. G. Isaak, C. Kramer, R. Meijerink, D. A. Naylor, D. B. Sanders, H. A. Smith, M. Spaans, L. Spinoglio, G. J. Stacey, I. Veenendaal, S. Veilleux, F. Walter, A. Weiß, M. C. Wiedner, M. H. D. van der Wiel, and E. M. Xilouris. The *Herschel* Comprehensive (U)LIRG Emission Survey (HERCULES): CO Ladders, Fine Structure Lines, and Neutral Gas Cooling. , 801:72, March 2015.

[189] M. Rowan-Robinson, A. Efstathiou, A. Lawrence, S. Oliver, A. Taylor, T. J. Broadhurst, R. G. McMahon, C. R. Benn, J. J. Condon, C. J. Lonsdale, P. Hacking, T. Conrow, W. S. Saunders, D. L. Clements, R. S. Ellis, and I. Robson. The ultraviolet-to-radio continuum of the ultraluminous galaxy IRAS F10214 + 4724. , 261:513–521, April 1993.

[190] D. B. Sanders and I. F. Mirabel. Luminous Infrared Galaxies. , 34:749, 1996.

[191] L. Sargsyan, D. Weedman, V. Lebouteiller, J. Houck, D. Barry, A. Hovhannisyan, and A. Mickaelian. Infrared Spectra and Spectral Energy Distributions for Dusty Starbursts and Active Galactic Nuclei. , 730:19, March 2011.

[192] D. Schaerer, F. Boone, T. Jones, M. Dessauges-Zavadsky, P. Sklias, M. Zamojski, A. Cava, J. Richard, R. Ellis, T. D. Rawle, E. Egami, and F. Combes. ALMA detection of [C ii] 158 μm emission from a strongly lensed z = 2.013 star-forming galaxy. , 576:L2, April 2015.

[193] K. Schroder, V. Staemmler, M. D. Smith, D. R. Flower, and R. Jaquet. Excitation of the fine-structure transitions of C in collisions with ortho- and para-H_2. *Journal of Physics B Atomic Molecular Physics*, 24:2487–2502, May 1991.

[194] N. Scoville, K. Sheth, H. Aussel, P. Vanden Bout, P. Capak, A. Bongiorno, C. M. Casey, L. Murchikova, J. Koda, J. Álvarez-Márquez, N. Lee, C. Laigle, H. J. McCracken, O. Ilbert, A. Pope, D. Sanders, J. Chu, S. Toft, R. J. Ivison, and S. Manohar. ISM Masses and the Star formation Law at Z = 1 to 6: ALMA Observations of Dust Continuum in 145 Galaxies in the COSMOS Survey Field. , 820:83, April 2016.

[195] S. Serjeant. Up to 100,000 Reliable Strong Gravitational Lenses in Future Dark Energy Experiments. , 793:L10, September 2014.

[196] E. S. Sheldon, C. E. Cunha, R. Mandelbaum, J. Brinkmann, and B. A. Weaver. Photometric Redshift Probability Distributions for Galaxies in the SDSS DR8. , 201:32, August 2012.

[197] J. Singal, M. Shmakova, B. Gerke, R. L. Griffith, and J. Lotz. The Efficacy of Galaxy Shape Parameters in Photometric Redshift Estimation: A Neural Network Approach. , 123:615, May 2011.

[198] John Y. H. Soo, Bruno Moraes, Benjamin Joachimi, William Hartley, Ofer Lahav, Aldée Charbonnier, Martn Makler, Maria E. S. Pereira, Johan Comparat, Thomas Érben, Alexie Leauthaud, Huanyuan Shan, and Ludovic Van Waerbeke. Morpho-z: improving photometric redshifts with galaxy morphology. , 475(3):3613–3632, Apr 2018.

[199] M. Spaans, A. G. G. M. Tielens, E. F. van Dishoeck, and E. L. O. Bakes. Photon-dominated regions around cool stars: The effects of the color temperature of the radiation field. , 437:270–280, December 1994.

[200] Joshua S. Speagle and Daniel J. Eisenstein. Deriving photometric redshifts using fuzzy archetypes and self-organizing maps - I. Methodology. , 469(1):1186–1204, Jul 2017.

[201] Joshua S. Speagle and Daniel J. Eisenstein. Deriving photometric redshifts using fuzzy archetypes and self-organizing maps - II. Implementation. , 469(1):1205–1224, Jul 2017.

[202] SPICA Study Team Collaboration. SPICA Assessment Study Report for ESA Cosmic Vision 2015-2025 Plan. *ArXiv e-prints*, January 2010.

[203] J. S. Spilker, D. P. Marrone, J. E. Aguirre, M. Aravena, M. L. N. Ashby, M. Béthermin, C. M. Bradford, M. S. Bothwell, M. Brodwin, J. E. Carlstrom, S. C. Chapman, T. M. Crawford, C. de Breuck, C. D. Fassnacht, A. H. Gonzalez, T. R. Greve, B. Gullberg, Y. Hezaveh, W. L. Holzapfel, K. Husband, J. Ma, M. Malkan, E. J. Murphy, C. L. Reichardt, K. M. Rotermund, B. Stalder, A. A. Stark, M. Strandet, J. D. Vieira, A. Weiß, and N. Welikala. The Rest-frame Submillimeter Spectrum of High-redshift, Dusty, Star-forming Galaxies. , 785:149, April 2014.

[204] J. S. Spilker, D. P. Marrone, M. Aravena, M. Béthermin, M. S. Bothwell, J. E. Carlstrom, S. C. Chapman, T. M. Crawford, C. de Breuck, C. D. Fassnacht, A. H. Gonzalez, T. R. Greve, Y. Hezaveh, K. Litke, J. Ma, M. Malkan, K. M. Rotermund, M. Strandet, J. D. Vieira, A. Weiss, and N. Welikala. ALMA Imaging and Gravitational Lens Models of South Pole TelescopeSelected Dusty, Star-Forming Galaxies at High Redshifts. , 826:112, August 2016.

[205] L. Spinoglio, M. Benedettini, G. de Troia, M. A. Malkan, P. E. Clegg, J. Fischer, M. Greenhouse, S. Satyapal, H. A. Smith, G. J. Stacey, and S. J. Unger. ISO spectroscopy of Seyfert galaxies: fine structure line diagnostics in seven galaxies. In A. Salama, M. F. Kessler,

K. Leech, and B. Schulz, editors, *ISO Beyond the Peaks: The 2nd ISO Workshop on Analytical Spectroscopy*, volume 456 of *ESA Special Publication*, page 261, November 2000.

[206] L. Spinoglio, K. M. Dasyra, A. Franceschini, C. Gruppioni, E. Valiante, and K. Isaak. Erratum: "Far-IR/Submillimeter Spectroscopic Cosmological Surveys: Predictions of Infrared Line Luminosity Functions for z 4 Galaxies" <A href="/abs/2012ApJ...745..171S">(2012, ApJ, 745, 171)</A>. , 791:138, August 2014.

[207] L. Spinoglio and M. A. Malkan. Infrared line diagnostics of active galactic nuclei. , 399:504–520, November 1992.

[208] G. J. Stacey. Far-infrared spectroscopy of galaxies. In E. Böhm-Vitense, editor, *Infrared Spectroscopy in Astronomy*, volume 290 of *ESA Special Publication*, September 1989.

[209] G. J. Stacey, N. Geis, R. Genzel, J. B. Lugten, A. Poglitsch, A. Sternberg, and C. H. Townes. The 158 micron C II line - A measure of global star formation activity in galaxies. , 373:423–444, June 1991.

[210] G. J. Stacey, S. Hailey-Dunsheath, C. Ferkinhoff, T. Nikola, S. C. Parshley, D. J. Benford, J. G. Staguhn, and N. Fiolet. A 158 μm [C II] Line Survey of Galaxies at z 1-2: An Indicator of Star Formation in the Early Universe. , 724:957–974, December 2010.

[211] E. Sturm, E. González-Alfonso, S. Veilleux, J. Fischer, J. Graciá-Carpio, S. Hailey-Dunsheath, A. Contursi, A. Poglitsch, A. Sternberg, R. Davies, R. Genzel, D. Lutz, L. Tacconi, A. Verma, R. Maiolino, and J. A. de Jong. Massive Molecular Outflows and Negative Feedback in ULIRGs Observed by *Herschel*-PACS. , 733:L16, May 2011.

[212] E. Sturm, A. Poglitsch, A. Contursi, J. Graciá-Carpio, J. Fischer, E. González-Alfonso, R. Genzel, S. Hailey-Dunsheath, D. Lutz, L. Tacconi, J. Dejong, A. Sternberg, A. Verma,

S. Madden, L. Vigroux, D. Cormier, U. Klaas, M. Nielbock, O. Krause, J. Schreiber, and M. Haas. Star formation and the ISM in infrared bright galaxies - SHINING. In M. Röllig, R. Simon, V. Ossenkopf, and J. Stutzki, editors, *EAS Publications Series*, volume 52 of *EAS Publications Series*, pages 55–61, November 2011.

[213] E. Sturm, A. Verma, J. Graciá-Carpio, S. Hailey-Dunsheath, A. Contursi, J. Fischer, E. González-Alfonso, A. Poglitsch, A. Sternberg, R. Genzel, D. Lutz, L. Tacconi, N. Christopher, and J. de Jong. *Herschel*-PACS spectroscopy of IR-bright galaxies at high redshift. , 518:L36, July 2010.

[214] Ian Sullivan, Asantha Cooray, Ranga-Ram Chary, James J. Bock, Mark Brodwin, Michael J. I. Brown, Arjun Dey, Mark Dickinson, Peter Eisenhardt, Henry C. Ferguson, Mauro Giavalisco, Brian Keating, Andrew Lange, Bahram Mobasher, William T. Reach, Daniel Stern, and Edward L. Wright. Clustering of the IR Background Light with *Spitzer*: Contribution from Resolved Sources. , 657(1):37–50, March 2007.

[215] A. M. Swinbank, P. P. Papadopoulos, P. Cox, M. Krips, R. J. Ivison, I. Smail, A. P. Thomson, R. Neri, J. Richard, and H. Ebeling. The Interstellar Medium in Distant Star-forming Galaxies: Turbulent Pressure, Fragmentation, and Cloud Scaling Relations in a Dense Gas Disk at z = 2.3. , 742:11, November 2011.

[216] B. M. Swinyard, E. T. Polehampton, R. Hopwood, I. Valtchanov, N. Lu, T. Fulton, D. Benielli, P. Imhof, N. Marchili, J.-P. Baluteau, G. J. Bendo, M. Ferlet, M. J. Griffin, T. L. Lim, G. Makiwa, D. A. Naylor, G. S. Orton, A. Papageorgiou, C. P. Pearson, B. Schulz, S. D. Sidher, L. D. Spencer, M. H. D. van der Wiel, and R. Wu. Calibration of the *Herschel* SPIRE Fourier Transform Spectrometer. , 440:3658–3674, June 2014.

[217] R. Tagliaferri, G. Longo, S. Andreon, S. Capozziello, C. Donalek, and G. Giordano. Neural Networks for Photometric Redshifts Evaluation. *Lecture Notes in Computer Science*, 2859:226–234, 2003.

[218] T. Takahashi, J. Silk, and D. J. Hollenbach. H2O heating in molecular clouds - Line transfer and thermal balance in a warm dusty medium. , 275:145–162, December 1983.

[219] Cameron Thacker, Asantha Cooray, Joseph Smidt, Francesco De Bernardis, K. Mitchell-Wynne, A. Amblard, R. Auld, M. Baes, D. L. Clements, A. Dariush, G. De Zotti, L. Dunne, S. Eales, R. Hopwood, C. Hoyos, E. Ibar, M. Jarvis, S. Maddox, M. J. Michaowski, E. Pascale, D. Scott, S. Serjeant, M. W. L. Smith, E. Valiante, and P. van der Werf. H-ATLAS: The Cosmic Abundance of Dust from the Far-infrared Background Power Spectrum. , 768(1):58, May 2013.

[220] Cameron Thacker, Yan Gong, Asantha Cooray, Francesco De Bernardis, Joseph Smidt, and Ketron Mitchell-Wynne. Cross-correlation of Near- and Far-infrared Background Anisotropies as Traced by *Spitzer* and *Herschel*. , 811(2):125, October 2015.

[221] Rodger I. Thompson, Daniel Eisenstein, Xiaohui Fan, Marcia Rieke, and Robert C. Kennicutt. Evidence for a z < 8 Origin of the Source-subtracted Near-Infrared Background. , 666(2):658–662, September 2007.

[222] A. P. Thomson, R. J. Ivison, I. Smail, A. M. Swinbank, A. Weiss, J.-P. Kneib, P. P. Papadopoulos, A. J. Baker, C. E. Sharon, and G. A. van Moorsel. VLA imaging of ^{12}CO J = 1-0 and free-free emission in lensed submillimetre galaxies. , 425:2203–2211, September 2012.

[223] A. G. G. M. Tielens and D. Hollenbach. Photodissociation regions. I - Basic model. II - A model for the Orion photodissociation region. , 291:722–754, April 1985.

[224] N. Timmons, A. Cooray, D. A. Riechers, H. Nayyeri, H. Fu, E. Jullo, M. D. Gladders, M. Baes, R. S. Bussmann, J. Calanog, D. L. Clements, E. da Cunha, S. Dye, S. A. Eales, C. Furlanetto, J. Gonzalez-Nuevo, J. Greenslade, M. Gurwell, H. Messias, M. J. Michaowski, I. Oteo, I. Pérez-Fournon, D. Scott, and E. Valiante. Multi-wavelength Lens Reconstruction of a Planck and *Herschel*-detected Star-bursting Galaxy. , 829:21, September 2016.

[225] B. D. Uzgil, C. M. Bradford, S. Hailey-Dunsheath, P. R. Maloney, and J. E. Aguirre. Constraining the ISM Properties of the Cloverleaf Quasar Host Galaxy with *Herschel* Spectroscopy. , 832:209, December 2016.

[226] I. Valtchanov, J. Virdee, R. J. Ivison, B. Swinyard, P. van der Werf, D. Rigopoulou, E. da Cunha, R. Lupu, D. J. Benford, D. Riechers, I. Smail, M. Jarvis, C. Pearson, H. Gomez, R. Hopwood, B. Altieri, M. Birkinshaw, D. Coia, L. Conversi, A. Cooray, G. de Zotti, L. Dunne, D. Frayer, L. Leeuw, A. Marston, M. Negrello, M. S. Portal, D. Scott, M. A. Thompson, M. Vaccari, M. Baes, D. Clements, M. J. Michaowski, H. Dannerbauer, S. Serjeant, R. Auld, S. Buttiglione, A. Cava, A. Dariush, S. Dye, S. Eales, J. Fritz, E. Ibar, S. Maddox, E. Pascale, M. Pohlen, E. Rigby, G. Rodighiero, D. J. B. Smith, P. Temi, J. Carpenter, A. Bolatto, M. Gurwell, and J. D. Vieira. Physical conditions of the interstellar medium of high-redshift, strongly lensed submillimetre galaxies from the *Herschel*-ATLAS. , 415:3473–3484, August 2011.

[227] Ivan Valtchanov, Rosalind Hopwood, Edward Polehampton, Dominique Benielli, Trevor Fulton, Peter Imhof, Tomasz Konopczynski, Tanya Lim, Nanyao Lu, Nicola Marchili, David Naylor, and Bruce Swinyard. Relative pointing offset analysis of calibration targets with repeated observations with *Herschel*-spire fourier-transform spectrometer. *Éxperimental Astronomy*, 37(2):207–223, 2014.

[228] F. F. S. van der Tak, J. H. Black, F. L. Schöier, D. J. Jansen, and E. F. van Dishoeck. A computer program for fast non-LTE analysis of interstellar line spectra. With diagnostic plots to interpret observed line intensity ratios. , 468:627–635, June 2007.

[229] A. van der Wel, M. Franx, P. G. van Dokkum, R. E. Skelton, I. G. Momcheva, K. E. Whitaker, G. B. Brammer, E. F. Bell, H.-W. Rix, S. Wuyts, H. C. Ferguson, B. P. Holden, G. Barro, A. M. Koekemoer, Y.-Y. Chang, E. J. McGrath, B. Häussler, A. Dekel, P. Behroozi, M. Fumagalli, J. Leja, B. F. Lundgren, M. V. Maseda, E. J. Nelson, D. A. Wake, S. G. Patel, I. Labbé, S. M. Faber, N. A. Grogin, and D. D. Kocevski. 3D-HST+CANDELS: The Evolution of the Galaxy Size-Mass Distribution since z = 3. , 788:28, June 2014.

[230] P. P. van der Werf, A. Berciano Alba, M. Spaans, A. F. Loenen, R. Meijerink, D. A. Riechers, P. Cox, A. Weiß, and F. Walter. Water Vapor Emission Reveals a Highly Obscured, Star-forming Nuclear Region in the QSO Host Galaxy APM 08279+5255 at z = 3.9. , 741:L38, November 2011.

[231] P. P. van der Werf, K. G. Isaak, R. Meijerink, M. Spaans, A. Rykala, T. Fulton, A. F. Loenen, F. Walter, A. Weiß, L. Armus, J. Fischer, F. P. Israel, A. I. Harris, S. Veilleux, C. Henkel, G. Savini, S. Lord, H. A. Smith, E. González-Alfonso, D. Naylor, S. Aalto, V. Charmandaris, K. M. Dasyra, A. Evans, Y. Gao, T. R. Greve, R. Güsten, C. Kramer, J. Martn-Pintado, J. Mazzarella, P. P. Papadopoulos, D. B. Sanders, L. Spinoglio, G. Stacey, C. Vlahakis, M. C. Wiedner, and E. M. Xilouris. Black hole accretion and star formation as drivers of gas excitation and chemistry in Markarian 231. , 518:L42, July 2010.

[232] E. Vanzella, S. Cristiani, A. Fontana, M. Nonino, S. Arnouts, E. Giallongo, A. Grazian, G. Fasano, P. Popesso, P. Saracco, and S. Zaggia. Photometric redshifts with the Multilayer

Perceptron Neural Network: Application to the HDF-S and SDSS. , 423:761–776, August 2004.

[233] S. Venturini and P. M. Solomon. The Molecular Disk in the Cloverleaf Quasar. , 590:740–745, June 2003.

[234] O. Vince and I. Csabai. Toward more precise photometric redshift estimation. In A. Vazdekis and R. Peletier, editors, *Stellar Populations as Building Blocks of Galaxies*, volume 241 of *IAU Symposium*, pages 573–574, August 2007.

[235] Y. Wadadekar. Estimating Photometric Redshifts Using Support Vector Machines. , 117:79–85, January 2005.

[236] John S. Ward, Jonas Zmuidzinas, Andrew I. Harris, and Kate G. Isaak. A 12co j = 6-5 map of m82: The significance of warm molecular gas. *The Astrophysical Journal*, 587(1):171, 2003.

[237] J. L. Wardlow, A. Cooray, W. Osage, N. Bourne, D. Clements, H. Dannerbauer, L. Dunne, S. Dye, S. Eales, D. Farrah, C. Furlanetto, E. Ibar, R. Ivison, S. Maddox, M. M. Michaowski, D. Riechers, D. Rigopoulou, D. Scott, M. W. L. Smith, L. Wang, P. van der Werf, E. Valiante, I. Valtchanov, and A. Verma. The interstellar medium in high-redshift submillimeter galaxies as probed by infrared spectroscopy. *ArXiv e-prints*, January 2017.

[238] M. J. Way. Galaxy Zoo Morphology and Photometric Redshifts in the Sloan Digital Sky Survey. , 734:L9, June 2011.

[239] M. J. Way and A. N. Srivastava. Novel Methods for Predicting Photometric Redshifts from Broadband Photometry Using Virtual Sensors. , 647:102–115, August 2006.

[240] Rogier A. Windhorst, Seth H. Cohen, Nimish P. Hathi, Patrick J. McCarthy, Jr. Ryan, Russell E., Haojing Yan, Ivan K. Baldry, Simon P. Driver, Jay A. Frogel, David T. Hill, Lee S.

Kelvin, Anton M. Koekemoer, Matt Mechtley, Robert W. O'Connell, Aaron S. G. Robotham, Michael J. Rutkowski, Mark Seibert, Amber N. Straughn, Richard J. Tuffs, Bruce Balick, Howard E. Bond, Howard Bushouse, Daniela Calzetti, Mark Crockett, Michael J. Disney, Michael A. Dopita, Donald N. B. Hall, Jon A. Holtzman, Sugata Kaviraj, Randy A. Kimble, John W. MacKenty, Max Mutchler, Francesco Paresce, Abihit Saha, Joseph I. Silk, John T. Trauger, Alistair R. Walker, Bradley C. Whitmore, and Erick T. Young. The Hubble Space Telescope Wide Field Camera 3 Early Release Science Data: Panchromatic Faint Object Counts for 0.2-2 μm Wavelength. , 193(2):27, Apr 2011.

[241] D. Wittman. What Lies Beneath: Using p(z) to Reduce Systematic Photometric Redshift Errors. , 700:L174–L177, August 2009.

[242] David Wittman, Ramya Bhaskar, and Ryan Tobin. Overconfidence in photometric redshift estimation. , 457(4):4005–4011, Apr 2016.

[243] M. G. Wolfire, D. Hollenbach, and A. G. G. M. Tielens. CO(J = 1-0) line emission from giant molecular clouds. , 402:195–215, January 1993.

[244] J. J. Wray and J. E. Gunn. A New Technique for Galaxy Photometric Redshifts in the Sloan Digital Sky Survey. , 678:144–153, May 2008.

[245] J. Wu, P. A. Vanden Bout, N. J. Evans, II, and M. M. Dunham. Continuum Observations at 350 Microns of High-Redshift Molecular Emission Line Galaxies. , 707:988–999, December 2009.

[246] R. Wu, E. T. Polehampton, M. Etxaluze, G. Makiwa, D. A. Naylor, C. Salji, B. M. Swinyard, M. Ferlet, M. H. D. van der Wiel, A. J. Smith, T. Fulton, M. J. Griffin, J.-P. Baluteau, D. Benielli, J. Glenn, R. Hopwood, P. Imhof, T. Lim, N. Lu, P. Panuzzo, C. Pearson, S. Sidher,

and I. Valtchanov. Observing extended sources with the *Herschel* SPIRE Fourier Transform Spectrometer. , 556:A116, August 2013.

[247] S. Wuyts, N. M. Förster Schreiber, R. Genzel, Y. Guo, G. Barro, E. F. Bell, A. Dekel, S. M. Faber, H. C. Ferguson, M. Giavalisco, N. A. Grogin, N. P. Hathi, K.-H. Huang, D. D. Kocevski, A. M. Koekemoer, D. C. Koo, J. Lotz, D. Lutz, E. McGrath, J. A. Newman, D. Rosario, A. Saintonge, L. J. Tacconi, B. J. Weiner, and A. van der Wel. Smooth(er) Stellar Mass Maps in CANDELS: Constraints on the Longevity of Clumps in High-redshift Star-forming Galaxies. , 753:114, July 2012.

[248] R. Yamada, S. Oyabu, H. Kaneda, M. Yamagishi, D. Ishihara, J. H. Kim, and M. Im. A Relation of the PAH 3.3 μm Feature with Star-forming Activity for Galaxies with a Wide Range of Infrared Luminosity. , 65:103, October 2013.

[249] T. Yamakawa, K. Horio, and R. Kubota. A som association network. In *Advances in Self-Organising Maps*, pages 15–20, London, 2001. Springer London.

[250] C. Yang, Y. Gao, A. Omont, D. Liu, K. G. Isaak, D. Downes, P. P. van der Werf, and N. Lu. Water Vapor in nearby Infrared Galaxies as Probed by *Herschel*. , 771:L24, July 2013.

[251] Bin Yue, Andrea Ferrara, Ruben Salvaterra, and Xuelei Chen. The contribution of high-redshift galaxies to the near-infrared background. , 431(1):383–393, May 2013.

[252] Bin Yue, Andrea Ferrara, Ruben Salvaterra, Yidong Xu, and Xuelei Chen. Infrared background signatures of the first black holes. , 433(2):1556–1566, August 2013.

[253] Bin Yue, Andrea Ferrara, Ruben Salvaterra, Yidong Xu, and Xuelei Chen. The brief era of direct collapse black hole formation. , 440(2):1263–1273, May 2014.

[254] M. S. Yun, I. Aretxaga, M. A. Gurwell, D. H. Hughes, A. Montaña, G. Narayanan, D. Rosa-González, D. Sánchez-Argüelles, F. P. Schloerb, R. L. Snell, O. Vega, G. W. Wilson,

M. Zeballos, M. Chavez, R. Cybulski, T. Dáz-Santos, V. De La Luz, N. Erickson, D. Ferrusca, H. B. Gim, M. H. Heyer, D. Iono, A. Pope, S. M. Rogstad, K. S. Scott, K. Souccar, E. Terlevich, R. Terlevich, D. Wilner, and J. A. Zavala. Early Science with the Large Millimeter Telescope: CO and [C II] Emission in the z = 4.3 AzTEC J095942.9+022938 (COSMOS AzTEC-1). , 454:3485–3499, December 2015.

[255] J. A. Zavala, M. S. Yun, I. Aretxaga, D. H. Hughes, G. W. Wilson, J. E. Geach, E. Egami, M. A. Gurwell, D. J. Wilner, I. Smail, A. W. Blain, S. C. Chapman, K. E. K. Coppin, M. Dessauges-Zavadsky, A. C. Edge, A. Montaña, K. Nakajima, T. D. Rawle, D. Sánchez-Argüelles, A. M. Swinbank, T. M. A. Webb, and M. Zeballos. Early Science with the Large Millimeter Telescope: observations of dust continuum and CO emission lines of cluster-lensed submillimetre galaxies at z=2.0-4.7. , 452:1140–1151, September 2015.

[256] Michael Zemcov, Joseph Smidt, Toshiaki Arai, James Bock, Asantha Cooray, Yan Gong, Min Gyu Kim, Phillip Korngut, Anson Lam, Dae Hee Lee, Toshio Matsumoto, Shuji Matsuura, Uk Won Nam, Gael Roudier, Kohji Tsumura, and Takehiko Wada. On the origin of near-infrared extragalactic background light anisotropy. *Science*, 346(6210):732–735, November 2014.

[257] H. Zhan and L. Knox. Baryon Oscillations and Consistency Tests for Photometrically Determined Redshifts of Very Faint Galaxies. , 644:663–670, June 2006.

[258] Y. Zhao, N. Lu, C. K. Xu, Y. Gao, S. Lord, J. Howell, K. G. Isaak, V. Charmandaris, T. Diaz-Santos, P. Appleton, A. Evans, K. Iwasawa, J. Leech, J. Mazzarella, A. O. Petric, D. B. Sanders, B. Schulz, J. Surace, and P. P. van der Werf. A *Herschel* Survey of the [N II] 205 μm Line in Local Luminous Infrared Galaxies: The [N II] 205 μm Emission as a Star Formation Rate Indicator. , 765:L13, March 2013.

[259] Y. Zhao, N. Lu, C. K. Xu, Y. Gao, S. D. Lord, V. Charmandaris, T. Diaz-Santos, A. Evans, J. Howell, A. O. Petric, P. P. van der Werf, and D. B. Sanders. The [NII] 205 μm Emission in Local Luminous Infrared Galaxies. , 819:69, March 2016.